Institut für Geowissenschaften
Mathematisch-Naturwissenschaftliche Fakultät
Universität Potsdam

Tectonic and climatic forcing in orogenic processes: the foreland basin point of view, Alborz mountains, N Iran

Paolo Ballato

Dissertation zur Erlangung des akademischen Grades
Doktor der Naturwissenschaften (Dr. rer. nat.)
in der Wissenschaftsdisziplin Geologie

eingereicht an der Mathematisch-Naturwissenschaftlichen Fakultät
der Universität Potsdam

Potsdam, im August 2009

Tag der Disputation: 26 November 2009

Gutachter

Prof. Dr. Manfred Strecker	Prof. Dr. Anke Friedrich
Potsdam Universität	LMU München

Abstract

Foreland-basin systems are excellent archives to decipher the feedbacks between surface and tectonic processes in orogens. The sedimentary architecture of a foreland-basin system reflects the balance between tectonic subsidence causing long-term accommodation space and sediment influx corresponding to efficiency of erosion and mass-redistribution processes. In order to explore the effects of climatic and tectonic forcing in such a system, I investigated the Oligo-Miocene foreland-basin sediments of the southern Alborz mountains, an intracontinental orogen in northern Iran, related to the Arabia-Eurasia continental collision.

This work includes absolute dating methods such as ^{40}Ar/^{39}Ar and zircon (U-Th)/He thermochronology, magnetostratigraphy, sedimentological analysis, sandstone and conglomerate provenance study, carbon and oxygen isotope analysis, and clay mineralogy study. Results show a systematic correlation between coarsening-upward cycles and sediment accumulation rates in the basin on 10^5 to 10^6yr time scales. During thrust loading phases, the coarse-grained fraction supplied by the uplifting range is stored in the proximal part of the basin (sedimentary facies retrogradation), while fine-grained sediments are deposited in distal sectors. Variations in sediment provenance during these phases of enhanced tectonic activity give evidence for erosional unroofing phases and/or drainage-reorganization events. In addition, enhanced tectonic activity promoted the growth of topography and associated orographic barrier effects, as demonstrated by sedimentologic indicators and the analysis of stable C and O isotopes from calcareous paleosols and lacustrine/palustrine samples.

Extensive progradation of coarse-grained deposits occurs during phases of decreased subsidence, when the coarse-grained fraction supplied by the uplifting range cannot be completely stored in the proximal part of the basin. In this environment, a reduction in basin subsidence is associated with laterally stacked fluvial channel deposits, and is related to intra-foreland uplift, as documented by growth strata, tectonic tilting, and sediment reworking. Increase in sediment accumulation rate associated with progradation of vertically-stacked coarse-grained fluvial channels also occurs. Paleosol O-isotope data shows that this increase is related to wetter climatic phases, suggesting that surface processes are more efficient and exhumation rates increase, giving rise to a positive feedback. Furthermore, isotopic and sedimentologic data show that starting from 10-9 Ma, climate became less arid with an increase in seasonality of precipitation. Because important changes were also recorded in the Mediterranean Sea and Asia at that time, the evidence for climatic variability observed in the Alborz mountains most likely reflects changes in Northern Hemisphere atmospheric circulation patterns.

This study has additional implications for the evolution of the Alborz mountains and the Arabia-Eurasia continental collision zone. At the orogenic scale, the locus of deformation did not move steadily southward, but stepped forward and backward since Oligocene time. In particular, from ~ 17.5 to 6.2 Ma the orogen grew by a combination of frontal accretion and wedge-internal deformation on time scales of ca. 0.7 to 2 Ma. Moreover, the provenance data suggest that prior to 10-9 Ma the shortening direction changed from NW-SE to NNE-SSW, in agreement with structural data.

On the scale of the entire collision zone, the evolution of the studied basins and adjacent mountain ranges suggests a new geodynamic model for the evolution of the Arabia-Eurasia continental collision zone. Numerous sedimentary basins in the Alborz mountains and in other locations of the Arabia-Eurasia collision zone record a change from a tensional (transtensional) to a compressional (transpressional) tectonic setting by ~ 36 Ma. I interpret this to reflect the onset of subduction of the stretched Arabian continental lithosphere beneath central Iran, leading to moderate plate coupling and lower- and upper-plate deformation. The increase in deformation rates in the southern Alborz mountains from ~ 17.5 Ma suggests that significant upper-plate deformation must have started by early Miocene time, most likely in response to an increase in degree of plate coupling. I suggest that this was related to the subduction of thicker Arabian continental lithosphere and the consequent onset of hard continental collision. This model reconciles the apparent lag time of 15-20 Ma between the late Eocene to early Oligocene age for the initial Arabia-Eurasia continental collision and the onset of widespread deformation across the collision zone to the north in early to late Miocene time.

Zusammenfassung

Systeme von Vorlandbecken repräsentieren bedeutende geologische Archive und dienen dem Verständnis von Rückkopplungen zwischen oberflächennahen und tektonischen Prozessen. Außerdem dokumentieren sie die Entwicklung unmittelbar angrenzender Bergketten. Die sedimentären Abfolgen in Vorlandbecken reflektieren das Gleichgewicht zwischen tektonischer Subsidenz, der Bildung langzeitlichen Akkommodationsraumes und des Sedimenteintrages, welcher wiederum die Wirksamkeit von Erosions- und Massenneuverteilungsprozessen wiederspiegelt. Um die Effekte von Klima und Tektonik in einem solchen System zu erforschen, untersuchte ich die Oligo-Miozänen Sedimente in den Vorlandbecken der südlichen Elburs Bergkette, einem intrakontinentalen Gebirge in Nord-Iran, das im Zuge der Arabisch-Eurasischen Kontinent-Kollision herausgehoben wurde.

In dieser Studie der Vorlandbeckensedimente wurden Datierungstechniken angewandt (^{40}Ar/^{39}Ar, (U-Th)/He Thermochronologie und Magnetostratigraphie), die Sedimente und deren Herkunft analysiert und die Tonmineralogie, sowie Sauerstoff- und Kohlenstoffisotope untersucht. Die Ergebnisse zeigen, dass auf einer Zeitskala von 10^5 bis 10^6 Jahren eine systematische Korrelation zwischen „coarsening upward“ Zyklen und den sedimentären Akkumulationsraten besteht. Während sukzessiver Überschiebungsphasen werden die durch Hebung der Bergkette bereitgestellten groben Kornfraktionen in proximale Bereiche des Beckens geliefert und feinkörnige Fazies in distalen Beckenregionen abgelagert. Variationen in der Sedimentherkunft in Phasen größerer tektonischer Aktivität zeugen von erosionaler Abdeckung und/oder der Umorganisation natürlicher Entwässerungsstrukturen. Außerdem zeigen die Untersuchungen an stabilen Isotopen, dass die verstärkte tektonische Aktivität das Anwachsen der Topographie förderte und damit die Wirksamkeit einer topographischen Barriere erhöhte.

Wenn aufgrund nachlassender Beckenabsenkung die grobe Kornfraktion nicht vollständig im Nahbereich des Beckens aufgenommen werden kann breitet sie sich in ferne Beckenregionen aus. Im Elburs wird die verringerte Subsidenz durch eine interne Hebung des Vorlandes hervorgerufen und ist mit einer lateralen Stapelung von Flussbetten assoziiert. Dokumentiert wird dies anhand konsequenten Schichtwachstums, tektonischer Schrägstellung und sedimentärer Umlagerung. Gleichzeitig nehmen die Sedimentationsraten zu. Die Sauerstoff-Isotope der Paläoböden zeigen, dass dieser Anstieg mit einer Phase feuchteren Klimas einhergeht, wodurch Oberflächenprozesse effizienter werden und Heraushebungssraten steigen, was eine positive Rückkopplung erzeugt. Des Weiteren zeigen die isotopischen und sedimentären Daten, dass seit 10-9 Millionen Jahren das Klima durch saisonalen Anstieg der Niederschläge zunehmend feuchter wurde. Da bedeutende klimatische Veränderungen zu dieser Zeit auch im Mittelmeerraum und Asien beobachtet wurden, ist anzunehmen, dass die klimatische Veränderung, die im Elburs Gebirge beobachtet wird, höchstwahrscheinlich Änderungen der atmosphärischen Zirkulationen der nördlichen Hemisphäre reflektiert.

Aus den Ergebnissen dieser Studie lassen sich zusätzliche Implikationen für die Entwicklung des Elburs Gebirges und die Arabisch-Eurasische kontinentale Kollisionszone ableiten. Die orogen-weite Hauptdeformation propagierte nicht gleichmäßig nach Süden, sondern seit dem Oligozän schrittweise vorwärts und rückwärts. Insbesondere von ~17,5 bis 6,2 Millionen Jahren wurde das Gebirge durch eine Kombination aus frontaler Akkretion und interner Keildeformation in Schritten von 0,7 bis 2 Millionen Jahren herausgehoben. Darüber hinaus deuten die Sedimentherkunftsdaten darauf hin, dass sich noch vor 10-9 Millionen Jahren die Haupteinengungsrichtung von NW-SE nach NNE-SSW veränderte.

Regional erlaubt die Geschichte der untersuchten Becken und angrenzenden Gebirgszüge Rückschlüsse auf ein neues geodynamisches Model zur Entwicklung der Arabisch-Eurasischen kontinentalen Kollisionszone. Zahlreiche Sedimentbecken des Elburs Gebirges und anderer Lokalitäten der Arabisch-Eurasischen Deformationszone belegen einen Wechsel von einem tensionalen (transtensionalen) zu einem kompressionalen (transpressionalen) tektonischen Regime vor ~36 Millionen Jahren . Dieser Wechsel könnte den Beginn der Subduktion von gedehnter arabischer kontinentaler Lithosphäre unter Zentral-Iran bedeuten, was zu einer moderaten Plattenkopplung und Deformation von Unter- sowie Oberplatte geführt

hat. Der Anstieg der Deformationsraten im südlichen Elburs Gebirge seit ~17,5 Millionen Jahren lässt vermuten, dass die Oberplatte, wahrscheinlich aufgrund steigender Plattenkopplung, seit dem frühen Miozän signifikant deformiert wurde. Diese Veränderung könnte der Subduktion mächtigerer arabischer kontinentaler Lithosphäre zugeschrieben werden und den Anfang echter kontinentaler Kollision bedeuten. Dieses Model erklärt daher die Zeitverzögerung zwischen der Initiation der Arabisch-Eurasischen kontinentalen Kollision (Eozän-Oligozän) and dem Beginn ausgedehnter Deformation in der Kollisionszone (Miozän).

Allgemeine Zusammenfassung

Vorlandbecken sind Akkumulationsbereiche zwischen Orogenen und undeformierter Kruste, in denen große Sedimentvolumen aufgenommen werden können. Sie bilden sich durch Biegeprozesse (tektonische Absenkung) aufgrund von topographischer Auflast (tektonische Auflast) und sind von der tektonischen Aktivität und angreifenden Oberflächenprozessen abhängig, welche wiederum an klimatische Bedingungen geknüpft sind. Die Heraushebung von Gebirgsregionen fördert das Abregnen entlang der entstandenen Topographie (orographische Niederschläge). Die Niederschläge wiederum führen zu effizienter Erosion und Umverteilung von Massen, was wiederum die Heraushebung des Gebirges verstärkt. Sedimentäre Ablagerungsbedingungen und Zusammensetzung in Vorlandbecken spiegeln das Gleichgewicht zwischen tektonischer Absenkung und Sedimenteintrag wieder. Um diese Beziehungen zu erfassen, wurden die Oligo- bis Miozänen Sedimente eines Vorlandbeckens des südlichen Elbursgebirges untersucht. Der Elburs ist ein intrakontinentaler Gebirgszug im Nordiran, welcher sich im Zuge der Arabisch-Eurasischen Kontinentkollision gebildet hat. Er stellt eine orographische Barriere für die niederschlagsreichen Nordwinde dar. Derzeit fallen bis zu 1.7 m Niederschlag pro Jahr an den Nordhängen, aber weniger als 0.3 m pro Jahr an der Südseite.

Auf Zeitskalen von 10^5 bis 10^6 Jahren zeigen die Miozänen Ablagerungen eine systematische Beziehung zwischen im Profilverlauf ansteigende Korngrößen und Sedimentakkumulationsraten im Becken. Hohe Raten spiegeln eine hohe tektonische Absenkung wieder, ausgelöst durch verstärkte topographische Auflast und daher verstärkter tektonischer Aktivität im Orogen. Die Ablagerung von feinkörnigem Material in den vom Gebirge mittel (medial) bis weit entfernten (distal) Bereichen des Vorlandbeckens fand in einer Phase mit hohen Sedimentakkumulationsraten (ca. 0.8 bis 2.2 mm/a) statt. Zeitgleich gab es Änderungen in der Sedimentzusammensetzung. Auch das deutet auf tektonische Auflast hin, in deren Folge neue Gesteinseinheiten aufgeschlossen wurden und/oder das Entwässerungsnetz geändert wurde. Während dieser Phase verstärkter tektonischer Aktivität wurde die grobkörnige Sedimentfraktion, die aus dem herausgehobenen Gebirge abgetragen wurde, am Gebirgsrand (proximal) abgelagert, während die feinkörnige Fraktion bis in mediale bis distale Beckenbereiche transportiert wurde. Demgegenüber wurden in Phasen geringer Sedimentakkumulation (ca. 0.3 mm/a) die grobkörnigen Sedimente in den medialen und distalen Vorlandbeckenbereichen abgelagert. Das ging mit Änderungen in der Geometrie der Sedimentschichten einher und deutet auf ein Nachlassen der tektonischen Absenkung hin. Ursache ist eine lokale Hebung innerhalb des Beckens, die einen weit reichenden Transport der grobkörnigen Sedimente vom Orogen weg ermöglicht. Alternativ ist möglich, dass das Voranschreiten der Grobfraktion in Phasen moderater Sedimentakkumulation stattfand (ca. 0.6 mm/a), wenn diese Fraktion nicht komplett vom proximalen Beckenbereich aufgenommen wurde. Sauerstoffisotopendaten zeigen eine zeitgleiche feuchtere Phase an, was vermuten lässt, dass effiziente Oberflächenprozesse zu einem vermehrten Sedimenteintrag ins Becken führten. Die Isotopendaten zeigen außerdem Änderungen in den Paläoumweltbedingungen und im Paläoklima vor 17 Ma und erneut beginnend vor 10-9 Ma. Die älteren Änderungen sind wahrscheinlich auf lokale Prozesse, wie verstärkte Effizienz der orographischen Barriere gegen die niederschlagsreichen Nordwinde, zurückzuführen. Die jüngeren Änderungen dagegen spiegeln möglicherweise Variationen im Westwindsystem der Nordhalbkugel wieder, ausgelöst durch Prozesse, die mit dem Tibet Plateau in Verbindung stehen.

Hinsichtlich der orogenen Entwicklung im Kontext der Arabisch-Eurasischen Kontinentkollision zeigt die Studie einen bedeutenden Wechsel von einem Dehnungs- zu einem Einengungsmilieu vor etwa 36 Ma. Das könnte durch das Abtauchen gedehnter Arabischer kontinentaler Lithosphäre unter Zentraliran hervorgerufen worden sein, was in der Frühphase der Kollision zu moderater Plattenkopplung mit mäßiger Deformation geführt hat. Anschließend kam es im frühen Miozän zu verstärkter Plattenkopplung mit signifikanter Deformation der oberen Platte. Deren Ursache könnte im Abtauchen dicker Arabischer kontinentaler Lithosphäre zu finden sein und damit den Beginn der eigentlichen Kontinentkollision markieren.

Contents

List of figures

List of tables

Acknowledgements

Before starting this PhD, Iran was for me an Islamic country with fuzzy borders associated to a never-ending war in the times of my childhood. Once I visited it, I discovered a millenary culture and a variegated society, where modernity and tradition form a delicate equilibrium. I was impressed by the generosity and the curiosity of people, which stimulated my mind and opened my eyes to alternative views on life. I thank my Iranian colleagues, friends, drivers and their families (Saeid, Mohammad, Houssein, Amir, Mahdi, Majid, Morteza, Reza, Bobak, Ali, Bashir among others), institutions (Building and Housing Research Center, Geological Survey of Iran, Municipality of Kilan), and all those people which I met only for a cup of the in a remote village or in the chaotic Tehran.

This experience was possible, because my advisor Manfred Strecker let me play this game, supporting my research, and allowing me to follow my interests. I would like to thank him for all of this. Anke Friedrich, and Maria Mutti, are also thanked because they gave me the chance to be a graduate student in Potsdam, during a pessimistic phase of my life.

I have crossed the Iranian pathway with my friend and colleague Gela Landgraf. Together we spent few months in the field collecting data, and many days/weeks in the traffic of Tehran, learning a more calm and patient style of life. She was also fundamental in solving daily problems related to life in Germany In addition, together with Henry Wichura she helped me to organize the German part of this thesis.

During these years I had the chance to collaborate with many experts in different fields, which provided introductions and insights to new techniques, allowing me to obtain the results presented in these chapters. In particular I thank Barbara Carrapa, Brian Horton, Andreas Mulch, Norbert Nowaczyk, Daniel Stockli, Masa Sudo, Ed Sobel, Cornelius Uba and the reviewers Eduardo Garzanti and Hugh Sinclair.

At Potsdam University, I found many friends and colleagues, which stimulated my scientific interests and more in general my life. Rather than writing a long list of names risking forgetting someone, I thank all those people which passed through the Institute of Geosciences in the last four-five years. I also thank Tania Roeper and Dana Pilz who provided valuable help in sample processing.

The financial support was provided by the German Research Foundation (Leibniz Award to M. Strecker and grant STR 373/19-1 to M. Strecker and A. Friedrich), and the Graduate School of the University of Potsdam. In addition, for the first twenty-eight years of my life, most of the financial support was provided by my parents who supported my education and my choices even the more questionable.

Finally, my love and thank go to Jessica who makes my life so beautiful, and to Elvira who nicely entered in our life one month ago.

1. Introduction

Over the past two decades, an increasing number of theoretical, analog and numerical modeling studies, as well as sedimentological and thermochronologic investigations recognized the feedbacks between tectonic and surface processes at the scale of the orogens (e.g., Dahlen, 1990; Molnar and England, 1990; Hoffman and Grotzinger, 1993; Willet et al., 1993; Masek and Duncan, 1998; Willet, 1999; Montgomery and Brandon, 2002; Sobel et al., 2003; Sobel and Strecker, 2003; Sinclair et al., 2005; Hoth et al., 2006; Simpson, 2006; Whipple an Meade 2006; Naylor and Sinclair, 2007; Bookhagen and Strecker 2008). These studies have demonstrated that focused orographic precipitation, which reflects the response of moisture bearing winds to topographic relief generated by rock uplift on time scales of several 10^5 to 10^6 years, has a fundamental impact on the locus of erosion. This may influence the magnitude and location of long-term exhumation, promoting different styles of tectonic deformation and variability in orogenic growth (e.g., Willet et al., 1993; Masek and Duncan, 1998; Willet, 1999; Sobel and Strecker, 2003; Sinclair et al., 2005; Thiede et al., 2005; Hoth et al., 2006; Simpson, 2006; Whipple and Meade 2006; Naylor and Sinclair, 2007; Mora et al., 2008; Parra et al., 2009; Thiede et al., 2009). In fact, mass redistribution processes modify the state of stress of the lithosphere, dictating the locus of active deformation in the orogen (e.g. Willet, 1999; Sobel et al, 2003; Sobel and Strecker, 2003; Beaumont et al., 2006). These processes can lead to advection of hot, mechanically weak rocks, causing enhanced localized exhumation (e.g., Zeitler et al 2001; Koons et al., 2002; Thiede et al., 2005; Mora et al., 2008; Beaumont et al., 2006; Parra et al., 2009; Thiede et al., 2009). The magnitude and the spatial distribution of exhumation has been quantified with thermochronology (e.g., Reiners and Brandon, 2006 for a review; Huntington et al., 2007; Lock and Willet, 2008). In particular, improvements in dating techniques have allowed for exhumation studies over different time windows, from which complex variations in denudation rates can be deciphered on 10^5 to 10^6 time scales (e.g, Reiners, et al., 2001; Carrapa et al., 2009; Parra et al., 2009; Thiede et al., 2009). In light of these considerations, localized fast exhumation rates have been interpreted to reflect climate-driven erosion processes rather than an increase in shortening rate (e.g., Wobus et al., 2003; Cederbom et al., 2004; Thiede et al., 2005; Mora et al., 2008; Thiede et al., 2009). However, paleoclimatic and sufficiently reliable precipitation data are not always available in order to test these issues at the desired level of detail.

In the orogenic belts related to the India-Eurasia continental collision, paleoclimatic constraints have been mainly obtained from deep sea cores (e.g., Clift, 2006). Marine basins in the vicinity of these orogens receive sediments from different continental areas, where the presence of high mountains and pronounced relief can influence atmospheric circulation patterns, giving rise to local and disparate climatic and erosional conditions. Therefore, the extrapolation of climate data from marine basins to the sediment source areas in mountain ranges is inherently difficult. Another problem concerns the long-term validity of paleoclimate data and inferred amounts of precipitation that may have governed the surface-process regime for protracted periods. Often, such inferences are difficult to prove and the assumption that such conditions prevailed over long time scales needs to be demonstrated on geological time scales. For instance, the advance of deformation fronts through the reactivation of inherited structures without a predictable pattern in significantly pre-strained crust in the South American Sierra Pampeanas and in the North American Laramide province created a complex, along-strike array of partial and local rain shadows, promoting disparate climatic and surface-processes regimes (e.g., Jordan and Allmendiger,1986; Strecker et al., 2007). Against the backdrop of these difficulties, an unambiguous causal relationship between mountain growth and climate has been clearly demonstrated in only a few studies (e.g., Brozovic et al., 1997; Sobel et al, 2003; Sobel and Strecker, 2003; Strecker et al., 2007; Mora et al., 2008).

In the orogenic system, weathering and erosion generates clastic sediments, which are redistributed across the mountain belt and adjacent areas by a variety of sediment dispersal processes. Large volumes of sediment can be stored in foreland basins, which represent regions of accumulation located between orogens and undeformed sectors of lithospheric plates (e.g., Dickinson, 1974; DeCelles and Giles, 1996). In continental settings, foreland basins form mainly through flexural processes in response to tectonic load induced by crustal shortening and thickening processes (e.g., Allen and Allen, 2005 and references therein). The geometry of a foreland basin is a function of the spatial distribution of topographic load, the elastic properties of the foreland plate (flexural rigidity), the geometry of the plate (e.g., broken versus continuous plate), and to a lesser extent, deep mantle flow processes (dynamic subsidence; see Allen and Allen, 2005 and references therein). Because in an actively deforming orogen the thrust load tends to propagate towards the undeformed plate, a foreland basin represents a highly dynamic system that not only receives sediment from the deforming orogen, but eventually will become an integral part of the migrating deformation front.

The balance between tectonic subsidence causing long-term accommodation and sediment influx determines the nature and distribution of sedimentary facies in the foreland basin (e.g., Heller et al., 1988; Flemings and Jordan, 1990; Paola et al., 1992; Marr et al., 2000). For example, it has been predicted that progradation of coarse-grained facies up to medial and distal sectors within the basin can reflect decrease in thrust loading, erosion, and subsequent isostatic rebound (postorogenic phase) (e.g., Heller et al., 1988; Flemings and Jordan, 1990; Burbank, 1992; Paola et al., 1992; Marr et al., 2000). However, it has also been shown that progradation of coarse grained facies can occur during phases of enhanced tectonic activity (synorogenic phase) as documented in the Himalayan foreland basin (e.g., Burbank et al., 1988; Brozović and Burbank, 2000). The sediment influx is function of surface erosion rates and may be linked to the exposure of new source areas with different erodibility (e.g, DeCelles et al., 1991; Carroll et al., 2006), or from climate change on regional (e.g., Horton and DeCelles, 2001; Uba et al., 2007) or global scales (e.g., Zhang et al., 2001; Molnar, 2004).

Importantly, the foreland-basin sediment composition offers the possibility to track the tectonic evolution and the erosion history of the source terrains, and therefore helps to unravel the mechanisms and timing of orogenic growth and to explore the relationship between basin deposition and orogenic phases. Well established methodologies for studying foreland basin sediments include sandstone petrography, heavy mineral analysis (e.g., Garzanti et al., 2007), and provenance studies using conglomerate clasts counts (e.g., Davila and Astini, 2007), as well as mudstone geochemistry (e.g., DeCelles et al., 2004) and detritial thermochronology (e.g., Coutand et al., 2006). Furthermore, independent paleoclimatic proxy can be obtained from foreland basin deposits by means of sedimentological (e.g., Uba et al., 2005), stable isotope (e.g., Kleinert and Strecker, 2001) and biomarker studies (e.g, Köster et al., 1998). Collectively, foreland basin deposits can provide independent information on both climatic and tectonic processes affecting the adjacent orogenic wedge, helping to clarify the complex interaction between tectonic and surface processes.

To explore the feedbacks between tectonic and surface processes at the orogenic scale, I focused on the central southern Alborz mountains, located in northern Iran between the Caspian Sea and central Iran. The Alborz mountains represent an intracontinental, double-verging orogen, related to the Arabia-Eurasia continental collision. The range is less than 150 km wide and characterized by a steep flanks with peaks in excess of 4.5 km. Today the Alborz mountains constitute an efficient orographic barrier to moisture sourced in the Caspian Basin and Mediterranean Sea, separating northern slopes receiving up to 1.7 m/yr of precipitation from southern slopes receiving less than 0.3 m/yr (Alijani et al., 2007). This range was selected for this study because it has a limited areal extent, but is characterized by significant elevation, with the rain shadow strongly influencing climate, geomorphic processes, and sedimentary facies distribution of the foreland-basin deposits on the leeward side. These deposits are continuous, only deformed to a minor degree, exhibit long-term cyclicity, and show lateral facies continuity for tens of kilometers. Furthermore, available thermochronological data allow for linking the tectonic processes in the orogen with foreland basin evolution.

In light of these advantages, I focused on Tertiary sedimentary strata exposed in the central southern Alborz mountains, where I performed a multidisciplinary study to unravel the tectonic and climatic history of the Alborz mountains in the context of Arabia-Eurasia continental collision. My approach involves: 1) absolute dating methods including $^{40}Ar/^{39}Ar$ and zircon (U-Th)/He thermochronology to understand the temporal extent of the arc magmatism predating the Arabia-Eurasia continental collision; 2) relative dating methods such as magnetostratigraphy to establish timing and rates of sedimentation, and to date the changes in sediment provenance; 3) sedimentological study to constrain depositional processes and environments; 4) provenance study on sandstones and conglomerates to detect sediment source areas and their evolution; and 5) carbon and oxygen isotope analysis coupled with a quantitative clay mineralogy study to constrain paleoclimatic and paleoenvironmental conditions. The results and conclusions are subdivided into three manuscripts presented here in form of three chapters.

In chapter two, I establish for the first time the chronology of the Miocene Upper Red Formation of the southern Alborz mountains using magnetostratigraphy, and I attribute the sedimentary facies distribution within the foreland basin to tectonic processes in the hinterland and within the basin. Moreover, I relate intra-foreland uplift to orogenic-wedge growth cycles on time scales of 0.7 to 2 Ma. This chapter has been published in *Tectonics*, vol. 27, TC6001, 2008 by Paolo Ballato, Norbert Nowaczyk Angela Landgraf, Manfred Strecker, Anke Friedrich and Saeid Tabatabaei.

In chapter three, I analyze two additional basins located in the central and south-east Alborz, and I expand the investigated time window to the late Eocene/Oligocene, developing an evolutionary model for these basins and their sediment source areas. Furthermore, I link the evolution of the Alborz range to the Arabia-Eurasia continental collision, propose a new geodynamic model, and assess the timing of collision processes. This chapter has been submitted in May 2009 to the *Bulletin of the Geological Society of America* by Paolo Ballato, Cornelius Uba, Angela Landgraf, Manfred Strecker, Masafumi Sudo, Daniel Stockli, Anke Friedrich and Saeid Tabatabaei.

In chapter four, I present for the first time in the realm of the Arabia-Eurasia continental collision zone a paleoclimatic record for the early to late Miocene using stable oxygen and carbon isotopes measured on pedogenic and lacustrine/palustrine carbonates. I link the trends observed in the isotopic data to an increase in the efficiency of the orographic barrier and to the development of less arid conditions with enhanced seasonality in precipitation, possibly in response to a combination of tectonics and global climate change. This chapter will be submitted to *Earth and Planetary Science Letter*s, by Paolo Ballato, Andreas Mulch, Angela Landgraf, Manfred Strecker, Chiara Dalconi, Anke Friedrich and Saeid Tabatabaei.

Finally, in chapter five I summarize my results and develop a comprehensive evolutionary model for the southern Alborz mountains including the entire spectrum of data generated in the curse of this study. Moreover, I distinguish climatic from tectonic forcing in the development of sedimentary architecture of the foreland basin system on 10^5 to 10^6 Ma time scales.

2. Tectonic control on sedimentary facies pattern and sediment accumulation rates in the Miocene foreland basin of the southern Alborz mountains, northern Iran

Abstract

The southern Alborz mountains of N Iran are an integral part of the Arabia/Eurasia collision zone. A magnetostratigraphic and rock magnetic investigation of the Eyvanekey stratigraphic section in the southern Alborz mountains reveals the spatiotemporal character of sedimentary facies migration in the Alborz foreland-basin. The section constitutes three coarsening upward units (Unit 1, 2, and 3), comprising the Upper Red and Hezardarreh formations. Our data reveals that the Upper Red Formation was deposited between 17.5 and 7.5 Ma, while the depositional age of the top of the Hezardarreh Formation can be extrapolated to ~ 6.2 Ma. Slow sediment accumulation rates correlate with sedimentary facies comprising prograding, coarsening-upward units. This is likely the result of intra-foreland uplift (Unit 1 and 2) and basin inversion, probably associated with a growth syncline located in the proximal foreland (Unit 3). In contrast, fine-grained strata at the bottom of each cycle are associated with faster sediment accumulation rates, testifying to enhanced flexural basin subsidence in the course of thrust loading. Progradation of coarse-grained facies also occurred during relatively fast sediment accumulation (top of Unit 2), suggesting that the influx of coarse-grained sediment outpaced the storage capacity of the proximal foreland. Thus, despite an overall southward propagation of deformation into the southern Alborz foreland, the locus of active deformation must have migrated back and forth on a time scale of ca. 0.7 to 2 Ma.

2.1 Introduction

One of the salient features in many foreland-basin systems is the occurrence of prograding coarse-grained deposits, which have often been interpreted as the direct response to intensified tectonic activity in the orogen (e.g., Armstrong and Oriel, 1966; Burbank et al., 1988; Brozović and Burbank, 2000). The interpretation that coarse-grained facies reflect tectonic activity has been proven in proximal foreland sectors with growth strata (e.g., Riba, 1976; DeCelles et al., 1991). However, over the past two decades, the progradation of coarse-grained facies in medial to distal foreland sectors has been increasingly associated with waning tectonic activity (e.g., Heller et al., 1988; Flemings and Jordan, 1990; Paola et al., 1992; Marr et al., 2000). In this case, progradation of coarse facies is time transgressive and due to a reduction in thrust loading, erosion, and subsequent isostatic rebound. Presumably this could lead to a decrease in flexural subsidence accompanied by the dispersion of coarse-grained sediments. As a consequence, the onset of conglomerate deposition in a foreland basin should vary spatially and not coincide with the chronology of thrust loading and coeval subsidence (Heller et al., 1988; Jordan et al., 1988, Flemings and Jordan, 1990; Burbank, 1992). In order to better understand and refine the characteristics of these relationships, a high-resolution chronology of foreland-basin strata and independent information on the timing of thrust initiation in the adjacent orogen are needed (e.g., Burbank et al., 1988; Meigs et al., 1995; Bullen et al., 2001; Echavarria et al., 2003).

Matters may be even more complicated, because foreland basins may not necessarily constitute simple asymmetric systems, and may become compartmentalized with the development of thrust-sheet top basins (Ori and Friend, 1984). Such compartmentalization may result from intra-foreland uplifts, which can induce progradation of coarse-grained facies (e.g., Clevis et al., 2004; Horton et al., 2004; Mortimer et al., 2007; Heermance et al., 2007). Changing surface erosion rates may also affect the temporal evolution of grain size and sedimentation rate, resulting from new source areas of differing erodibility exposed during erosional unroofing (e.g, DeCelles et al., 1991; Carroll et al., 2006) or from climate change on regional (e.g., Horton and DeCelles, 2001; Uba et al., 2007) or global scales (e.g., Zhang et al., 2001; Molnar, 2004). The complex interplay among all of these factors will cause vertical and lateral grain-size changes associated with variations in sedimentation rate, which are strongly dependent on the time scale over which these processes occur (Paola et al., 1992; Marr et al., 2000).

In the southern Alborz mountains of northern Iran, well-preserved, late Cenozoic synorogenic clastic deposits in the Upper Red and Hezardarreh formations are organized in three basin-wide coarsening and upward-thickening cycles. This configuration represents an ideal natural laboratory to evaluate and understand the significance of progradational coarse-grained facies within a foreland basin. Despite the lateral continuity and good exposure of sedimentary units, very little is known about their sedimentary facies evolution, subsidence patterns, and age. Unfortunately, due to the virtual absence of biostratigraphic markers and radiometrically datable strata, age constraints on these continental successions are ambiguous, with the Upper Red Formation considered to be post Burdigalian in age on the base of its relative stratigraphic position (see Jackson et al., 1990 and references therein). The Hezardarreh Formation is inferred to be Pliocene on the base of lithostratigraphic correlation with the better-studied Bakhtiyari Formation of the Zagros mountains farther south (Rieben, 1955). However, a recent study has shown that the Bakhtiyari Formation does not represent a regionally contiguous deposit postdating late Miocene-Pliocene shortening (e.g., Berberian and King, 1981), but instead a progradational sedimentary body, whose distal sectors advanced toward the foreland starting in early Miocene and probably Oligocene time (ca. 200 km in more than 20 Ma) (Fakhari et al., 2008). Dating the sedimentary sequence in the Alborz foreland is therefore crucial not only for unraveling the nature of foreland depositional cycles, but also for establishing the regional deformation history of this poorly-studied area within the Arabia Eurasia collision zone.

Here, we present new data from a magnetostratigraphic and rock-magnetic study of the Eyvanekey section of the southern Alborz mountains at approximately 35°20`N latitutde and

52°10`E longitude. This investigation provides the first detailed chronology for the late Cenozoic syntectonic sedimentary units of this region. We combine facies cyclicity, variation in sediment accumulation rates, stratal relationships, and independent information on the timing of deformation in the orogen (eg., Axen et al., 2001; Guest et al., 2006b; Rezaeian 2008) to advance our understanding of the causes of sedimentary facies-pattern development. In particular, we show how intrabasinal uplift can perturb the overall flexural foreland subsidence, thus modifying sedimentary facies distributions within a foreland-basin system. Furthermore, our study offers new constraints on the late Cenozoic spatial evolution of deformation in the Alborz mountains, and the initiation of flexural subsidence in the southern Alborz foreland basin.

2.2 Geodynamic and structural setting

The closure of the Neotethys and the subsequent continental collision between the Arabian and Eurasian plates has produced a large region of intracontinental contractional deformation that extends from Turkey to Afghanistan and Pakistan (e.g., Jackson and McKenzie, 1984). The timing of the collision has been placed anywhere between late Cretaceous and Pliocene due to insufficient data coverage (for reviews see McQuarrie et al., 2003, Guest et al., 2006b and references therein). However, an increasing amount of new evidence suggests that the onset of the Arabia-Eurasia collision in Iran occurred between late Eocene and late Oligocene time (Argard et al., 2005; Vincent et al., 2005; Verdel et al., 2007; Vincent et al., 2007, Allen et al., 2008; Fakhari et al., 2008; Horton et al., 2008).

The present-day convergence between Arabia and Eurasia is primarily accommodated by distributed shortening and strike-slip faulting in the Zagros, Alborz, and Kopeh Dagh ranges of Iran as well as along major intracontinental strike-slip faults, including the Nayband-Gowk and Neh-Zahedan fault systems (e.g., Jackson and McKenzie, 1984; Berberian and Yeats, 1999) (Fig.1). These deformation belts separate rigid, aseismic crustal blocks, such as the South Caspian Basin, Central Iran, the Lut Block, and the Helman Block (e.g., Jackson and McKenzie, 1984; Berberian and Yeats, 1999) (Fig.1). At the longitude of Tehran, space-geodetic measurements indicate N-directed convergence between Arabia and Eurasia at a rate of ~ 22 mm/a (Vernant et al., 2004a; Masson et al., 2007) (Fig. 2.2.1). Shortening is partitioned and accommodated by the Zagros fold and thrust belt at ~ 6.5 mm/a and the Alborz mountains at ~ 5 mm/a (Vernant et al., 2004a; Masson et al., 2007). The remainder is absorbed by subduction of the South Caspian Basin beneath the Apsheron Balkhan Sill, and strike-slip motion in the Alborz and Zagros mountains (Jackson et al., 2002; Vernant et al., 2004a; Walpersdorf et al., 2006). The NNE-oriented shortening direction is thus oblique with respect to the overall strike of these ranges, leading to strain partitioning into dip-slip and strike-slip faulting (Jackson et al., 2002; Talebian and Jackson, 2002). Strike-slip faulting is associated with the extrusion of the South Caspian Basin, which is moving northwestward at a rate of 11±2 mm/a with respect to Eurasia (Copley and Jackson, 2006; Hollingsworth, 2006). This relative motion is responsible for left-lateral shearing in the Alborz at a rate of 4±2 mm/a (Vernant et al., 2004b). Since middle Pleistocene time, left-lateral strike-slip faulting has been locally associated with transtension in the inner domain of the orogen (Ritz et al., 2006; Zanchi et al., 2006; Landgraf et al., 2008).

The Alborz mountains are up to 4850 m high and have an unusual crustal thickness of 35-40 km, which appears to be too thin for a mountain range of such height, suggesting the lack of a crustal root and the presence of a shallow asthenosphere (Dehghani and Makris, 1984). The Alborz range records a complex geological history, including: (1) the middle-late Triassic Eo-Cimmerian orogeny; (2) late Cretaceous-Paleocene shortening; (3) middle-late Eocene back-arc extension; (4) and finally, late Cenozoic shortening (for an overview see Guest et al., 2006b and references therein). The final phase of deformation generated 15 km of relief between the crest of the range and the basement of the South Caspian Sea (Guest et al., 2007).

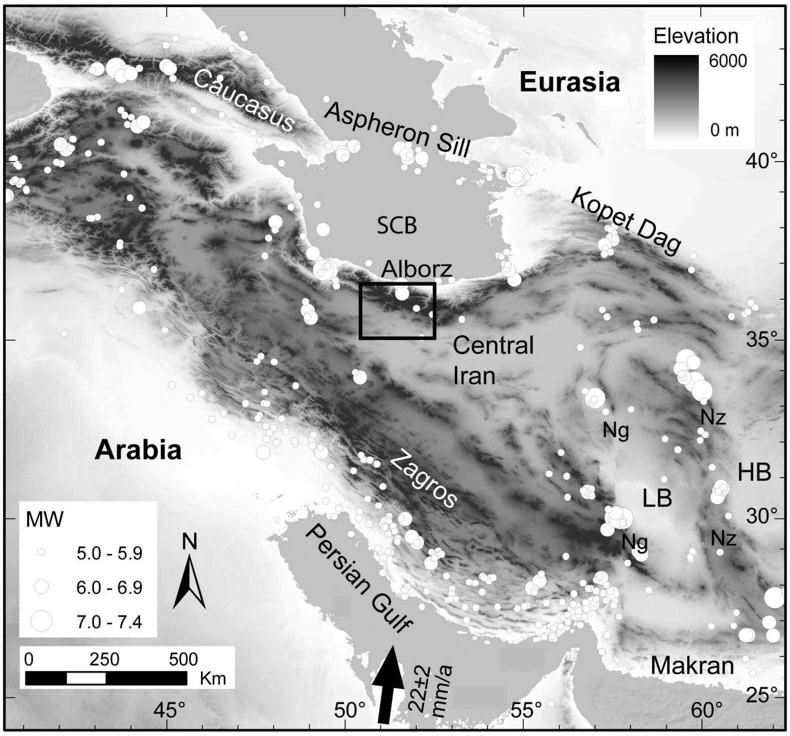

Figure 2.1: Simplified tectonic map of Iran and adjacent regions showing shortening and shearing rates measured with GPS (Vernant et al., 2004a; Masson et al., 2007). The South Caspian Basin is marked by SCB, the Lut Block by LB, the Helmand Block by HB, the Nayband-Gowk fault system by Ng, and the Neh-Zahedan fault system by Nz. Black frame outlines location of Fig. 2.2 (modified after Vernant et al., 2004a).

The overall style of deformation in the Alborz is characterized by a system of double-verging reverse faults (e.g., Allen et al., 2003; Guest et al., 2006a) (Fig. 2.2). Folds and faults are generally subparallel to the trend of the range, but also display complex anastomosing patterns, suggesting that deformation was also accommodated by oblique slip (Guest et al., 2006a; Zanchi et al., 2006; Landgraf et al., 2008) (Fig. 2.2). While thrusting and folding dominated the margins of the range, strike-slip faults were active in the interior, reflecting a long history of strain partitioning (Jackson et al., 2002; Guest et al., 2006a). A recent study of the Central Alborz mountains reported inverted normal faults that were developed during the Eo-Cimmerian orogeny (Zanchi et al., 2006). This inherited fault pattern appears to be responsible for the strain partitioning during the late Cenozoic inversion, which occurred under an earlier NW- to N-oriented shortening direction, followed by a neotectonic NE-oriented contraction (Zanchi et al., 2006; Landgraf et al., 2008). The Alborz mountains thus represent a crustal weak zone with evidence for repeated reactivation of inherited crustal fabrics.

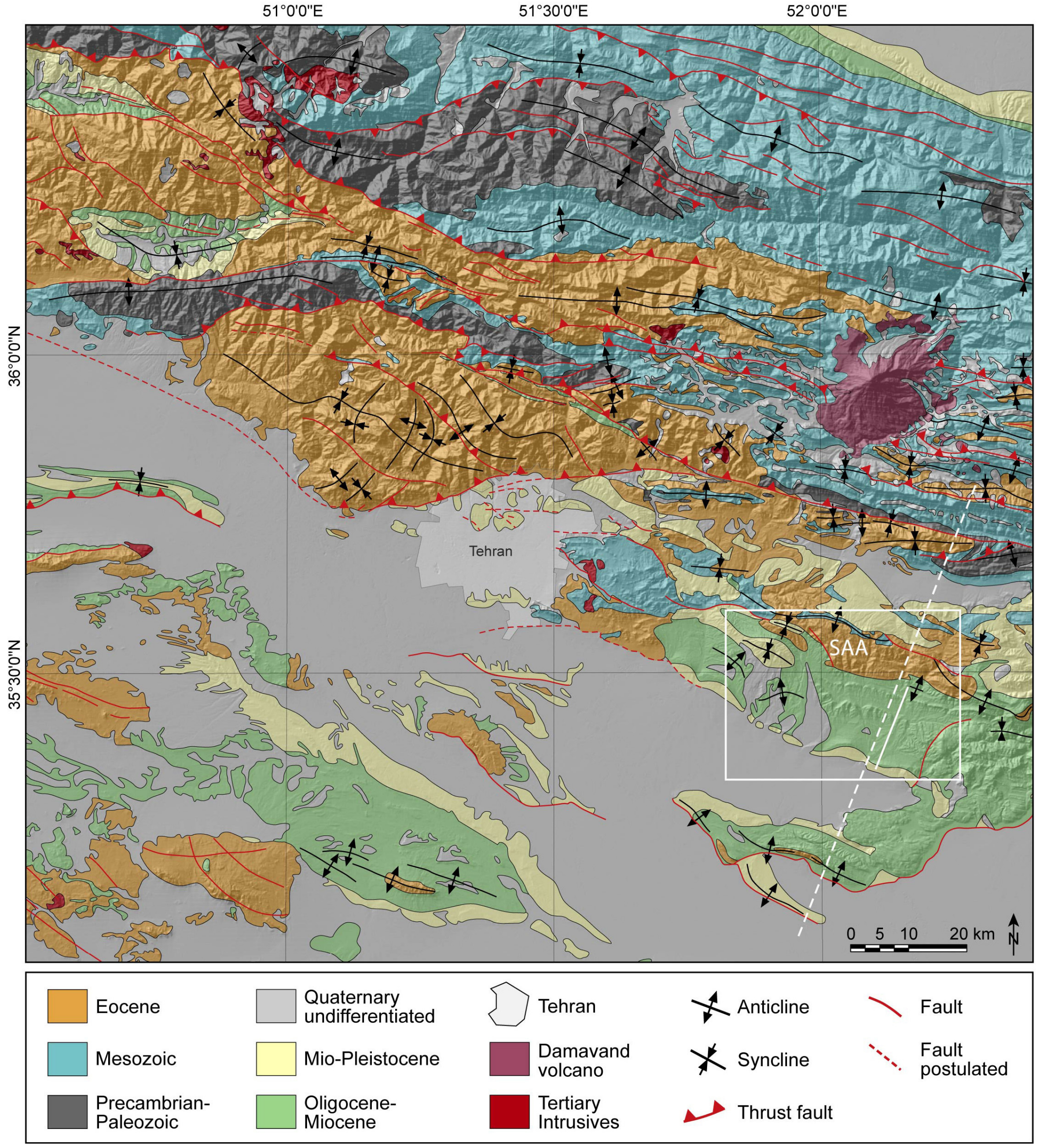

Figure 2.2: Geological map of central Alborz, superposed on DEM, modified after Haghipour et al., (1987), Vahdati Daneshmand et al., (1991), Amini et al., (2004) and Guest et al., (2006a). Study area is denoted by a white frame (Fig. 2.3). Solid white line indicates position of the stratigraphic section (Fig. 2.4), while dashed white line shows approximate location of Fig. 2.10. The Southern Alborz Anticline is marked by SAA.

2.3 Stratigraphy of the southern Alborz mountains

The rock successions of the Alborz mountains and adjacent areas constitute a complex and variable stratigraphy due to numerous tectonic events that have left their imprint on northern Iran (see Guest et al., 2006b and references therein). Here, we summarize the most important characteristics of the sedimentary units, with particular emphasis on late Cenozoic deposits exposed in the southern Alborz.

The oldest units exposed in the Alborz are Precambrian low-grade metasediments (Assereto, 1966). The following Paleozoic to early Cenozoic sedimentary sequence is discontinuous, contains several angular unconformities, and consists of quartzites, sandstones, limestones, shales, dolomites, and a minor component of volcanic rocks, deposited in continental and shallow marine depositional environments (Assereto, 1966). The Pre-Cambrian to early Cenozoic sedimentary sequence locally reaches ca. 10 km thickness (Assereto, 1966).

The superseding Karaj Formation (early to late Eocene), consists of volcanoclastic sediments, which in the southern Alborz attain a thickness of up to 6 km and pinch out toward the northern part of the range (Davoudzadeh et al., 1997). These deposits are widespread in NW Iran and are composed of lavas and green tuffs, with a lesser amount of shales, sandstones, mudstones, and calcareous tuff, deposited in a marine deep-water system (Davoudzadeh et al., 1997). The protracted episode of voluminous volcanic deposition was associated with regional rifting, ending in late Eocene time and followed by deposition of the evaporitic Kond Formation (Jackson et al., 1990; Davoudzadeh et al., 1997). This unit is locally 500 m thick and associated with fine-grained clastic rocks. An angular unconformity separates this unit from the overlying (Oligocene?) Lower Red Formation, a conglomerate up to 50-m thick in the study area. Towards the south, this conglomerate grades laterally into approximately 1-km-thick evaporites (Jackson et al., 1990; Davoudzadeh et al., 1997). These strata are covered by late Oligocene/early Miocene shallow-water limestone, marl and minor gyprocks, with variable thickness, ranging from a few meters up to 1 km in Central Iran (e.g., Bozorgnia, 1966; Reuter et al., 2007). In the southern foothills of the Alborz mountains, the superseding Qom Formation, with strata as young as Burdigalian in age (Daneshian and Ramezani Dana, 2006), also contains conglomerates, and is a few hundred meters thick. The following (early to late Miocene?) Upper Red Formation comprises red mudstones, evaporites, sandstones, and conglomerates, and is locally up to 6 km thick (Jackson et al., 1990; Davoudzadeh et al., 1997). At the base, these red-bed deposits reflect a restricted marine and lagoonal environment that records the upsection transition to a terrestrial depositional setting (Jackson et al., 1990; Rahimpour-Bonab and Kalantarzadeh, 2006). The Upper Red strata are covered by up to 1.5-km-thick conglomerates and sandstones of the Hezardarreh and Kahrizak formations (also known as Unit A and B), which were deposited in an alluvial-fan system along the southern flank of the Alborz (Rieben, 1955). Although poorly constrained, the Hezardarreh Formation has been lithostratigraphically correlated with the coarse-grained Pliocene Batkhyari Formation of the Zagros mountains (Rieben, 1955). This correlation, however, is probably an oversimplification. New data from the proximal part of the foreland-basin system of the Zagros mountains show that the onset of foreland-basin sedimentation occurred during Oligocene to early Miocene time, and that the coarse-grained facies of the Batkhyari Formation advanced toward the foreland rather than being uniformly deposited after a major phase of late Miocene-Pliocene shortening (Fakhari et al., 2008).

2.4 Stratigraphy of the Eyvanekey section

The Eyvanekey section is located ca. 70 km east of Tehran. The studied section is perpendicular to the southern limb of an anticline, here called the Southern Alborz Anticline (SAA), which we interpret as a breached north-verging fault-propagation fold (Figs. 2.2, 2.3, and 2.4). Combined, the terrestrial deposits of the Upper Red and Hezardarreh formations (Amini et al., 2004) (Fig. 2.2) are approximately 7400 meters thick, and constitute three coarsening upward units (Unit 1, 2 and 3) (Figs. 2.3 and 2.4). Units 1, 2 and part of Unit 3 correspond to the Upper Red Formation, while sub-unit 3C represents the Hezardarreh Formation.

2.4.1 Unit 1

The first coarsening upward unit is ca. 1.8 km thick and consists of sub-units 1A, 1B, and 1C. Sub-unit 1A is composed of ca. 800-m-thick, brick-red mudstones interbedded with grayish-green mudstones, gypsum layers, and tabular siltstones to fine-grained sandstone bodies. These layers are typically 5 to 50 cm thick. The red mudstones have a massive or laminated texture and occasionally display mudcracks, indicating protracted subaerial exposure in a hot, arid climate. Syneresis cracks are also present, suggesting subaqueous dewatering of sediments probably due to a high salinity contrast. The grayish-green mudstones are common at the bottom of the section, where they are organized in packages of 3-4 m thickness. The salt layers are a few centimeters thick and are abundant at the bottom of the sequence. The siltstones and fine-grained sandstones have a sheet-like geometry and occasionally display ripples. Sub-unit 1B comprises ca. 500-m-thick red mudstones interbedded with siltstones and fine- to medium-grained sandstone bodies. The mudstones are massive to laminated, while the siltstone bodies have a sheet-like geometry and contain ripples. The sandstone bodies have a gentle erosional base, and are up to 3 m thick and up to 50 m wide. They are amalgamated and form a branching geometry. Cross bedding at the base of each sandstone body generally evolves to ripple structures upsection, and the tops of the sandstone bodies are usually bioturbated. Sub-unit 1C consists of 500-m-thick, light brown sandstone bodies with interbedded lenses and layers of pebble conglomerates. Intercalated reddish centimeter-thick mudstones and very fine tabular sandstones, grading into siltstones, also occur. The sandstone bodies are 1-10 m thick and several hundreds of meters wide. Generally, they have an erosional base with rip-up clasts. The sandstones constitute a fining upward-sequence with small- to medium-scale horizontal and trough-cross bedding and ripples toward the top. The tops of the sandstone bodies are generally bioturbated. In addition, these deposits frequently have small- to medium-scale water-escape structures, suggesting a relatively high sediment-accumulation rate. The thin-bedded sandstones and siltstones (0.5-1 m) are characterized by ripples and have a sheet-like or wedging geometry with a gentle erosional surface. The interbedded mudstones may display mud cracks and are occasionally bioturbated. Importantly, to the west, the conglomeratic facies overlies the finer-grained units unconformably and pinches out to the north (Fig. 2.3). Sub-unit 3C is marked by a progressive decrease in stratal dip angle from 38° to approximately 30°.

We interpret Unit 1 to represent a playa-lake, fluvial channel, crevasse splay, and overbank depositional environment. Taken together, the succession may reflect the transition from a playa (sub-unit 1A) to a distal river (sub-unit 1B) and braided-river (sub-unit 1C) setting.

2.4.2 Unit 2

The second coarsening upward unit is ca. 1.9 km thick and comprises two sub-units (2A and 2B). Sub-unit 2A is ca. 200 m thick and composed of red mudstones interbedded with tabular siltstones to fine-grained sandstone bodies, few gypsum layers, and rare grayish-green mudstones. This unit is similar to sub-unit 1A, but additionally contains isolated sandstone bodies with trough cross bedding evolving to horizontal bedding and ripples. The following sub-unit 2B constitutes ca. 1700 m of thick sandstone bodies with floating pebbles interlayered with reddish thin-bedded mudstones and fine-grained sandstones and siltstones. The sandstone bodies increase in frequency and thickness toward the top of the unit (up to 40 meters), with a width of several hundreds of meters. Generally, they have an erosional base and reactivation surfaces marked with rip-up clasts. Water-escape structures are also common. The thin-bedded sandstones and siltstones are characterized by ripples and have a sheet-like or wedging geometry with a gentle erosional surface. The mudstones are moderately bioturbated and contain gypsum-filled fractures. Sub-unit 2A and the base of sub-unit 2B have onlap geometries against sub-unit 1C in the west (Fig. 2.3).

Unit 2 is therefore interpreted to constitute fluvial channel, crevasse splay, and overbank deposits, with minor playa-lake strata. Collectively, these deposits reflect an evolution from a playa-lake (sub-unit 2A) to a braided-river (sub-unit 2B) depositional system.

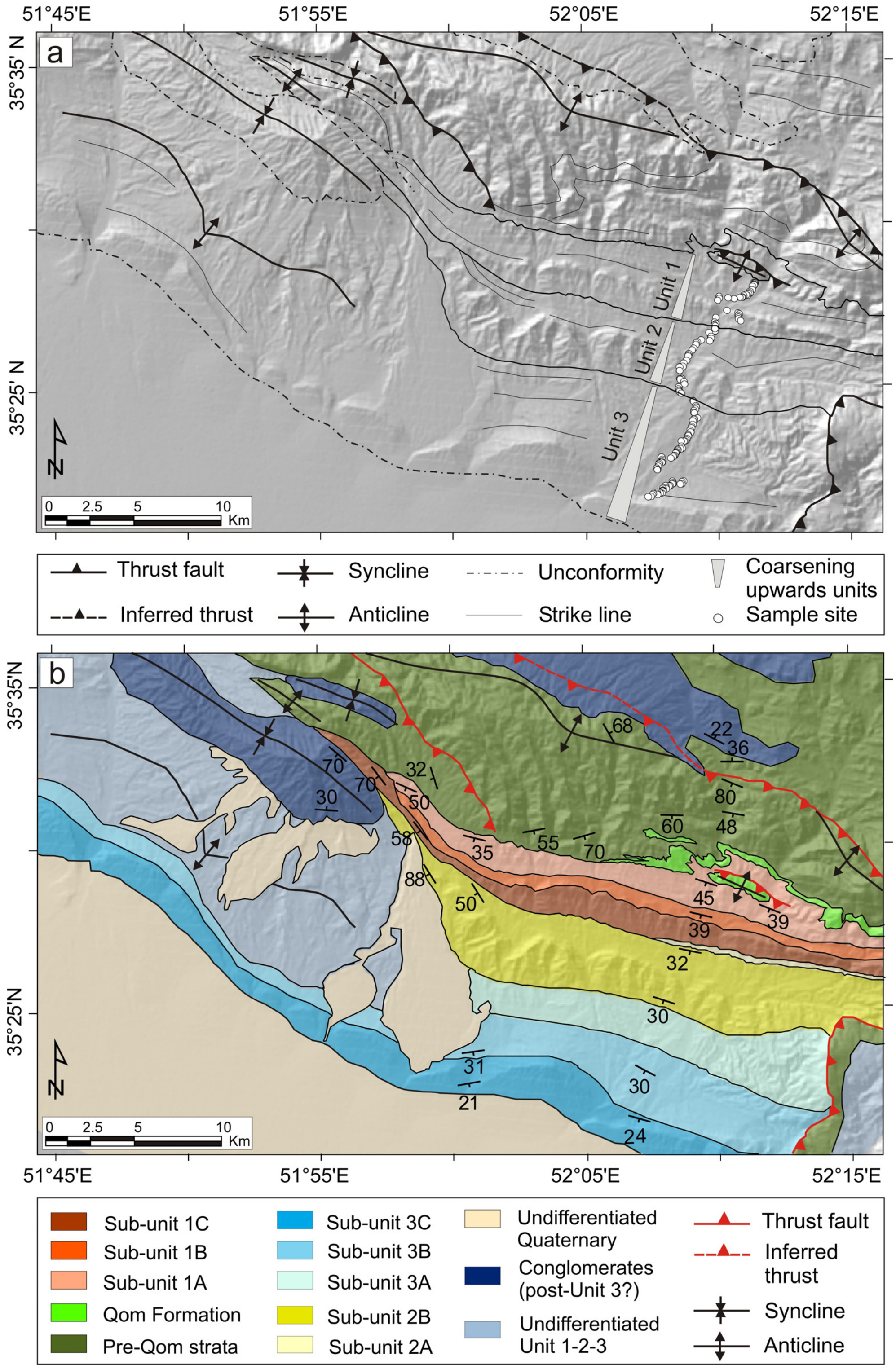

Figure 2.3: (a) Shaded relief map of the study area showing location of 3 coarsening upward units, main geological structures, unconformities and paleomagnetic sample localities. The occurrence of coarse grained facies within the three coarsening upward units is also reflected by areas of higher topography. (b) Geological map of the study area, compiled from our own field mapping (Amini et al., 2004), and ASTER imagery. The map shows the geometric relationship between the undifferentiated pre Miocene deposits (pre-Qom strata), the early Miocene Qom Formation (Daneshian and Ramezani Dana, 2006), the subunits 1A, 1B, 1C, 2A, 2B, 3A, and 3B representing the Upper Red Formation (early to late Miocene), the sub-unit 3C constituting the Hezardarreh Formation (late Miocene, after this study) and younger strata of unknown age. Note that sub-unit 1C truncates the underlying sub-units 1A and 1B, while sub-units 2A and 2B onlap onto sub-unit 1C. A progressive decrease of stratal dip angles marks the onset of sub-units 1C and 3C deposition.

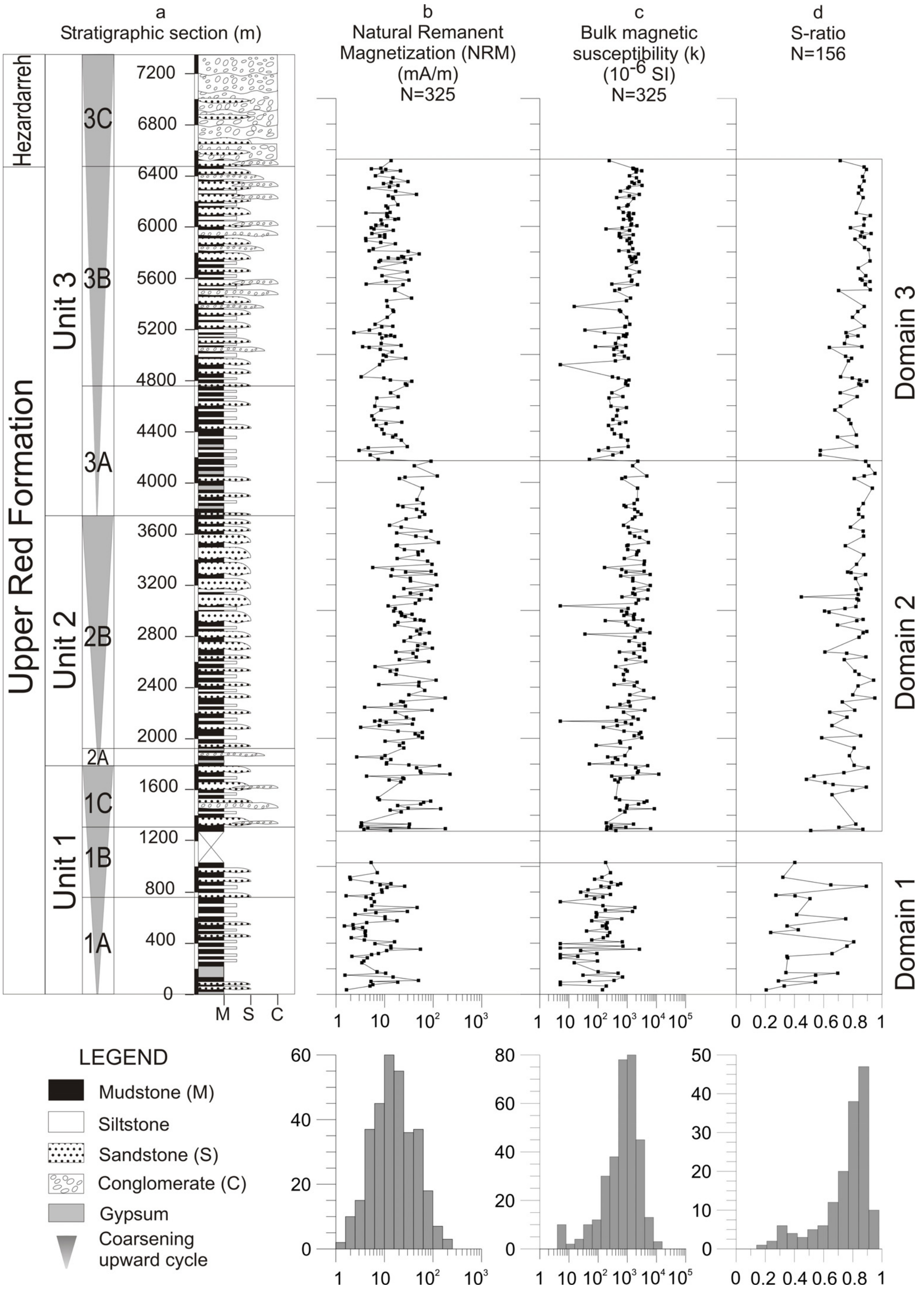

Figure 2.4: (a) Eyvanekey stratigraphic section representing the Upper Red (early to late Miocene) and the Hezardarreh (late Miocene, after this study) formations; see Figs. 2.1, 2.2 and 2.3 for location. (b, c, and d) Rock magnetic properties versus stratigraphic thickness including the Natural Remanent Magnetization (NRM) (b), the bulk magnetic susceptibility (k) (c), and the S-ratio (d). Note the logarithmic scale for NRM and k. Formations and recognized units corresponding to three coarsening upward cycles are shown. Frequency plots for NRM, k and S-ratio are also represented. The asymmetric Gaussian pattern for k and S-ratio indicates the dominance of magnetite as the most common phase carrying the magnetization.

2.4.3 Unit 3

The third coarsening-upward unit is ca. 3.7 km thick and comprises sub-units 3A, 3B and 3C. Sub-unit 3A is made up of 1100 m light brown mudstones and gypsum layers. This unit also contains sandstones, whose occurrence decreases up-section. These fine-grained deposits are generally coarser than the sediments of the bottom of unit 1 and 2 and contain abundant gypsum-filled fractures. Sub-unit 3B is made up of 1700 m light brown and rare light green sandstones and siltstones, interbedded with reddish sandy mudstones and conglomerates. Individual beds generally do not exceed 2 m thickness. The sandstones exhibit a wedging geometry, with an erosional base, horizontal lamination and ripple structures. The frequency of the sandstone bodies increases upsection. The sandy mudstones have a tabular geometry and may contain mud cracks. The thickness and the occurrence of conglomerate bodies increases upsection. Finally, the upper part of the section is a 900-m-thick, light brown pebble to cobble conglomerate (sub-unit 3C). This polymictic conglomerate is moderately to poorly sorted, mainly clast-supported with sub-rounded to well-rounded clasts. The deposit is poorly stratified and has crudely developed parallel and through cross bedding. Clasts are poorly imbricated, suggesting a medium to low-energy stream-flow regime. At the bottom of this unit medium- to coarse-grained strata and lenses of sandstones occur. Toward the top the sandstones disappear. A progressive decrease of stratal dip angles (ca. 7°) marks the onset of conglomerate deposition of sub-unit 3C, suggesting syntectonic sedimentation (Fig. 2.3).

Based on these observations, we interpret Unit 3 to be comprised of playa-lake, fluvial channel, crevasse splay, overbank, and alluvial-fan deposits. Therefore, this sequence characterizes a transition from playa-lake (sub-unit 3A) to braided river (sub-unit 3B), and alluvial-fan depositional environments (sub-unit 3C). Paleocurrent data document that the sediment source, at least since deposition of sub-unit 1C, was located to the north. The section does not contain any faults or unconformities, suggesting that sedimentation was relatively continuous (Fig. 2.3).

2.5 Methodology

2.5.1 Magnetostratigraphic sampling strategy

The currently available age information for the deformed and exposed sedimentary units along the southern Alborz mountains is tentative at best and fraught with many errors that make a rigorous assessment of the tectono-sedimentary evolution of this region difficult. In this study we focus on the Upper Red Formation (Amini et al., 2004). We sampled a 6500-m-thick section from the bottom of Unit 1 to the top of sub-unit 3B for magnetostratigraphy (Figs. 2.3 and 2.4). The last conglomeratic sub-unit 3C, which approximately corresponds to the Hezardarreh Formation (Amini et al., 2004), was not sampled due to the lack of suitable fine-grained facies. The last 300 meters of sub-unit 1B could not be sampled due to poor exposure. The lack of fresh outcrops, coupled with the effects of weathering and the development of soil profiles, limited the density of sampling to an average distance of 17 m between sites. Sample spacing within sub-unit 2B was up to 35 meters due to the frequent channelized coarse-grained sandstones up to 40 meters thick. We drilled at least three oriented standard cores per sample from a total of 369 oriented hand samples.

2.5.2 Analytical techniques

The samples were analyzed at the Geoforschungszentrum Potsdam, Section 3.3. The majority of the specimens were subjected to stepwise thermal demagnetization, using at least 10 to 16 demagnetization steps ranging from 50°C to 680°C. The thermal treatment was performed with an ASC Scientific TD48 oven, while natural remanent magnetization (NRM) analysis was performed using a 2G Enterprises automatic DC-SQUID 755SRM cryogenic magnetometer (noise level=1x10^{-6} A/m). In some cases, alternating field demagnetization was also carried out using the in-line triaxial alternating field demagnetizer of the cryogenic magnetometer. Magnetic susceptibility was measured after each demagnetization step with a Bartington MS2B sensor in order to detect mineralogical alteration of the magnetic fraction induced by heating. The direction of the characteristic remanent magnetization (ChRM) was calculated with the principal component analysis (PCA) (Kirschvink, 1980), applied to at least 3 successive data points (Appendix 1)

Isothermal remanent magnetization (IRM) was conducted with a 2G Enterprise 660 pulse magnetizer and measured with a Molyneux MiniSpin fluxgate magnetometer (noise level=0.2x10^{-3} A/m). Samples were exposed stepwise to peak fields of 5.7 to 2700 mT along the positive z-axis of the specimens in order to record complete IRM acquisition curves (Appendix 1).

2.6 Paleomagnetic results

2.6.1 Magnetic mineralogy

A suite of 156 samples was selected for IRM experiments in order to identify the ferromagnetic mineralogy. Two end-member spectra are recognized (Fig. 2.5): (1) samples sutured between 100 and 200 mT containing low-coercivity fraction, which can be ascribed to magnetite; (2) samples that acquired the majority of IRM between 600 and 1000, dominated by a high-coercivity component that can be attributed to hematite. The S-ratio, which is a (nonlinear) estimate of the abundance of magnetite compared to that of antiferromagnetic minerals, mainly hematite, was also calculated. Hematite-dominated samples have an S-ratio ranging from 0.2 to 0.4, while in magnetite-dominated samples the S-ratio generally varies between 0.7 and 1 (Figs. 2.4 and 2.5). Most of the samples present a mixture of the two components in different proportions. The inflection point in the acquisition curve around 200-300 mT marks the boundary between the saturation of magnetite and the onset of magnetization of hematite (Fig. 2.5). Furthermore, most of the samples are not saturated at maximum field of 2700 mT indicating the presence of another high-coercivity phase, such as goethite. This is in agreement with the 40 to 20% drop of the initial NRM below 200°C (Fig. 2.6). Interestingly, the majority of the samples are associated with goethite, suggesting post-depositional chemical weathering.

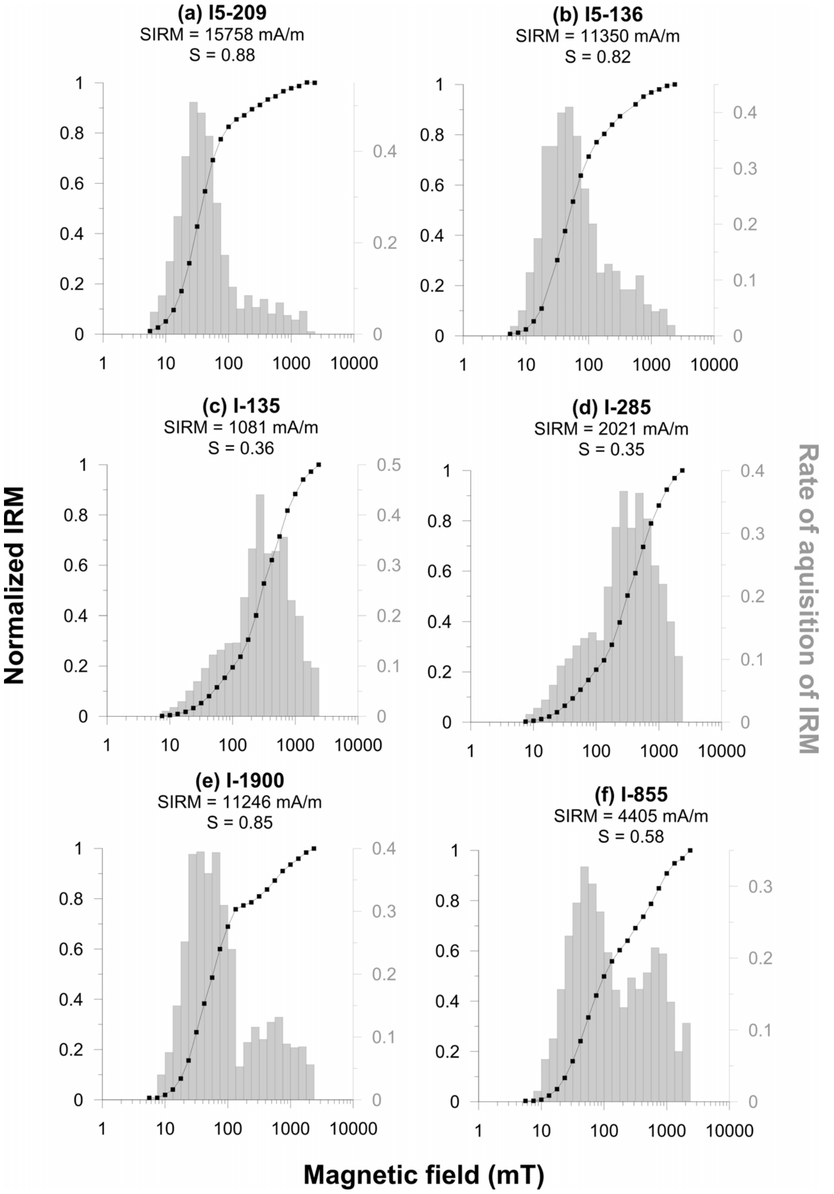

Figure 2.5: Isothermal Remanent Magnetization (IRM) acquisition curve with a field up to 2700 mT, showing samples with a different proportion of the magnetic mineralogical phases: (a-b) magnetite-dominated, (c-d) hematite-dominated, and (e-f) mixed curves. S-IRM represents the maximum IRM recorded with a magnetic field of 2700 mT.

2.6.2 Remanent magnetization

NRM intensities are characterized by a large range of values (2 to 224 mA/m), indicating a variable content of ferromagnetic minerals (Figs. 2.4 and 2.6). Two vectorial components have been commonly observed and in 75% of the samples a stable ChRM has been successfully isolated (Fig. 2.6). The lower temperature component is ascribed to a viscous overprint due to the local present-day direction of the magnetic field. This contribution is probably related to the presence of unstable magnetite and is commonly removed below 400°C. In some cases, the viscous component can account for up to 80% of the NRM intensity. The remaining stable component has a maximum unblocking temperature between 450 and 680°C and represents the ChRM, which reveals both normal and reverse polarities. IRM acquisition curves are in agreement with the demagnetization curve (Figs. 2.5 and 2.6). Samples with magnetite exhibit a gradual decrease in magnetization starting from ca. 450°C (Ti-magnetite) up to 550-580°C. Samples with hematite show a sharp decrease in NRM intensity above 600°C and the signal generally tends to zero at ca. 680°C (Fig. 2.6).

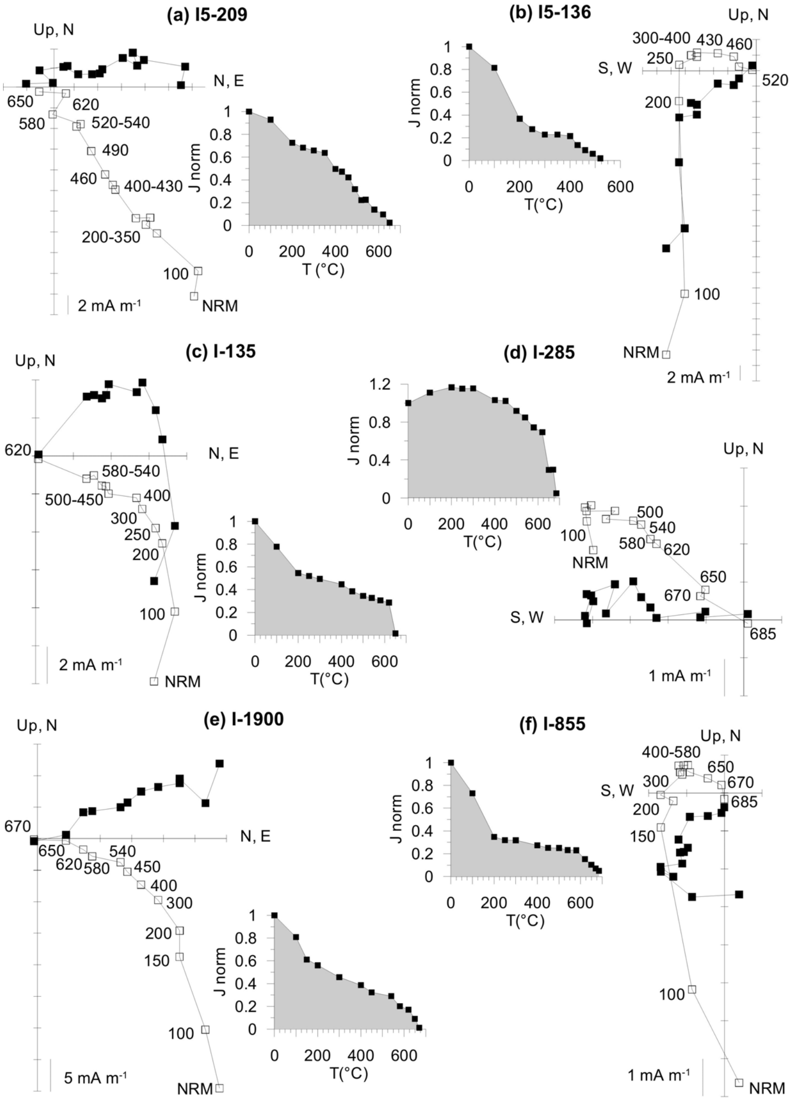

Figure 2.6: Vector end-point diagrams plotted in tilt-corrected coordinates and normalized intensity decay curves illustrating thermal demagnetization of NRM for the specimens documented in Fig. 2.5. Black and open squares are projected onto horizontal and vertical planes respectively.

The reversal test (e.g., McFadden and McElhinny, 1990) was negative at the 95% confidence level, primarily because the mean reversed polarity inclination is ca. 20° shallower than the expected inclination (Fig. 2.7). This could be due to an incompletely removed magnetic component (e.g., Gilder et al., 2001). Interestingly, the mean declination of all samples shows a clockwise rotation of ca. 17° (Fig. 2.7). The magnetostratigraphic sequence was established from samples having a high-temperature stable component, using the principal component analysis (Fig. 2.8) (auxiliary material, Table 1). This resulted in the identification of twenty nine normal (1-26) and twenty seven reverse (a-y) main chrons.

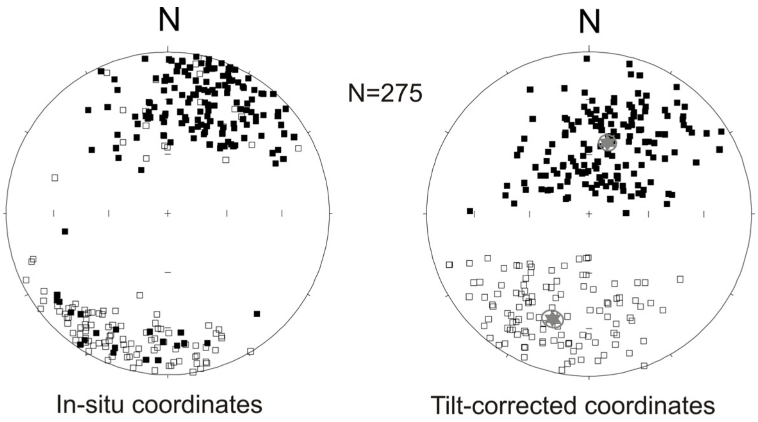

	N	Dec	Inc	k	Alpha95
Normal	161	14.6	52.5	8.2	4.2
Reverse	114	199.2	-32.2	8.7	4.8

Figure 2.7: Equal-area stereographic projection of ChRM directions used to constrain the magnetostratigraphy shown in Fig. 2.8. Black and open squares are projected on the lower and upper hemisphere respectively. The mean direction (star) and 95% confidence ellipses are also shown.

2.6.3 Magnetostratigraphic correlation

We correlate the magnetostratigraphic sequence from the Upper Red Formation with the geomagnetic polarity time scale (Cande and Kent, 1995) using the following criteria: (1) paleontological data indicate the youngest strata of the Qom Formation are Burdigalian in age (20.5 to 16.4 Ma) (Daneshian and Ramezani Dana, 2006); (2) the bottom of the magnetostratigraphic sequence is located within reversal event (y) of relatively long duration; (3) the upper half of the section is characterized by several normal events of long duration (8 to 12), separated by short reverse events (h to k); (4) the youngest age component in detrital apatite fission-track data (AFT) from the investigated section at about 3900 meters of thickness is 13.3 Ma (Fig. 2.8) (Rezaeian 2008), implying that the depositional age of this sample must be younger. Fig. 2.8 shows our correlation and provides the best fit in terms of interval numbers.

Because the youngest strata of the shallow-water marine carbonates are Burdigalian in age (Daneshian and Ramezani Dana, 2006), our section must be younger than 20.5 Ma.

Considering that within the Burdigalian and shortly afterwards there are only three long-duration reversal chrons (Fig. 2.8), we place our first long-duration reverse event (y) at the top of chron C5Dn. The relatively long-reversal chron at 15 Ma is not represented here, because it appears to coincide with the 300-m-wide outcrop gap at the top of sub-unit 1B. The following magnetozones recorded in our study are characterized by a mixed polarity with short to medium-term periods (reversal events k to x, and normal events 12 to 25), which correlate with the interval between chron C5Bn.2n and C5r.1n. Upsection, the normal polarities are dominant (8 to 11) and associated with a relatively long normal event (8). We correlate this magnetozone pattern (8 to 11) with the C5n.2n chron. This chron contains three cryptochrons of very short duration, which we correlate with our reverse events h, i, and j. The upper part of the section contains the three long-duration normal events 2, 4, and 6, which have been linked with chrons C4n.2n, C4An, and C4Ar.2n. Finally, detritial apatite fission-track dating of a sample collected at about 3900 meters in the profile provides a depositional age of ca. 10.1 Ma, which is younger than the youngest AFT detrital cooling age of 13.3 Ma recorded (Rezaeian 2008).

Our magnetostratigraphic sequence suggests that in this area the Upper Red Formation (units 1, 2 and part of Unit 3), was deposited between ~ 17.5 and ~ 7.6 Ma. This would imply that the deposition of sub-unit 3C, which corresponds to the overlying Hezardarreh Formation, started during late Miocene and not in Pliocene time, as previously inferred (Rieben, 1955; Amini et al., 2004). Importantly, there is a clear correlation between coarsening upward cycles and accumulation rate (Fig. 2.9). The fastest sediment accumulation rates correlate with fine-grained sediments, while the coarsest lithologies are associated with slow rates. If we consider that the sediment accumulation rate during the deposition of sub-unit 3C could have been ≤ 0.65 mm/a, the extrapolated age of the top of the section (i.e., the top of the Hezarderrah Fm.) might be younger than or equal to 6.2 Ma. These findings imply that the pronounced thickness of ~ 7400 m of sediment must have been deposited in a relatively short time period (~ 11 Ma) in this part of the basin.

2.6.4 Rock-magnetic properties

The bulk magnetic susceptibility (k) and the NRM for the entire set of measured samples (369), associated with the S-ratio for the samples selected for IRM acquisition (156), were plotted as a function of stratigraphic thickness (Fig. 2.4) (auxiliary material, Table 2 and 3). The three parameters are correlated and track three different domains. The first domain extends from the bottom upward to sub-unit 1C, and is characterized by k values generally lower than 500 x 10^{-6} SI, NRM values lower than 30 mA/m, and S-ratio values between 0.2 and 0.8. The second domain coincides with the onset of coarse-grained sedimentation of sub-unit 1C and ends at the bottom of sub-unit 3A. This domain is characterized by scattered values of k (from ca. 200 to 12.000 x 10^{-6} SI), NRM values ranging from 2 to 224 mA/m, and an S-ratio between 0.5 and 0.9. The third domain begins at the bottom of sub-unit 3A and is characterized by a sharp decrease in k and NRM up to one order of magnitude with respect to the second domain, while the S-ratio does not change significantly. Since the magnetic susceptibility of magnetite is greater than that of hematite (goethite) by up to 100 (1000) times (Thompson and Oldfield, 1986), the bulk susceptibility is very sensitive to the presence of magnetite. The first domain is clearly enriched in hematite, although some levels may reflect the presence in magnetite. The second domain records a sharp increase in magnetite and the high susceptibility values suggest the existence of multi-domain grains (Butler, 1998). Finally, the third domain exhibits susceptibility values intermediate with respect to the first and second domain, suggesting that magnetite is still the dominant magnetic fraction.

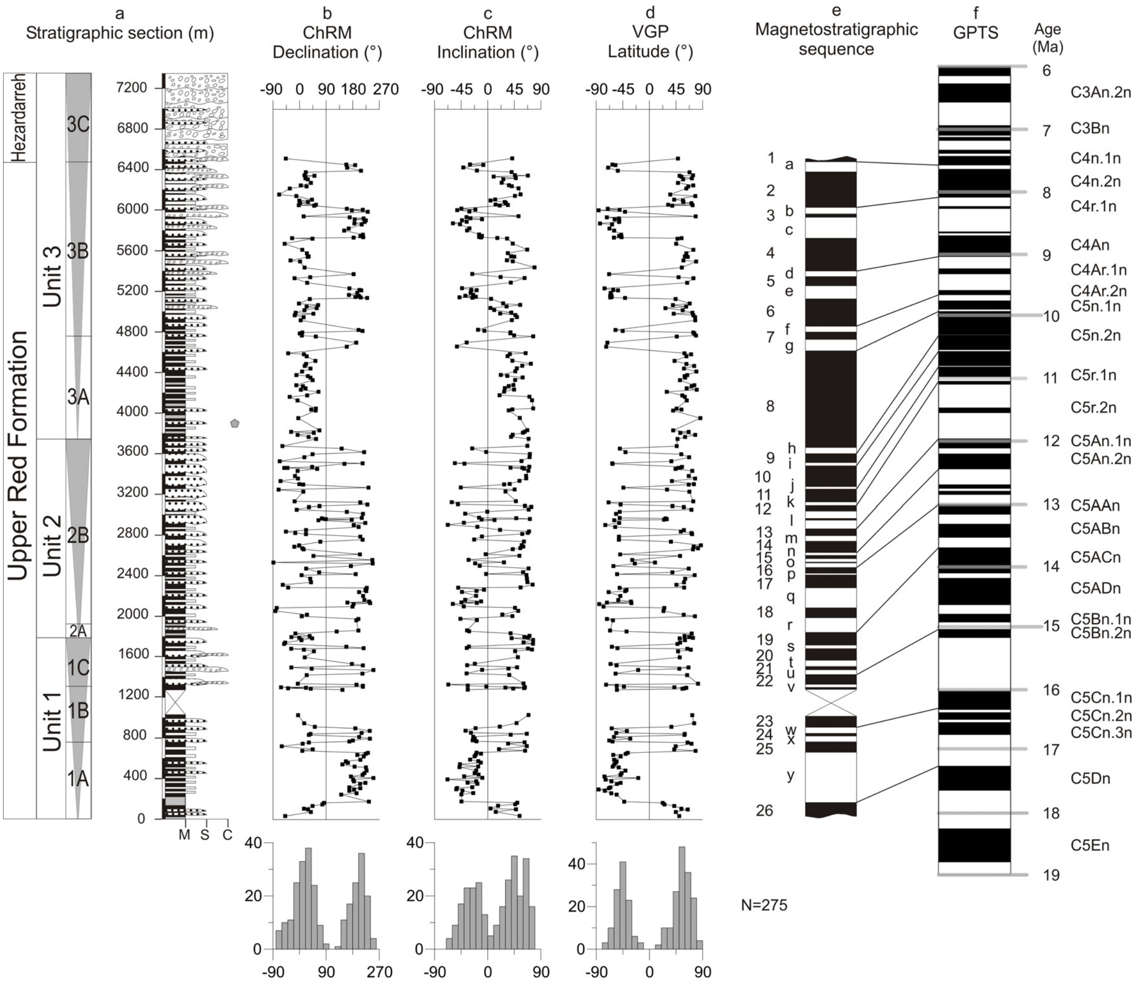

Figure 2.8: Eyvanekey sedimentary section (a) and detailed magnetostratigraphy including declinations (b), and inclinations (c) plotted in tilt-corrected coordinates, Virtual Geomagnetic Pole VGP (d), and the correlation between our magnetostratigraphic sequence (e) and the global geomagnetic polarity time scale (f) of Cande and Kent (1995). Boundaries between magnetozones were defined by the midpoint between two samples with opposite polarity. Frequency plots of inclination, declination and VGP indicate a Gaussian bimodal data distribution. Grey diamond at ca. 3900 m shows the position of the fission-track dated sample, which youngest cooling age is 13.3 Ma (Rezaeian 2008). See Fig. 2.4 for legend.

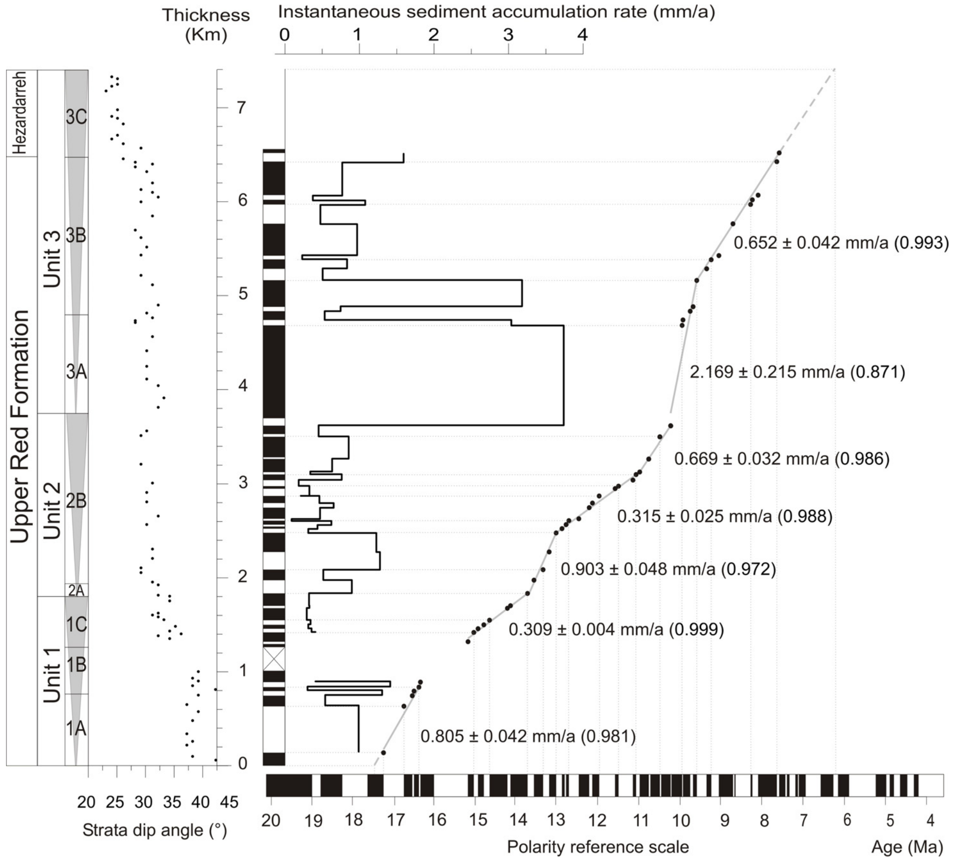

Figure 2.9: Long-term and instantaneous sediment accumulation rate for the Eyvanekey section in mm/a. Lines for each curve have been interpolated using a linear best fit. R-squared coefficient is indicated in parenthesis. The variation of the strata dip angle is also shown. Note that the dip angle decreases at the base of sub-units 1C and 3C

2.7 Discussion

2.7.1 Variation of magnetic properties

In the studied section, variations in NRM, magnetic susceptibility, and S-ratio allowed us to recognize three domains (Fig. 2.4). The first domain is hematite-dominated and it spans the sub-units 1A and 1B, while the second (sub-unit 1C, Unit 2, and bottom of sub-unit 3A) and third domains (sub-units 3A and 3B) are magnetite-dominated. Variations in magnetic properties have been linked to pedogenetic processes, tracing short-lived paleoenviromental changes (e.g., Maher and Thompson, 1991) or alternatively, to changes in sediment source, drainage pattern, sediment transport conditions or depositional environment (e.g., Gilder et al., 2001). In the Eyvanekey stratigraphic section, the lack of well-developed paleosol horizons, coupled with the relatively high sediment-accumulation rate, suggests that pedogenetic processes did not control the composition of the magnetic fraction. Based on the relatively long duration of the three domains and the coincidence between the shift to the third domain as well as a compositional change in the sandstones (Ballato, unpublished data), we suggest that the magnetic composition was probably controlled by changing source areas. This may have involved discrete erosional unroofing events and/or drainage pattern reorganization triggered by tectonic activity.

2.7.2 Significance of coarsening upward cycles and trends in accumulation rate

Our new data from the Eyvanekey section comprises a continental clastic sequence approximately 7400-m thick, organized in three coarsening upward cycles, deposited between ~ 17.5 and ~ 6.2(?) Ma (Figs. 2.8 and 2.9). The large amount of sediment deposited during this short interval suggests that the foreland basin was controlled by tectonic loading in the Alborz mountains. The average accumulation rate calculated for the Eyvanekey section is 0.65 mm/a. This is 2 to 3 times higher than rates obtained from similar studies carried out in several Central Asian basins associated with the India-Eurasia collision zone (e.g., Charreau et al., 2005), but it is within the range of highest long-term accumulation rates (0.5 to 0.7 mm/a) determined for the Himalayan and the Andean foreland basins (e.g., Meigs et al., 1995; Echavarria et al., 2003). The overall high accumulation rate obtained in the Eyvanekey section is punctuated by three prominent rate increases that started at ~17.5, 13.8, and 10.3 Ma. We interpret these unusually high rates to reflect the onset of rapid tectonic uplift, loading, and fast exhumation (~ 17.5 Ma), coupled with pulses of accelerated exhumation at ~ 13.8 and 10.3 Ma.

2.7.2.1 First cycle (Unit 1, ~ 17.5 to ~ 13.8 Ma)

The first relatively high accumulation rate (0.8 mm/a) is documented in the strata at the bottom of the section, which were deposited subsequent to the marine carbonates of the Qom Formation (Fig. 2.9). These carbonates, which in the southern Alborz foothills range in thickness between 250 (Eyvanekey section) and 400 meters (Deh Namak section), were deposited between Aquitanian pp. and Burdigalian pp. (Daneshian and Ramezani Dana, 2006). This implies an accumulation rate of ~ 0.05 to ~ 0.13 mm/a. The onset of deposition of sub-unit 1A marked a five- to tenfold increase in the sediment accumulation rate, which was associated with a sharp lithologic and sediment grain-size change. At Eyvanekey, the Qom Formation constitutes marine shallow-water carbonates associated with several channelized gravel bodies, while the coarsest grain fraction in the following sub-unit 1A is fine to medium sand. This drastic variation documents fundamental changes in the depositional environment, basin geometry, and surface gradients by ~ 17.5 Ma.

In this context, we interpret these patterns to reflect Miocene foreland-basin initiation due to flexural subsidence in the course of crustal shortening and thickening. This probably took place in the inner domain of the central Alborz, as suggested by fission-track cooling ages (Rezaeian 2008). The increase in sediment-accumulation rate is in agreement with the results of numerical modeling, which predicts enhanced subsidence in a foreland basin responding to thrust loading (e.g., Heller et al., 1998; Flemings and Jordan, 1990; Sinclair et al., 1991) (Fig.

2.10). However, the onset of thrust loading could have occurred 1-2 Ma earlier than 17.5 Ma, since the basinward sediment-accumulation history may have been progressively out of phase with thrusting (Flemings and Jordan, 1990). Collectively, the onset of flexural subsidence indicates quasi-continuous deformation in the southern central Alborz starting from the early Miocene. This followed an earlier Oligocene phase of uplift documented by the deposition of the conglomeratic Lower Red Formation and the clastic facies of the Qom Formation (Allen et al., 2003).

Fine-grained deposition until ~15.2 Ma indicates that subsidence outpaced sediment supply until the arrival of conglomerates in the foreland basin (e.g., Heller et al., 1998; Flemings and Jordan, 1990). The sediments at the bottom of the Eyvanekey section were probably deposited in an intermediate to distal position within the foreland. Interestingly, the influx of conglomerates correlates with the sharp decrease in the accumulation rate from 0.8 to 0.31 mm/a at ~ 15.2 Ma (Fig. 2.9). This reduction appears to have been linked with a decrease in the flexural subsidence due to the growth of an anticline within the foreland basin, which corresponds to the present-day SAA. Stratal geometric relationships support this interpretation, with the folded sub-units 1A and 1B truncated and overlain by sub-unit 1C (Figs. 2.3 and 2.9). Overall, the setting suggests that this part of the foreland system was incorporated into a wedge-top depozone (e.g., DeCelles and Giles, 1996, Simpson, 2006) by ~15.2 Ma. The progradation of coarse-grained facies in the first cycle may have therefore been related to the onset of uplift within the foreland realm (Clevis et al., 2004; Horton et al., 2004; Heermance et al., 2007), rather than to post-thrusting processes (e.g., Heller et al., 1988; Flemings and Jordan, 1990) (Fig. 2.10).

Alternatively, the coarse-grained sedimentation may have also been forced by high-frequency climate change and a trend toward more erosive climate conditions, similar to what has been inferred for the global increase in the deposition of coarse conglomerates in different orogens during the Pliocene (e.g., Zhang et al., 2001; Molnar, 2004). Global climate reconstructions document global cooling during the expansion of Antarctic ice sheet at approximately 14.5 Ma (e.g. Zachos et al., 2001). Unfortunately, detailed paleoclimatic data for the Middle East during Miocene time are not available to test whether this was a time of enhanced precipitation, erosion, and sediment production. Available sedimentologic and stratigraphic data record protracted evaporite deposition in central and northern Iran since the late Eocene, suggesting a hot, arid climate (Jackson et al., 1990; Davoudzadeh et al., 1997). However, moisture sourced in the Caspian and Black seas (Paratethyan basins, e.g., Allen and Armstrong, 2008) could have been forced into focused precipitation along the uplifting Alborz, Caucasus, and Kopeh Dagh ranges. Such a scenario of enhanced rock uplift and construction of an orographic barrier could have eventually caused increased sediment production and gravel progradation into the adjacent forelands (Paola et al., 1992; Marr et al., 2000; Mora et al., 2008).

Thus, even if there is evidence for the incorporation of foreland sectors into a wedge-top depozone, middle Miocene climatic forcing as a reason for the progradation of coarse strata cannot be excluded.

In summary, the first coarsening-upward cycle records (1) the onset of flexural subsidence (~ 17.5 Ma), indicating the beginning of quasi-continuous deformation in the southern central Alborz followed by (2) a decrease in subsidence (~ 15.2 Ma), due to local-scale uplift in the basin, and possibly an additional superposed forcing effect related to climate change (Fig. 2.10).

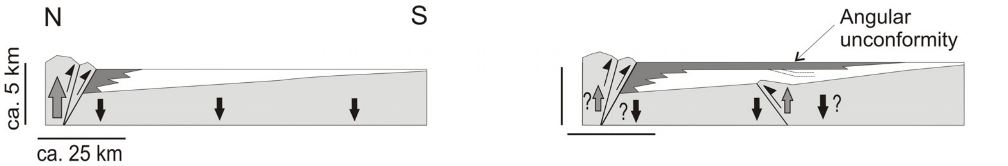

Sub-unit 1A and 1B (17.5-15.2 Ma): fine-grained facies

High accumulation rate (0.8 mm/a) due to active thrusting in the inner orogen

Sub-unit 1C (15.2-13.8 Ma): progradation of coarse-grained facies

Decrease in accumulation rate (0.31 mm/a) induced by uplift within the foreland

Sub-unit 2A and base of 2B (13.8-13 Ma): fine-grained facies

High accumulation rate (0.9 mm/a) due to active thrusting with foreland subsidence exceeding local uplift

Top of sub-unit 2B (11-10.3 Ma): progradation of coarse-grained facies

Relatively high accumulation rate (0.67 mm/a), associated with high sediment influx, overfill, and progradation

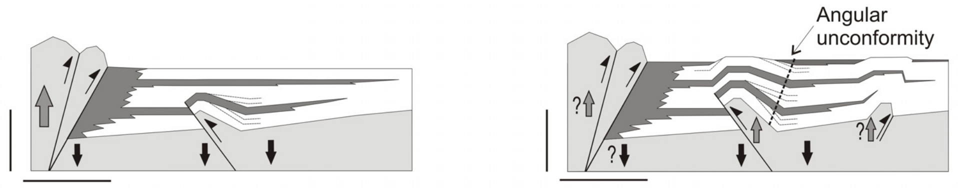

Sub-unit 3A and base of 3B (10.3-9.6 Ma): fine-grained facies

Very high accumulation rate (2.17 mm/a) induced by active thrusting in the orogen, coupled with erosional unroofing

Sub-unit 3B and 3C (9.6-6.2? Ma): progradation of alluvial-fan facies

Decrease in accumulation rate (0.65 mm/a) induced by inversion of buried foreland structures. Coarse-grained facies bypass folded region and are deposited in more distal area

Legend

▨ Pre-Upper Red Formation deposits
☐ Fine-grained deposits
■ Coarse-grained deposits
⬇ Flexural subsidence
⬆ Uplift
⋰ Approximate location of study section
⫽ Faults

Figure 2.10: N-S-oriented sketch depicting the evolution of foreland basin and the spatiotemporal patterns of sedimentary facies with respect to tectonic activity. For simplicity only two faults have been shown for illustrating the tectonic activity of the inner domain of the orogen.

2.7.2.2 Second cycle (Unit 2, ~ 13.8 to ~ 10.3 Ma)

The second increase in accumulation rate (0.31 to 0.9 mm/a) occurred at the beginning of the second coarsening-upward cycle at ~ 13.8 Ma. It is associated with the deposition of fine-grained deposits (Fig. 2.9). Fig. 2.3 shows the onlap of sub-unit 2A and part of sub-unit 2B onto the top of Unit 1, suggesting continued coeval growth of the anticline in the foreland basin. These relationships show that the overall flexural subsidence exceeded local uplift and burial of the growing structure beneath a thick cover of sediments (Fig. 2.10). Therefore, the increase in accumulation rate at ~ 13.8 Ma reflects a backward shift in the locus of the tectonic activity, with enhanced tectonic loading induced by crustal shortening and growth of the southern central part of the orogenic belt. Like Unit 1, a lag time might have occurred between the enhanced activity in the orogen and the flexural response of the foreland basin (Flemings and Jordan, 1990).

The upsection increase in the coarse-grained fraction is coupled with a progressive increase in thickness and frequency of coarse-grained, channelized sandstones, associated with a decrease in the accumulation rate to 0.3 mm/a at ~ 13 Ma (Fig. 2.9). It is not possible to determine, however, if the slowing down of foreland subsidence at ~ 13 Ma is linked to increased uplift of the intrabasinal anticline or to reduced thrust loading and subsequent isostatic rebound resulting from enhanced erosion, possibly associated with changes in precipitation.

Interestingly, during deposition of the last 400 meters of channelized sandstones in this sequence, an increase in the sediment accumulation rate to 0.67 mm/a occurred at ~ 11 Ma (Fig. 2.9). This value is smaller than the rate recorded at the bottom of the unit (0.9 mm/a), but much greater than the value obtained for the progradation of coarse-grained facies (0.3 mm/a). This rate increase is not associated with a change in sedimentary facies and maximum grain size, but does coincide with an increase in sandstone thickness and frequency. Possibly, the increase in sediment-accumulation rate is linked to faster exhumation recorded at ca. 12 Ma based on apatite (U-Th)-He thermochronology in the central western Alborz (Guest et al., 2006b). If true, a lag time of ~ 1 million years would have occurred between the faster exhumation in the orogen and the onset of flexural subsidence in the foreland basin. The occurrence of thick sandstones coupled with a relatively high sediment accumulation rate (0.67 mm/a) suggests that the amount of coarse-grained sediment available at that time was probably too voluminous for having been stored along the basin margin (e.g., Heller et al., 1988; Paola et al., 1992; Marr et al., 2000) (Fig. 2.10). This scenario thus suggests an overfilled basin allowing extensive syntectonic progradation of coarse-grained facies into the foreland during a period of increased subsidence within 1 million years of major exhumation, analogous to observations in the Himalayan foreland basin (e.g., Burbank et al., 1988; Brozović and Burbank, 2000).

In summary, the second coarsening-upward cycle consists of three episodes with long-term sediment accumulation rates of ~ 0.9, 0.3, and 0.67 mm/a. We conclude that this reflects:

(1) intensified shortening, uplift, and erosional exhumation at ~ 13.8 Ma associated with foreland-basin subsidence, which outpaced the uplift of a local-scale structure within the foreland; (2) decrease in subsidence (~ 13 Ma), probably due to intrabasinal uplift and possibly the effect of superposed climate change and/or isostatic rebound; (3) renewed subsidence at ~ 11 Ma, most likely correlated with accelerated exhumation recorded in the orogen at ~ 12 Ma. This last event led to a phase of pronounced sediment production and progradation of coarse-grained sediment toward the distal part of the foreland (Fig. 2.10).

2.7.2.3 Third cycle (Unit 3, ~ 10.3 to ~ 6.2(?) Ma)

The third episode characterized by high-accumulation rates began at ~ 10.3 Ma. It was coupled with an orogen-ward shift of the sedimentary facies belt and dominant deposition of fine-grained sediments. Similar to the previous cycles, the association of fast sediment-accumulation rate and fine-grained facies reflects enhanced tectonic loading in the southern central part of the orogen. The accumulation rate of 2.2 mm/a is the highest recorded in this section, and lasted approximately 0.7 myr (Fig. 2.9). During this episode, a sharp change in magnetic parameters is recorded. This is reflected by bulk magnetic susceptibility and NRM (Fig. 2.4), indicating an important variation in sediment-source areas. Taken together, these observations suggest an important erosional unroofing event, which led to the exposure of different source rocks and/or major drainage reorganization in response to an intense phase of tectonic activity within the orogen (Fig. 2.10).

The upsection increase in the mean grain-size is associated with a decreased accumulation rate (from 2.2 to 0.65 mm/a) starting at ~ 9.6 Ma, which was sustained until the onset of deposition of sub-unit 3C (Fig. 2.9). Compared to the previous cycles, the upsection decrease in accumulation rate during the third cycle is much larger, but the accumulation rates are more than double those of the previous cycles (fine-grained accumulation of 2.2 versus 0.8 to 0.9 mm/a, and conglomerate accumulation of 0.65 versus 0.3 mm/a). Throughout the entire third cycle, the relatively high accumulation rates, the progressive increase of the coarse-grained, progressively tilted fraction culminating in the deposition of 900 meters of coarse conglomerates (sub-unit 3C), as well as recycling of clasts, suggest important tectonism in the orogen (see chapter 3) (Figs. 2.3, 2.9 and 2.10). These relationships indicate that the deformation front, and hence the sediment source, must have advanced while the SSA was still actively growing. We suggest that the decrease in sediment-accumulation rate at ~ 9.6 Ma was linked to basin inversion, accompanied by the incorporation of the foreland sediments into a growth syncline in the hanging wall of the blind thrust responsible for the uplift of the SAA (Fig. 2.10). Incorporation of the basin into the orogenic wedge along the SSA forced the coarse grained facies to bypass the uplifted folded region and be deposited farther south, leading to a translocation of the depozone into the proximal foreland. Climate forcing cannot be completely excluded to explain these phenomena, but the ~ 7° tilt of the strata suggests dominant tectonic control (Figs. 2.9 and 2.10). Based on our new magnetostratigraphy results, basin inversion must have started at ca. 9 Ma and could have been completed by about 6.2 Ma, as suggested by the extrapolated age for the youngest strata of this section.

Uplift of the SAA between ca. 9.6 and 6.2(?) Ma appears to have been coeval with rapid exhumation of the inner domain of the central Alborz range, recorded by rapid cooling at approximately 7 Ma (Axen et al. 2001). This phase of accelerated tectonism has been associated with the reorganization of the Arabia-Eurasia deforming zone at ca. 5 Ma (Westaway, 1994; Axen et al., 2001; Allen et al., 2004; Copley and Jackson, 2006). Although the timing of the reorganization is quite well constrained, the causes of this process are not yet known (e.g., Copley and Jackson, 2006).

Summarizing, the third coarsening-upward cycle reflects two main processes: (1) an intense phase of thrust loading by ~10.3 Ma, followed by (2) basin inversion between ca. 9.6 and 6.2(?) Ma when the final uplift of the southern Alborz mountains was accomplished. These processes put the region of the Eyvanekey section into a proximal position in the foreland, promoting southward propagation of the foreland-basin depozones (Fig. 2.10).

2.7.3 Regional vs local tectonic effect on foreland-basin sedimentation

The occurrence of fine-grained deposits associated with high sediment accumulation rate at the base of the Upper Red Formation (sub-unit 1A) suggests foreland-basin initiation in the southern Alborz starting from early Miocene. Surprisingly, and in contrast with the evolution of our study area, the South Caspian Basin, immediately to the north of the Alborz mountains, does not record any significant increase in subsidence pattern earlier than 5 Ma (Nadirov et al., 1997). Presently, ca. 75% of the suspended river load from the central western Alborz is delivered to the Caspian Basin, while the remainder enters basins in Central Iran (Rezaeian et al., 2004). This imbalance in sediment budgets is clearly reflected by the drainage pattern north of the range, where the majority of rivers drain into the Caspian Sea. Nevertheless, a comparison of the sediment thickness deposited in Central Iran and in the South Caspian Basin during Miocene (5 versus 3 km, respectively), and since Pliocene time (ca. 2 versus 8 to 12 km respectively) (Jackson et al., 1990; Davoudzadeh et al., 1997; Allen et al., 2002; Brunet et al., 2003), suggests that an important reorganization of the drainage pattern had occurred sometime between late Miocene and Pliocene time (Guest et al., 2006b). Drainage reorganization might have been triggered by the regional sea-level low stand phase the during the Messinian salinity crisis at 5.5 Ma (Jones and Simmons, 1997), possibly in association with tectonic activity. The prominent increase in tectonic subsidence in the South Caspian Basin from the Pliocene onward may have also been coeval with the onset of Red Sea oceanic spreading and the westward extrusion of Turkey, suggesting an important plate tectonic reorganization of the Arabia-Eurasia collision zone at ca. 5 Ma (Westaway, 1994; Axen et al., 2001; Allen et al., 2004; Copley and Jackson, 2006). Therefore, during the earliest stages of mountain building in the Alborz, deformation was probably located in the inner sectors of the present-day central Alborz range (Rezaeian 2008) and the tectonic load mainly forced subsidence in the southern foreland basin. In contrast, during the Pliocene, accelerated tectonic subsidence in the South Caspian Basin was probably triggered by regional events (Westaway, 1994; Axen et al., 2001; Allen et al., 2004; Copley and Jackson, 2006) and facilitated by lateral lithospheric strength contrasts (Mangino and Priestley 1998; Guest et al., 2007a), rather than tectonic loading induced by processes in the Alborz mountains.

2.7.4 Deformation pattern

The relationship between sediment-accumulation rates, sedimentary facies, and stratal geometries within the Alborz foreland documents an overall southward propagation of the deformation front. However, the locus of deformation did not move steadily southward, but rather stepped forward and backward through time. Thus, on shorter-time scales of ca. 0.7 to 2 Ma, the orogen grew by a combination of frontal accretion and wedge-internal deformation, similar to predictions based on modeling studies (e.g., Hoth et al., 2007; Naylor et al., 2007). Interestingly, the ratio between the fastest and the slowest sediment-accumulation rate for each cycle is ca. 3, suggesting a possible cyclicity in the relation between thrust activity and surfaces processes. Furthermore, a high sediment-accumulation rate associated with the onlapping strata at the bottom of Unit 2 indicates contemporaneous activity of both frontal and internal structures, suggesting that the strain between active structures was transferred gradually (e.g., Hoth et al., 2007).

The inferred temporal shifts in the locus of deformation are compatible with deformation processes in a critical orogenic wedge (e.g., Davis et al., 1983; Dahlen, 1990). Internal wedge deformation through out-of-sequence thrusting thus alternated with wedge accretion and frontal thrusting associated with a change from a subcritical to a critical state, and vice versa (e.g., Davis et al., 1983; Dahlen, 1990; Hoth et al., 2007; Naylor et al., 2007). In such a system, the deformation patterns may have been dictated by the spatiotemporal distribution of erosion, the mode of erosion, and the rate of surface processes with respect to the rate of deformation (e.g., Willet, 1999; Whipple and Meade, 2004; Hoth et al., 2006; Simpson, 2007). Although speculative, the evolution of the Alborz mountains and their orientation with respect the modern rainfall distribution (e.g., Alijani et al., 2008) and the disparate nature of current erosion processes in the orogen (Rezaeian et al., 2004) suggests that the propagation of the deformation front might have been linked to the growth of an orographic barrier. In such scenario topographic growth would have promoted a shift in erosion from the pro-wedge (southern flank) to the retro-wedge (northern flank). In turn, this could have led to a southward propagation of the deformation front, coupled with the development of a wider orogen (e.g., Willet, 1999; Whipple and Meade, 2004; Hoth et al., 2006; Simpson, 2007).

2.8 Conclusions

1) Our magnetostratigraphic investigation of the foreland-basin deposits of the southern Alborz mountains documents that the Upper Red Formation, which corresponds to our coarsening upward units 1, 2 and sub-units 3A and 3B, was deposited approximately between 17.5 and 7.6 Ma. Assuming a constant accumulation rate for the last part of the section, the depositional age of the top of the Hezardarreh Formation (sub-unit 3C) in this area can be extrapolated to ~ 6.2 Ma. These foreland strata are thus older than the previously-inferred Pliocene age. We correlate the base of the Upper Red Formation with the onset of flexural subsidence related to crustal shortening and thickening in the central southern Alborz.

2) We observe a systematic correlation between coarsening upward cycles and accumulation rates (Fig. 2.9). Fine-grained sedimentation and an increase in sediment accumulation rates characterize the onset of each coarsening upward cycle. As predicted by numerical modeling (e.g., Heller et al., 1998; Flemings and Jordan, 1990; Sinclair et al., 1991), thrust loading induces maximum subsidence adjacent to the thrust belt. Here, the coarse-grained fraction supplied by the uplifting range is spatially restricted to the immediate vicinity of the range, while fine-grained sediments are deposited in distal sectors of the foreland basin. An increase in sediment accumulation rate together with the occurrence of fine grained facies therefore reflects enhanced tectonic activity in an actively deforming orogenic belt as documented for the units 1, 2, and 3, starting at ~ 17.5, 13.8, and 10.3 Ma, respectively. The subsequent progradation of coarse-grained facies is associated with a decrease in sediment-accumulation rates, suggesting that the overall tectonic subsidence decreased. This was likely the result of a combination of several factors, including (1) onset and modifying influence of intra-foreland basin uplift as documented for Unit 1 and partially for Unit 2 at ~ 15 and 13 Ma, respectively, and (2) basin inversion associated with the uplift of the SAA and the incorporation of the study area into a growth syncline located in a proximal foreland sector as documented for Unit 3 by ~ 9.6 Ma (Fig. 2.10). Although the progradation of coarse-grained facies in each cycle is apparently related to tectonic forcing, an additional contribution due to decreased tectonic activity in the orogen with related flexural rebound, and an influence of climate change cannot be ruled out.

3) The deposition of the coarse-grained facies comprising the top of Unit 2 at ~ 11 Ma, was associated with a relatively high sediment-accumulation rate. This increase in accumulation rate might be correlated with a phase of rapid exhumation and thrust loading in the orogen at about 12 Ma, documented by thermocronological. Such syntectonic progradation suggests that

the supply of the coarse-grained fraction outpaced the storage capacity of the proximal part of the foreland.

4) Our detailed chronology of the foreland-basin deposits allows us to trace the long-term tectonic evolution of the Alborz mountains. Our data suggest that orogen growth was related to a combination of thrust activity within the orogen and frontal accretion, as documented by the intra-foreland uplift. This implies a back and forward migration of the locus of tectonic activity superimposed on a longer-term southward migration of deformation fronts on a time scale of ca. 0.7 to 2 Ma.

Acknowledgments

This research was founded by the German Science Foundation (Leibniz Award to M. Strecker and grant STR 373/19-1 to M. Strecker and A. Friedrich) and the graduate school program of the University of Potsdam. We are indebted to the Tehran Building and Housing Research Center and the municipality of Kilan for logistical support. A Entezari, B. Keshavarzi, T. Roeper and D. Pilz are kindly thanked for help with sampling and sample preparation. B. Fabian is thanked for figure drafting. We thank S. Gilder, B. Guest, B. Horton, J. Jackson, D. Melnik, D. Michalk, A. Mora, M. Parra, M. Rezaeian, J. F. Ritz, H. D. Sinclair, M. Szurlies, J. Zamagni and G. Zeilinger for fruitful discussions and suggestions that improved this work. C. E. Uba provided a fundamental contribution for the interpretation of the sedimentary facies pattern within the foreland basin. S. Hoth reviewed an earlier version of the manuscript and provided helpful comments. T. Schildgen is thanked for her help with the text and constructive comments. We also acknowledge the constructive reviews provided by M.B. Allen and M.F. Brunet. The analysis and presentation of paleomagnetic data was in part performed with PMag Tools Version 4.2a by M. H. Hounslow

3. Arabia-Eurasia continental collision: insights from late Tertiary foreland-basin evolution in the Alborz mountains, northern Iran

Abstract

A poorly-understood lag time of 15-20 m.y. exists between a late Eocene to early Oligocene age for the initial Arabia-Eurasia continental collision and the acceleration of tectonic and sedimentary processes across the collision zone in the early-late Miocene. The late Eocene to Mio-Pliocene clastic and shallow-marine sedimentary rocks of the Kond, Eyvanekey, and Semnan basins in the Alborz mountains (northern Iran) offer the possibility to track the evolution of this orogen in the framework of collisional processes. A transition from volcaniclastic submarine deposits to shallow-marine evaporites and terrestrial sediments occurred shortly after 36 Ma in association with reversals in sediment provenance, strata tilting, and erosional unroofing. These events followed the termination of subduction arc magmatism and marked a changeover from an extensional to a contractional regime in response to initiation of continental collision with the subduction of stretched Arabian lithosphere. This early stage of collision produced topographic relief associated with shallow foreland basins, suggesting that shortening and tectonic loading occurred at low rates. Starting from the early Miocene (17.5 Ma) flexural subsidence in response to foreland basin initiation occurred. Fast sediment accumulation rates and erosional unroofing trends point to acceleration of shortening by the early Miocene. We suggest that the lag time between the initiation of continental collision (36 Ma) and the acceleration in regional deformation (20-17.5 Ma) reflects the effects of a two-stage collision processes involving the “soft” collision of stretched lithosphere at first and “hard” collision following the arrival of unstretched Arabian continental lithosphere in the subduction zone.

3.1 Introduction

The process of continental collision involves plate accretion and terrane suturing, and is associated with the formation of areally extensive deformation zones with variable kinematics and high-elevation regions (e.g., Molnar and Tapponnier 1975). The Arabia-Eurasia collision zone is a tectonically active region, where shortening, crustal thickening, and uplift are accommodated within several orogenic belts (e.g., Zagros, Alborz, Kopeh Dagh, Talesh and Caucasus mountains). This region is furthermore characterized by the subduction of the South Caspian basin beneath the North Caspian sea along the Aspheron Sill, and by large intracontinental strike-slip faults (e.g., Nayband-Gowk and Neh-Zahedan fault systems) that bound virtually undeformed rigid blocks (e.g., Southern Caspian basin, Central Iran, Lut and Helmad blocks (Fig., 3.1; e.g., Jackson et al., 1995).

The timing of the Arabia-Eurasia continental collision is controversial, with estimates ranging from Late Cretaceous to Mio-Pliocene time (e.g., McQuarrie et al., 2003; Guest et al., 2006b). An increasing number of studies has led to the proposition that the onset of collision began in latest Eocene to early Oligocene time (Fig., 3.1; e.g., Jolivet and Faccenna, 2000; Hessami et al., 2001; Ershov et al., 2003; Keskin, 2003; Agard et al., 2005; Vincent et al., 2005; Hafkenscheid et al., 2006; Robertson et al., 2006; Boulton and Robertson, 2007; Vincent et al., 2007; Allen and Armstrong 2008; Horton et al., 2008; Rezaeian 2008; Homke, et al., 2009). However, thermochronologic data (Axen et al., 2001; Guest et al., 2006b, Verdel et al., 2007; Rezaeian 2008), syntectonic sedimentation (Hessami et al., 2001; Ershov et al., 2003; Homke et al., 2004; Guest et al., 2007; Ballato et al., 2008; Farzipour-Saein et al., 2009), and comparison of total shortening estimates and extrapolated geodetic strain rates (Allen et al., 2004; Mouthereau et al., 2006; Guest et al., 2006a) have been used to posit an acceleration of collision-related uplift, exhumation and subsidence in adjacent basins beginning in the early to late Miocene (Fig. 3.1). This implies a lag time of 15-20 m.y. between the early stages of continental collision and subsequent enhanced tectonic deformation, uplift, and exhumation (Horton et al., 2008). Interestingly, the early to late Miocene phase of enhanced deformation in the Arabia-Eurasia collision zone pre-dates the regional plate-tectonic reorganization at 5 ± 2 Ma, which eventually led to the westward extrusion of Turkey perpendicular to the present-day shortening direction (Westaway, 1994).

A similar lag time exists in the India-Eurasia collision zone, with collision beginning between 55 and 45 Ma (e.g., Garzanti, 2008) and superseding major tectonic processes during the Neogene (e.g., Métivier et al., 1999; Najman and Garzanti, 2000; Najman, 2006; Sobel et al., 2006; Clift et al., 2008). These observations suggest that such a time lag between ocean-basin closure and the beginning of widespread deformation across the continental collision zone might represent a common phenomenon under certain tectonic boundary conditions. The observations from both collision environments therefore raise general questions concerning the mechanisms, timing, and magnitude of upper-plate crustal deformation during continental collision in addition to the particular processes inherent to the specific setting of the Arabia-Eurasia collision zone. In light of these issues several questions may be raised. For example, why did the acceleration of tectonic processes occur several millions of years after the ocean-basin closure? How did deformation evolve through time across the continental collision zone? Did deformation propagate outward once areas with thick crust had been generated (e.g., Allen et al., 2004) or was the onset of deformation spatially disparate, but coeval across a wide zone (Dayem et al., accepted for publication in Tectonics) Answering these important questions can be attempted by a detailed study of the evolution of sedimentary basins of the Alborz mountains in northern Iran, which may eventually help understand intracontinental deformation processes on a global scale.

Late Eocene to Mio-Pliocene sedimentary sequences are well exposed in the basins that are closely linked to the Alborz mountains, thus covering the time span between the onset of collision-related deformation and the ongoing present-day deformation processes. These partly dated clastic successions are ideal archives for tracking the evolution of the Alborz orogen in the context of upper-plate collisional processes. Here, we present new geochronological, sedimentological and provenance data from the shallow-marine and terrestrial clastic deposits of the Kond, Semnan and Eyavaneky basins in the Alborz mountains and we asses the termination of arc magmatism in this region. The Kond and Semnan basins are here investigated in detail for the first time, while the Mio-Pliocene clastic deposits of the Eyvanekey basin have been previously dated by magnetostratigraphy (Ballato et al., 2008). A thorough study of this area allows to: (1) better constrain the termination of Eocene magmatism associated with the latest stages of subduction of oceanic crust; (2) unravel the sedimentary processes and tectonic evolution of the sedimentary basins straddling the southern Alborz; (3) define the spatiotemporal patterns of deformation and decipher the evolution of the shortening direction during the late Cenozoic, and (4) refine the timing and characterize the mechanisms of major tectonic events during the Arabia-Eurasia continental collision.

Collectively, our data show that contractional deformation in the Alborz mountains started shortly after 36 Ma at low rates, and that tectonic rates increased prior to 17.5 Ma. We suggest that the time interval between ca. 36 and ca. 17.5 Ma reflects the subduction of stretched Arabian continental lithosphere. This interval apparently predates the subduction of unstretched continental lithosphere, which ultimately caused an acceleration in upper- and lower-plate tectonic deformation.

3.2 Tectonic and structural setting

The E-W oriented Alborz mountains constitute a tectonically active, intracontinental orogen located between the Southern Caspian Basin and Central Iran (Fig. 3.1). The Alborz are characterized by a system of double-verging reverse faults and subvertical strike slip-faults subparallel to the trend of the range (Fig. 3.2; e.g., Haghipour et al., 1987; Vahdati Daneshmand, F., 1991). GPS data record 6±2 mm/yr of NNE-oriented shortening and 4±2 mm/yr of left-lateral shearing in the central part of range (Vernant et al., 2004b; Masson et al., 2007), reflecting the ongoing collision between Arabia and Eurasia. Earthquake focal mechanisms around the South Caspian basin show that NNE-oriented shortening is partitioned into dip-slip and strike-slip faulting on separate structures (Jackson et al., 2002). Left-lateral strike-slip motion apparently accommodates NW-ward extrusion of the South Caspian basin, which started ca. 10 m.y. ago (Hollingsworth et al., 2008). Despite evidence of present-day strain partitioning, new fault kinematic data, anastomosing faults, and obliquely oriented fold axes suggests that oblique thrusting has accommodated transpressional deformation in this region (e.g., Allen et al., 2003; Guest et al., 2006a; Zanchi et al., 2006; Landgraf et al., 2009). This caused a transpressional duplex system in the hanging wall of the North Tehran Thrust, which delimits the central Alborz mountains to the south (Fig. 3.2). Along this structure oblique shortening was accommodated by NW-SE oriented frontal and E-W striking oblique ramps (Fig. 3.2, Guest et al., 2006a; Landgraf et al., 2009). These processes furthermore resulted in the development of en échelon fold systems in both, hanging wall and footwall of the Mosha Fasham Fault (Fig. 3.2), a structure that merges with the North Tehran Fault and which is currently characterized by sinistral strike-slip faulting. Moreover, the occurrence of refolded NW-oriented fold axes in the hanging wall of the North Tehran Trust and the results of a fault-kinematic analysis in the central and western parts of the range suggest that the present-day NNE-oriented shortening direction was preceded by NW-directed shortening associated with right-lateral transpression (Allen et al., 2003; Guest et al., 2006a; Zanchi et al., 2006; Landgraf et al., 2009). Cross-cutting relationships indicate that the present-day shortening direction has been sustained during the last 7 Ma (Axen et al., 2001). In the western Alborz mountains, dextral transpression has been explained by the extrusion of a crustal block bounded by both left- and right-lateral strike-slip faults (Guest et al., 2006a). Alternatively, older N-S shortening may have been caused by a rigid southward translation of the Southern Caspian basin, causing conjugate right- and left-lateral faults on the western and eastern side of the Alborz range, respectively (Allen et al., 2003).

Regarding the timing of late Tertiary deformation in the Alborz, thermochronological data reveal different pulses of exhumation. Apatite fission-track cooling ages document two age clusters during the early Oligocene (ca. 32 Ma) and the early Miocene (ca. 16 Ma; Rezaeian, 2008). Apatite (U-Th)/He thermochronology from different intrusive bodies, as well as across some of the fault bounded ranges in the central-western Alborz mountains yields cooling ages between 10 and 4 Ma (Axen, 2001, Guest et al., 2006b; Rezaeian, 2008), indicating that 2 to 3 km of crust has been exhumed since the late Miocene.

3.3 Tectono-stratigraphic evolution of the southern Central Alborz mountains

The Alborz mountains form an orographic barrier between the Southern Caspian basin, where most of the moisture is sourced, and the semiarid to arid Central Iran basin (e.g., Rezaeian 2008). Deformation in this range reflects a history of contractional and extensional reactivation of inherited structures since the early Paleozoic (e.g., Assereto, 1966; Guest et al., 2006a; Zanchi et al., 2006; Yassaghi and Madanipour, 2008; Wilmsen et al., 2009). This has resulted in a complex and discontinuous stratigraphic record, with significant lateral variation in sedimentary facies and thickness (Assereto et al., 1966).

The Pre-Cambrian to Mesozoic strata experienced a regional phase of shortening, uplift, and erosion during the Late Cretaceous to early Paleocene (Stöcklin, 1968; Berberian and King, 1981). In the Alborz mountains, this deformation was associated with the deposition of terrestrial clastic deposits (Fajan Formation, Late Cretaceous? to early Eocene?). The Fajan Formation comprises conglomerates and red sandstones in angular unconformity on a folded substratum. These deposits have a variable thickness and attain a maximum of ca. 0.8 km in the hanging wall of the Mosha Fasham Fault (Fig. 3.2).

An intense volcanic eruptive phase occurred during the Eocene along the southern margin of the Eurasian plate in response to renewed Africa-Arabia northward motion and subduction (e.g., Dewey et al., 1973). In Iran, extensive, largely submarine volcanic activity occurred north of the Zagros suture zone encompassing northwest, central and eastern Iran (e.g., Berberian and King, 1981). The northwest-southeast oriented Urumieh-Dokhtar volcanic arc is considered to be a major volcanic province at that time (Fig. 3.1; e.g., Brunet et al., 2003; McQuarrie et al., 2003; Vincent et al., 2005; Verdel, 2008; Ahmadian, et al., 2009). This Eocene magmatic episode led to deposition of a thick pile of volcaniclastic sediments in rapidly subsiding marine basins between ca. 55 and 37 Ma (Berberian and King, 1981; Brunet et al., 2003; Vincent et al., 2005; Verdel, 2008). These deposits are composed of varying proportions of green tuffs, andesites, sandstones and shales, with a thickness ranging from 6 to 12 km (e.g., Berberian and King, 1981; Davoudzadeh et al., 1997; Vincent et al., 2005; Verdel 2008). In the Alborz mountains these deposits pinch out northward, while they are absent on the northern slope of the range, suggesting paleorelief during the Eocene (e.g., Davoudzadeh et al., 1997; Guest et al., 2006a). The volcanics have a complex geochemistry, interpreted to reflect the partial melting of hydrated lithospheric mantle typical of arc magmatism and related to the northward subduction of Neo-Tethyan oceanic crust (e.g., Brunet et al., 2003; Vincent, 2005; Verdel, 2008; Ahmadian, et al., 2009). Syndepositional normal faults in the Alborz mountains (Brunet et al., 2003; Guest et al., 2006a), and an Eocene metamorphic core complex in central and eastern Iran (Moritz et al., 2006; Verdel et al., 2007), indicate that this magmatic episode occurred during regional extension. In particular, in eastern Iran east-west oriented middle Eocene (ca. 49 to 40 Ma) extension was associated with magmatism and sedimentation that predated early Miocene shortening (Fig. 3.1; Verdel et al., 2007). In this context, extensional tectonism, arc magmatism, submarine deposition, fast accumulation rates, and indicators of slumping and soft-sediment deformation have been interpreted to reflect sedimentation in a rapidly subsiding backarc extensional basin related to the rollback of the Neo-Tehthys slab (e.g., Brunet et al., 2003; Vincent et al., 2005; Verdel, 2008). Subsequently, volumetrically less-important ocean-island basalts were deposited locally, which have been interpreted to be related to asthenospheric upwelling over thinned lithosphere, starting at ca. 33 Ma (Berberian and King, 1981; Verdel, 2008).

In places, the volcaniclastic sequence is superseded by upper Eocene marine evaporites of the Kond Formation (e.g., Jackson et al., 1990, Davoudzadeh et al. 1997). The Karaj and Kond formations are in turn unconformably overlain by terrestrial clastic and evaporitic deposits of the Oligocene Lower Red Formation (e.g., Jackson et al., 1990, Amini, 1997; Davoudzadeh et al. 1997), inferred to have been associated with a regional phase of shortening during the late Eocene-early Oligocene (Stöcklin, 1968; Berberian and King, 1981). During the late Oligocene-early Miocene, a shallow-water epicontinental sea (Qom Sea), existed in central and northern Iran, leading to the deposition of carbonates up to 1 km thick (Qom Formation, e.g., Reuter et al., 2008). The superseding 17.5 to 7.5 Ma Upper Red Formation comprises 6- to 7- km-thick playa lake and fluvial sediments, exposed in the southern Alborz (Amini, 1997; Ballato et al., 2008). In the southern Alborz, the Upper Red Formation has been linked to the onset of flexural subsidence and foreland-basin development induced by crustal shortening and thickening (Ballato et al., 2008). Similar deposits have been described in the intermontane Taleghan-Alamut basin, where they record syndepositional contractional deformation (Guest et al., 2007). Along the southern flank of the Alborz mountains, the Upper Red Formation is overlain by the 1.5-km-thick conglomeratic Hezardarreh and Kahrizak formations (units A and B, Rieben, 1955). These formations were interpreted as alluvial-fan deposits of late Miocene to Pleistocene age, reflecting an enhanced phase of exhumation and superposed effects of climate change (Rieben, 1955). In the southern Alborz mountains, the Hezardarreh Formation has an age of 7.5 to possibly 6.2 Ma (Ballato et al., 2008).

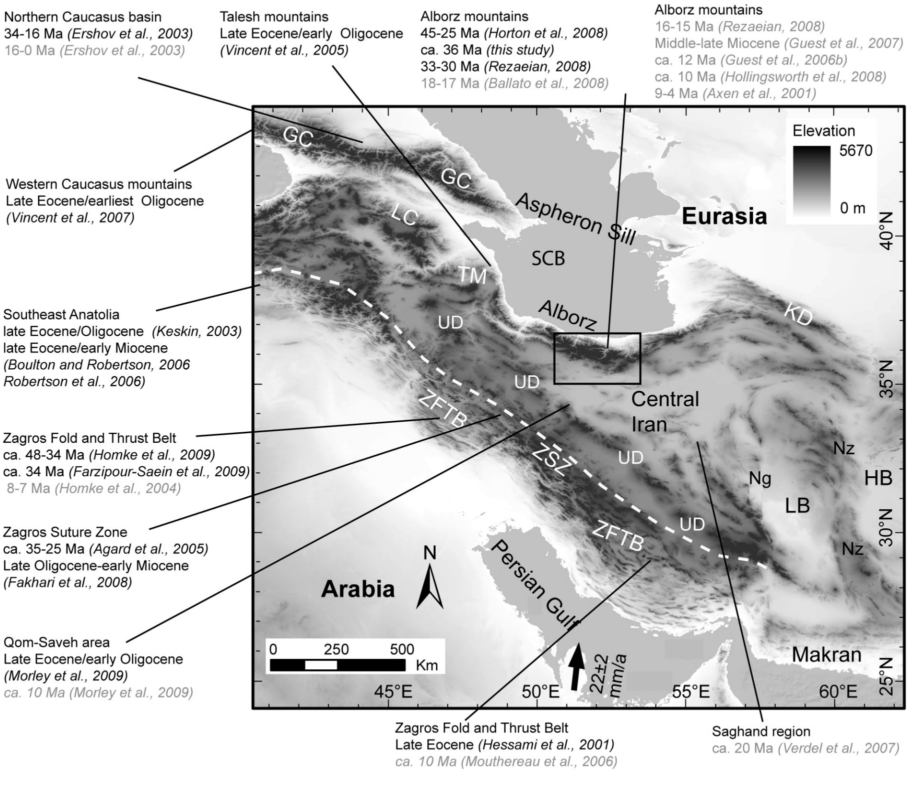

Figure 3.1. Digital Elevation Model (DEM) of Iran and adjacent regions based on SRTM data that shows the locations where evidence of a late Eocene-early Oligocene collision (black labels), and an early-late Miocene rejuvenation or initiation of tectonic activity (grey labels), have been found. The black arrow is in the direction of the present-day motion of the Arabian plate relative to Eurasia (Vernant et al., 2004a). The dashed white line indicates the approximate location of the Zagros suture zone. The black frame outlines the location of Figure 2. HB: Helmand Block; LB: Lut Block; SCB: South Caspian Basin; Ng: Nayband-Gowk fault system; Nz: Neh-Zahedan fault system; UD: Urumieh Dokhtar magmatic arc; ZSZ: Zagros suture zone; ZFTB: Zagros fold and thrust belt; GC: greater Caucasus; LG: Lesser Caucasus; and TM: Talesh mountains.

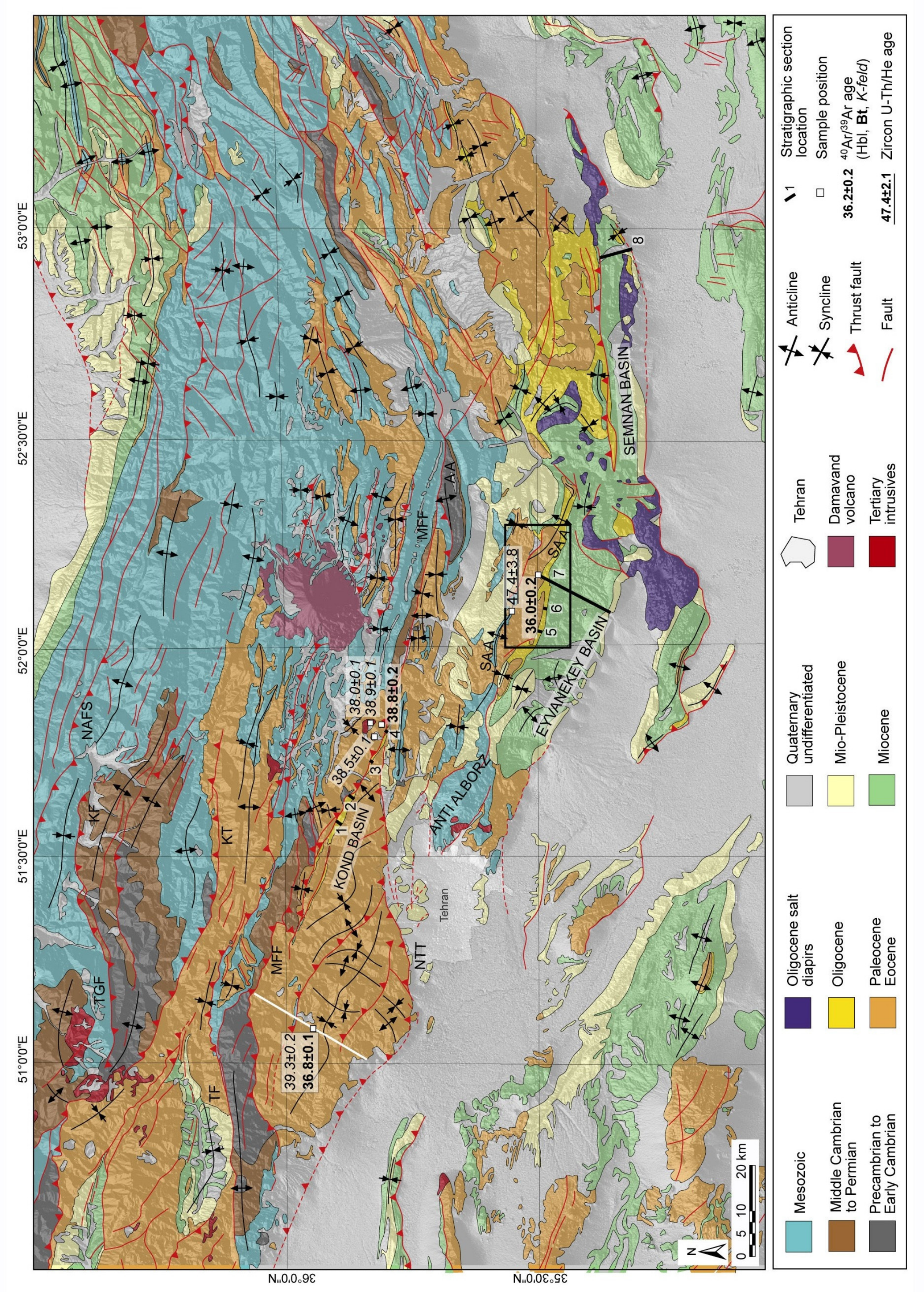

Figure 3.2 Geologic map of the central Alborz mountains superimposed on a SRTM-based DEM, includes the geochronologic data and the locations of the stratigraphic sections from this study. The black frame outlines the location of Figure 8. The white line shows the approximate location of the Chalus road transect, where rocks were dated by Verdel (2008). The Geology is modified after Amidi, (1984), Haghipour et al., (1987), Vahdati Daneshmand, (1991), Vahdati Daneshmand, F., and Saidi, A., (1991), Aghanabati, A., and Hamedi, A.R, (1994), and Guest et al., (2006a). The Precambrian to Early Cambrian units include the Kahar, Soltanieh, Barut, Zaigun, Lalun and Mila formations; the Middle Cambrian to Permian units constitute the Geirud, Dorud and Ruteh formations; Mesozoic strata consist of the Elika, Shemshak, Dalichai, Lar, Tiz Kuh formations, and the Late Cretaceous limestones; Paleocene-Eocene units are composed of the Fajan, Karaj and Kond formations; the Oligocene-Miocene is represented by the Lower Red and Qom formations, while Miocene and Mio-Pliocene strata are represented by the Upper Red and Hezardarreh formations, respectively. AA: Ayeverdan Anticline; KF: Khashachal fault; KT: Kandavan Thrust; MFF: Mosha Fasham Fault; NAFS: North Alborz Fault System; NTT: North Tehran Thrust; SAA: Southern Alborz Anticline; TF: Taleghan fault; TR: Taleghan range; and TGF: Tang e Galu fault zone.

3.4 Methodology

Analyzing the evolution of the sedimentary facies in the Kond, Eyvanekey, and Semnan basins, can provide crucial records to decipher the spatiotemporal characteristics of deformation, uplift, and fluvial network development in the Alborz mountains during late Cenozoic contractional deformation. The Kond basin is located in the central part of the range and recorded sedimentation until the early Miocene. The Eyvanekey and the Semnan basins are situated in the southern foothills of the Alborz mountains, where deposition lasted until the late Miocene and possibly the Pliocene (Fig. 3.2; Ballato et al., 2008). The combined study of these basins allows investigating sedimentary processes in the Oligocene to Miocene interval, thereby providing information about the succession of tectonic events.

Compressional deformation postdates Eocene magmatism in this region. To develop a chronostratigraphic framework for the studied basins, we therefore constrained the temporal extent of this magmatic phase by means of ^{40}Ar/^{39}Ar and zircon (U-Th)/He thermochronology (Fig. 3.2, Appendix 2).

The geochronological study was augmented by a detailed sedimentological analysis of the Oligo-Miocene continental sediments, including the Lower Red, Upper Red and Hezardarreh formations, and the shallow-water marine deposits of the Qom Formation. Eight stratigraphic sections located in the three basins were studied in detail (Figs. 3.2, 3.3, and 3.4). Eighteen lithofacies types (Table 1) were documented based on lithological, sedimentary structure and fabric analysis according to the classification of Miall (1996). The combination of the different lithofacies and the geometric characteristics of the sedimentary bodies allow distinguishing between eight facies associations, and provide the means for an assessment of their depositional environments (Table 2; Figs. 3.5 and 3.6).

A provenance study of sandstones and conglomerates, furthermore allowed identification of compositional variations, which were related to exposure of new sources and/or drainage-pattern reorganization through time. More than eighty sandstones were analyzed and ca. 450 points were counted according to the Gazzi Dickinson method (Appendix 3). Conglomerate clasts were counted throughout the studied stratigraphic sections at more than fifty localities. At each site we identified clasts of different lithologies every 5 to 10 cm, depending on grain size, within a 50 x 50 cm grid for a total of at least 100 points.

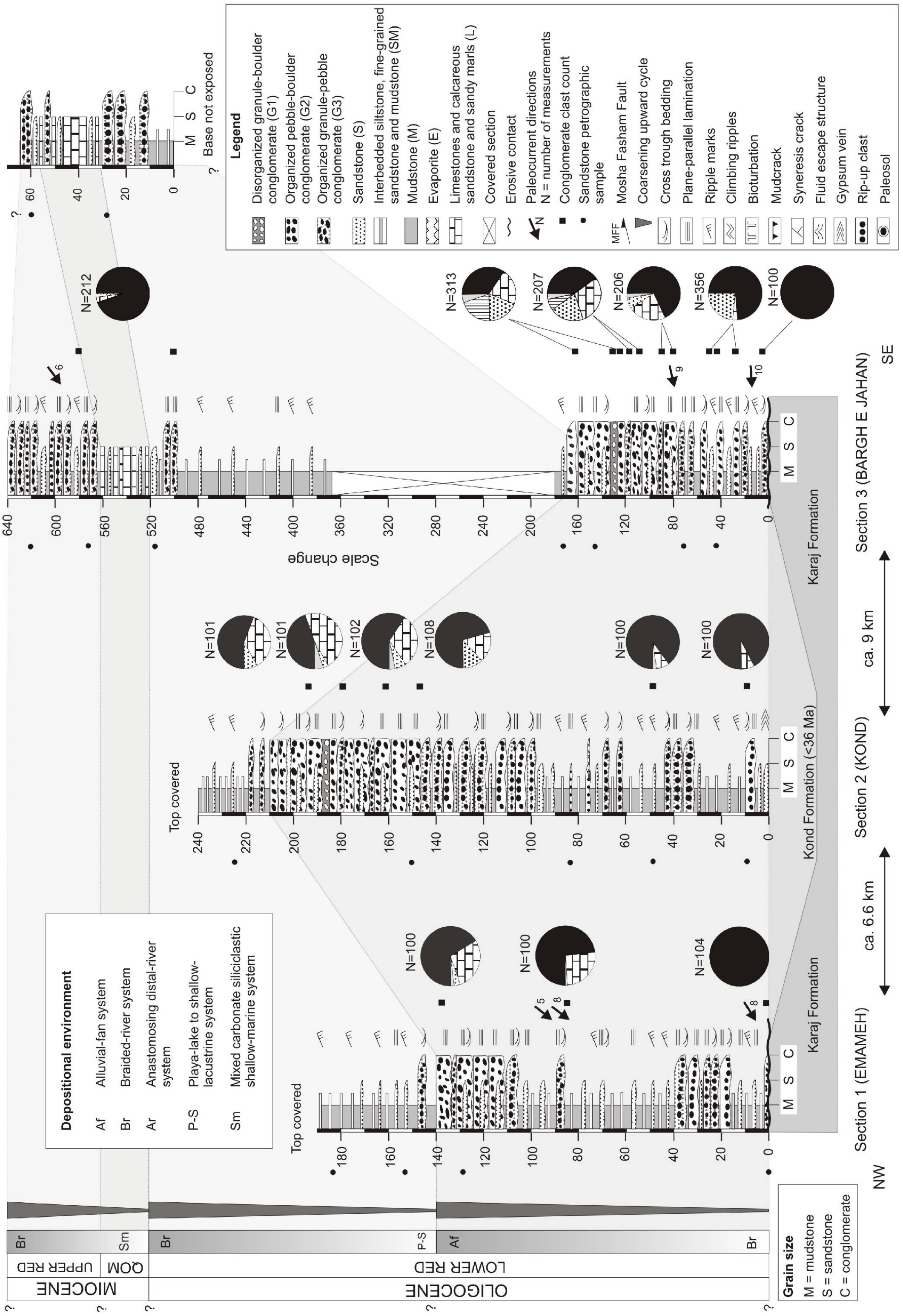

Figure 3.3. Measured stratigraphic sections for the Kond basin showing sedimentary facies distributions, depositional environments, stratigraphic correlations, paleocurrent data, and conglomerate-clast compositions (see Figure 4 for the clast type description).

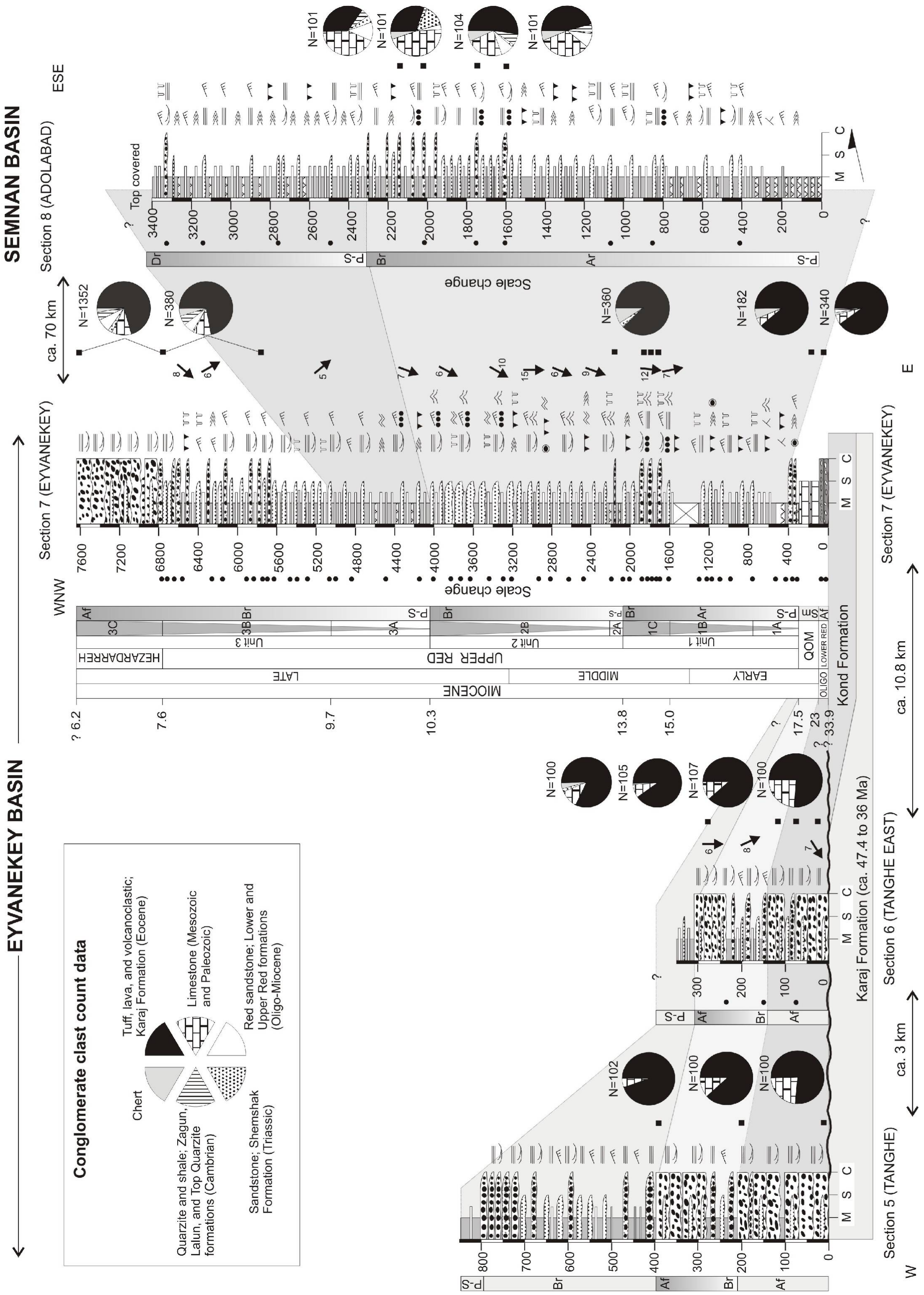

Figure 3.4. Measured stratigraphic sections for the Eyvanekey and Semnan basins, showing sedimentary facies distributions, depositional environments, stratigraphic correlations, paleocurrent data, and conglomerate-clast compositions. The Eyvanekey stratigraphic section is modified after Ballato et al. (2008).

TABLE 3.1: DESCRIPTION AND INTERPRETATION OF LITHOFACIES

Facies code	**Lithofacies**	**Interpretation**
Gmd	Disorganized, structurless matrix-supported monomictic to polymictic conglomerate. Granules to boulders, subangular to rounded, maximum diameter 0.8 m.	Mass flow deposited from hyperconcentrated or turbulent flow.
Gcd	Disorganized, structurless clast-supported monomictic to polymictic conglomerate. Pebbles to boulders, subangular to rounded, maximum diameter 0.8 m.	Rapid deposition by stream-floods with concentrated clasts.
Gco	Moderately organized, clast-supported monomictic to polymictic conglomerate. Granules to boulders, inverse to normal grading, weak imbrication. maximum diameter 0.8 m.	Traction bedload,
Gt	Matrix to clast-supported monomictic to polymictic conglomerate. Crude trough cross-stratification and imbrication, normal grading. Granules to boulders, subangular to rounded, maximum diameter 0.3 m.	Bar bedforms, channel fills.
Gh	Matrix to clast-supported monomictic to polymictic conglomerate. Horizontal bedding, normal to inverse grading with crude imbrication. Granules to boulders, subangular to rounded, maximum diameter 0.3 m.	Bar bedforms, lag deposits.
St	Trough cross-stratified sandstone. Fine to coarse-grain size, occasionally with pebbles, moderate to well sorting.	Dunes migration, upper to lower flow regime.
Sh	Horizontally stratified sandstone. Fine to coarse-grain size, occasionally with pebbles, flat parallel lamination, moderate to well sorting.	Planar bed flow, upper flow regime.
Ss	Scour surface. Medium to coarse grained sandstone and conglomerate, filled with intraformational mud-chip clasts.	Scour fills.
Sm	Massive-structureless sandstone. Very fine to coarse-grain size, pebbly, moderate to well sorting.	Rapid deposition, sediment gravity flow.
Sr	Ripple cross-stratified sandstone. Very fine to medium-grain size, generally asymmetric, occasionally climbing ripple.	Ripples, lower flow regime. Climbing ripples, during rapid accumulation.
Sc	Centimetric to metric-scale convoluted bedded sandstone.	Deformation by different load and dewatering.
Fl	Fine laminated mudstone to siltstone. Flat parallel lamination, very small-scale ripples, desiccation cracks common, generally calcareous.	Suspension deposits, overbank or abandoned channels.
Fm	Massive or platy mudstone to siltstone. Poor lamination, desiccation cracks common, generally calcareous. Locally mottled.	Suspension deposits, overbank or abandoned channels.
Ev	Evaporites layers.	Evaporation of standing water.
P	Poorly to moderate developed paleosol with rhizoliths and locally with calcretes and gypcretes.	Incipient paleosol formation.
Bl	Bioclastic, massive to bedded, limestones, including peloidal-coated grain packstone/grainstone, and miliolids-mollusk-bryozoan packstone, locally with coralline algae and coral debris. Siliciclastic fraction locally dominant. Fine to coarse-grain size.	In situ carbonate accumulation and wave reworking.
Ms	Green, locally sandy marls.	Suspension deposits.
Cg	Disorganized, matrix to clast-supported, very well-cemented, monomictic calcareous conglomerate. Pebbles to cobbles, subangular to rounded, maximum diameter 0.3 m.	Hyperconcentrated flows and debris flow.

TABLE 3.2: DESCRIPTION AND INTERPRETATION OF FACIES ASSOCIATION AND THEIR OCCURRENCE

Facies association	**Description**	**Lithofacies**	**Stratigraphic occurrence**	**Interpretation and depositional environment**
Disorganized granule-boulder conglomerate (G1)	Structurless to poorly organized, matrix- to clast-supported, ungraded to poorly reverse-graded, light brown to red conglomerate. Beds 0.5 to 3 m thick with lateral extent of tens of meters. Flat to slightly erosive basal contacts. Interbedded with facies G2 and G3.	Gmd, Gcd	Kond basin, LRF. Eyvanekey basin, LRF.	Sediment gravity flows (hyperconcentrated to debris flow) in poorly confined channel and sheet flow. Alluvial-fan system.
Organized pebble - boulder conglomerate (G2)	Moderately to well organized, clast-supported, ungraded to normally-graded, moderately to poorly sorted, poorly imbricated, light brown to red conglomerate. Moderate to poor horizontal and trough-cross stratification. Beds 0.5 to 3 m thick, with lateral extent of tens of meters. Erosional basal contacts. Interbedded with facies G2, G3, and SM.	Gco, Gh, Gt	Kond and Eyvanekey basin, LRF and URF.	Traction bed load; transverse and longitudinal gravel bars in poorly to well confined channel. Alluvial-fan system.
Organized granule-pebble conglomerate (G3)	Channelized, horizontally and trough-cross bedded, moderately sorted, fining-upward, medium to coarse grained, light brown to red granule-pebble conglomerate. Dewatering structures very common in Miocene strata. Geometrically, two end members are present: laterally extensive bodies (few tens of meters) 0.5 to 2 m thick, and smaller lenses 0.2 to 1 meter thick. Erosional contacts locally marked by intraformational mud-chip clasts. Interfingered with facies G2, and S; interbedded with S, G2, SM and rarely M.	Gco, Gt, Gp, Gh, Sm, Sh, St, Sc, Ss	Kond and Eyvanekey basin, LRF and URF. Senman basin, URF.	Traction bed load transport; channel fills deposits in sandy and gravelly fluvial, poorly to well confined channel. Braided-fluvial system.
Sandstone (S)	Channelized, fining-upward, fine- to medium-grained, locally coarse-grained to pebbly, light brown to red sandstone. Sedimentary structures include, horizontal, trough-cross bedding, ripples, bioturbation and flute cast. Dewatering structures very common in Miocene strata. Beds 1 to 50 m thick with a later extent from tens meters to few hundred of meters. Locally, ribbon geometries occur (1 to 3 m of thickness, with a lateral extent smaller than 80 m). Erosive slightly concave-up base contacts, locally marked by intraformational mud clasts. Flat non erosive base are rare. Interbedded with facies G3, SM, M, and rarely E.	Sm, Sh, St, Ss, Sr, Sc	Kond basin, LRF and URF. Eyvanekey basin, URF. Senman basin, URF.	Traction bed load transport; channel fills deposits in sandy fluvial channel. Braided- and anastomising distal-fluvial system.
Interbedded siltstone, fine grained sandstone and mudstone (SM)	Tabular to wedging, massive to fining-upward, fine-grained light brown to red sandstone, and siltstone. Sedimentary structures include horizontal and flaser lamination, ripples, climbing ripples, and load structures. Red colored calcareous mudstones, massive to laminated with a tabular geometry. Locally, mudcracks, bioturbation, rhizoliths, gypsum-filled fractures, calcretes, and gypcretes occur in both mudstone and siltstone/sandstone. Beds 0.1 to 2 m thick, laterally very extensive. Basal contacts flat, non erosive, and rarely slightly concave up. Proportion between mudstone and siltstone/sandstone variable. Interbedded with facies S, G3, and G2.	Sm, Sh, Sl, Sc, Sr, Fl, Fm, P	Kond basin, LRF and URF. Eyvanekey basin, URF. Senman basin, URF.	Sheetflows deposits. Floodplain system.
Mudstone (M)	Tabular, massive and laminated dark to light red and locally green or mottled calcareous mudstone and minor siltstone. Mudcracks, syneresis cracks, and gypsum-filled fractures are common. Locally, poorly developed calcrete and gypcrete occur. The green mudstone rarely contains ostracods. Soft-sediment deformation is also present. Beds 0.05 to 0.5 m thick with lateral extent up to few hundreds of meters and a flat non-erosive contact. Interbedded with facies S, SM, and E.	Fl, Fm, P	Kond basin, LRF. Eyvanekey basin, URF. Senman basin, URF.	Suspension deposits in standing water. Playa-lake and shallow-lacustrine system.
Evaporite (E)	Massive to poorly laminated white evaporitic facies. Beds 0.05 to 0.2 m thick with lateral extent up to few hundreds of meters. Generally associated with small-scale diapirs and gypsum-filled fractures. Interbedded with facies M, rarely with SM and S.	Ev	Eyvanekey basin, URF. Senman basin, URF.	Evaporation deposits from standing water. Playa-lake system.
Limestone, calcareous sandstone and sandy marls (L)	Bioclastic limestones (foraminiferal wackstone, packstone) and calcareous sandstones, intercalated with green sandy marl. Locally channelized gravel bodies containing green and yellow tuff are present. Sedimentary structures include horizontal, wavy and low angle stratification. Limestone beds 0.1 to 2 m thick with lateral extent of few tens to hundred of meters. Sandy marls package up to 20 m thick.	Bl, Cg, Ms	Kond and Eyvanekey basin, Qom Formation.	Bidirectional flow deposits. Mixed carbonate siliciclastic shallow-water marine system,

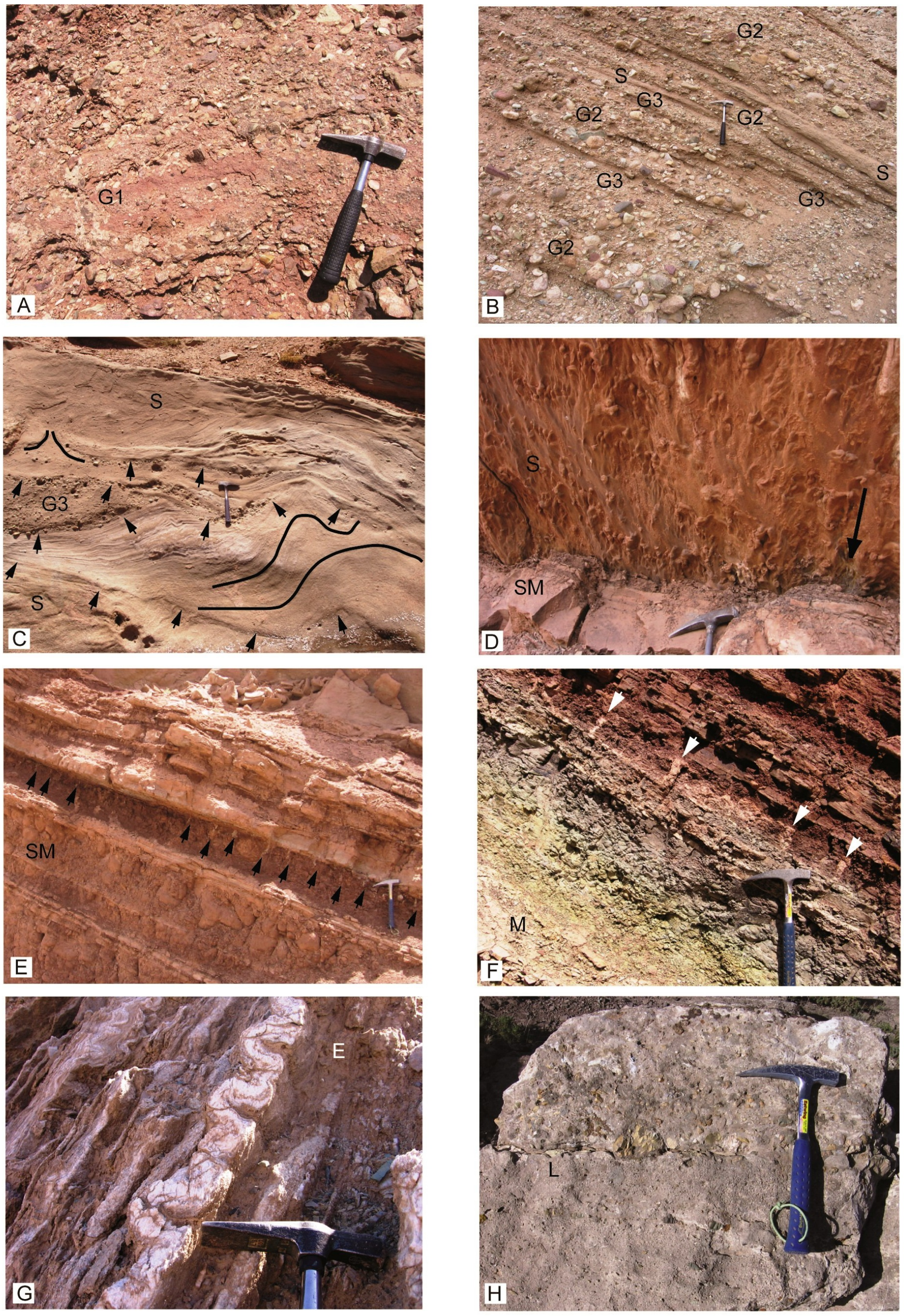

Figure 3.5. Outcrop photographs of facies associations. (A) Poorly organized to disorganized pebble-boulder conglomerate (facies association G1) (Lower Red Formation, Eyvanekey basin). (B) Organized pebble-boulder conglomerate (facies association G2) occurring with lenses of coarse-grained sandstone (facies association S) and granule-pebble conglomerate (facies association G3) (Hezardarreh Formation, Eyvanekey basin). (C) Sandstone (facies association S) and organized granule-pebble conglomerate (facies association G3), showing trough-cross bedding and metric-scale dewatering structures, highlighted by black lines; also shown are the bounding surfaces, which are marked by black arrows, and suggest changes in the flow conditions (Upper Red Formation, sub-unit 1C, Eyvanekey basin). (D) Base of channel (facies association S) with flute casts; the black arrow shows the paleoflow direction (Upper Red Formation, sub-unit 1C, Eyvanekey basin). (E) Interbedded siltstone, fine-grained sandstone and mudstone (facies association SM) with mudcracks, indicated by the black arrows (Upper Red Formation, sub-unit 1B, Eyvanekey basin). (F) Mudstone facies association (M); the gradual variation from pale green to red strata records the transition from standing-water to desiccation, associated with carbonate crusts and mudcracks indicated by the white arrows (Upper Red Formation, sub-unit 1A, Eyvanekey basin). (G) Bioclastic packstone and conglomerate comprising of the limestone facies association (L) (Qom Formation, Kond basin). (H) Evaporite facies association (E), with ptygmatic folds in gypsum layers embedded in gypsiferous mudstone (Upper Red Formation, Semnan basin).

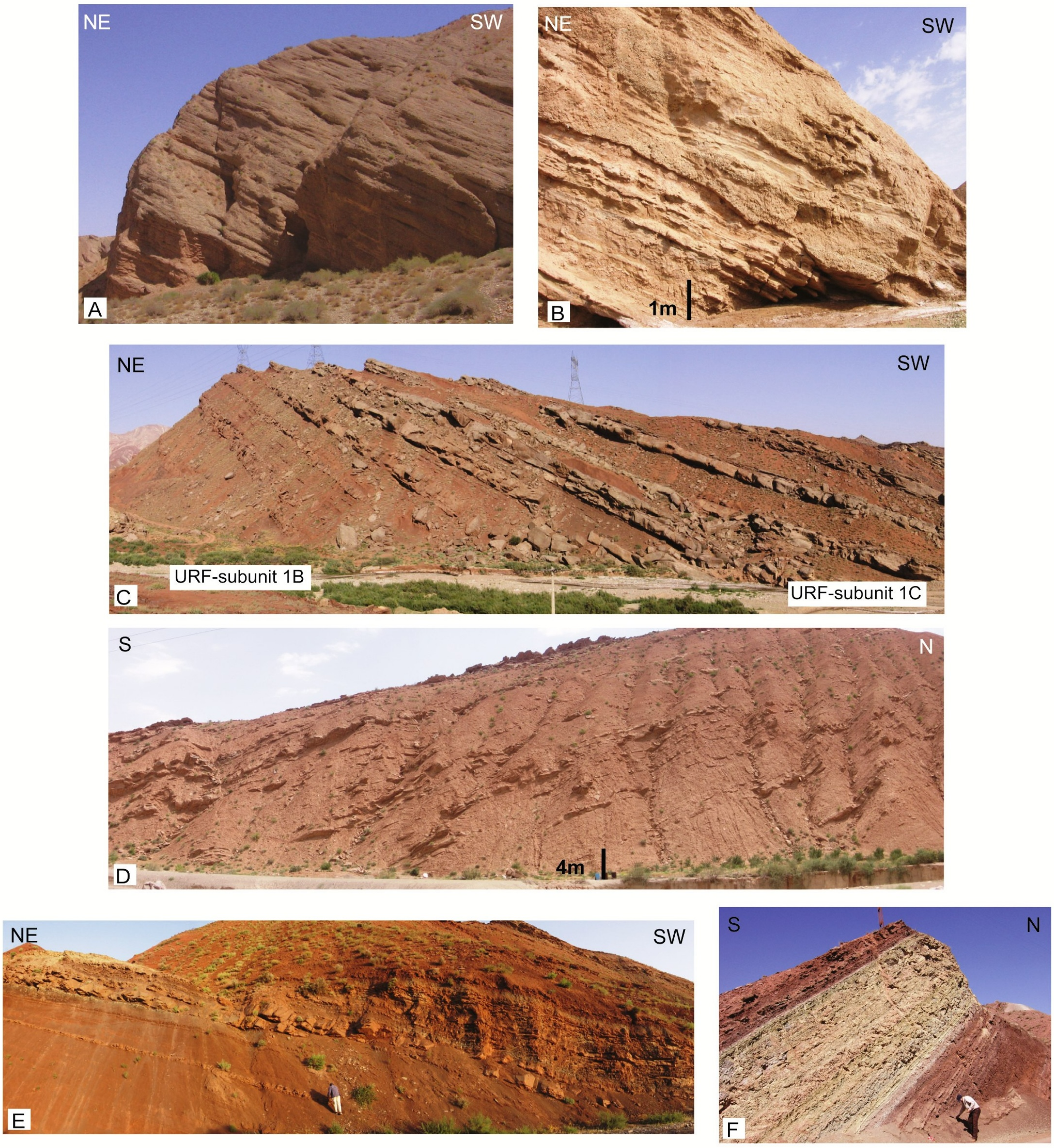

Figure 3.6. Outcrop photographs showing the relationships between the deposits of different depositional systems. (A) Conglomerates (facies associations G2 and G3) representing an alluvial-fan depositional setting (Hezardarreh Formation, sub-unit 3C, Eyvanekey basin). (B) Channelized to tabular coarse-grained facies (facies associations G3 and S) alternating with fine-grained strata (facies association SM), representing a braided-river and a floodplain depositional setting, respectively (Upper Red Formation, sub-unit 3B, Eyvanekey basin). (C) Channelized bodies (facies associations S and G3), up to 10 m thick with a lateral extent of several tens of meters alternating with fine-grained floodplain deposits (facies association SM). The upward increase in channel frequency and thickness marks the transition from subunits 1B to 1C of the Upper Red Formation (URF). In comparison with Figure 6B, the channels are wider, have gentler banks, and consist of finer sediments; the floodplain deposits are also finer and contain more mudcracks and pedogenic calcareous nodules (Upper Red Formation, sub-units 1B and 1C, Eyvanekey basin). (D and E) Channelized sandstones deposited in an anastomosing distal-river setting (facies association S), that are up to 2 m thick, with a lateral extent ranging from a few to several tens of meters. These bodies are embedded in fine-grained clastic deposits (facies association SM) representing floodplain deposits (Upper Red Formation; D: sub-unit 1B, Eyvanekey basin and E: first coarsening upward cycle, Semnan basin). (F) Shallow-lake deposits with alternating pale green and red calcareous mudstones (Upper Red Formation, sub-unit 1A, Eyvanekey basin).

3.5 Geochronology of Eocene volcanism

The Eocene volcaniclastic Karaj Formation reflects a voluminous regional magmatic episode in central and northern Iran. Here, we present absolute ages for the Karaj Formation and associated intrusive bodies in the Kond and Eyvanekey basin. Zircons from an andesite at the base of the Karaj formation yield a (U-Th)/He age of 47.4 ± 3.8 Ma, and biotite from a fine-grained green tuff collected at the top of the formation yields an $^{40}Ar/^{39}Ar$ age of 36.0 ± 0.2 Ma (Fig. 3.2). $^{40}Ar/^{39}Ar$ magmatic cooling ages were also obtained from intrusive bodies located in the Mosha Fasham Fault footwall (Kond Basin). Biotite and K-feldspar from a monzodiorite-monzogranite sill, which intruded the Karaj Formation across the middle tuff and Asara shale members along the Chalus road (Fig. 3.2), have plateau-weighted mean ages of 39.3 ± 0.2 Ma and 36.8 ± 0.1 Ma, respectively (Fig. 3.2). Additional cooling ages were acquired from intrusive bodies located in the Mosha Fasham Fault hanging wall, such as a small pluton (hornblende, 38.5 ± 0.1 Ma), a larger quartz-diorite porphyric stock (K-feldspar, 38.9 ± 0.1 Ma and 38.0 ± 0.1 Ma), and a dike (biotite, 38.8 ± 0.2 Ma) (Fig. 3.2). These data are consistent with available geochronological data from the same area, where zircons along the Chalus road transect yield U-Pb ages of 49.3 ± 2.9 Ma (middle tuff member), 45.3 ± 2.3 Ma (Asara shale), and 41.1 ± 1.6 Ma (upper tuff member) (Verdel, 2008).

3.6 Depositional system

Five depositional environments characterize the late Tertiary clastic deposits of the Alborz mountains: alluvial-fan, braided-river, anastomosing distal-river, playa-lake to shallow-lacustrine, and mixed carbonate-siliciclastic shallow-water marine systems. Because the lithofacies and facies associations comprising the depositional settings are described in Tables 1 and 2, we will focus in this section on the interpretation of depositional processes and environments.

3.6.1 Alluvial-fan depositional environment

Alluvial-fan deposits are well exposed in the Eyvanakey and Kond basins, reaching up to 800 m in thickness (Figs. 3.3, 3.4, and 3.6A). This depositional environment constitutes three facies associations (Table 2): 1) a disorganized granule-boulder conglomerate (G1); 2) an organized pebble-boulder conglomerate (G2); and 3) an organized granule-pebble conglomerate (G3). The G1 and G3 facies association are generally subordinate, but may dominate locally.

(1) The disorganized granule-boulder conglomerate facies association (G1) is interpreted to represent sediment gravity-flow deposits (hyperconcentrated flow and debris

flow) mostly related to sheet flow and poorly confined channels (Fig. 3.5A; e.g., Stanistreet and McCarthy, 1993; Miall, 1996; Blair 1999). The lack of organized textures, together with flat basal contacts suggests deposition during cohesive laminar flow, with limited development of bedforms or bars.

(2) The organized pebble-boulder conglomerate facies association (G2) is interpreted to reflect traction-current deposits in poorly to well confined gravel channels (Figs. 3.5B and 3.5C; e.g., Stanistreet and McCarthy, 1993; Miall, 1996; Blair 1999). The coarsest horizontal-bedded layers were probably deposited under conditions of higher bed shear stress, while the finer clasts and the sandy matrix infiltrated into an open-clast framework during waning flow (e.g., Miall, 1996). Maximum clast size (rarely > 50 cm in diameter), together with moderate grading, sorting, and poor imbrication suggests that flow energy was probably episodic.

(3) The organized granule-pebble conglomerate facies association (G3) is interpreted to reflect traction-current deposits (bars), related to the waning stage of high-energy flow (Fig. 3.5B; e.g., Stanistreet and McCarthy, 1993; Miall, 1996; Blair 1999). These deposits may exhibit a lenticular and a tabular geometry with a variable gravel/sand ratio. Limited preservation of these deposits may have been caused by erosion during subsequent floods.

3.6.2 Braided-fluvial depositional environment

Braided-stream deposits are common at different stratigraphic levels of the studied sections and range in thickness from 50 to 1100 m (Figs. 3.3, 3.4, 3.6B, and 3.6C). These deposits are mainly composed of three facies associations (Table 2): 1) sandstone (S); 2) organized granule-pebble conglomerate (G3); and 3) interbedded siltstone, fine-grained sandstone and mudstone (SM).

(1) The sandstone facies association (S) is interpreted to reflect deposition in sand-bed channels (Fig. 3.5C). The lateral extent of the channelized bodies of up to a few hundred meters and the lack of lateral accretion elements suggests low-sinuosity channel morphology with a wide and poorly confined channel belt (e.g., Miall, 1996). Flute and chevron marks at the channel base (Fig. 3.5D) along with intraformational mud-chips (rip-up clasts) and scour fills indicate high stream-power and flow turbulence, which led to erosion of cohesive mud-overbank deposits. The complex channel-fill texture with repeated reactivation surfaces, locally bounded by rip-up clasts, suggests unsteady fluvial competence. This is compatible with ephemeral hydrological conditions with repeated and rapid migration of the channel network over the alluvial plain. This led to the formation of stacked sandstone bodies with no intervening mudstone (multi-storey channels). The occurrence of meter- to centimeter-scale dewatering structures (Fig. 3.5C; dish structures) suggests high sedimentation rates, in agreement with sedimentation rates obtained from magnetostratigraphy (Ballato et al., 2008). In addition, the occurrence of *Scoyenia* and *Taenidium* ichnogenera in the upper fine-grained

section of individual channels suggests channel abandonment or protracted partial emergence of sand bars (e.g., Buatois and Mangano, 2002).

(2) The organized granule-pebble conglomerate facies association (G3) represents channel-fill deposits in a sand-dominated river channel with variable gravel input (Figs. 3.5B and 3.5C; e.g., Miall, 1996). The lateral extent of horizontally bedded conglomerates (up to 100 m) suggests deposition in a poorly-confined, high-energy stream. The occurrence of lenticular geometries with horizontal- and trough-cross bedded conglomerate grading laterally and upward into sandstone bodies points to traction transport in confined channels.

(3) The interbedded siltstone, fine-grained sandstone and mudstone facies association (SM) is interpreted as overbank and floodplain deposits related to sheet flow (Fig. 3.5E; e.g., Miall, 1996; McCarthy et al., 1997; Bridge, 2003). Sand deposition took place during overbank flooding, resulting in unconfined flow (crevasse splay) and rare confined crevasse channels during an upper-flow regime. Mud and rippled sand deposition occurred during the waning-flow stage or from standing flood-plain water. Trace fossils (*Taenidium*) in the upper part of the sandstone bodies indicate channel abandonment and subaerial exposure. This is supported by mudcracks, paleosol horizons enriched in rhizoliths, and subordinate moderately developed calcretes and gypcretes. The lack of well-developed paleosols, however, suggests fast flood-plain aggradation, probably driven by high basin subsidence (Ballato et al., 2008). The proportion of sand/silt and mud is variable, and the floodplain could have been mud or sand dominated (e.g., Uba et al., 2005).

3.6.3 Anastomosing distal-fluvial depositional environment

Anastomosing distal-fluvial deposits are well exposed in the Eyvanekey and Semnan basins, reaching up to 800 m in thickness, but in the Kond basin, these deposits were not observed (Figs. 3.3, 3.4, and 3.6). Typically, the anastomosing distal-fluvial depositional environment is composed of two facies associations: 1) interbedded siltstone, fine-grained sandstone and mudstone (SM), and 2) sandstone (S) (Table 2; Figs. 3.3, 3.4, and 3.5). Compared to the braided system, the anastomosing distal-fluvial system is characterized by a higher proportion of floodplain deposits and smaller channelized sand bodies.

(1) The SM FA (Fig. 3.5) is interpreted to reflect overbank and floodplain deposits. Sand sedimentation occurred during unconfined to confined overbank flooding in an upper-flow regime (e.g., Miall, 1996; Bridge, 2003). Mudstones and rippled sandstone are generally dominant and were deposited during the waning flow stage or from standing flood-plain water (e.g., Miall, 1996). Similar to modern analogues (e.g., Wright and Tucker, 1991) subareal exposure is indicated by the occurrence of rhizoliths, calcretes and gypcretes.

(2) The S FA (Fig. 3.5) is interpreted to represent channel deposits. The fine to medium grain size and the fining-upward tendency in these strata suggests that they represent channel

deposits of a sand-bed river (e.g., Miall, 1996). Channels have ribbon geometries and can exhibit an isolated or a closely spaced stacking pattern indicating limited lateral channel migration and low-sinuosity channel morphology, typical of an anastomosing river (eg., Smith and Smith, 1980; Smith, 1986; Kirschbaum and McCabe, 1992; Makaske et al., 2002). This facies association is characterized by a channel-fill complex including a gradual transition from trough cross lamination to ripples, indicating gradual waning flow, channel abandonment, and subaerial exposure. This interpretation is further supported by the presence of *Scoyenia and Tanenidum* ichnogenera (e.g., Buatois and Mangano, 2002).

3.6.4 Playa-lake to shallow-lacustrine depositional environment

The playa-lake deposits are comprise four facies associations (Table 2): 1) mudstone (M); 2) interbedded siltstone, fine-grained sandstone and mudstone (SM); 3) sandstone (S); and 4) evaporite (E). These facies are well developed in the Eyvanekey and Semnan basins, where they form successions, 150 to 1100 m thick (Figs. 3.3, 3.4, and 3.6F). In the Kond basin, as well as in some portions of the Eyvanekey basin, evaporitic deposits are either absent or are very rare, suggesting protracted lacustrine deposition.

(1) The mudstone facies association (M) documents sedimentation from suspension in a lacustrine environment (Fig. 3.5F). The dark red mudstones associated with mudcracks suggest deposition in an arid to semiarid, oxidizing environment with frequently dried-up playas (Fig. 3.5F; e.g., Smoot, 1983; Lowenstein and Hardie, 1985; Paik and Kim 2006). Syneresis cracks indicate high salinity due to intense evaporation (e.g., Burst 1965). In addition, calcrete and gypcrete horizons imply prolonged subaerial exposure and incipient paleosol development. Conversely, the less abundant light-green mudstones probably represent periods of prolonged standing water as a result of fresh water input (flooding stage) and/or decreased evaporation (e.g., Lowenstein and Hardie, 1985). Both, the red and green strata have soft-sediment deformation, suggesting surface instability when the sediments were still water-saturated and/or a high sediment input.

(2) The interbedded siltstone, fine-grained sandstone and mudstone facies association (SM) is interpreted to represent sheet-flow deposits (Figs. 3.5D and 3.5F; e.g., Hogg, 1982; Smoot, 1983; Lowenstein and Hardie, 1985; Paik and Kim 2006). The tabular, horizontally laminated siltstones and sandstones, and the presence of load casts, indicate rapid deposition under an upper-flow regime during a flooding stage of the playa (e.g., Lowenstein and Hardie, 1985). The fining-upward trend, together with ripples, flaser, and lenticular laminations, indicates deposition under waning-flow conditions. Locally, these deposits contain oxidized plant remains, suggesting erosion and reworking of the adjacent floodplain during flooding. Symmetric ripples are interpreted to reflect sediment reworking as a result of wind-induced current oscillation in standing water (e.g., Bridge, 2003).

(3) The sandstone facies association (S) is interpreted to represent a channel-fill complex of sand-bed channels (Fig. 3.5C). The tens of meters of lateral extent of these bodies indicate that the channels were moderately confined. They locally contain lenses of conglomerates. Rare channelized sandstones in this depositional setting suggest short phases of fluvial progradation.

(4) The evaporite facies association (E) reflects precipitation of saline minerals from a super-satured solution within a pond during phases of intense evaporation, which occasionally led to complete desiccation, as shown by the presence of mudcracks (Fig. 3.5G; e.g., Lowenstein and Hardie, 1985).

3.6.5 Mixed carbonate-siliciclastic shallow-water marine system

Strata of the mixed carbonate-siliciclastic shallow-water marine facies association (Table 2) are exposed in the Kond basin and along the southern foothills of the Alborz range (Figs. 3.2 and 3.3). Detailed microfacies and biostratigraphic studies have been performed in central Iran (e.g., Schuster and Wielandt, 1999; Reuter et al., 2009), and in the Semnan basin (Daneshian and Ramezani Dana, 2007). In the Kond and Eyvanekey basins, these deposits are composed of bioclastic limestone with molluscs, bryozoa, miliolids, red algae, corals, coated grains, and peloids. This reflects *in situ* carbonate precipitation in a low-energy shallow-marine depositional environment similar to a lagoon (packstone), with sporadic wave reworking leading to the deposition of shoals (grainstone) (Tucker and Wright, 1990). Carbonate-bearing conglomerates (Fig. 3.5H) and sandy green marls suggest variable input of coarse and fine-grained siliciclastic material, with basinward redistribution via tidal or gravity-flow currents along the northern margin of the Qom sea (e.g., Schuster and Wielandt, 1999; Reuter et al., 2009).

3.7 Basin stratigraphy

3.7.1 Kond basin

The Kond Basin is located in the central part of the Alborz range and is bounded by the north dipping North Tehran Thrust and the Mosha Fasham Fault, to the south and the north, respectively (Figs. 3.2 and 3.3). Volcanic deposits of the Karaj Formation are up to 8-10 km thick in the central part of the basin, and are overlain by the Kond Formation (Fig. 3.7A). The deposits of the Kond Formation are ca. 100 m thick and comprise green sandstone, saccharoidal gypsum, and light yellow to brown marly limestone. Nummulitids of late Eocene age indicate deposition in a shallow-water marine setting (Assereto, 1966). Outcrops of the Kond Formation are discontinuous and locally only small lenses, generally < 5 m thick, are preserved (Fig.

3.7B). Virtually everywhere, the Karaj Formation is covered by red clastic deposits with a gentle angular unconformity contact (Fig. 3.7C; Vahdati Daneshmand, 1997).

These red strata, mapped as undifferentiated Miocene deposits (Vahdati Daneshmand, 1997), are characterized by three basinwide coarsening upward cycles with a thickness of a few hundreds of meters (Figs. 3.3 and 3.7D). The first cycle comprises mudstone interlayered with channelized sandstone and conglomeratic lenses deposited in a braided-river system (maximum thickness ca. 100 m thick), grading upward into a ca. 100- to 200-m-thick conglomeratic sequence of alluvial-fan deposits (Figs. 3.3 and 3.7D). The second coarsening upward cycle constitutes red tabular mudstone and minor siltstone of an inferred shallow lake, up to 200 m thick. This unit grades upward into 20-m-thick channelized coarse grained sandstone and conglomerate lenses, indicating a braided-river system (Figs. 3.3 and 3.7D). The third coarsening upward cycle consists of a 60-m-thick sequence of limestone beds (bioclastic peloidal packstones), up to 1 m thick. These strata are interlayered with conglomerates and marls, probably documenting deposition in a siliciclastic shallow-water marine setting (Figs. 3 and 7D). Overlying the limestones are channelized sandstone and conglomeratic lenses interlayered with mudstones, indicating a braided-river depositional system. The top of these continental strata is not exposed since they are cut by the Mosha Fasham Fault (Figs. 3.3 and 3.7D).

The shallow-water marine carbonates comprising the base of the third coarsening upward cycle have been mapped as the Kond Formation of late Eocene age (Vahdati Daneshmand, 1997). Based on along-strike continuity of the sedimentary facies belt, together with the lack of diagnostic foraminifera of Eocene age (nummulitids are not here present and the foraminiferal assemblage is dominated by miliolids), we rather attribute these limestones to the Qom Formation (Figs. 3.3 and 3.7D). Thus, following stratigraphic regional relationships and the Iranian stratigraphic nomenclature, we consider the red deposits beneath these shallow-water limestones to be equivalent to the Lower Red Formation, while the continental strata above represent the Upper Red Formation (Figs. 3.3 and 3.7D). Because paleontological data for the Kond basin are not available, we infer an early Miocene age for the Qom Formation marine limestones, based on correlation with similar deposits paleontologically dated in the Semnan basin (Daneshian and Ramezani Dana, 2007).

3.7.2 Eyvanekey basin

The Eyvanekey basin is located in the southern foothills of the Alborz mountains where Late Cretaceous-Paleocene to Mio-Pliocene deposits are exposed along the southern limb of the north-verging Southern Alborz anticline (Figs. 3.2, 3.4, and 3.8; Ballato et al., 2008). The along-strike continuity of the sedimentary strata allows unraveling the Tertiary evolution of this area starting from the episode of Eocene magmatism. In the Eyvanekey basin, the Karaj Formation consists of a ca. 3-km-thick sequence of purple andesite, passing upward into green tuff and blue-grey shales. An erosional unconformity separates the Karaj from the overlain Kond Formation (Figs. 3.4, 3.7E, and 3.7F). The Kond Formation is composed of gypsum banks interbedded with green, yellow and red marls, and minor sandstones. These strata represent a restricted shallow-marine setting (sabkha) of late Eocene age (e.g., Jackson et al., 1990), similar to the deposits observed in the Kond basin. In the central part of the basin, alluvial-fan deposits of the Lower Red Formation rest in an angular unconformable relationship on these deposits (Figs. 3.4, 3.7G, and 3.8). These coarse strata pinch out to the east, where they conformably overlie the Kond Formation (Fig. 3.8). The transition to the overlying shallow-water marine carbonates of the Qom Formation is gradual in the eastern part of the basin (Figs. 3.4, 3.7H, and 3.8). Toward the west, these carbonates interfinger with alluvial-fan deposits, while farther west in the central part of the basin, only terrestrial coarse-grained deposits occur, indicating subaerial sedimentation (Figs. 3.4, 3.7G, and 3.8). The Qom Formation has been paleontologically dated as early Miocene in the adjacent Semnan basin (Daneshian and Ramezani Dana, 2007). If this age is extended along strike up to the Eyvanekey basin, the underlying Lower Red Formation should be Oligocene, as it is inferred to be in Central Iran (e.g., Jackson et al., 1990, Davoudzadeh et al., 1997).

The transition from the Qom Formation to the Upper Red Formation varies from W to E. In the central part of the basin, this transition is characterized by coarse-grained deposits, ca. 200 m thick. Eastward these deposits thin to ca. 80 m and are associated with evaporites (Figs. 3.4, and 3.8). Well developed paleosols with calcrete and gypcrete were observed only within these thinner deposits. The 17.5- to 7.5-m.y.-old Upper Red Formation is composed of three basinwide coarsening upward cycles (Unit 1, 2 and 3), which have been furthermore divided into sub-units on the basis of different depositional environments that they reflect (Fig. 3.4; Ballato et al., 2008). These three units are characterized by a transition from a mudstone-dominated sequence representing a playa and areally limited lacustrine depositional system (Fig. 3.6F), to coarse-grained sediments representing deposition in an anastomosing distal- (Fig. 3.6E) to braided-river system (Figs. 3.6B and 3.6C; Ballato et al., 2008). The transition to the alluvial-fan deposits of the Hezardarreh Formation (Fig 6A) is marked in the eastern part of the basin by a gradually southward increasing tilt of 10° to 7°. Age control for this formation does not yet exist. If a constant sedimentation rate for the conglomeratic sequence is assumed, however, the youngest strata of this unit would correspond to an age of 6.2 Ma (Ballato et al., 2008).

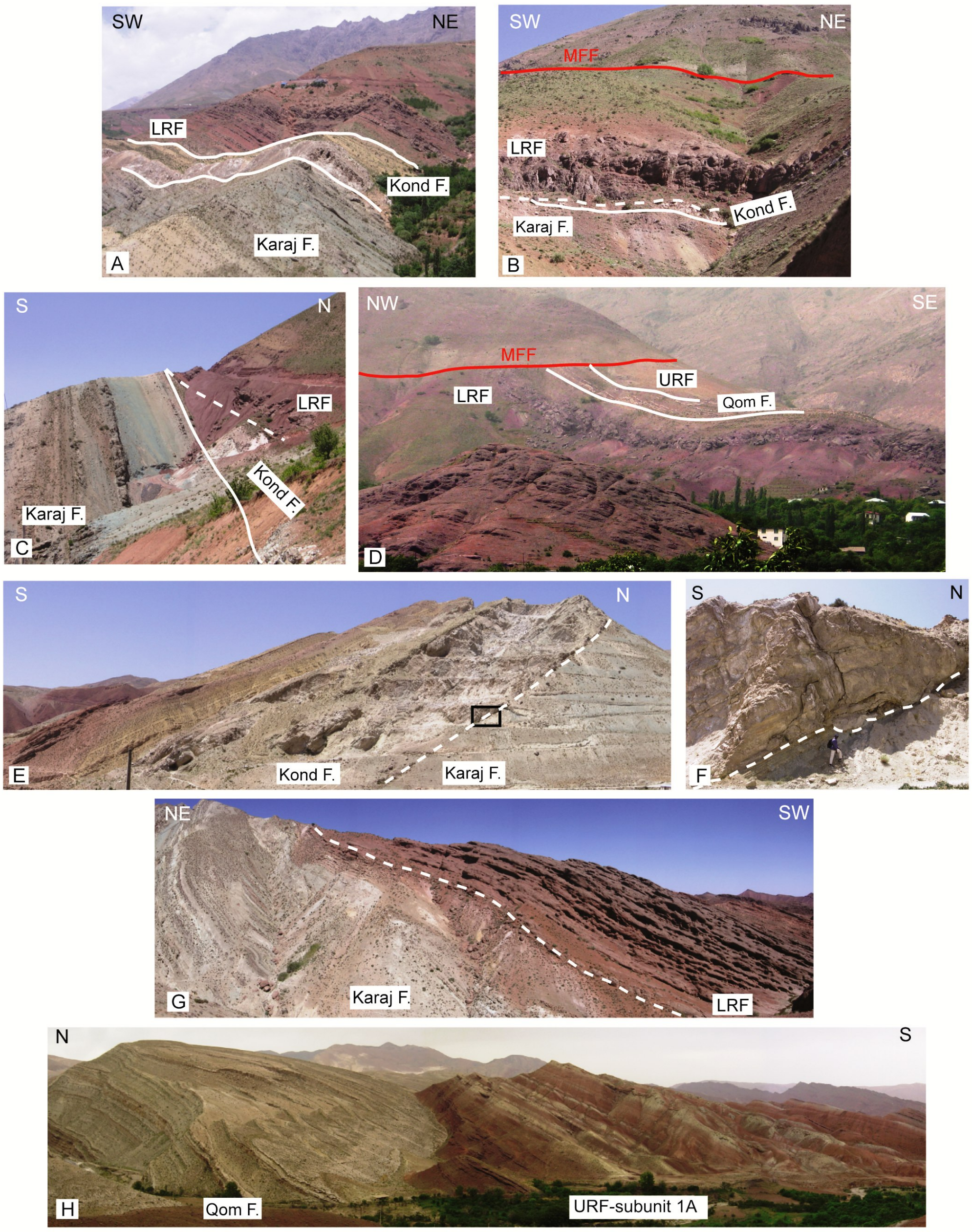

Figure 3.7. Contacts between sedimentary units in the Kond (A, B, C, and D) and Eyvanekey basins (E, F, G, and H). (A) Stratigraphic contact between the Karaj, Kond and Lower Red (LRF) formations (stratigraphic section 2) (B) Lens of nummulitic limestone (Kond Formation) in stratigraphic contact with the Karaj Formation (white line), overlain by the Lower Red Formation (LRF) with an erosional unconformity (white dashed line), and located ca. 2 km west of the stratigraphic section 3. (C) Stratigraphic contact between the Karaj and Kond formations (white solid line), and angular unconformity (white dashed line) separating the Karaj and Kond formations from the superseding Lower Red Formation (LRF), found ca. 3 km west of stratigraphic section 1. (D) Stratigraphic section 3 showing the Lower Red, Qom and Upper Red (URF) formations. Note the footwall cut-off angle between sedimentary layers and fault splay of the Mosha Fasham Fault (MFF). The hill in the foreground is composed of conglomerates from the first coarsening upward cycle, while fine- and coarse-grained red strata found below the Qom Formation represent the second coarsening-upward cycle. (E) Erosional contact between the Karaj and Kond formations (white dashed line) in the eastern part of the Eyvanekey basin; the Kond Formation pinches out to the north. (F) Close-up of the sector denoted by the black frame in Figure E, showing the irregular erosional contact between the Karaj and Kond formations. The topmost tuff layer of underlying Karaj Formation was deposited at ca. 36 Ma. (G) Angular unconformity (white dashed line) between the volcaniclastic strata of the Karaj Formation (bedding N80E-60SE) and the gravel layers of the Lower Red Formation (bedding N100-38SW), in the central part of the Eyvanekey basin (stratigraphic section 5). (H) Stratigraphic contact between the Qom and Upper Red (URF) formations (stratigraphic section 7).

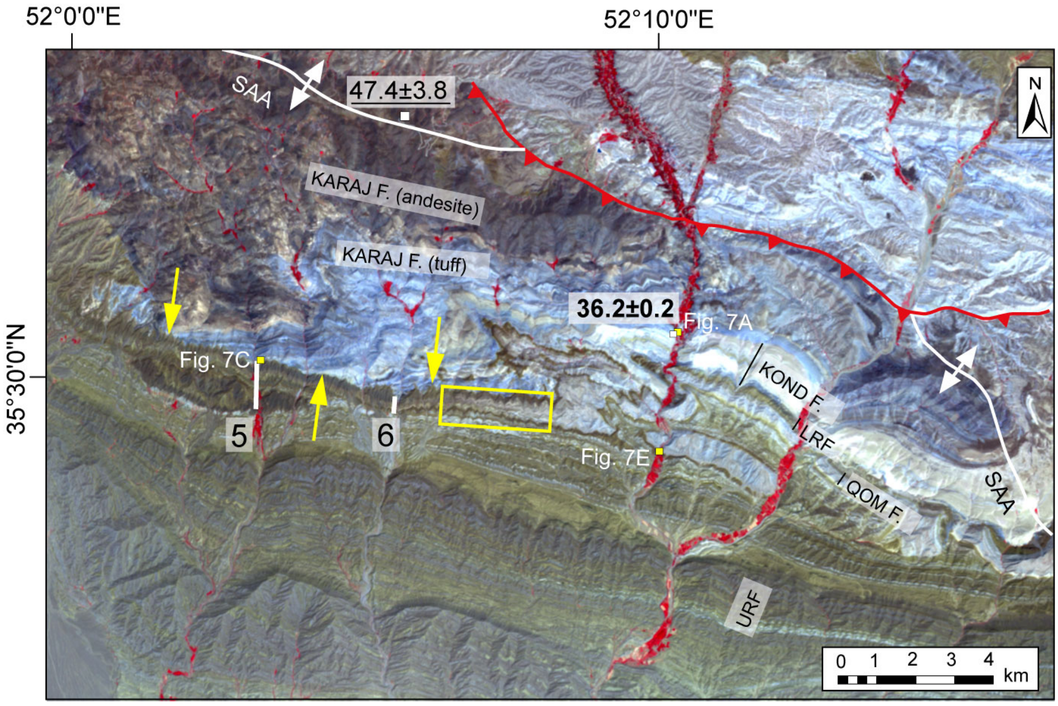

Figure 3. 8. ASTER satellite image (Red Green Blue: 3, 2 and 1) of the Eyvanekey basin, showing principle geological structures and geochronologic data, as well as locations of stratigraphic sections 5 and 6, and the photographs shown in Figure 7 (yellow squares). Yellow arrows mark the angular unconformity between the Karaj and Lower Red (LRF) formations (Figure 7C). The yellow box denotes the westward transition from shallow-water marine limestone (Qom Formation) to terrestrial red deposits.

3.7.3 Semnan basin

The Semnan basin is in the southern foothills of the eastern Alborz, and it represents the along-strike continuation of the Eyvanekey basin (Fig. 3.2). Here, we focus on the Miocene clastic deposits of the Upper Red Formation in order to perform an along-strike comparison with the Eyvanekey basin (Figs. 3.2 and 3.4). The Upper Red Formation is thinner in the Semnan basin than in the Eyvanekey basin (probably less than 4 km) and it is composed of two coarsening upward cycles instead of three as observed in the Eyvanekey basin (Fig. 3.4). The first cycle comprises fine-grained red mudstones interlayered with evaporites, which were deposited in a playa-lake and shallow-lacustrine setting. These strata grade upwards into mudstones interbedded with channelized sandstones and conglomeratic lenses, reflecting an anastomosing distal- to braided-river system. These channel deposits exhibit an increase in thickness and frequency westward, similar to the channelized deposits comprising the 2B sub-unit of the Eyvanekey basin.

The deposits of the second cycle comprise basal mudstone and gypsum of a playa-lake. In places, despite erosion and a Quaternary cover, the upward transition to the alluvial-fan deposits of the Hezardarreh Formation is similar to that in the Eyvanekey basin. Because age information for the Upper Red Formation in the eastern Alborz basin is not available, we are forced to make a lithostratigraphic correlation with the Eyvanekey basin. Although poorly constrained, the basal sections of the first and second cycles may correspond to the bases of

Unit 1 and Unit 3, respectively (Fig. 3.4). Taken together, the Upper Red Formation in the eastern Alborz is composed of finer-grained sediments with a higher proportion of evaporites, while the coarser facies constitutes thinner channelized sandstones that contain a lower proportion of conglomerates.

3.8 Provenance

3.8.1 Sandstone data

Oligo- to early Miocene framework grains of sandstones of the Lower Red and the base of the Upper Red formations were analyzed from samples collected in the Eyvanekey (Fig. 3.9A) and Kond (Fig. 3.9B) basins. These samples are mainly composed of lithic and feldspar (plagioclase) clasts, and in a Q/F/L ternary plot, they cluster in a restricted area. The associated fine-grained lithics (clasts with grain constituents < 63µm; Lm/Lv/Ls+C ternary plots; Figs. 3.9A and 3.9B) also have a low compositional variability dominated by volcanic clasts of glass to partially microcrystalline glass, suggesting a homogeneous source of sediments during the Oligocene to early Miocene.

Samples of early to late Miocene age belonging to the Upper Red Formation were collected in the Eyvanekey (Fig. 3.9A) and Semnan (Fig. 3.9B) basins and show a minor tendency toward increasing quartz/feldspar ratios upsection. In the Eyvanekey basin, the fine-grained lithics (Lm/Lv/Ls+C plots; Figs. 3.9A and 3.9C) are characterized by two prominent compositional changes during the deposition of fine-grained sediments. The first occurs in sub-unit 1A with the increase in low-grade metamorphic constituents (up to ca. 50 %) and carbonates (up to ca. 30 %). The second occurs in sub-unit 3A and is characterized by an increase in carbonate clasts (up to ca. 75 %) and a sharp decrease in low-grade metamorphic grains (Figs. 3.9C and 3.9D). The samples from the Semnan basin record a similar pattern (3. 9B). These upsection compositional variations testify to a complex spatiotemporal evolution of the source areas during the early to late Miocene.

3.8.2 Conglomerate data

Oligocene to early Miocene conglomerate clast-count data from the Kond basin reveal a uniform composition in the basal sections that are dominated by volcanic clasts (Figs 3.3 and 3.4). Upsection, there is more variability with the appearance of quartzites, carbonates and sandstones of Mesozoic and Pre-Cambrian to Paleozoic age (Fig. 3.3). During the deposition of the second-coarsening upward cycle, the variability in clast composition decreases and volcanic clasts become dominant. These data apparently reflect composite pebble sources changing through time. Oligocene to early Miocene conglomerate clast data from the Eyvanekey basin document a westward increase in carbonate clasts (Fig. 3.4). In the eastern part of the basin, along the Eyvanekey stratigraphic section, conglomerate clast counts exhibit a relatively uniform composition dominated by volcaniclastic pebbles until the third coarsening upward cycle (Fig. 3.4; sub-unit 3B, late Miocene), where quartzites, carbonates, and sandstones appear. Only few conglomeratic layers occur and volcanic clasts are dominant in the Semnan basin, generally with a modal composition of less than 50 % (Fig. 3.4).

3.9 Discussion

Lateral and vertical variations in sedimentary strata and clast composition, the geometric relationship between different formations, and our new radiometric age information provide the basis for a reconstruction of the evolution of the Kond, Eyvanekey and Semnan basins and their sediment source areas during the Oligo-Miocene. This information, furthermore, serves as a proxy for the topographic evolution of the Alborz mountains and their foreland basins and thus offers important insights into the regional tectonic evolution of the Arabia-Eurasia collision zone.

3.9.1 Termination of Eocene volcanism

The extensive Eocene arc-magmatism phase peaked during the middle Eocene and terminated abruptly in the late Eocene, suggesting the end of northward subduction of Neo-Tethyan oceanic crust in central Iran (e.g., Ernst, 1999). The spatiotemporal characteristics of this arc magmatism are consequently instrumental for an attempt to unravel the timing of geodynamic processes in the Arabia-Eurasia collision zone.

Our zircon (U-Th)/He age of 47.4 ± 3.8 Ma from an andesite collected at the base of the Karaj Formation represents the first manifestation of the regionally important volcanism in the Eyvanekey basin. This age is interpreted to reflect a volcanic cooling phase because there are no indications that this area was subsequently buried below 8-9 km causing a resetting of the zircon (U-Th)/He system (e.g., Reiners and Brandon, 2006). Partial reheating due to minor burial may have caused limited He diffusion, resulting in a slightly younger age. Our biotite ^{40}Ar/^{39}Ar age of 36.0 ± 0.2 Ma from a fine-grained green tuff collected at the top of the Karaj Formation represents the last manifestation of the Eocene magmatism in the Eyvanekey basin. Based on the overall stratigraphic relationships we estimate that the volcaniclastic sedimentation in the Southern Alborz mountains lasted for at least 11.4 ± 4 m.y.

In the Kond Basin, the youngest ^{40}Ar/^{39}Ar cooling age of 36.65 ± 0.09 Ma from the monzodiorite-monzogranite sill cutting the middle tuff and Asara shale members of the Karaj Formation suggests that Eocene magmatism there finished at ca. 36 Ma, similar to the situation in the Eyvanekey basin. In addition, tuffs as old as 49.3 ± 2.9 Ma in the middle tuff member

(Verdel 2008) indicate that volcaniclastic sedimentation in the Kond basin lasted at least 13 ± 3 Ma.

The termination of volcaniclastic sedimentation at ca. 36 Ma represents the most precise age to date for the termination of the magmatic activity in the central Alborz mountains. This agrees with previous assessments for the waning of volcanic activity of the Urumieh-Dokhtar volcanic arc and in the Talesh mountains at 37.3 ± 1.2 Ma (Verdel, 2008) and 38.3 Ma (Vincent et al., 2005), respectively.

3.9.2 Basin evolution

3.9.2.1 Kond basin (Oligocene to early Miocene)

With the termination of volcaniclastic sedimentation in the central Alborz mountains at ca. 36 Ma (Karaj Formation) a shift from deep, open marine conditions to a shallow, evaporative marine setting took place (Kond Formation). This was followed by northward tilting of the sediments, which triggered the partial erosion of the evaporitic deposits and the deposition of the continental Lower Red sediments (Figs. 3.3, 3.7B, and 3.7C). The onset of terrestrial sedimentation also marked a change in sediment source from the southern volcanic arc to the northern sectors, which is documented by paleocurrent data (Fig. 3.3). Coarse-grained braided fluvial to alluvial-fan sediments (first coarsening upward cycle, Fig. 3.3) suggest proximal deposition adjacent to high topography bounded by north dipping thrust faults located to the north (Fig. 3.10A). The Kond basin was thus in a subsiding footwall and the northward tilt of sedimentary strata was most likely related to lithospheric flexure induced by thrust loading. One of the major structures accommodating this contractional deformation is inferred to have been the currently active Mosha Fasham strike-slip fault (Fig. 3.10A). This structure is a long-lived crustal anisotropy, reordering normal faulting during the Devonian and the Permo-Triassic and compressional reactivation during the Late Cretaceous-early Paleocene (Zanchi et al., 2007; Yassaghi and Madanipour, 2008).

The sedimentological changes observed in the Alborz mountains at ca. 36 Ma and the coeval termination of arc magmatism herald a changeover from an extensional to a contractional tectonic regime. This also caused fundamental variations in subsidence mechanisms and rates, from normal-faulting controlled tectonic subsidence (Karaj Formation) to possibly post-rift thermal subsidence (Kond Formation), and finally flexural subsidence during contraction (Lower Red Formation). The evolution of the sedimentary deposits in the Kond basin thus reflects the onset of late Tertiary shortening and concomitant foreland-basin development. This inference is confirmed by late Eocene to early Oligocene apatite fission-track cooling ages across different structural blocks of the Alborz mountains, which have been interpreted to record the onset of regional compressional deformation, tectonic uplift, and exhumation

(Rezaeian, 2008). The relatively small thickness of the thickest stratigraphic sequence (section 3, minimum thickness 640 m) suggests that deposition occurred in a shallow basin, which probably formed in response to low shortening and exhumation rates.

The subsequent second and third coarsening upward cycles are difficult to assess because data on the exact timing of deposition and basin subsidence is not available. The transition from coarse- to fine-grained sediments could be related to an orogenward retreat of the foreland-basin system, which would imply a redistribution of tectonic loads due to out-of-sequence thrusting (e.g., Parra et al., 2009). In this context, the subsequent increase in grain size may reflect one or a combination of the following processes: 1) expansion of the foreland basin due to tectonic quiescence and erosional unloading (e.g., Heller et al., 1988; Flemings and Jordan, 1990); 2) basinward progradation of the orogenic front, and thus changes in the topographic load and sediment source (e.g., Parra et al., 2009); and/or 3) an increase in sediment discharge due to increased precipitation and erosional unroofing (e.g., Marr et al., 2000; Densmore et al., 2007).

Because the youngest strata exposed in the basin are early to middle Miocene in age, the onset of basin uplift and erosion, which led to the formation of the neotectonic transpressional duplex on the hanging wall of the North Tehran Thrust, must be younger than early to middle Miocene.

3.9.2.2 Eyvanekey basin (Oligocene to late Miocene)

As in the Kond basin, the termination of submarine volcaniclastic sedimentation and extensional tectonism at ca. 36 Ma was superseded by restricted marine conditions with evaporite deposition, possibly related to thermal basin subsidence (e.g., McKenzie, 1978). The subsequent deposition of unconformable alluvial-fan deposits sourced from northern sectors (Lower Red Formation) was accompanied by southward tilting of sediments (Figs. 3.7G, and 3.8). The onset of terrestrial sedimentation in this basin thus marks a reversal in sediment provenance from the southern Urumieh Dokhtar volcanic arc to the developing topographic relief sectors in the northern and western of the Alborz (Fig. 3.10B). As the main thrust fault beneath the Eyvanekey basin dips southward (Ballato et al., 2008), the northward stratal pinch-out suggests that deposition took place along a former basin margin. This may have taken place on the southern flank of a growing north-vergent anticline (Fig. 3.10A). Because the pinch-out geometry is also recorded in the evaporites, the change from an extensional to a contractional setting occurred during the latest Eocene (Kond Formation). This is in agreement with an early Oligocene fission-track cooling age in the Anti-Alborz ca. 20 km to the west, which has been interpreted to reflect exhumation processes related to crustal shortening and thickening in that region (Fig. 3.2; Rezaeian, 2008). Paleorelief in the central-western part of the basin is also corroborated by the westward transition of marine (Qom Formation) to terrestrial deposits along the basin axis during the early Miocene (Figs. 3.8 and 3.10A).

The deposition of up to 400 m of coarse-grained and mixed siliciclastic shallow-water marine facies (Lower Red and Qom formations) between about 36 and 17.5 Ma suggests sedimentation along a slowly subsiding basin margin. The subsequent deposition of more than 7 km of sediments (Upper Red and Hezardarreh formations) between ca. 17.5 and 6.2 Ma testifies to increased subsidence during foreland-basin development (Fig., 3.10B; Ballato et al., 2008). The lack of well-developed Oligocene foreland-basin deposits in the Eyvanekey basin, suggests that the magnitude of shortening, and hence topographic load and creation of accommodation space during that time was not as great as later deformation processes (e.g., Allen and Allen, 2005). Given the lag time between crustal shortening/thickening processes, the development of topographic relief and related flexural subsidence, the late Tertiary crustal deformation in the Alborz range must have started several million years prior to 17.5 Ma. We point that this occurred at approximately 20 Ma, when the Arabia-Eurasia convergence rate began to decrease (McQuarrie et al., 2003). This is also in agreement with the early Miocene fission-track cooling ages from the Alborz mountains (Rezaeian, 2008).

The three coarsening upward units comprising the Upper Red and the Hezardarreh formations are associated with variations in sediment-accumulation rates, suggesting tectonic control (Ballato et al., 2008). Higher sediment accumulation rates correlate with fine-grained facies (Unit 1 between 17.5 and ca. 15.2 Ma; Unit 2 between 13.8 and 13 Ma; Unit 3 between 10.3 and 9.6 Ma; Fig. 3.4) testifying to enhanced subsidence during crustal shortening and thickening as expected in the proximal sectors of a foreland basin (e.g., Heller et al., 1988; Flemings and Jordan, 1990). Thus, if a basin is underfilled, coarse-grained facies are mainly deposited in the proximal part of the basin, while the fine-grained facies dominate the sedimentary basin-fills in the medial distal part (e.g., Heller et al., 1988; Flemings and Jordan, 1990). Conversely, slower rates are associated with coarser sedimentary facies, unconformities, and stratal dip-angle variations. This suggests that the progradation of coarse-grained sediments in the southern Alborz foreland was related to a reduction in accommodation space and proximal storage capacity. The reduction in accommodation space was caused by intra-foreland uplift as testified by the occurrence of along-strike unconformities and tilted strata related to the growth of the southern Alborz anticline (Ballato et al., 2008). The intra-foreland uplift processes culminated with final basin uplift and erosion between ca. 9 Ma and possibly 6 Ma, when the upper parts of the Upper Red and Hezardareh formations were deposited (Fig. 3.10C).

In summary, our data show that the locus of active deformation in the Alborz migrated back and forth during Oligocene and Miocene times, without following a predictable foreland-directed pattern. This was probably influenced by inherited zones of crustal weakness that dictated the locus of tectonic activity and differentiated sedimentary basin evolution. Similar disparate spatiotemporal deformation and sedimentation patterns have been observed in other mountain belts with reactivated crustal anisotropies, such as in the broken foreland of Andes (e.g., Jordan and Allmendinger, 1986; Hilley et al., 2005; Mortimer et al., 2008; Strecker et al., 2009) and the Tien Shan (e.g., Sobel et al., 2006).

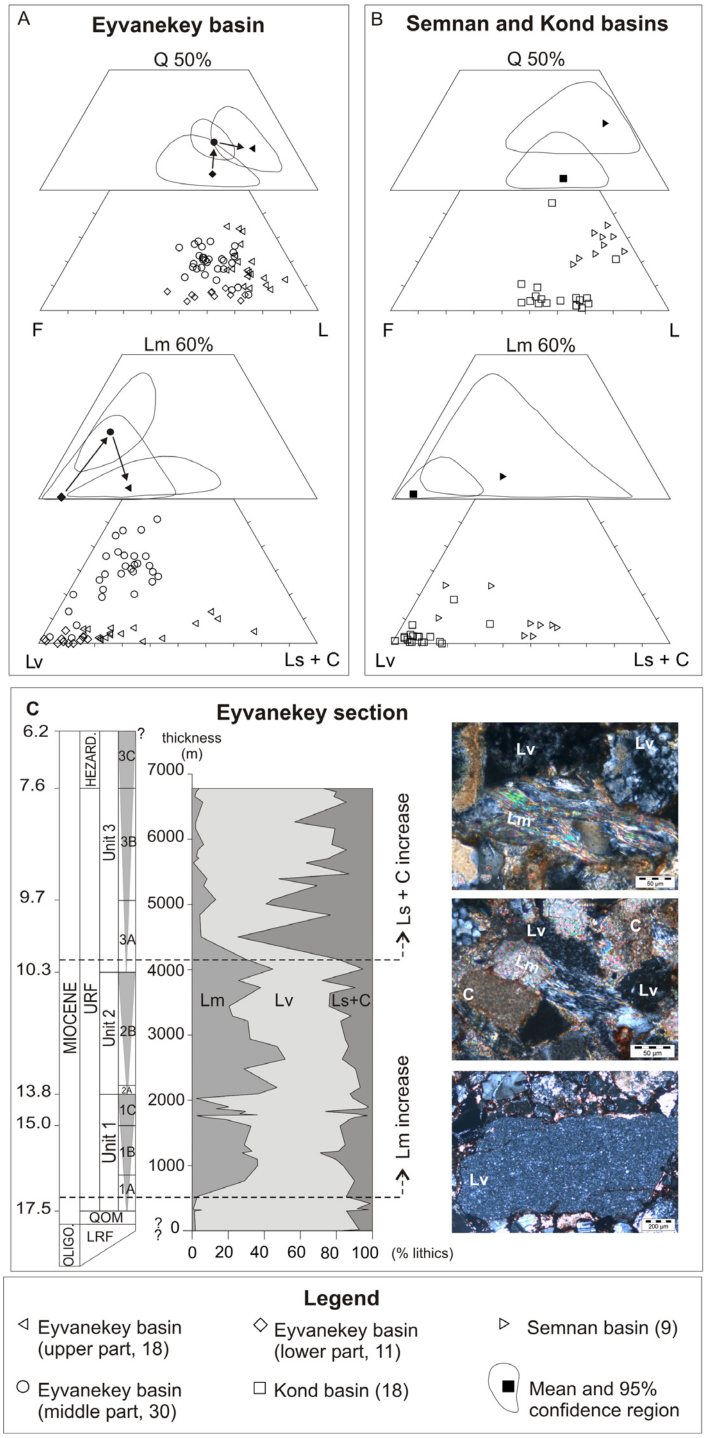

Figure 3.9. Sandstone petrographic data from the Lower and Upper Red formations, including Q/F/L (quartz, feldspar, and lithic clasts) and Lm/Lv/Ls+C (metamorphic, volcanic, and sedimentary plus carbonate lithics with grain constituents < 63µm) ternary plots for: (A) the Eyvanekey basin, and (B) the Kond and Semnan basins. (C) Evolution of the detritial modes of the fine lithic grains for the Eyvanekey stratigraphic section. (D) Microphotographs showing the typical texture of volcanic, metamorphic and carbonate clasts.

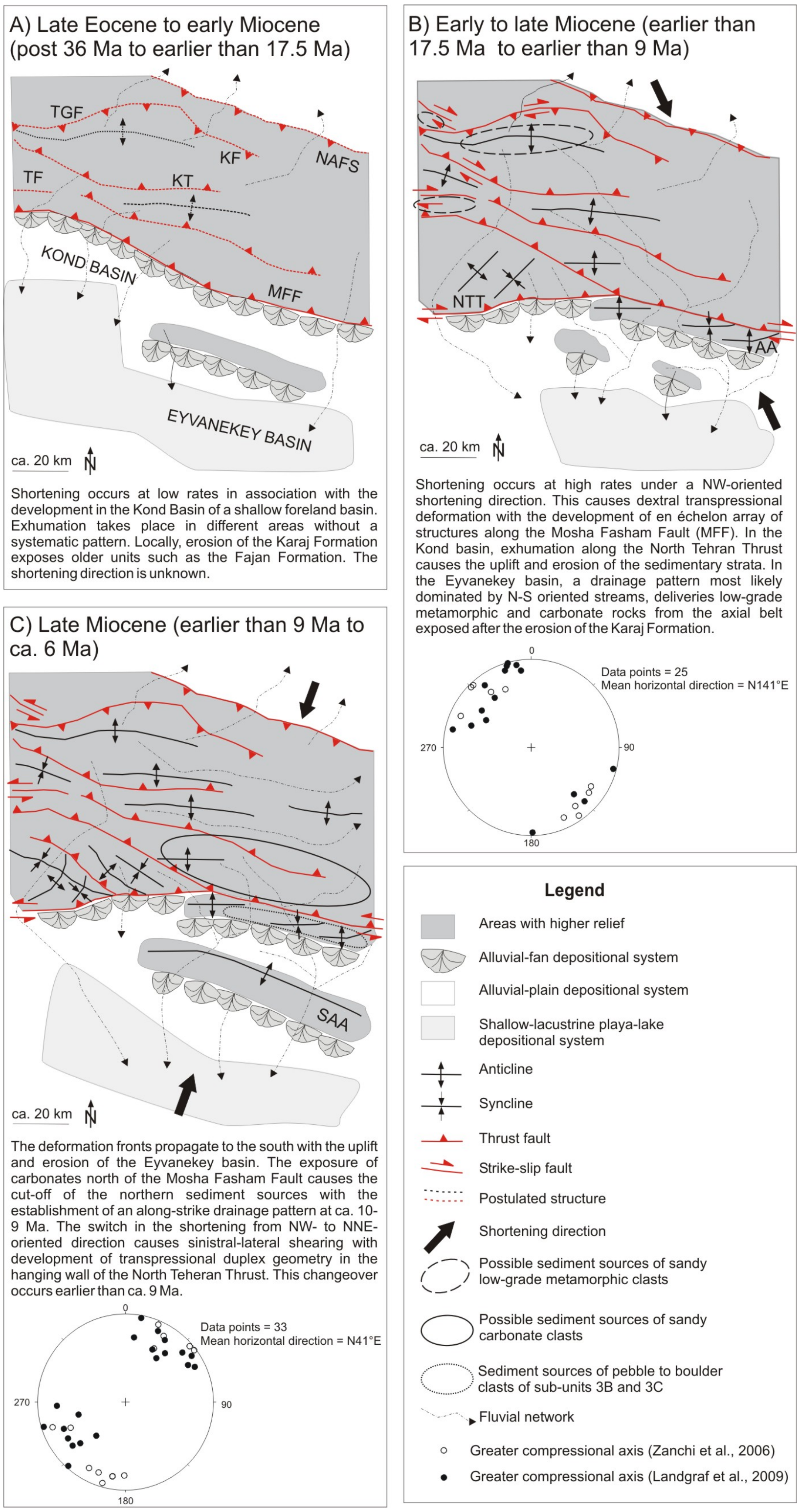
A) Late Eocene to early Miocene (post 36 Ma to earlier than 17.5 Ma)

Shortening occurs at low rates in association with the development in the Kond Basin of a shallow foreland basin. Exhumation takes place in different areas without a systematic pattern. Locally, erosion of the Karaj Formation exposes older units such as the Fajan Formation. The shortening direction is unknown.

B) Early to late Miocene (earlier than 17.5 Ma to earlier than 9 Ma)

Shortening occurs at high rates under a NW-oriented shortening direction. This causes dextral transpressional deformation with the development of en échelon array of structures along the Mosha Fasham Fault (MFF). In the Kond basin, exhumation along the North Tehran Thrust causes the uplift and erosion of the sedimentary strata. In the Eyvanekey basin, a drainage pattern most likely dominated by N-S oriented streams, deliveries low-grade metamorphic and carbonate rocks from the axial belt exposed after the erosion of the Karaj Formation.

C) Late Miocene (earlier than 9 Ma to ca. 6 Ma)

The deformation fronts propagate to the south with the uplift and erosion of the Eyvanekey basin. The exposure of carbonates north of the Mosha Fasham Fault causes the cut-off of the northern sediment sources with the establishment of an along-strike drainage pattern at ca. 10-9 Ma. The switch in the shortening from NW- to NNE-oriented direction causes sinistral-lateral shearing with development of transpressional duplex geometry in the hanging wall of the North Teheran Thrust. This changeover occurs earlier than ca. 9 Ma.

Figure 3.10. Cartoons depicting the tectonic evolution of the central Alborz mountains, and the sedimentary facies distributions in the Kond and Eyvanekey basins during the (A) Oligocene, (B) early-middle Miocene, and (C) late Miocene. The stereonet plots (Schimdt´s projection, lower hemisphere) represent a data compilation showing the distribution of (B) NW- and (C) NE-oriented greater compressional axes obtained by fault kinematic analysis along the Mosha Fasham Fault (MFF), the North Tehran Trust (NTT) and the Taleghan fault (TF). This data is from Zanchi et al., (2006; open square) and Landgraf et al., (2009; solid square). AA: Ayeverdan Anticline; KF: Khashachal fault; KT: Kandavan Thrust; NAFS: North Alborz Fault System; SAA: Southern Alborz Anticline; and TGF: Tang e Galu fault zone.

3.9.2.3 Semnan basin (Miocene)

Similar to the Eyvanekey basin at 17.5 Ma, the onset of fine-grained and evaporitic sedimentation at the base of the first coarsening-upward cycle after the early Miocene marine transgression manifests the onset of foreland-basin sedimentation. In this context, we interpret the base of the second coarsening-upward cycle to reflect renewed tectonism and increased subsidence at ca. 10 Ma, as documented in the Eyvanekey basin (sub-unit 3A; Fig. 3.4; Ballato et al., 2008). The prograding coarse-grained facies at the top of the first-coarsening upward cycle might reflect a combination of processes, including reduced subsidence during tectonic quiescence, basinward thrust advance or an increase in sediment flux. The along-strike lateral continuity of the sedimentary strata, however, suggests that this basin was not affected by intra-foreland uplift.

In contrast to the Eyvanekey basin, the generally smaller thickness of the Upper Red Formation deposits together with a higher proportion of evaporites, a decrease in soft-sediment deformation and dewatering structures, a decrease in channel thickness, and increased lateral channel stacking pattern suggest deposition in a slowly subsiding basin combined with drier climatic conditions. This can be due to a variety of factors. These include deposition in a more distal area of the foreland basin (e.g., Uba et al., 2005), higher flexural rigidity of the subsiding crust (e.g., Jordan, 1981), lower input of clastic material into the basin (e.g., Marr et al., 2000; Densmore et al., 2007), lower erodibility of source rocks (e.g., Carroll et al., 2006), and/or the existence of a shallower foreland basin in the eastern Alborz mountains. Topographic relief and hence tectonic load are interpreted to have been smaller than in the central and western sectors of the orogen in this case (e.g., Jordan, 1981). Given the present-day distribution of topography with the highest peaks located in the central western Alborz mountains, we favor the last hypothesis as the most viable mechanism.

3.9.3 Evolution of sediment-source areas

3.9.3.1 Oligocene to early Miocene

Detrital records from the Kond basin apparently present a contrast between our sandstone (uniform composition; Fig. 3.9B) and conglomerate provenance data (complex composition; Fig. 3.3). We interpret this to reflect the erosion of two major sources located in the north to north-eastern sectors of the Alborz mountains involving the volcaniclastic Karaj and the underlying conglomeratic Fajan formations. The former provided both, fine-grained sediment and coarser clasts, while the latter supplied Pre-Cambrian to Mesozoic pebbles and cobbles. Because the basin depocenter was most likely located in the hanging wall of the paleo-Mosha Fasham Fault during the deposition of the Fajan Formation where the maximum thickness of these deposits is preserved (Assereto, 1966), it is likely that the Pre-Cambrian to

Mesozoic pebbles were reworked and redeposited after a short transport distance. This may have led to reduced abrasion and production of fine-grained material. In section three, however, the increase in quartzite clasts is associated with a relative increase in the total quartz fraction (Q). The variation in conglomerate-clast composition among different stratigraphic sections in the basin was probably related to local compositional changes and the relatively small size of the drainage basins. An analogous situation exists in the present-day drainage network in the hanging wall of the central Mosha Fasham Fault segments. The unroofing of the Karaj Formation near the base of the first coarsening-upward cycle confirms that the thickness of the Karaj Formation was not uniform and that these strata pinched out toward the northern sectors where higher paleo-relief already existed (e.g., Berberian and King, 1981; Davoudzadeh et al., 1997; Guest et al., 2006a). In the second and third coarsening-upward cycles, conglomerate and sandstone compositions are dominated by volcaniclastics while Pre-Cambrian to Mesozoic pebbles and cobble clasts disappear (Fig. 3.3). This indicates that the source of sediments was located within the Karaj Formation, and that the previous source terrains comprising the conglomerates of the Fajan Formation were cut off. Because erosional unroofing processes would expose formations older than the Fajan Formation, the change of provenance terrains to outcrops of the younger Karaj Formation suggests that drainage-pattern reorganization must have taken place.

In the Eyvanakey basin, the dominance of volcanic clasts within the Oligocene strata of the Lower Red Formation in both conglomerates and sandstones shows that the source area was dominated by the Karaj Formation. The westward increase in limestone clasts, however, is indicative of the exposure of these lithologies in the Anti-Alborz. This implies that exhumation in the southern Alborz mountains of Mesozoic carbonates related to contraction has been active since the Oligocene (Fig. 3.10A).

3.9.3.2 Early to late Miocene

The detrital modes of fine lithic grains in Miocene strata of the Upper Red Formation in the Eyvanekey and Semnan basins indicate the exposure of low-grade metamorphic rocks of the Precambrian Kahar Formation and possibly the micaceous shales of the Precambrian to early Cambrian Soltanieh, Barut and Zaigun formations. All of these units are well preserved in the central and eastern axial part of the orogen (e.g., hanging wall of the Kandavan thrust), and in the core of anticlines in the central southern and eastern part of the range (e.g., Taleghan range and Ayevardan anticline) (Figs 2 and 10B). Low-grade metamorphic rocks may also have been sourced from adjacent mountain ranges in the collision zone, such as the Talesh, Caucasus, Kopeth Dagh and Zagros mountains, but given the present-day absence of well developed fluvial connectivity and large rivers traversing these different ranges to allow redistributing sediments over large areas, we suggest that these sediments were locally sourced.

Both volcanic- and metamorphic-dominated clast compositions are recorded during deposition of fine-grained facies in the foreland basin during enhanced tectonic activity in the orogen. This provides important constraints on regional spatiotemporal deformation and erosion patterns. In the fine-grained sub-unit 1A, a composition of dominant low-grade metamorphic and carbonate clasts is furthermore characterized by a sudden decrease in volcanic clasts (Fig. 3.9C). Because a gradual and progressive exposure of older rocks is not recorded, we interpret this compositional change in the context of erosional unroofing (Fig. 3.10B). In this scenario the erosional removal of the Eocene volcanic deposits exposed the Pre-Cambrian to Cambrian low-grade metamorphic rocks and Paleozoic to Mesozoic limestones, that had been uplifted and partially eroded during the Cretaceous to Paleocene shortening event. The subsequent increase in carbonate clasts in the fine-grained sub-unit 3A is interpreted to reflect another erosional unroofing event associated with the exposure of Mesozoic to Paleozoic limestones, which at present are widely exposed north of the Mosha Fasham Fault and to a lesser extent to the south in the Ayevardan anticline (Figs. 3.2 and 3.10). This was probably associated with the establishment of an along-strike drainage network similar to the present-day fluvial pattern, which would have cut off the northern sources, leading to a dominance of carbonate clasts delivered to the basin (Fig. 3.10C).

3.9.4 Shortening direction

The evolution of the compositional trends in conglomerates in the Eyvanekey basin also furnishes information on the kinematic change from the prior NW- to the present-day NNE-oriented shortening. Starting from ca. 9 Ma (sub-unit 3B) conglomerate-clast counts record Pre-Cambrian to Mesozoic rocks, while no clasts older than Eocene occur within the conglomerates of the first coarsening upward cycle (subunit 1C, 15 to 13.8 Ma; Fig. 3.4). Based on the present-day drainage network we attribute the occurrence of the Pre-Cambrian to Mesozoic clasts to the growth and coeval erosion of the Ayevardan anticline, which constitutes the closest source for these lithologies (Fig. 3.2). This composition implies that the anticline started to be unroofed prior to the deposition of sub-unit 3B (Fig. 3.10B). This inference is in agreement with a middle Miocene fission-track cooling age from the anticline (Rezaeian, 2008). The Ayevardan anticline is part of an E-W oriented right-stepping system of en échelon folds in the footwall of the WNW-ESE-striking Mosha Fasham Fault (Figs. 3.2 and 3.10B). This is compatible with the old NW-oriented shortening direction, which was responsible for dextral transpressional features (Fig. 3.10B; Guest et al., 2006a, Zanchi et al., 2006; Landgraf et al., 2009). In contrast, contractional deformation in the Eyvanekey basin between ca. 9 and 6 Ma (Ballato et al., 2008) led to the growth of the Southern Alborz anticline, an undulate WNW-ESE oriented fold generated during NNE-shortening (Fig. 3.10C). Consequently the present-day shortening direction must have been by at least 9 Ma

The causes for this reorganization are uncertain. GPS (Vernant et al., 2004b; Masson et al., 2007) and seismicity data (e.g., Jackson et al., 1995) show that regional contractional deformation across the collision results from the northward motion of the Arabian plate. The relative motion of different crustal blocks, however, can trigger contrasting kinematic regimes as observed in NW Iran. For example, west of the Talesh mountains, the present-day northward motion of the South Caspian basin has induced extension at a rate of ca. 4 mm/yr (Masson et al., 2006). Based on these observations, the changeover in the shortening direction observed in the Alborz could have been associated with a change in the relative motion between the rigid blocks comprising the collision zone. This assessment is supported by the tectonic history of the Qom Saveh area along the western edge of the Central Iranian block (Fig. 3.1). Here, the NNE-oriented shortening direction has produced a dextral transpressional belt along W- to NW- and N-striking faults during the last 10 Ma (Morley et al., 2009). The same fault system, however, accommodated sinistral transtension during widespread regional contractional deformation between ca. 17 and 10 Ma (Morley et al., 2009). This suggests that the Central Iranian block moved first northward causing sinistral transtension, while it began moving southward subsequently producing dextral compression. Overall, the northward motion of the Central Iranian block between ca. 17 to 10 Ma possibly triggered NW-oriented shortening in the Alborz mountains. Conversely, the subsequent southward motion might have caused the establishment of the present-day NNE-oriented shortening in the Alborz mountains and the Qom Saveh area. Importantly, this changeover thus agrees with our sediment-provenance data, structural cross-cutting relationships (prior to 7 Ma; Axen et al., 2001), and the onset of extrusion of the south Caspian basin associated with subduction along the Aspheron Sill at ca. 10 Ma (Hollingsworth et al., 2008).

3.9.5 Regional tectonic implications

Taking our observations and the results of prior studies into account, crustal shortening in the Alborz mountains must have started shortly after the end of the arc-magmatic phase at ca. 36 Ma and superseded a prior extensional regime. Because compressional deformation occurred across most of the present-day deformation zone during the latest Eocene to early Oligocene (Fig. 3.1), a regional variation in the plate-tectonic boundary conditions is inferred to have taken place at that time. Furthermore, although diachronous, the acceleration of tectonic processes during the early-late Miocene is regionally significant. Below, we will thus interpret the evolution of the Alborz mountains in this regional context and address to variations in the collision processes (Fig. 3.11).

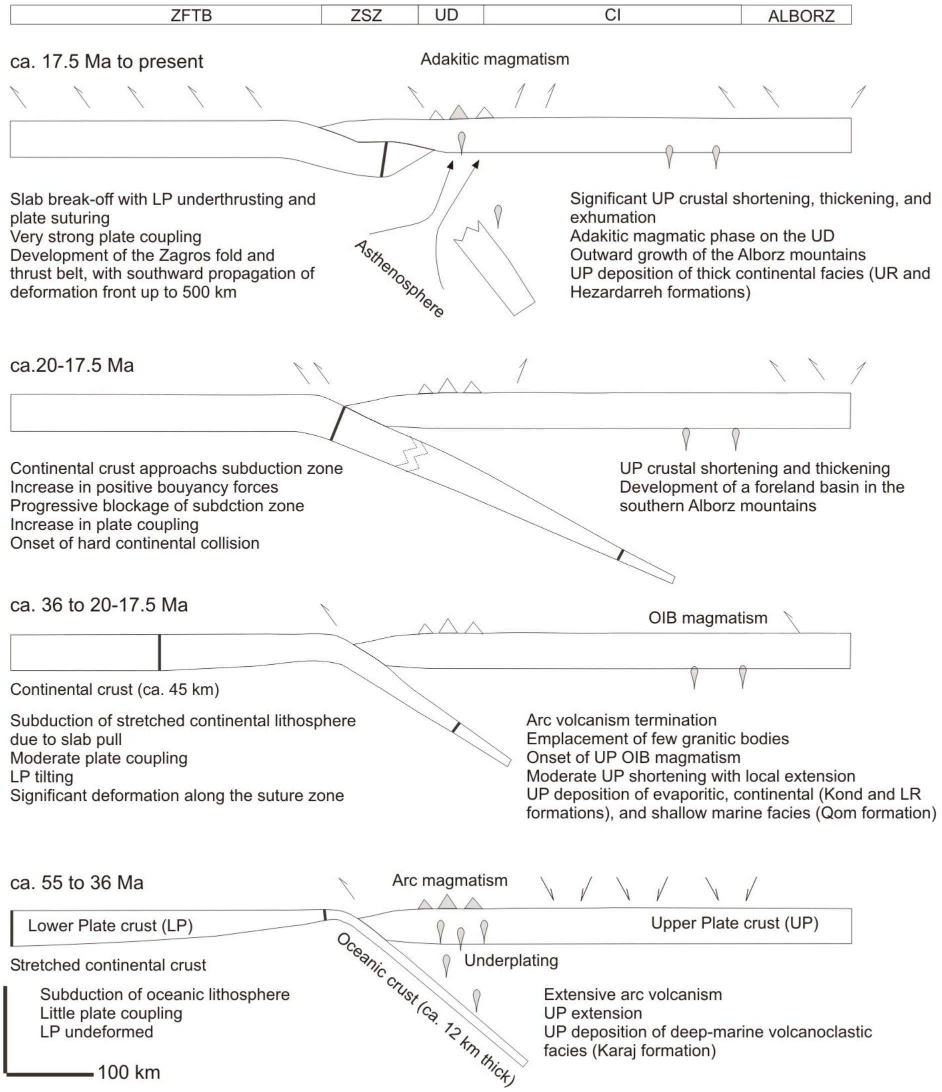

Figure 3.11. North-south oriented cross section showing the evolution of the Arabia-Eurasia plate boundary since the Eocene. The present-day crustal thicknesses are from Paul et al. (2006). The two black tick lines mark the location of stretched continental lithosphere, inferred to be between 350 and 400 km in length, like the western Atlantic margin (e.g., Al-Damegh et al., 2005). ZFTB: Zagros fold and thrust belt; ZSZ: Zagros suture zone; UD: Urumieh Dokhtar magmatic arc; and CI: Central Iran.

3.9.5.1 Initial stage of continental collision: continental subduction

The changes in the kinematic regime, the spatial characteristics of deformation across the deformation zone, and the magmatic history of the Alborz can be better understood in light of subduction-zone modeling and comparisons with other collision zones. Analog laboratory experiments (e.g., Chemenda et al., 1996, 2000; Regard et al., 2003), numerical modeling (e.g., Ranalli et al., 2000; Toussaint et al., 2004; Faccenda et al., 2008) and seismicity data from other collision zones (e.g., Burtman and Molnar, 1993) show that continental crust can be subducted to depths between 50 and 450 km. This is function of a variety of factors, such as plate-convergence rate, subduction zone geometry, type of plate contact, plate coupling, rheological properties of the lithosphere, fluid flow, and the efficiency of surficial mass-redistribution processes (e.g., De Franco et al., 2008). During subduction of continental lithosphere most of the plate convergence is absorbed by subduction processes associated with partial decoupling of sediments from the subducting continental crust, deformation along the accretionary prism, and possible delamination of subducted continental crust at depth (Chemenda et al., 1996, 2000; Regard et al., 2003; Toussaint and Burov, 2004). A minor fraction of plate convergence can be accommodated within the colliding plates by deformation in a fold-and-thrust belt on the lower plate and a intracontinental mountain belt on the upper-plate (e.g., Regard et al., 2003). This suggests that far-field tectonic stresses may be transferred from the subduction zone to the upper- and lower-plate interiors. Because most of the convergence would be still absorbed by subduction, deformation rates would be highest here, whereas upper-and lower-plate deformation rates would be lower (Regard et al., 2003). These models are compatible with the style of deformation in the Alborz mountains and in the Arabia-Eurasia collision zone (Fig. 3.1). Indeed, the inferred change in kinematics from an extensional to a contractional regime and the termination of arc magmatism at ca. 36 Ma are compatible with the initiation of continental collision with the subduction of stretched continental Arabian lithosphere ("soft" collision) beneath Eurasia (Figs. 3.11A and 3.11B).

Plate tectonic reconstructions for the Middle East do not reveal variations in convergence rates until ca. 20 Ma, when the Arabian plate motion slowed from 3 cm/yr to 2 cm/yr (McQuarrie et al., 2003), implying that between 36 and 20 Ma ca. 480 km of continental lithosphere had been subducted. Such estimates are similar to those of the India-Asia collisional zone, where 400 ± 140 km of Indian crust had been subducted between 55 Ma and 50-45 Ma (Najman and Garzanti, 2000; Guillot et al., 2003;) before the India-Asia convergence rate decreased by 60-70% at ca. 45 Ma (Molnar and Stock, 2009).

Subducted continental lithosphere has been detected by seismic tomography and seismicity studies in many collision orogens, including the Himalaya (van der Voo et al., 1999), the Pamir (Burtman and Molnar, 1993; Pavlis and Das, 1999), southern New Zealand (Eberhart-Phillips and Reyners, 1997), the Betic Cordillera (Morales et al., 1999), the Carpathians (Fan et al., 1998), and the Pyrenees (Sourieau and Granet, 1995). This suggests that continental subduction is still an important process accommodating plate convergence after collision and suturing (e.g., Negredo et al., 1997; Marchant and Stampfli, 1998; Najman and Garzanti, 2000; Guillot et al., 2003). Remnants of subducted continental lithosphere have not yet been detected in the Arabia-Eurasia collision zone. Variations in crustal thickness across the suture zone between ca. 45 km and ca. 75 km, however, suggest understhrusting of Arabia, which has resulted in more than 30 km of crustal thickening (Paul et al., 2006).

Alternatively, diachronous propagation of widespread contractional deformation in the upper plate is also a characteristic of flat-slab subduction (e.g., Barazangi, and Isacks, 1976, Jordan et al 1983). This scenario, however, is incompatible with ocean-island basalt magmatism that has been recorded in Iran beginning in Oligocene time (e.g., Verdel, 2008). In addition, low-angle subduction would influence mantle-flow circulation, producing higher dynamic subsidence in the upper plate (e.g., Mitrovica et al., 1989; Gurnis, 1992; Burgess and Moresi, 1999). This is not observed in central and northern Iran, where sediment accumulation rates between late Eocene and early Miocene were lower than those recorded for the Paleocene to Eocene interval (Davoudzadeh et al., 1997; up to 2-3 km of sediments from ca. 36 to 17.5 Ma versus 6 to 12 km from ca. 55 to 35 Ma). Instead, in an environment with subduction of stretched continental crust the thermal contrast between mantle and slab would be decreased, causing limited dynamic subsidence and upper-plate accommodation space (e.g., Mitrovica et al., 1989; Gurnis, 1992; Burgess and Moresi, 1999).

3.9.5.2 Final stage of continental collision: plate suturing

"Soft" continental collision with the subduction of stretched continental lithosphere by ca. 36 Ma heralded the subsequent arrival of buoyant Arabian lithosphere in the subduction zone. This must have caused the progressive severing of subduction processes, which was exacerbated at ca. 20 Ma when the Arabia-Eurasia convergence rate decreased (e.g., McQuarrie et al., 2003), and at ca. 17.5 Ma when foreland basin initiation occurred in southern Alborz mountains. With the onset of this new kinematic regime, deformation was accommodated by upper- and lower-plate crustal shortening and thickening coupled with lateral extrusion of crustal blocks. In light of these regional plate tectonic changes, the lag time between the late Eocene-early Oligocene onset of continental collision and the early to late Miocene acceleration of tectonic and sedimentary processes is interpreted to reflect "hard" collision and continental accretion following the subduction of stretched continental lithosphere.

Tomography studies of the upper mantle have revealed extensive sectors with positive anomalies in the Middle East that occur at depths of up to 2200 km (Bijwaard et al., 1998; Van der Voo et al., 1999). These anomalies have been inferred to correspond to the subducted slab of the Neo-Tethys oceanic lithosphere beneath central and southern Iran. Local tomography studies in Iran indicate that along the Zagros mountains these inferred slab relicts are only partially connected to the Arabian plate (Alinaghi et al., 2007). Earthquake hypocenters (Maggi et al., 2000; Talebian and Jackson 2004) and GPS data (Walpersdorf et al., 2006) do not show active deformation across the suture zone. The tomography studies also suggest that beneath central and northwestern Iran temperatures of the uppermost mantle are anomalously high (Maggi and Priestley 2005; Alinaghi et al., 2007). Taken together this suggests that subduction is no longer active, and that the Neo-Tethys slab has been partially detached following the continental collision. Such a slab detachment (or slab break-off, *sensu* Davis and von Blanckenburg, 1995) would have induced asthenosphere upwelling resulting in the juxtaposition of hot asthenosphere and upper-plate mantle lithosphere/lower crust, triggering a new pulse of magmatic activity (Fig. 11D). Indeed, Mio-Pliocene adakitic magmatism along the Urumieh

Dokhtar volcanic arc (Jahangiri, 2007; Omrani et al., 2008) may have been caused by the partial melting of mafic- to intermediate-lower crust (e.g., Guo et al., 2007; Mo et al., 2007).

The severing of subduction processes by ca. 20 Ma was responsible for the progressive reduction of connectivity between the Indian and the Atlantic oceans throughout the gradual shallowing of the Neo-Tethys seaway. The timing of this process is in agreement with paleooceanographic data (Woodruff and Savin, 1989; Stille et al., 1996) and benthic faunal distributions (Harzhauser et al., 2002; Reuter et al., 2008) suggesting a gradual reduction in the influx of Pacific seawater into the North Atlantic via the Neo-Tethys between ca. 25 Ma and ca. 14 Ma, when the exchange of water was cut off.

3.10 Conclusions

Sedimentological, provenance and geochronologic data from the foreland basins of the Alborz mountains of Iran suggest that a changeover from an extensional to a contractional tectonic regime occurred shortly after the termination of arc magmatism along the Neo-Tethyan subduction zone at ca. 36 Ma. These events are interpreted to represent the initiation of Arabia-Eurasia collisional processes with the subduction of stretched Arabian continental lithosphere beneath central Iran. During the initial, “soft” stage of continental collision, plate convergence was absorbed along the subduction zone, while a minor fraction was accommodated by upper plate contractional deformation. We infer that the decrease in convergence rate by 20 Ma was associated with the “hard” collision of unstretched Arabian lithosphere, which ultimately caused widespread upper-plate deformation, and acceleration in exhumation and sedimentation rates in the Alborz mountains by 17.5 Ma with foreland-basin initiation. In analogy with the history of the India-Eurasia collision zone we suggest that these phenomena are compatible with a two-stage collision scenario where initial “soft” collision of stretched Arabian lithosphere, was superseded by “hard” collision of unstretched continental crust associated with stronger plate coupling and an increase in deformation.

Acknowledgments

This research was funded by the German Science Foundation (Leibniz Award to M. Strecker and grant STR 373/19-1 to M. Strecker and A. Friedrich) and the graduate school program of the University of Potsdam. We are indebted to the Tehran Building and Housing Research Center and the municipality of Kilan for logistical support. T. Roeper and D. Pilz are thanked for helping with sample preparation, and C. for thin sections preparation and B. Fabian for figure drafting. T. Schildgen provided insightful reviews of an earlier version of this manuscript. B. Carrapa, E. Garzanti, M. Ghassemi, E. Macaulay, H. Sinclair, G. Vezzoli and J. Zamagni are thanked for fruitful discussions and suggestions that improved this work. We are grateful to L. Buatois for providing the trace fossils determination. M. Ahmadi is thanked for field assistance. We also acknowledge editor J. B Murphy, and constructive revisions provided by associate editor E. Bozkurt, and the reviewers D.C.P. Peacock and H.A. Koyi.

4. Middle to late Miocene Middle Eastern climate from stable oxygen and carbon isotope data, southern Alborz mountains, N Iran

Abstract

The Alborz mountains of northern Iran intercept and divert the northern hemisphere westerlies carrying moisture from the Mediterranean Sea, and form an orographic barrier to moisture sourced in the Caspian Sea. This implies that sediments along the leeward side of the southern Alborz mountains can potentially track changes in the moisture regime and mirror local to regional and global variations in atmospheric circulation, especially for the Miocene when the present-day climate conditions started to develop. Here, we present the results of a stable isotope analysis and a clay mineral study of the Miocene Upper Red Formation in the foreland of the southern Alborz mountains. Sedimentological processes, depositional age, and evolution of the sediment source areas of these deposits are well constrained. The changes recorded by stable oxygen and carbon isotope data from the southern Alborz mountains suggest: 1) an increase in aridity related to the topographic evolution of the Alborz orographic rain shadow, which became more efficient between 17.5 and 17.2 Ma; 2) an increase in precipitation between 11 and 10.3 Ma, possibly related to perturbations in atmospheric circulation pattern in the northern hemisphere, and 3) a decrease in aridity from ca. 10 to 7.6 Ma due to an increase in seasonality of precipitation, probably in response to the topographic evolution of the Himalayan-Tibetan system.

4.1 Introduction

Stable isotopes records of continental depositional systems are valuable tools for paleoenvironmental, paleoclimatic, and paleoaltimetric reconstructions (e.g., Quade et al., 1995; Cerling, et al., 1997; Kleinert and Strecker, 2001; Blisniuk et al., 2005; Rowley and Currie, 2006; Garzione et al., 2006; Mulch et al., 2006 and 2008; Kent-Corson et al., 2009). Many studies in Asia, North and South America have demonstrated that the growth of high mountains and characteristics orogenic plateaus have profoundly influenced local, regional, and hemispheric climate (e.g., Dettman et al., 2003; Blisniuk et al., 2005; Garzione et al., 2008; Mulch et al. 206 and 2008; Ehlers and Poulsen 2009; Kent-Corson et al., 2009, Mulch et al., 2010). Very little, however, is known about regions in the Middle East, which are also characterized by the presence of high mountain chains with peaks over 4 km (e.g., Zagros, Caucasus and Alborz), and the relatively high and extensive Turkish-Iranian plateau with a mean elevation of ca. 1.5 km (Fig. 4.1A). These topographic features resulted from the Arabia-Eurasia continental collision and are of particular importance for the late Cenozoic climatic evolution of the northern hemisphere, as they represent the topographic (and tectonic) link between the Alpine-Dinaride system in Europe and the Himalayan chain including the Tibetan plateau.

Middle East regions are mostly characterized by an arid to semiarid climate with a strong seasonality in precipitation including relatively wet winters and dry summers (Figs. 4.1B and 4.1C). The heterogeneous spatial distribution of precipitation is dictated by the occurrence of orographic barriers intercepting moisture sourced from Caspian Sea, Persian Gulf and Mediterranean Sea (Fig. 4.1). The limited amount of moist air reaching central Iran and west Asia is mainly derived from the Mediterranean Sea and is transported to the east by the mid-latitude westerly winds (Alijani and Harman, 1985; Barry and Chorley, 1992; Alijni, 2002). During winter months the westerlies expand southward bringing extratropical cyclones and enhancing precipitation, while in summer months they move northward because of atmospheric subsidence caused by the subtropical high pressure belt triggering extensive aridity (Figs. 4.1B and 4.1C; Alijani and Harman, 1985; Barry and Chorley, 1992; Alijni, 2002).

Climatic modeling studies indicate that the pattern of westerly winds across Asia and Middle Eastern regions was significantly perturbed by the growth of the Himalayan-Tibetan system (e.g., Kutzbach et al., 1989; Ruddiman and Kutzbach, 1989; Manabe and Broccoli 1990; Broccoli and Manabe 1992; Raymo and Ruddiman, 1992), which induced regional climatic changes between ca. 9 and 6 Ma (Molnar, 2005). In particular, the uplift of the Tibetan plateau promoted stronger seasonality in precipitation, very dry summers, and a northward shift of the westerlies at mid latitudes in Asia. The lack of paleoclimatic studies for the late Cenozoic in Middle East, however, does not allow understanding if, how, and when this uplift may have influenced the climate, and eventually how different stages in plateau growth may have impacted the climate and surface process dynamics at spatial scales beyond the immediate vicinity of the Tibetan plateau.

The Alborz mountains of northern Iran represent an intracontinental, E-W oriented orogen formed in response to crustal shortening and thickening processes induced by the ongoing Arabia-Eurasia convergence (Fig., 4.1A; e.g., Jackson et al., 1995). This has produced more than 5 km of regionally extensive tectonic denudation (Guest et al., 2006b) with mountain peaks higher than 4.5 km, and the formation of an efficient rain shadow (Fig. 4.2). At present, up to 1.7 m/yr of precipitation falls on the windward, northern flanks of the Alborz in contrast to less than 0.3 m/yr on the leeward side, and less than 0.1 m/yr in the desert area of central Iran (Alijani and Harman, 1985). Climatologic data from Tehran (leeward side of the Alborz mountains) show a strong seasonality in precipitation with more than 80% of rainfall occurring between November and April (Fig. 4.3). This seasonality is reflected in the $\delta^{18}O$ values of precipitation. $\delta^{18}O$ values correlate strongly with temperature and precipitation amount and attain minimum values of -9 ‰ in December and January and maximum values of -2 to -3 ‰ in summer and early autumn (Fig. 4.3).

The southern Alborz mountains comprise deformed Cenozoic sediments, including the Miocene terrestrial deposits of the Upper Red and Hezardarreh formations (Fig. 4.2E). These sediments record the evolution of the foreland basin and adjacent sediment source areas between 17.5 and ~ 6.2? Ma, and thus represent a potential archive for the Miocene paleoclimatic conditions in the Middle East (Ballato et al., 2008; Ballato et al., in rev.). In particular, the leeward location of the basin with respect to moisture sourced from the Caspian Sea, and the windward position with respect to the westerlies and the Tibetan-Himalayan system allows the foreland basin deposits to potentially record the combined effects of local topography and atmosphere hemispheric-scale perturbations in dictating precipitation patterns during late Cenozoic.

Here, we present for the first time in Middle Eastern regions long-term oxygen and carbon isotope record coupled with a study of clay minerals from foreland basin deposits of early to late Miocene age. This record results from the climatic and topographic effects of landscape development in the Alborz mountains on isotopes in precipitation and provides a detailed paleoclimatic and paleoenvironmental reconstruction for northern Iran. We conclude that the Alborz rain shadow exerted an important influence starting from 17.5 to 17.2 Ma, and that an increase in precipitation between 11 and 10.3 Ma promoted extensive syntectonic progradation of coarse-grained sedimentary facies in the basin. Finally, an increase in seasonality of precipitation beginning at about 10 Ma led to a general decrease in aridity.

4.2 Materials and methods

The studied sedimentary section in the southern Alborz mountains comprises the terrestrial Upper Red and Hezardarreh formations (Eyvanekey stratigraphic section, Ballato et al., 2008 Ballato et al., in rev.). These units are organized in three coarsening-upward cycles (units 1, 2 and 3), reflecting deposition in playa to shallow lacustrine (sub-units 1A, 2A, and 3A), fluvial (anastomozing, sub-units 1B; braided, subunits 1C, 2B, and 3B), and alluvial-fan (sub-unit 3C) sedimentary systems (Fig. 4.4A). The Upper Red Formation (units 1, 2 and sub-units 3A and 3B) is a ~ 6.5-km-thick fluvio-lacustrine succession deposited between ~ 17.5 and ~ 7.6 Ma, interpreted to record foreland basin evolution in the course of crustal shortening and thickening. The Hezardarreh Formation (sub-unit 3C) is a ~800-m-thick alluvial sequence deposited between ~7.6 and 6.2(?) Ma. The Hezardarreh Formation and upper part of the Upper Red Formation together reflect basin uplift and erosion associated with the southward propagation of the Alborz deformation front (Ballato et al., 2008; Ballato et al., in rev.). All samples were collected from the Upper Red Formation. We differentiated mudstone and carbonate samples representing floodplain and lacustrine/playa lake deposits (Fig. 4.5B) from rhizoliths (Fig. 4.5C) and calcretes (Figs. 4.5A and 4.5D) that originate from poorly to moderately developed paleosols. The former represent calcite precipitation from standing water, while the latter reflect carbonate precipitation from soil water during pedogenetic processes.

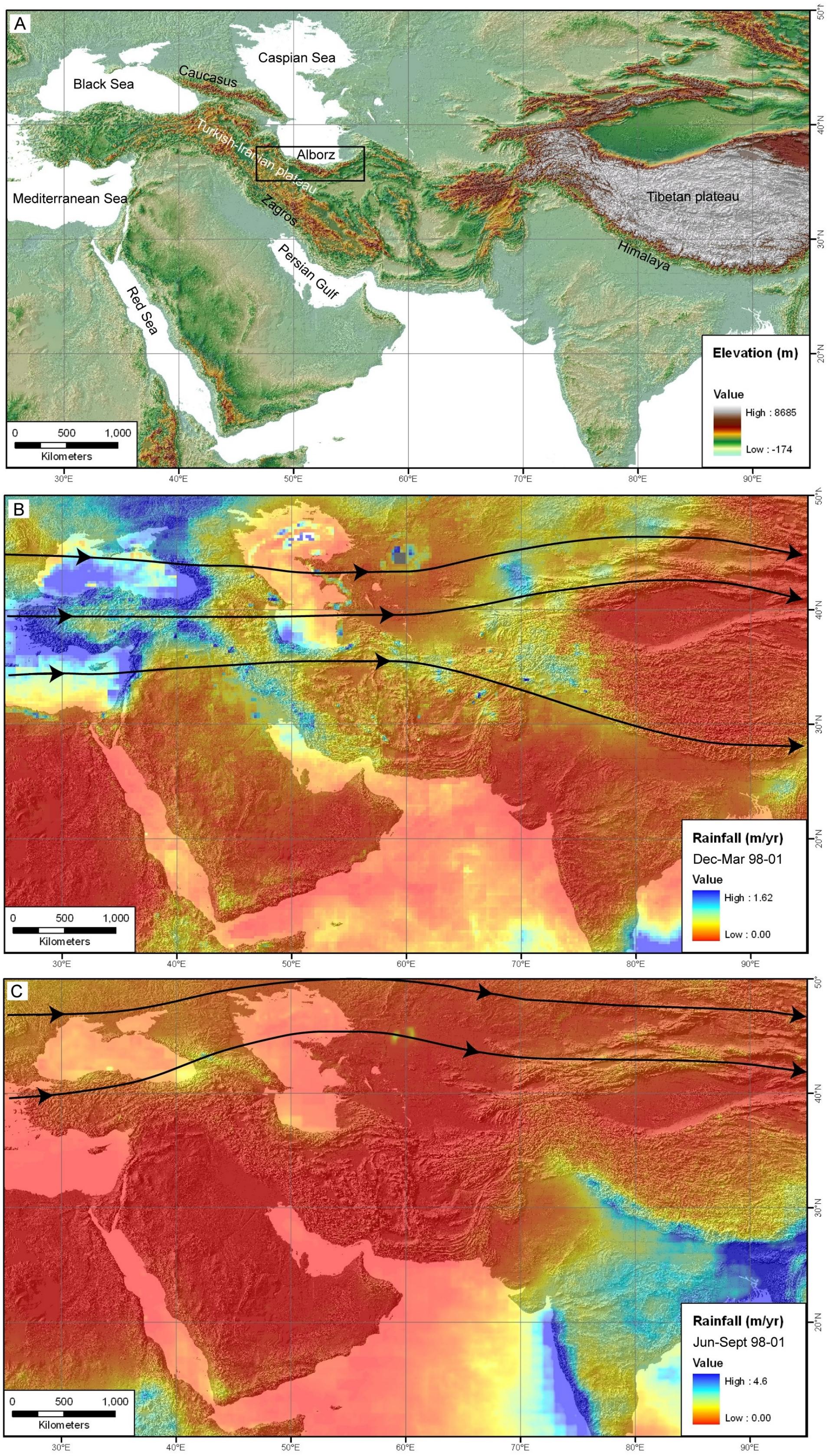

Figure 4.1: (A) Topography of western Asia based on a ca. 1-km digital elevation model (HYDRO 1K). The black rectangle highlights the location of figure 2. (B) TRMM rainfall data for winter months (December to March) and (C) for summer months (June to September) for the period 1998 to 2001 with a spatial resolution of ca. 30 km (Bookhagen pers. communication). Note the change in the rainfall scale between B and C. The black lines show the location the 500 hPa westerlies during (B) January and (C) July (Barry and Chorley, 1992).

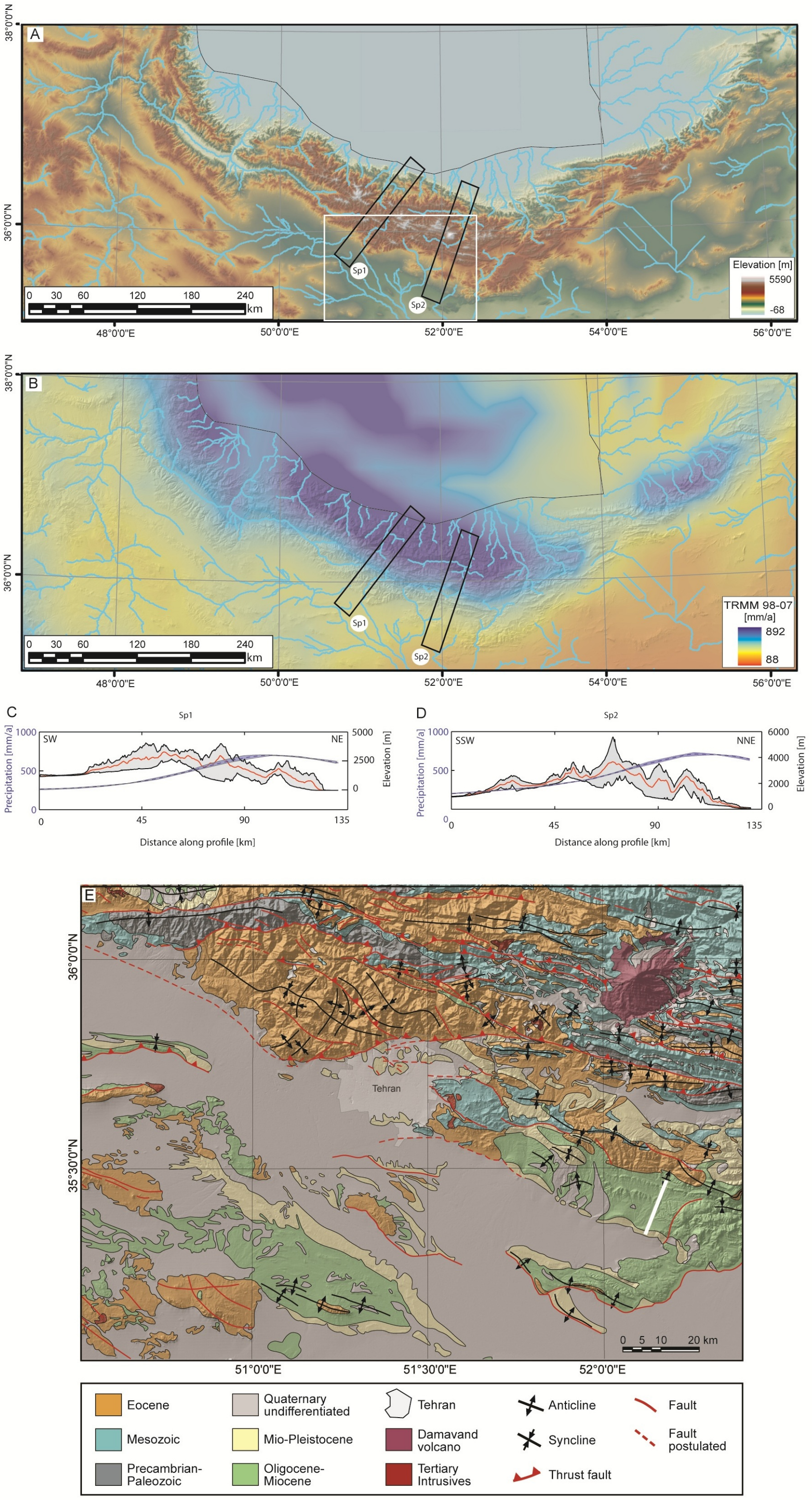

Figure 4.2: (A) Topography and drainage pattern of the Alborz mountains based on a 90-m digital elevation model. The black rectangles show the location of figures 4.2C and 4.2D, while the white rectangle displays the location of figure 4.2E. (B) Annual rainfall data based on TRMM 3B42 (Bookhagen pers. communication) superimposed on a digital elevation model showing the rain shadow effect induced by the Alborz mountains. (C and D) Topographic (grey area) and precipitation-distribution (blue area) swath profiles across the central Alborz mountains. (E) Geological map of central Alborz, superposed on DEM, modified after Haghipour et al., (1987), Vahdati Daneshmand et al., (1991), Amini et al., (2004) and Guest et al., (2006a). The solid white line indicates the position of the Eyvanekey stratigraphic section of figure 4.4.

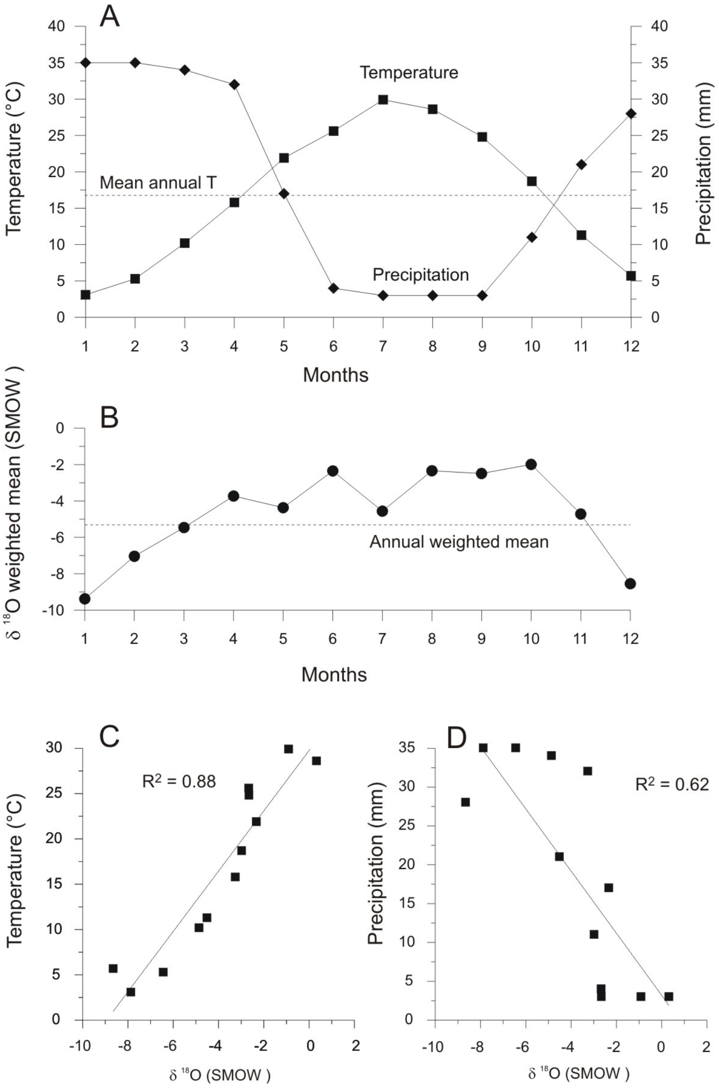

Figure 4.3: Monthly distribution of (A) temperature, precipitation, and (B) δ^{18}O weighted mean for Tehran for the period 1960-1981 (data from International Atomic Energy Agency-World Metereological Organization, available at http://www.iaea.org). (C) Correlation plot between temperature and δ^{18}O and (D) between precipitation and δ^{18}O.

4.2.1 X-ray diffraction analysis

For x-ray diffraction analysis, ten mudstone samples were collected and crushed by hand with an agate mortar, dispersed in deionised water, and disaggregated using ultrasonic treatment, The clay-sized fraction (<2 µm) was separated by differential settling. The aqueous suspension of each fraction was pipetted and dried at 50°C on zero-background sample holders. The oriented air-dried samples were glycolated and then heated up to 330°C and 530°C for 30 minutes. After each treatment, X-ray diffraction patterns were recorded using a Bruker AXS D8 Advance diffractometer equipped with a Sol-X energy dispersive detector at the Department of Earth Science, University of Ferrara. The following instrumental settings were used: Cu $K\alpha_{1,2}$ radiation, tube voltage and current of 40 kV and 40 mA, 0.6 mm divergence and antiscattering slits, 0.2 mm receiving slit, 2° - 30° 2θ range, 0.02° scanning step, counting 4 s per step. Bulk-rock mineral compositions were determined by x-ray diffraction of randomly oriented whole-rock powders (side-loading method) and measuring a 4° - 90° 2θ range. Quantitative analysis of the crystalline phase fractions was performed by means of the Rietveld method (e.g., Rietveld, 1969; Bish & Howard, 1988; Hill, 1991; Bish & Post, 1993, Ballato et al., 2005), using TOPAS software (Bruker AXS, 2003) (Table 4.1, Appendix 4).

4.2.2 Stable isotope analysis

One hundred and thirty-five mudstone and carbonate samples, and forty-seven rhizolith and calcrete samples were collected and powderized using a dental drill. Between 0.18 and 0.60 mg of these powders were loaded in sealed reaction vessels, then flushed with helium gas and reacted at 72°C with phosphoric acid using a Thermo GasBench II. Isotope ratios were measured in continuous flow mode using a Thermo DeltaV Advantage mass spectrometer in the Stable Isotope Laboratory at Leibniz Universität Hannover. Due to the variable carbonate contents of the samples, we adjusted the sample sizes to match standard sample sizes during the mass spectrometric measurements. Based on repeated analyses of reference material NBS-19, and two different in-house standards (MERCK CaCO3 and Lausanne1) analytical precision is determined to be ±0.06 ‰ ($\delta^{13}C$) and ±0.08 ‰ ($\delta^{18}O$) for carbonate-rich samples and <0.2 ‰ ($\delta^{13}C$ and $\delta^{18}O$) for carbonate-poor samples. Random samples were duplicated and tested for consistency and the raw isotope data were corrected for mass bias, signal size, and offset from the certified reference values following Spötl and Vennemann (2003). $\delta^{18}O$ and $\delta^{13}C$ values are presented with respect to SMOW and PDB, respectively (Fig., 4.4, Appendix 5). In fifteen cases, two samples per horizon were analyzed in order to test the occurrence of isotopic compositional heterogeneities, and the average was plotted. In ten cases, rhizoliths and mudstones from the same horizons were analyzed in order to compare the isotopic composition of palustrine/lacustrine and pedogenic calcite..

4.3 Results

4.3.1 X-ray diffraction analysis

Quantitative phase analysis of bulk-mudstone samples reveal the occurrence of quartz (23 to 33%), plagioclase (13 to 22%), calcite (17 to 34%), dolomite (0 to 4%), analcime (0 to 4%), hematite (0 to 1%) gypsum (1%), and clay minerals (16 to 39%) (Table 4.1). The clay mineralogy displays an increase in variability from the base of the section, where only illite (11 to 24%) and chlorite (2 to 9%) occur, towards the top, where expandable clays (vermiculite group, up to 7%) and palygorskite (up to 9%) appear (Table 4.1).

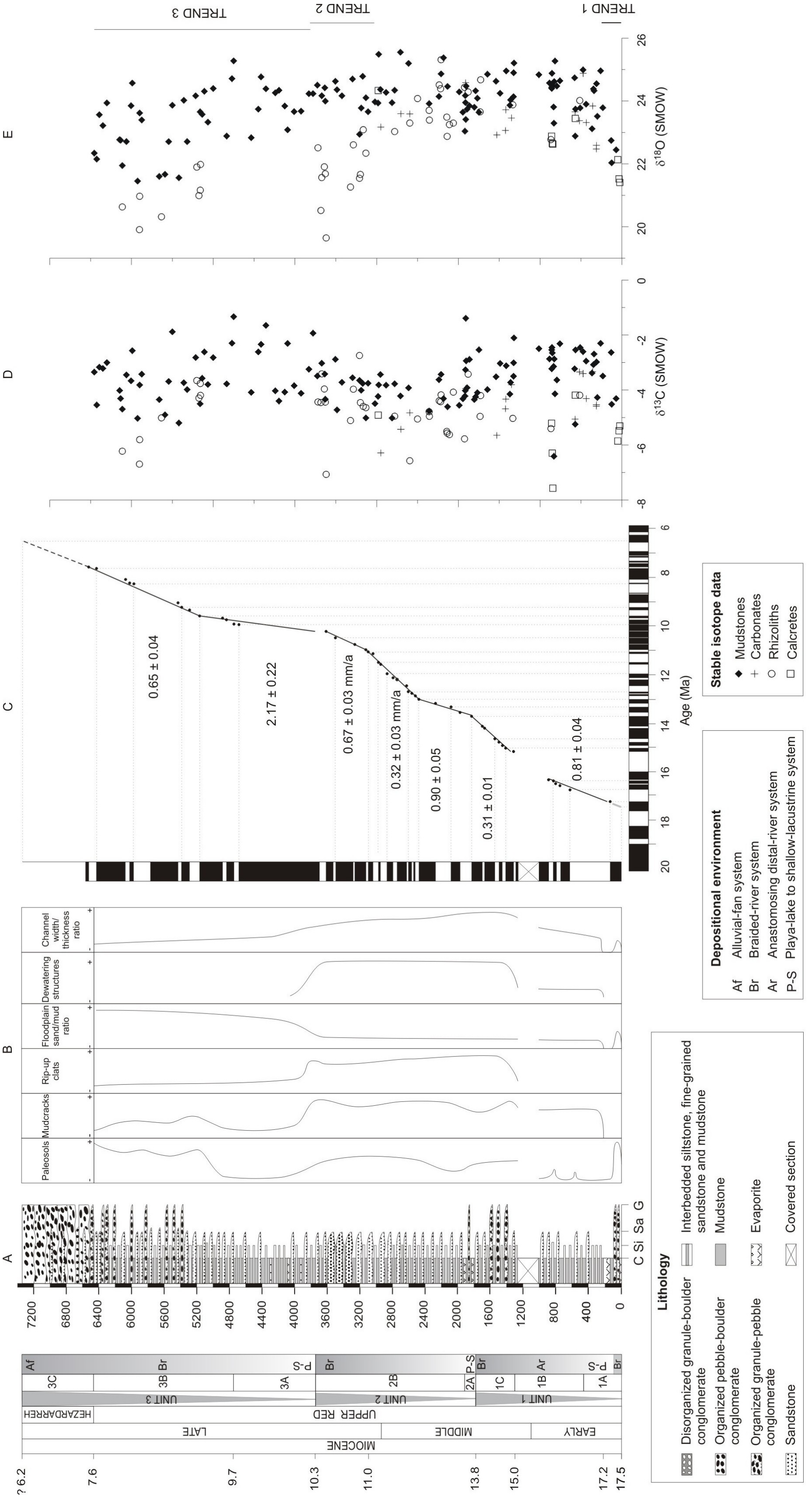

Figure 4.4: (A) Eyvanekey stratigraphic section representing Upper Red and Hezardarreh formations. (B) Upsection stratigraphic variation in sedimentary and pedogenetic climate indicators. (C) Long-term sediment accumulation rates in mm/a (Ballato et al., 2008). (D) Carbon and (E) oxygen isotope data. The vertical bars mark the three recognized trends.

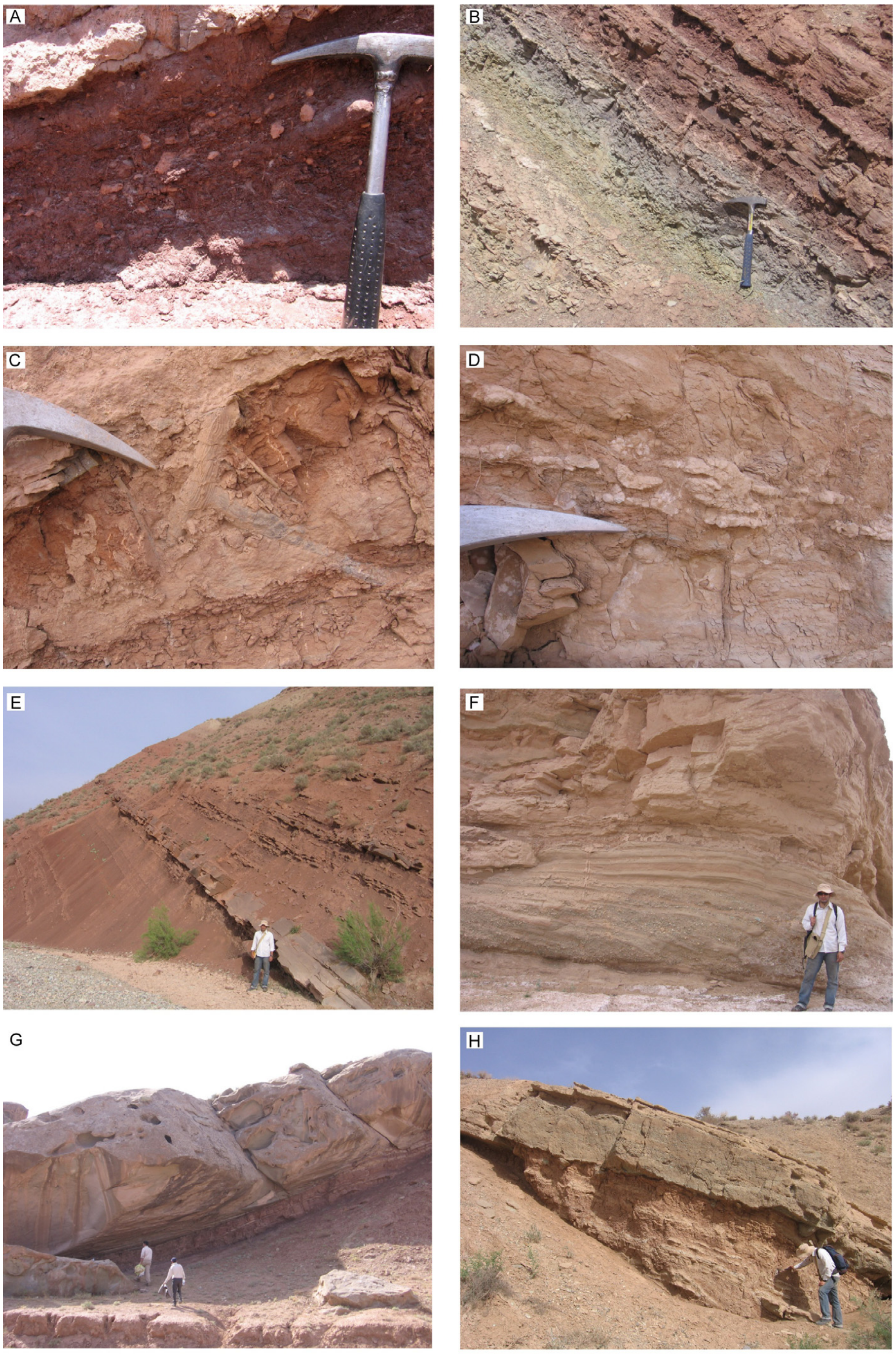

Figure 4.5: Outcrop views of analyzed samples and depositional environments. (A) Well developed calcareous paleosol with carbonate nodules (calcrete sample types) formed in flood plain deposits of a braided river system exposed at the base of the stratigraphic section. (B) Alternation of green and red mudstones (mudstone sample types) representing shallow lacustrine and playa lake deposits with desiccation cracks (sub-unit 1A). The transition between lacustrine and playa deposits is marked by carbonate horizons (carbonate sample type). (C) Well preserved branching downward root concretions (rhizolith sample types) formed on mud-dominated floodplain deposits of a braided river system (sub-unit 2B). (D) Well developed calcareous paleosols with calcretes and small rhizoliths formed on sandy floodplain deposits of a braided river system (sub-unit 3B). (E) Mud-dominated floodplain deposits of a distal river system (sub-unit 1B) with tabular sandstone and mudstones bodies. (F) Poorly channelized gravel body grading upward to tabular and wedging sandy floodplain deposits of a braided river system (sub-unit 3B). (G) Channelized, well-sorted, coarse-grained sandstone body with a lateral extent of few hundreds of meters and a gentle down-cutting erosive base marked by mud-chips representing deposition in a braided river system (sub-unit 2B). The underlie deposits are tabular red mudstones recording flood plain deposition. (H) Channelized poorly-sorted cobble conglomerate to coarse-grained sandstone with a pronounced down-cutting erosive base representing deposition in braided river system (sub-unit 3B). The underlie deposits are small (few meters of lateral extent) wedging light brown siltstones and sandstones reflecting flood plain deposition.

TABLE 4.1: QUANTITATIVE PHASE ANALYSIS: RESULTS IN MINERAL PERCENTAGE (WT%); LAST SIGNIFICANT DIGIT UNCERTAINITIES (1σ) GIVEN IN PARENTHESES

Sample ID	Position (m)	Ages (Ma)	Sub-unit	Quartz (%)	Plagioclase (%)	Calcite (%)	Dolomite (%)	Analcime (%)	Hematite (%)	Gypsum (%)	Illite (%)	Chlotite (%)	Vermiculite (%)	Palygorskite (%)
6155c	6060	8.4	3B	24.3(2)	18.0(4)	27.6(3)			0.8(1)		13.8(3)	6.4(2)	4.1(4)	5.0(5)
5840c	5735	9.1	3B	23.6(4)	20.4(4)	22,1(4)					11.7(5)	6.2(3)	5.6(3)	9.9(5)
5050c	5170	9.6	3B	32.5(4)	21.8(5)	23.0(3)	2.0(1)	4.0(1)			11.5(5)	2.4(3)	3.2(3)	
4670c	4790	9.8	3A	23.0(3)	16.4(6)	19.7(3)	3.4(2)	3.4(1)			15.2(4)	5.2(3)	4.8(4)	8.9(5)
3700a	3820	10.3	3A	23.9 (2)	13.5(4)	24.4(2)	4.4(1)		1.2(1)		23.5(4)	9.0(3)	?	
2985c	3105	10.9	2B	26.3(3)	15.6(5)	16.9(2)	0.7(1)	1.1(1)	0.9(1)		24.8(4)	7.2(3)	6.6(2)	
2005a	2125	13.3	2B	23.6(4)	22.0(4)	20.5(4)	1.6(2)		1.0(1)		20.8(4)	9.0(3)		
915a	915	16.3	1B	30.0(6)	22.0(4)	27.0(5)					13.0(5)	7.0(3)		
377c	377	17.0	1A	29.3(2)	17.9(4)	33.7(2)	1.9(1)		0.9(1)	0.9(1)	11.3(3)	4.5 (2)		
285c	285	17.2	1A	28.9(2)	18.6(4)	26.9(2)	2.7(1)		1.2(1)		17.0(4)	4.7(3)		

4.3.2 Stable isotopes

Carbonate oxygen isotope data from the foreland basin deposits reveal three major trends (Figs. 4.4D and 4.4E).

Trend one is recorded between 0 and 230 m (17.5 to 17.2 Ma), where $\delta^{18}O$ values increase from 22.0±0.5‰ (1σ, 0-130 m, n=6) to 24.0±0.7‰ (1σ, 230 to 3100 m, n=101). This change occurs across a ~ 100-m-thick evaporite package deposited at ~ 17.2 Ma. Upsection $\delta^{18}O$ values do not show significant variation until ca. 3100 (11 Ma). A t-test comparing the values below (0 to 130m) and above (230 to 3100 m) the evaporites yields p=1.2x10-4, indicating that the two populations are statistically different. A similar tendency towards less negative values is suggested in $\delta^{13}C$ data with values going from -4.7±1.2‰ (1σ, 0 to 130 m, n=6) to -4.0±1.1‰ (1σ, 230 to 3100 m, n=101) across the ~ 100-m-thick evaporite package. The carbon shift, however, is of smaller magnitude and greater error; therefore the two populations are not statistically different. Upsection, carbon isotope values in the mudstones are relatively constant. In the lower part of the section we observe one marked negative isotope spike at 830-845 m (~ 16.4 Ma) with $\delta^{13}C$ and $\delta^{18}O$ values of -6.4‰ and 23.3‰ (mudstones) and -7.6‰ and 22.7‰ (rhizoliths), respectively.

Trend two is recorded between 3100 and 3720 m (11 to 10.3 Ma), where rhizolith samples exhibit a negative oxygen isotope excursion of almost 5 ‰ from values of 24.4‰ to 19.6‰ (mean 21.7±0.9‰, 1σ, n=12), while palustrine/lacustrine mudstone and carbonate samples show values comparable to those of the interval 230 to 3100 m with a mean of 24.1±0.5‰ (1σ, n=12). The $\delta^{13}C$ rhizolith values show an overall similar (though more complicated) pattern within that time interval. We observe a negative carbon isotope peak (δ13C= -7.1‰) at 3618 m followed by an abrupt increase to $\delta^{13}C$ values of around -4.5 to -3.5‰ (3628 to 3682m).

Trend three occurs starting from 3720 m (10.3 Ma). Here, a general tendency towards lower $\delta^{18}O$ values is recorded in both rhizoliths (22‰ to 19.9‰) and to a lesser extent in palustrine/lacustrine mudstones and carbonates (25.3‰ to 21.5‰). In the palustrine/lacustrine samples this trend is partly masked by a significantly larger variability in $\delta^{18}O$ values until the top of the Upper Red Formation at 6455 m (~ 7.6 Ma). A t-test comparing the oxygen values of palustrine/lacustrine mudstones and carbonates between the interval 3100-3720 m (24.1±0.5‰, 1σ, n=12, 11 to 10.3 Ma) and the interval 3720-6455 m (23.5±1.0‰, 1σ, n=43, 10.3 to 7.6 Ma) yields a p=2.2x10-3, suggesting that despite the partial data overlap due to high data scattering, the two populations are significantly different. Carbon isotopes show a similar trend with a progressive decrease in $\delta^{13}C$ values in both rhizoliths (-3.7‰ to -6.7‰) and in palustrine/lacustrine mudstones and carbonates (-1.3‰ to -5.2‰). Lacustrine/palustrine samples also display an increase in data scatter between 3720 and 6455 m (10.3 to 7.6 Ma;-3.5±0.9‰, 1σ, n=43). It is important to note that post-11 Ma (3000 m) $\delta^{18}O$ values in rhizoliths and calcretes deviate significantly from the $\delta^{18}O$ mudstone values with $\delta^{18}O$ values in rhizoliths being generally ca. 2 ‰ more negative than $\delta^{18}O$ mudstone values. This occurs contemporaneously with the onset of larger scatter and variability in both $\delta^{18}O$ and $\delta^{13}C$ mudstone values.

4.4 Discussions

4.4.1 Burial and diagenetic effects on $\delta^{18}O$ and $\delta^{13}C$ carbonate values

Post-depositional recrystallization of calcite during diagenesis and burial can obliterate the primary isotopic signal leading to erroneous paleoclimatic and paleoenvironmental reconstructions (e.g., Morrill and Koch 2002; Garzione et al., 2004). A careful interpretation of the depositional environments and of the sedimentary microfabric is therefore crucial for deciphering isotopic data. Thin section analysis of mudstones, carbonates and rhizolithes reveals the dominance of micritic calcite, while microsparitic calcite is rare and sparry calcite is absent indicating that the original sedimentary fabric was not replaced after deposition. The analysis of ten rhizolith and mudstone samples from the same sedimentary horizons yield a difference in $\delta^{18}O$ up to -2.6‰ most likely in response to isotopic fractionation processes (Appendix 5). In case of diagenesis with extensive calcite replacement the isotopic signal would tend to be homogeneous. Thus, the observed isotopic differences between samples from the same horizons and the lack of secondary sparry calcite indicate that the primary $\delta^{18}O$ signal is preserved.

4.4.2 Detrital contamination

In lacustrine/palustrine depositional environments, contamination with fine-grained detrital carbonates during sedimentation can mask the primary isotopic signal. A clear understanding of the different sediment sources is therefore crucial for deciphering isotopic data. A sandstone petrographic study conducted throughout the sedimentary section shows an increase in fine carbonate lithics (sandy grains with constituents <63 μm) at ~ 4150 m (~ 10.1

Ma) (Ballato et al., in rev.). This significant increase in detrital carbonate is associated with an increase in the variability of $\delta^{18}O$ and $\delta^{13}C$ data and could be interpreted as the result of, variable contamination by detrital grains

In order to detect the potential contribution of detrital grains to the measured $\delta^{18}O$ and $\delta^{13}C$ values, stable isotope analysis of twelve marine limestone samples of Devonian to Miocene age from the sediment source areas was performed. $\delta^{13}C$ values of these limestones range from -1.8 to 3.0‰ (with the exception of one Devonian sample exhibiting a $\delta^{13}C$ of -7.2‰), while $\delta^{18}O$ values vary between 22.0 and 27.8‰ (Table 4.2). Most of palustrine/lacustrine mudstones and carbonates from the Eyvanekey section have $\delta^{13}C$ values smaller than -1.8‰, suggesting very limited detrital contamination from the more enriched source rocks. Greater detrital input might have slightly shifted $\delta^{13}C$ data toward less negative values resulting in an overestimation of the $\delta^{13}C$ values at the top of the section. In the case of oxygen isotopes, the overlap between the analyzed Miocene mudstones and the Devonian to Miocene limestones suggests that a potential detrital contribution might have scattered the signal without a predictable trend. In addition, the mineralogical quantitative phase analysis of mudstone samples does not show any significant increase in calcite starting from ~ 10.1 Ma, as expected in case of significant detrital contamination related to the increase in fine carbonate lithics. Based on the analysis of limestones from sediment source areas and the mineralogical quantitative phase analysis of mudstone bulk samples, we conclude that detrital contamination did not mask the primary signal.

TABLE 4.2: STABLE ISOTOPE ANALYSIS OF DEVONIAN TO MIOCENE LIMESTONES COMPRISING THE SEDIMENT SOURCE AREAS

Sample ID	$\delta^{18}O$ (SMOW)	$\delta^{13}C$ (PDB)	Formation	Age
Q-03	24.42	1.26	Qom	Oligo/Miocene
Q-02	23.16	-0.84	Qom	Oligo/Miocene
Q-01	27.49	1.47	Qom	Oligo/Miocene
KR-03	25.72	0.11	Cretaceous limestone	Cretaceous
KR-02	23.29	0.86	Cretaceous limestone	Cretaceous
KR-01	23.68	-0.48	Tiz-kuh	Cretaceous
LAR-02	27.83	2.34	Lar	Jurassic
LAR-01	26.41	3.04	Lar	Jurassic
EL-01	22.52	-1.77	Elika	Triassic
R-T01	24.12	1.54	Ruteh	Permian
MOB-01	21.99	1.03	Mobarak	Carboniferous
J-01	22.49	-7.23	Geirud	Devonian

4.4.3 Clay mineralogy

Clay minerals form through weathering of parent rocks during pedogenesis, and their occurrence and relative abundance in sedimentary deposits can record paleoclimatic and paleoenvironmental information (e.g., Chamley, 1989). In terrestrial sedimentary deposits, detrital clays reflect paleoconditions of the drainage basins, while authigenic clays record those of the sedimentary basin. Illite and chlorite frequently form in dry (cold and hot), high-relief regions where active mechanical weathering and low rainfall limit soil formation (Chamley, 1989). Vermiculite tends to form in temperate regions experiencing high seasonality, while palygorskite typically forms in arid to semiarid climates (Chamley, 1989).

The Eocene volcaniclastic deposits (Karaj Formation) represent the most important sediments source for the Miocene deposits of the southern Alborz mountains (Ballato et al., in rev.). Weathering processes tend to progress on volcanic rocks faster than other rocks due to the abundance of amorphous material facilitating hydrolysis (Chamley, 1989). Thus, we interpret illite, chlorite, and vermiculite in the Eyvanekey section to be of detrital origin and to have formed mainly through weathering of the Eocene volcaniclastic deposits and to a lesser extent of the Precambrian to Mesozoic rocks upstream of the basin. Conversely, palygorskite is probably authigenic and precipitated in lacustrine sediments and/or soil carbonates. The observed upsection increase in clay variability may not reflect a primary signal, because during burial at temperatures higher than 80°C, vermiculite tends to transform into illite (Chamley, 1989), while palygorskite disappears (Velde, 1995) (Table 4.1). Thus, the occurrence of illite and chlorite in the interval 0-3100 m (17.5 to 11 Ma) suggests that burial temperatures exceeded 80°C (Table 1). The presence of illite, chlorite, and vermiculite together (interval 3100-6455 m) suggests that since at least 11 Ma, the catchment areas experienced higher, most likely seasonal, precipitation. The variable occurrence of palygorskite (present since at least 9.8 Ma but absent in the 9.6 Ma sample 3700a2,) indicates aridity in the foreland basin since at least 9.8 Ma, which possibly alternated with wetter phases.

4.4.4 Oxygen isotopes

Variations in oxygen isotopic composition in continental stratigraphic records can be related to both global and regional-scale climatic and topographic factors, which can induce positive and negative feedbacks on precipitation patterns and hence oxygen and hydrogen isotopes in the meteoric water cycle (e.g. Quade et al. 2007a, Mulch and Chamberlain 2007) . These factors include changes in climate (e.g., sea surface temperature, air temperature, polar region ice volume, reorganization of atmospheric circulation and wind patterns, monsoonal variability, and seasonality), source of precipitation, local hydrology, surface elevation, and topography of adjacent regions (for recent reviews see Poage and Chamberlin, 2001; Blisniuk and Stern, 2005; Mulch and Chamberlain 2007; Quade et al., 2007a; Rowley and Garzione 2007). In the following paragraphs we will examine the possible causes for patterns observed in our $\delta^{18}O$ records in light of the detailed stratigraphic and sedimentologic data available for the different sedimentary sub-units of the Eyvanekey section.

4.4.4.1. Trend one: sub-unit 1A (~ 17.5 to 17.2 Ma)

At the base of the section (sub-unit 1A, ~ 17.5 to 17.2 Ma) $\delta^{18}O$ values shift by +2‰ from 22.0±0.5 to 24.0±0.7‰ (Fig. 4.4E). This enrichment in $\delta^{18}O$ is recorded by both paleosols and lacustrine/palustrine samples. The lack of terrestrial deposits beneath the Upper Red Formation precludes understanding the exact temporal extent and magnitude of this isotopic shift. Statistical analysis, however, suggests that this shift towards more positive values is robust and not an artifact related to a limited number of samples recording lower $\delta^{18}O$ values.

Global climate change is an unlikely cause for the observed positive shift, because paleoclimatic reconstructions indicate relatively stable conditions with minor warming preceding the mid Miocene climatic optimum (Zachos et al., 2001). A change in moisture source from the southern epicontinental Qom Sea, which was established across central Iran between the late Oligocene-early Miocene (e.g., Reuter et al., 2009) to the northern Paratethys Sea might explain the observed positive isotopic shift. The Qom Sea was shallower, most likely warmer, and more evaporative than the Paratethys Sea, which included deeper basins such as the Caspian Sea, Black Sea and Pannonian basin until the late Miocene Messinian salinity crisis. Thus, the change to a colder moisture source would have caused an increase in the $\delta^{18}O$ of precipitation on the order of -0.55‰/°C (Jouzel et al. 1997)

Alternatively, the observed +2‰ shift in δ18O values might reflect an increase in aridity due to the growth of an orographic barrier to precipitation upstream of the basin. Apatite fission track cooling ages from the inner domains of range (Rezaeian, 2008) suggest that exhumation rates accelerated by ~ 20 Ma, probably in response to enhanced crustal shortening and thickening processes, which triggered tectonic loading and foreland basin initiation in the southern sectors of the range at ~ 17.5 Ma (Ballato et al., 2008; Ballato et al., in rev.). Shortening processes may have caused the progressive increase in surface uplift with the formation of an effective barrier to moisture-bearing northerly winds and rain shadow development in the southern Alborz mountains. The effect of evaporation is difficult to quantify based solely on $\delta^{18}O$ and $\delta^{13}C$ values of carbonate (Mulch and Chamberlain 2007) but for the Miocene climate of the Iranian foreland basin it is likely to be large as suggested by the oxygen isotopic composition of present day soil and lake water in arid regions (Breecker et al 2009, Henderson and Shuman, 2009). In addition, the orographic rain shadow might have promoted an increase in local temperature, which would have resulted in a net increase of 0.36 ‰/°C in the $\delta^{18}O$ of pedogenic and lacustrine/palustrine carbonates. The increase in aridity is also corroborated by the upsection increase in desiccation cracks and the decrease in well developed carbonate paleosols (Figs. 4.4B, 4.5A and 4.5B). Overall, the coeval occurrence of enhanced rock uplift, foreland basin initiation, and increase in aridity during the Early Miocene, suggests that the growth of an orographic barrier is the most likely explanation for the observed positive isotopic shift at the base of the section between 17.5 and 17.2 Ma.

Finally, $\delta^{18}O$ of both paleosols and lacustrine/palustrine samples exhibit a marked negative spike at 16.4 Ma during the deposition of sub-unit 1B. This spike could reflect a short phase of enhanced precipitation either related to global climate changes (e.g., Mid-Miocene climatic optimum, Zachos et al., 2001), or to variation in the atmospheric circulation pattern.

4.4.4.2. Trend two: top of sub-unit 2B (~11 to 10.3 Ma)

Between 3100 and 3720 m (sub-unit 2B, 11 to 10.3 Ma) a negative oxygen isotopic excursion of up to 5 ‰ from values of 24.4‰ to 19.6‰ is recorded in pedogenic carbonates, while palustrine mudstone and carbonate samples show stable values of ca. 24‰ (Fig. 4.4E).

Climate in the sediment source area dictates flow hydraulics of a river, and thus lithofacies association and facies architecture, while floodplain deposits are primarily influenced by climate in the depositional basin (e.g., Miall, 1996). The negative $\delta^{18}O$ excursion recorded by rhizoliths is associated with up to 40-m-thick, vertically-stacked multi-storey channels deposited during an increase in sediment accumulation rate from 0.3 to 0.67 mm/a and terminates when accumulation rate increase rapidly to values of about 2 mm/a (Fig. 4.4C; Ballato et al., 2008). The occurrence of thick, coarse-grained, channelized sandstones was interpreted to reflect sedimentary facies progradation during high sediment influx, which outpaced the storage capacity of the proximal foreland in response to accelerated exhumation in the orogen at ~ 12 Ma (Guest et al., 2006b; Ballato et al., 2008). This implies higher fluvial system competence due to an increase in water discharge mainly derived from high elevation regions in the catchment areas. In soil profiles of arid to semiarid climates, soil water at depths > 0.5 m reflects the local mean annual precipitation, possibly slightly enriched in ^{18}O in response to evaporation and mixing with evaporated water in the shallow subsurface (e.g., Breecker et al., 2009). By contrast, isotopic composition of lacustrine/palustrine mudstones and carbonates should reflect river water and groundwater sourced from drainage basins at higher elevations, which is typically depleted in ^{18}O values (Dutton et al., 2005; Carroll et al., 2008). However, intense evaporation processes can cause ^{18}O enrichment of water in ponds and lakes leading to precipitation of calcite with more positive $\delta^{18}O$ values (e.g., Henderson and Shuman, 2009). The importance of evaporation in the foreland basin is also corroborated by the occurrence of mud cracks and gypsum-filled fractures (Fig: 4.4B). Therefore, while pedogenic carbonates recorded local rainfall composition, lacustrine/palustrine carbonates recorded rainfall composition of surrounding drainage basins with potential evaporation effect (e.g., Poage and Chamberlin, 2001; Rowley and Garzione, 2007). This is well expressed by our data where $\delta^{18}O$ values of paleosol samples between 11 and 10.3 Ma are systematically lower (up to 5‰) than palustrine samples (Fig. 4.4E). Collectively, the dominance of evaporation in the floodplain, the presence of thick multi-storey prograding channel bodies, and the negative $\delta^{18}O$ excursion in carbonate paleosols suggest that within an arid climate, an increase in precipitation occurred in both the sediment source area and the foreland basin. This increase occurred most likely during winter months when precipitations are generally depleted in δ^{18}O (Fig., 4.3; e.g., Vachon et al., 2007).

This increase in precipitation associated with the negative δ^{18}O excursion does not appear to reflect global-scale climate changes, because marine paleoclimate reconstructions show a monotonic late Tertiary global cooling trend starting at ~ 14.5 Ma (Zachos et al., 2001).

The variation in sediment accumulation rates, associated with the increase in precipitation, and the negative oxygen isotopic excursion suggest a causal link. If the source of water vapor was located in the Caspian Sea, a reduction in the orographic barrier elevation due to the exposure of easily erodible lithologies (Eocene volcaniclastic deposits) might have increased the southward penetration of moisture. The subsequent exposure of the more resistant shallow water Mesozoic limestones by 10.1 Ma (Ballato et al., in rev) could have triggered an increase in net elevation, which would have caused an increase in flexural subsidence as recorded (from 0.67 to 2.2 mm/a at 10.3 Ma; Fig 4.4C), and an efficient blockage of northerly moisture-bearing winds as suggested by the coeval termination of the negative isotopic excursion. If this interpretation fits variations in sediment accumulation rate and erosional unroofing trends, however, it raises two major questions: first, the oxygen isotopic excursion expected in case of elevation reduction of an orographic barrier should be positive and second, efficient erosion could trigger isostatic rebound possibly resulting in a net increase in elevation rather than a reduction (Molnar and England, 1990). Moreover, little of the rain formed in the elevated leeward clouds would reach the ground as it will fall through drier descending air masses and because of evaporation processes (e.g., Smith, 1982).

If the source of water vapor was located in Mediterranean regions, a change in the strength and/or in the pathway of the westerly winds might have caused the increase in precipitation. Regional-scale paleoclimatic reconstructions for southern Europe indicate that after relatively dry middle Miocene conditions, the precipitation level increased with a culmination between ca. 11 and 10 Ma (Van Dam, 2006; Böhme et al., 2008). This has been interpreted to reflect a relatively weak Subtropical High Pressure Zone, which led to the expansion of the European Temperate Wet Zone with anomalous cyclones over the eastern Mediterranean Sea (Van Dam, 2006, Böhme et al., 2008) likewise present-day processes (Eshel et al., 2000). A possible influence related to atmospheric variations induced by the Himalayan-Tibetan system cannot be excluded. However, it seems unlikely because major environmental and paleoclimatic changes in Asia and India occurred starting from ca. 9 Ma (Molnar, 2005). Therefore, the increase in precipitation on the southern slope of the orogen and in the foreland basin was most likely triggered by perturbation in atmospheric circulation patterns in the northern hemisphere, rather than variation in the orographic barrier elevation. This might have increased the efficiency of surface processes triggering enhanced tectonic exhumation in the Alborz range, syntectonic progradation of coarse-grained facies, and higher sediment influx in the foreland basin (e.g., Thiede et al., 2005; Densmore et al., 2007; Mora et al., 2008; Thiede et al., 2009). However, why the negative excursion ended with the subsequent increase in accumulation rate at 10.3 Ma is not clear. A possibility could be that the termination of this wetter phase (linked to atmospheric circulation factors) produced a decrease in the efficiency of surface processes, an increase in topographic elevation related to the exposure of more resistant rocks and finally, a significant increase in flexural subsidence.

4.4.4.3. Trend three, sub-units 3A and 3B (~10.3 to 7.6 Ma)

Between 3720 and 6455 m (sub-unit 3B, 10.3 to 7.6 Ma) lacustrine/palustrine samples show a tendency toward lower $\delta^{18}O$ values from 24.1±0.2 ‰ (1σ, n=21) to 23.3±1.0 ‰ (1σ, n=33), associated with an increase in data scattering, ranging from 21.5 to 25.3‰ (Fig. 4E). The negative trend of $\delta^{18}O$ values, up to 5‰ more negative than values for the lower part of the section once the rain shadow was established, together with the higher data variability suggests that significant variations in precipitation regime occurred from ca. 10 Ma. Interestingly, pedogenic carbonates of sub-unit 3B are more depleted in ^{18}O compared to Plio-Pleistocene and Quaternary calcrete samples collected from well-developed paleosol horizons in the Tehran region and adjacent areas, suggesting the re-establishment of more arid conditions sometime after the late Miocene (Table 4.3).

The progressive decrease in $\delta^{18}O$ is associated with significant changes in fluvial depositional style. Channel deposits of sub-units 1C and 2B are very wide (up to hundreds of meters), can be very thick (up to 40 m), are very well sorted, display a gentle down-cutting base, have complex filling pattern, and can represent multi-storey channels with rip-up clasts marking the base of each new channel (Figs. 4.4B and 4.5G). These strata present well developed macroforms, exhibit abrupt bounding surfaces on top, show a complex vertical and lateral stacking pattern, and are characterized by abundant centimeter- to meter-scale dewatering structures (Fig. 4.4B). The interbedded floodplain deposits can be locally dominant (up to hundreds of meters of thickness), display high mud/sand ratio, present abundant desiccation cracks, are characterized by poorly developed paleosols, and can have gypcretes (Figs. 4.4B and 4.5E). By contrast, channel deposits of sub-unit 3B are less extensive (a few tens of meters wide), less thick (up to 3 m), can be less sorted, and locally show a pronounced down-cutting base (Fig. 4.5H). These deposits display a simpler filling pattern, have poorly developed macroforms, and can exhibit a gradual transition to the overlying floodplain deposits (Fig. 4.5H). In addition, they are generally associated with single channels, and do not show dewatering structures and rip-up clasts (Fig. 4.4B). The interbedded floodplain deposits have a lower mud/sand ratio, are less thick (few tens of meters), do not contain desiccation cracks, and exhibit less frequent, but well developed paleosols (Figs. 4.4B and 4.5F).

These observations suggest that before ca. 10 Ma, the foreland basin was characterized by an arid to semiarid climate, with an ephemeral flash-flood style of sedimentation (rip-up clasts, dewatering structures, complex channel fill), most likely during enhanced rainfall in the sediment source areas, alternating with long dry seasons (desiccation cracks, evaporites, gypcretes) (Fig. 4.4B). These flooding events had high magnitude and low frequency similarly to present-day conditions of southern Iran, where heavy single rainfall events account for the greatest percentage of precipitation (Alijani and Harman, 1985). Starting from 10.3 Ma (deposition of sub-unit 3B), climatic conditions became less arid probably in response to increased intra and interannual rainfall seasonality (paleosols development, sand/mud ratio increase, channel width/thickness ratio decrease), associated with a decrease in flash-flood sedimentation, and with shorter dry seasons. This promoted an unstable and more dynamic depositional environment with lower magnitude and higher frequency flooding similarly to present-day conditions of northern Iran where many rainfall events of lower intensity occur (Alijani and Harman, 1985). Collectively, sedimentary climate indicators, oxygen isotopic scattering, and a δ^{18}O trend toward lower values suggest an increase in seasonality of precipitation, most likely during winter time when precipitation are more depleted in ^{18}O (Fig., 4.3), across both the sediment source area and the foreland basin (e.g, Smith et al., 1993; Vachon et al., 2007). These data seem to agree with our mineralogical study.

Southern Europe climate was characterized by pronounced dry seasons during the ca. 10-8 Ma interval and by ca. 5 Ma, alternated to wetter conditions between 8 and 7 Ma, probably in response to contraction/expansion of the Subtropical High Pressure Zone and associated expansion/contraction of the European Temperate Wet Zone (Van Dam, 2006). This situation does not appear to have influenced northern Iran, where a monotonic increase in precipitation level rather than an alternation of wet and dry climate occurred by ca. 10 Ma.

Alternatively, local-scale processes such as reduction of the orographic barrier elevation could be invoked. Our sandstone petrographic study, however, indicates that from 10.1 Ma, the highly resistant shallow water Mesozoic carbonates composing the inner and northern part of the orogen became exposed (Ballato et al., in rev.). Thus, significant reductions of elevation are not expected starting from that time.

Numerical modeling demonstrates that extensive high-elevation regions, such as the Tibetan plateau and the Himalaya, dictate atmospheric circulation patterns and climate (e.g., Kutzbach et al., 1989; Ruddiman and Kutzbach, 1989; Manabe and Broccoli, 1990; Broccoli and Manabe 1992; Raymo and Ruddiman, 1992). In particular, the growth of mountains related to the India-Asia continental collision modified the northern hemisphere atmospheric circulation system causing meandering and local blockage of the westerly low-level winds. This reduced moisture transport across the Eurasian interior triggering aridity and enhancing seasonality of precipitation as observed starting from ~ 9 to 6 Ma in Asia and India (Molnar, 2005). At present, at latitudes around 35°N low-level winter westerlies bifurcate in two branches over the Caspian Sea because of the Tibetan plateau topography (Fig. 4.1; e.g., Barry and Chorley, 1992; Liu and Yin, 2001). This seems to induce a southward shift of the westerlies with an increase in intra and interannual seasonality in precipitation in northern Iran as recorded by our sedimentological and isotopic data. However, why the westerlies perturbation occurred from ca. 10 Ma when most of Tibet had already attained an elevation similar to the present-day is not clear (e.g., Mulch and Chamberlin, 2006; Rowley and Currie, 2006). A recent plate tectonic reconstruction study document that India-Asia convergence rates decreased by more than 40% between 20 and 10 Ma probably in response to an increase in the mean elevation of the plateau of ca. 1 km, which induced the rapid outward growth of the plateau (Molnar and Stock 2009). This suggests that there might be a threshold either in elevation or in size (or both) of the plateau in triggering the hemispheric-scale rearrangement of circulation pattern with the establishment of present-day conditions. This assessment remains speculative until additional studies across Middle East and Asia are performed to evaluate the temporal and spatial extent of the late Miocene paleoenvironmental variations.

Similarly, the uplift of the Turkish-Iranian Plateau, which is thought to have occurred after 12 Ma (Dewey, 1986), might have influenced the pattern of the westerlies. A climate modeling study, however, show that most of the plateau influence occurs during summertime when heat-driven circulation inhibit precipitation (Zaitchik et al., 2007). Thus the Turkish-Iranian Plateau does not appear to have influenced the increase in seasonality recorded by ca. 10 Ma in the southern Alborz mountains.

TABLE 4.3: STABLE ISOTOPE ANALYSIS OF PLIO-PLEISTOCENE(?) AND QUATERNARY PALEOSOL SAMPLES FROM THERAN AND ADJACENT AREAS

Sample ID	δ^{18}O (SMOW)	δ^{13}C (PDB)	Age
CH08 07	22,98	-1,65	Plio-Pleistocene
CH08 06	24,70	-1,48	Plio-Pleistocene
CH08 05	22,83	-2,73	Plio-Pleistocene
CH08 04	21,45	-4,34	Plio-Pleistocene
CH08 03	22,05	-4,55	Plio-Pleistocene
CH08 02	22,68	-3,11	Plio-Pleistocene
CH08 01	22,50	-2,85	Plio-Pleistocene
CN04	23,18	-5,36	Quaternary
CN03	22,99	-8,77	Quaternary
CN02	22,91	-7,63	Quaternary
CN01	22,50	-7,69	Quaternary
IRA	23,69	-6,26	Quaternary

4.4.5 Carbon isotope ratios of pedogenic carbonates

Variations in δ^{13}C of pedogenic carbonates reflect soil CO_2 composition, which is either linked to photosynthetic pathways of local plants (C3 versus C4; e.g., Cerling and Quade 1993; Quade et al., 1995) or in arid climates, is linked to the soil respiration rate (a mixture between plant CO_2 and atmospheric CO_2; Quade et al., 2007a and 2007b). Soils dominated by C3 plants have pedogenic carbonates with δ^{13}C values of ~ -12 to -11 ‰, while soils dominated by C4 plants show $\delta^{13}C$ values of ~ 2 ‰ (e.g., Quade et al., 1995). C4 plants expanded globally between 8 and 6 Ma (Cerling et al., 1997), but they already coexisted with C3 plants since ~ 15 Ma in East Africa (Kingston et al., 1994), East Asia (Jia et al., 2003), and South America (MacFadden, et al., 1994; Blisniuk et al., 2005). Therefore, $\delta^{13}C$ values of pedogenic carbonates of -7 to -3 ‰ suggest either the existence of a mixed C3-C4 plant community or a strongly C3 dominated ecosystem with a relatively low soil respiration rate (Quade et al., 2007b).

The decrease in $\delta^{13}C$ of pedogenic carbonates from -3.7 to -6.7 ‰ between ~ 9.6 to 8.5 Ma (5150 to 6100 m) mimics the trend recorded by oxygen isotopes. The $\delta^{13}C$ trend would suggest either an increase in the proportion of C3 plants, or an increase in soil respiration rate. In both cases, this would imply an increase in soil water availability, in agreement with the oxygen data, which indicate less arid conditions with higher seasonality of precipitation. Finally, it should be noted that $\delta^{13}C$ values of soil carbonates are generally lower than those of mudstone. This is related to the decrease in $\delta^{13}C$ in soil CO_2 at depth, where pedogenic calcite precipitate, in contrast to calcite precipitation in mudstone, which occurs in ponds from evaporated water enriched in ^{13}C (e.g. Quade et al., 2007a).

4.5 Conclusions

Oxygen and carbon isotope data from Miocene continental sedimentary deposits of the southern Alborz mountains record the climatic, environmental and topographic evolution of this region in response to local, regional and global forcing factors. The positive 2 ‰ shift between 17.5 and 17.2 Ma recorded by both oxygen and carbon isotopes suggests that by that time the Alborz mountains became an efficient orographic barrier to moisture-bearing northerly winds and that a rain shadow was established. Between 11 and 10.3 Ma, a negative excursion of up to 5 ‰ in the oxygen isotopes suggests an increase in precipitation during a phase of enhanced rock exhumation in the orogen. This sharp excursion is coeval with a wetter climate in southern Europe, suggesting a perturbation of atmospheric circulation at the hemispheric scale. Wetter conditions promoted high sediment influx into the basin allowing syntectonic progradation of coarse-grained facies. Starting from ca. 10 Ma, both oxygen and carbon isotopes, together with clay mineralogy and sedimentary climate indicators show that the region evolved toward less arid conditions in association with an increase in seasonal precipitation. Importantly, this pattern is coeval with environmental and climatic changes recorded in Asia and India suggesting a link with the perturbations of the westerlies in response to processes affecting the Himalayan-Tibetan system. Overall, the variability of the stable isotope signals shown in this study highlights the importance of good constraints on sedimentological processes, sedimentation ages, sediment source areas, and paleotopography for a comprehensive and reliable paleoclimatic and paleoenvironmental.

Acknowledgements

This research was founded by the German Science Foundation (DFG) with a Leibniz Award to M. Strecker, a grant (STR 373/19-1) to M. Strecker and A. Friedrich, a grant to A. Mulch, and the graduate school program of the University of Potsdam. We are indebted to the Tehran Building and Housing Research Center, the municipality of Kilan, and Dr. M. Ghassemi for logistical support. M. Ahamadi and T. Roeper are kindly thanked for help with sampling and sample preparation. C. E. Uba is thanked for helping with field work. We are grateful to B. Bookhagen who kindly provided the TRMM data of figures 1 and 2. G. Frija, Y. Garcin, D.Scherler and J. Zamagni are thanked for fruitful discussions and suggestions that improved this work. T. Schildgen is thanked for her help with the text and constructive comments.

5. Conclusions

This study of tectonic, sedimentary, and climatic influences on the evolution of the central Alborz mountains and their foreland has resulted in a new understanding of the tectonic processes in the Arabia-Eurasia collision zone. For the first time, a chronology of sedimentary and tectonic processes based on rigorous magnetostratigraphic and sedimentologic analysis as well as (U-Th)/He and $^{40}Ar/^{39}Ar$ dating of key rock units can be presented. This helps unravel the complex and rich interactions between tectonic processes, the topographic growth, climate, and the surface-process regime. The results are summarized below and presented in a summary chart (Figure 5.1) and an evolutionary diagram (Figure 5.2)

In particular, this study allows for distinguishing climatic from tectonic forcing in the development of sedimentary architecture in a foreland basin system on 10^5 to 10^6 Ma time scales. As predicted by early modeling studies on sedimentary facies distribution in foreland-basin systems (e.g., Heller et al., 1998; Flemings and Jordan, 1990) and in more recent study in extensional basins (Densmore et al., 2007), a systematic correlation between coarsening upward cycles and accumulation rate was observed in the foreland strata of the Alborz mountains, with fine grained sedimentation coinciding with an increase in sediment accumulation rate (Figure 5.1 and 5.2). The analysis of the Alborz foreland shows that thrust loading induces maximum subsidence adjacent to the thrust belt where the coarse-grained sediment fraction supplied by the uplifting range is stored (sedimentary facies retrogradation), while fine-grained sediments are deposited in distal sectors of the foreland basin (Figure 5.1 and 5.2). These tectonic mechanisms can explain the observed sedimentary facies retrogradation in the absence of climatic forcing. In the case of a decrease in sediment flux due to climatic (decrease in precipitation) or lithologic factors (exposure of rocks with low erodibility), without a significant increase in tectonic subsidence, a similar sedimentary facies retrogradation would occur. However, the sediment accumulation rate would not increase as sharply as observed at the base of units 1, 2 and 3. Rather, two potential scenarios can be envisioned. First, sediment accumulation rate would decrease, because less sediment is routed into the basin (sediment load is reduced) or, as an alternative, rates may slightly increase, if the decrease in erosion rate allows building higher topography, promoting an increase in topographic load. A tectonic, rather than climatic forcing can be further corroborated by the results of the provenance study. During the thrusting phase, erosional unroofing phases and/or drainage pattern reorganization events are observed for units 1 and 3 at ~ 17 and ~ 10 Ma, respectively. In addition, it should be noted that the intensification of the rain-shadow effect is noted in the strata at the base of Unit 1 during enhanced subsidence at~ 17.2 Ma. This suggests that the thrust-loading phase, which triggered the onset of foreland basin sedimentation, generated sufficient relief to block moisture sourced in the Caspian Sea.

In contrast, the progradation of coarse-grained facies coincides with decrease in sediment accumulation rate (Figure 5.1 and 5.2). Intra-foreland uplift due to thrusting and folding induces a reduction in subsidence and possibly an increase in the depositional slope. This decrease in subsidence would cause extensive progradation in the distal part of the foreland of coarse-grained facies as observed in units 1 and 2 (Figure 5.1 and 5.2). Alternatively, a similar progradation would be observed in case of tectonic quiescence causing a decrease in tectonic subsidence with isostatic rebound, as predicted by numerical modeling studies (e.g., Heller et al., 1998; Flemings and Jordan, 1990; Densmore et al., 2007). These tectonic mechanisms can explain the observed progradation in the absence of climatic forcing. In case of increased sediment flux due to an increase in rainfall and a coeval increase in the efficiency of the surface-process regime or due to the exposure of easily erodible rocks without a significant decrease in tectonic subsidence, the progradation of coarse-grained facies would occur. However, the sediment accumulation rate is unlikely to decrease as sharply as observed for units 1 and 2. Rather, two potential scenarios that can be envisioned: sediment accumulation rates may increase, because more sediments enter the basin (sediment load increases), or, as an alternative, rates may slightly decrease if the increase in erosion rate triggers a reduction in topographic load and isostatic rebound.

Matters can be more complicated in case of a combined increase in surface-processes efficiency and tectonic deformation. During deposition of sub-unit 2B, between approximately ~ 11 and 10.3 Ma, the increase in sediment-grain size was associated with a pronounced increase in sediment accumulation rate. Stable C and O isotope data from calcareous paleosols show wetter climatic conditions for that interval (Figure 5.1). This is also in line with higher exhumation rates in the region from ~ 12 Ma, as shown by themochronologic data from the inner part of the orogen (Guest et al., 2006b). Thus, an increase in exhumation and precipitation in the orogenic realm may have triggered high subsidence, high sediment flux, and extensive syntectonic facies progradation in the Alborz foreland basin, highlighting a positive feedback mechanism between climate and tectonics. The provenance study using sandstone petrography and conglomerate clast counts corroborate the far-reaching effects of tectonic forcing in the sedimentary evolution of the Alborz foreland. The collected data show that intra-foreland uplift triggered sediment cannibalization and clast reworking, associated with growth strata and tilting, especially during deposition of sub-units 3B and 3C, when basin inversion occurred. While the overall evolution of the basin fill is determined by processes in the main range, it thus can be shown that intraforeland tectonic deformation can significantly modify the sedimentary architecture.

The presented analysis of the Alborz foreland-basin sediments also suggest that the channel-stacking patterns of prograding coarse-grained facies can help clarify tectonic and possible climatic forcing mechanisms. My study shows that in arid to semiarid environments with pronounced flash-flooding and corresponding deposits, the progradation of coarse-grained facies during an overall decrease in tectonic subsidence may result in a lateral stacking pattern (sub-Unit 1C and base of 2B). Conversely, an increase in sediment flux coupled with a wetter climate and associated with an increase in subsidence (thrust and sediment load) may promote a vertical stacking pattern (top of sub-Unit 2B). This channel-stacking pattern is not observed in sub-Unit 3B, because climatic conditions changed significantly during that depositional interval. In fact, the trends of oxygen and carbon stable isotopes in calcareous paleosols, together with sedimentary structures suggest that starting from 10-9 Ma, the climatic conditions underwent significant changes and the environment became less arid. Coupled with an increase in seasonality in the distribution of precipitation, this promoted a different style of sedimentation and fluvial architecture. More data on paleo-environmental conditions are needed for this region. However, my observations broadly fit with other regional observations. Pronounced environmental changes occurred in the Mediterranean Sea and Asia between ~ 9 and ~ 6 Ma (e.g., Molnar, 2005, Van Dam, 2006). Thus, in addition to topographic influences on the distribution of rainfall, the increase in seasonality in the Alborz range may also be related to variations in atmospheric circulation patterns in the Northern Hemisphere.

The results of my study have additional implications for the evolution of the Alborz mountains and the tectonic evolution of the entire Arabia-Eurasia continental collision zone. At the scale of the Alborz orogen, the relationships among sediment-accumulation rates, sedimentary facies, and stratal geometries within the Alborz foreland document that the locus of deformation did not move steadily southward, but rather stepped forward and backward through time since the Oligocene. In particular, during the middle to late Miocene, on time scales of ca. 0.7 to 2 Ma, the orogen expanded laterally by a combination of frontal accretion and internal wedge deformation. Moreover, in agreement with the results of a regional structural analysis (Landgraf et al., 2009), data from my provenance study of conglomerate clasts suggest that the shortening direction and creation of topography in the Alborz mountains shifted from NW-SE to NNE-SSW, most likely before the complete inversion of the foreland basin, which started between ~ 10 and 9 Ma.

On a regional temporal and spatial scale, this study allowed for the formulation of an alternative geodynamic model for the evolution of the sedimentary basins and their sediment provenance in the Alborz mountains. The numerous changes recorded by sedimentary basins in the Alborz mountains starting by ca. 36 Ma attest to fundamental changes in the tectonic boundary conditions. These include the termination of voluminous Eocene arc magmatism, a switch from submarine to restricted marine and terrestrial facies, regional tilting, a shift in sediment provenance from the southern volcanic arc to northern uplifting sectors, and trends in erosional unroofing (see chapter 3 for details). These changes were associated with a changeover from a tensional (transtensional) to a compressional (transpressional) tectonic setting. I suggest that these regional changes were triggered by the onset of subduction of the stretched Arabian continental lithosphere beneath central Iran, leading to moderate lower- and upper-plate deformation. This situation might have lasted for up to 20 Ma. In fact, the development of a foreland basin in the Alborz mountains beginning at ~ 17.5 Ma implies that significant upper-plate deformation must had already started by early Miocene time, most likely in response to an increase in the degree of plate coupling. This may have been related to the subduction of thicker continental lithosphere and the onset of hard continental collision. This new model reconciles the apparent 15-20 Ma lag time between late Eocene to early Oligocene age of the initial Arabia-Eurasia continental collision and the onset of regionally widespread deformation across the collision zone to the north in early to late Miocene time.

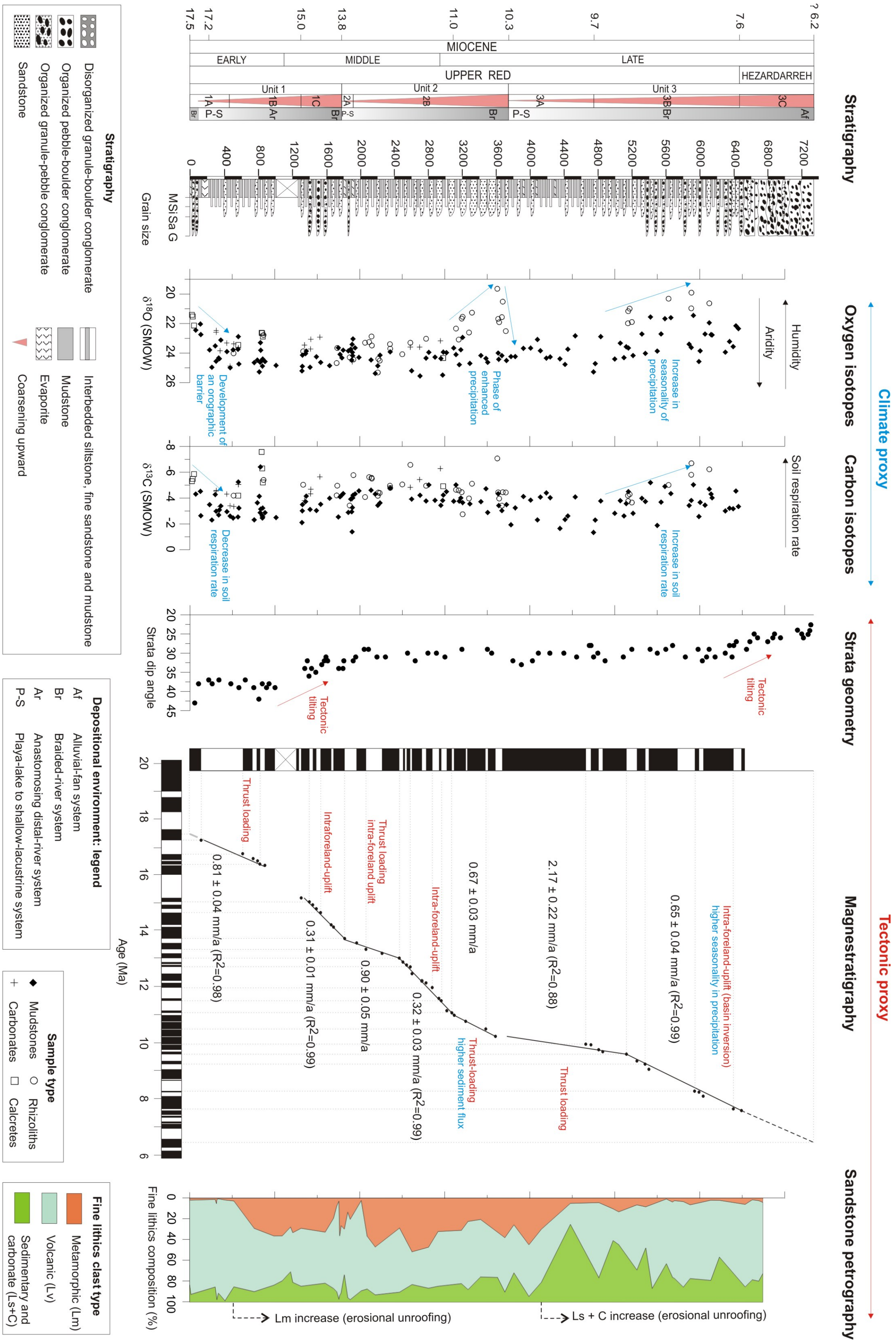

Figure 5.1: Summary chart, showing stratigraphy, stable isotope data, stratal dip-angle variations, magnetostratigraphy, and sandstone petrography.

Sub-unit 3A and base of 3B (10.3-9.6 Ma): very high sediment accumulation rate (2.2 mm/a), thrust loading, sedimentary facies retrogradation, erosional unroofing or drainage pattern reorganization

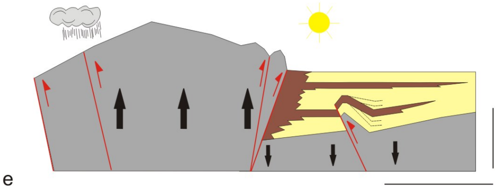

Sub-unit 3B and 3C (9.6-6.2? Ma): moderate sediment accumulation rate (0.6 mm/a), basin inversion, sedimentary facies progradation, sediment cannibalization, clast reworking, erosional unroofing, decrease in aridity, increase in seasonal precipitation possibly related to perturbation in atmospheric circulation pattern in Northern Hemisphere

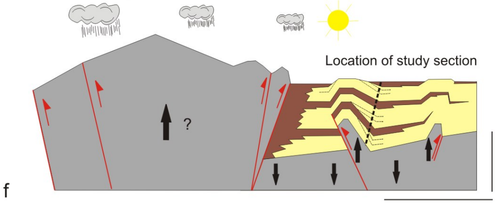

Sub-unit 2A and base of 2B (13.8-11 Ma): high sediment accumulation rate (0.9 mm/a), thrust loading associated with intra-foreland uplift, growth strata, sedimentary facies retrogradation

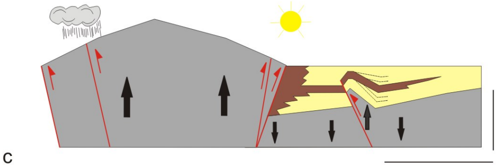

Top of sub-unit 2B (11-10.3 Ma): moderate sediment accumulation rate (0.7 mm/a), extensive sedimentary facies progradation, thrust loading coupled with enhanced precipitation, high sediment influx possibly related to perturbation in atmospheric circulation pattern in Northern Hemisphere

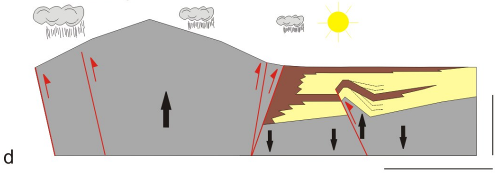

Sub-unit 1A and 1B (17.5-15.2 Ma): high sediment accumulation rate (0.8 mm/a), thrust loading, foreland basin initiation, sedimentary facies retrogradation, erosional unroofing and/or drainage pattern reorganization, development of an efficient orographic barrier to moisture-bearing northerly winds

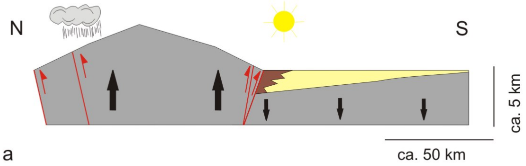

Sub-unit 1C (15.2-13.8 Ma): low sediment accumulation rate (0.3 mm/a), intra-foreland uplift, strata truncation, sedimentary facies progradation

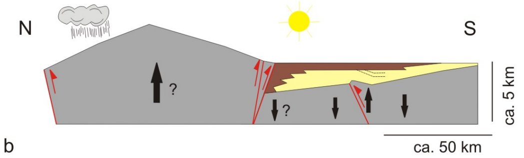

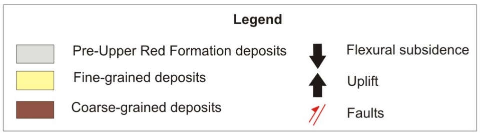

Figure 5.2: Evolutionary diagram showing the tectonic and climatic evolution of southern Alborz foreland basin during Miocene time. Faults pattern in the wedge is simplified.

References

Agard, P, Omrani, J., Jolivet, L., and Mouthereau, F., 2005: Convergence history across Zagros (Iran): constraints from collisional and earlier deformation: International Journal of Earth Science: v. 94, p. 401-419.

Aghanabati, A., and Hamedi, A.R, 1994, Geological map of Semnan quadrangle: Geological Survey of Iran, scale 1:250,000, 1 sheet.

Al-Damegh, K., Sandvol, E., and Barazangi, M., 2005, Crustal structure of the Arabian Plate: 456 new constraints from the analysis of teleseismic receiver functions: Earth Planet. Science Letters, 231, 177-196.

Alijani, B., 2002, Variations of 500 hPa flow patterns over Iran and surrounding areas and their relationship with the climate of Iran: Theoretical and Applied Climatology, v.72, p. 41-54.

Alijani B., and Harman, J.R, 1985, Synoptic climatology of precipitation Iran: Annals of the associations of American geographers, v. 75, p. 404-416.

Alijani, B., O`Brien, J, and Yarnal, B., 2007, Spatial analysis of precipitation intensity and concentration in Iran: Theoretical and Applied Climatology, v.94, p. 107-124.

Alinaghi, A., Koulakov, I., and Thybo, H., 2007, Seismic tomographic image of P- and S-waves velocity perturbations in the upper mantle beneath Iran: Geophysical Journal International, v. 169, p. 1089-1102.

Allen, P.A., and Allen, J.R., 2005, Basin Analysis: Principles and Applications, Second Edition, Blackwell Publishing, Oxford, 549p.

Allen, M.B., and Armstrong, H.A., 2008, Arabia–Eurasia collision and the forcing of mid-Cenozoic global cooling: Paleogeography, Paleoclimatology, Paleoecology, v. 265, p.52-58.

Allen, M., Ghassemi, M.R., Shahrabi, M., and Qorashi M., 2003, Accommodation of late Cenozoic oblique shortening in the Alborz range, northern Iran: Journal of Structural Geology, v. 25, p. 659-672.

Allen, M., Jackson, J., and Walker, R., 2004, Late Cenozoic reorganization of the Arabia-Eurasia collision and the comparison of short-term and long term deformation rates: Tectonics, v. 23, p. TC2008, p. 1-16.

Allen, M. B., Jones, S., Ismail-Zadeh, A., Simmons, M.D., and Anderson, L., 2002, Onset of subduction as the cause of rapid Pliocene-Quaternary subsidence in the South Caspian Basin: Geology, v. 30, p.775-778.

Ahmadian, J., Haschke, M., McDonald, I., Regelous, M., RezaGhorbani, M., Emami, H., and Murata, M. 2009, High magmatic flux during Alpine-Himalayan collision: constraints from the Kal-e-Kafi complex, central Iran: Geological Society of America Bulletin, v. 121, p. 857-868.

Amidi, S.M., 1984, Geological map of Saveh quadrangle: Geological Survey of Iran, scale 1:250,000, 1 sheet.

Amini, A, 1997, Provenance and depositional environment of Upper Red Formation, central zone, Iran [PhD. Thesis], University of Manchester, 320 p.

Amini, B, H. Rashid, M. Rezaian, S. Allahmadadi, M. R. Zabihi, B. Vahdati Daneshmand, and M. Haddadan (2004), Geological map of Iran, Garmsar sheet, scale 1:100,000, Geol. Surv. of Iran, Tehran.

Armstrong, F.C., and Oriel, S.S., 1965, Tectonic development of Idaho-Wyoming thrust belt: America Association of Petroleum Geology Bulletin, v. 49, p. 1847-1866.

Assereto, R., 1966, Explanatory notes on the geological map of Upper Djadjerud and Lar Valleys (Central Elburz, Iran): Institute of Geology, University of Milan, Italy, scale 1:50.000, p. 86.

Axen, G.J., Lam, P.J., Grove, M., Stockli, D.F., and Hassanzadeh, J., 2001, Exhumation of the west-central Alborz mountains, Iran, Caspian subsidence, and collision-related tectonics: Geology, v. 29, p. 559-562,

Ballato, P. Cruciani, G., Dalconi, M.C., Fabri, B., and Macchiarola, M., 2005, Mineralogical study of historical bricks from the Great Palace of Byzantine Emperors in Istanbul based on powder X-ray diffraction data: European Journal of Mineralogy, v. 17, p. 777-.784.

Ballato, P., Nowaczyk, N.R., Landgraf, A., Strecker, M.R., Friedrich, A., and Tabatabaei, S.H. 2008, Tectonic control on sedimentary facies pattern and sediment accumulation rates in the Miocene foreland basin of the southern Alborz mountains, northern Iran: Tectonics, v. 27, TC6001

Ballato P., Uba C.E., Landgraf, A., Strecker M., Sudo, M., Stockli, D.F., Friedrich A., and Tabatabaei, S.H., (in review), Arabia-Eurasia continental collision: insights from late Tertiary foreland-basin evolution in the Alborz mountains, northern Iran

Barazangi, M., and Isacks, B.L., 1976, Spatial distribution of earthquakes and subduction of the Nazca plate beneath South America: Geology, v. 4, p. 686-692

Barry, R.G., and Chorley, R.J., 1992, Atmosphere, weather and Climate, Sixth edition, Routledge, London, 416p.

Beaumont, C., Nguyen, M. H., Jamienson, R., A., and Ellis, S., 2006, Crustal flow modes in large hot orogens, in: Law, R.D., Searle, M.P., and Godin, L., eds, Channel Flow, Ductile Extrusion and Exhumation in Continental Collision Zones. Geological Society, London, Special Publications, v. 268, p. 91–145.

Berberian, M., and King, G.C.P., 1981, Towards a paleogeography and tectonic evolution of Iran: Canadian of Journal Earth Science, v. 18, p. 210-265.

Berberian, M., and Yeats, R.S., 1999, Patterns of historical earthquake rupture in the Iranian Plateau: Bulletin of Seismological Society of Am.erica, v.89, p.120–139.

Bijwaard, H., Spakman,W. and Engdahl, E.R., 1998, Closing the gap between regional and global travel time tomography: Journal of Geophysical . Research, v. 103, p. 30 055–30 078,

Bish, D.L. and Howard, S.A., 1988, Quantitative phase analysis using the Rietveld method: Journal of Applied Crystallography, v.21, p.86-91.

Bish, D. L. and J. B. Post, 1993, Quantitative mineralogical analysis using the Rietveld full-pattern fitting method: American Mineralogist. v. 78, p. 932-940.

Blair, T.C., 1999, Sedimentology of the debris-flow-dominated Warm Spring Canyon alluvial fan, Death Valley, California: Sedimentology, v. 46, p. 941-965.

Blisniuk, P.M., Stern, L.A., Chamberlain, C.P., Idleman, B., and Zeitler, P.K., 2005, Climatic and ecologic changes during Miocene surface uplift in the southern Patagonian Andes: Earth and Planetary Science Letters, v. 230, p. 125–142.

Blisniuk P.M., Stern L.A., 2005, Stable isotope paleoaltimetry: a critical review: American Journal of Science, v. 305, p. 1033-1074.

Böhme, M., Ilg, A., and Winklhofer, M., 2008, Late Miocene “washhouse” climate in Europe: Earth and Planetary Science Letters, v. 275, p. 393-401.

Bookhagen, B. and Strecker, M.R., 2008, Orographic barriers, high-resolution TRMM rainfall, hillslopes angles, and relief variations along the eastern Andes: Geophysical Research Letters, v. 35, L06403, p. 1-6.

Boulton S.J., and Robertson, A.H.F., 2007, The Miocene of the Hataya area, STurkey: transition from the Arabian passive margin to an underfilled foreland basin related closure of the Southern Neotethys Ocean: Sedimentary Geology, v. 198, p. 93-124.

Bozorgnia, F., 1966, Qom formation stratigraphy of the Central Basin of Iran and its intercontinental position: Bulletin of Iranian Petroleum Institute, v. 24, p. 69-75.

Breecker, D.O., Sharp, Z.D., and McFadden, L.D, 2009, Seasonal bias in formation and stable isotope composition of pedogenic carbonate in modern soils from central New Mexico, USA: Geological Society of American Bulletin, v. 121, p. 630-640.

Bridge, J.S, 2003, Rivers and floodplains: forms, processes and sedimentary record: Oxford, Blackwell Science Ltd, 491 p.

Broccoli, A.J., and Manabe, S., 1992, The effects of orography on midlatitude northern hemisphere dry climates. Journal of Climate, v, 5, p. 1181–1201.

Brozović, N., and Burbank, D.W., 2000, Dynamic of fluvial system and gravel progradation in the Himalayan foreland: Geological Society of America Bulletin, v. 112, p. 394-412.

Bruker AXS 2003. Topas V3.1: General Profile and Structure Analysis Software for Powder Diffraction Data ed. Bruker AXS, Karlsruhe.

Brunet, M. F., Korotaev, M.V., Ershov, A.V., and Nikishin, A.M., 2003, The South Caspian Basin: A review of its evolution from subsidence modeling: Sedimentary Geology, v. 156, p. 119-148.

Buatois L.A., and Mangano, M.G., 2002, Trace fossils from Carboniferous floodplain deposits in western Argentina: implications for ichnofacies models of continental environments: Palaeogeography, Palaeoclimatology, Palaeoecology, v. 183, p. 71-86.

Bullen, M. E., Burbank, D.W., Garver, J.I., and Abdrakhmatov, K.Y. (2001), Late Cenozoic tectonic evolution of the northwestern Tien Shan: new age estimates for the initiation of mountain building: Geological Society of America Bulletin, 113, 1544 – 1559.

Burbank, D.W., 1992, Causes of recent Himalayan uplift deduced from deposited patterns in the Ganges basin: Nature, v. 357, p. 680 – 682.

Burbank, D.W., Beck, R.A., Raynolds, R.G.H, Hobbs, R., and Tahirkheli R.A.K., 1988, Thrusting and gravel progradation in foreland basins: A test of post-thrusting gravel dispersal: Geology, v. 16, p. 1143-1146.

Burgess, P.L., and Moresi L.N., 1999, Modeling rates and distribution of subsidence due to dynamic topography over subducting slabs: Is it possible to identify dynamic topography from ancient strata?: Basin Research., v. 11, p. 305–314.

Burst, J.F., 1965, Subaqueously formed shrinkage cracks in clay: Journal of Sedimentary Research, v. 35, p. 348-353.

Burtman, V.S., and Molnar, P., 1993, Geological and geophysical evidence for deep subduction of continental crust beneath the Pamir: Special Publication of Geological. Society of America, v. 281, 76 p.

Butler, R.F., 1992, Paleomagnetism: Magnetic Domains to Geologic Terranes: , Boston, MA, Blackwell Scientific Publications, 319 p.

Cande, S.C., and Kent D.V., 1995, Revised calibration of the geomagnetic polarity time scale for the Late Cretaceous and Cenozoic: Journal of Geophysical Research, v. 100, p. 6093-6095.

Carrapa, B., DeCelles, P.G., Reiners, P.W., Gehrels, G.E., and Sudo, M., 2009, Apatite triple dating and white mica ^{40}Ar/^{39}Ar thermochronology of syntectonic detritus in the Central Andes: A multiphase tectonothermal history: Geology, 37, p. 407-410.

Carroll, A.R., Chetel, L.M., and Smith, M.E., 2006, Feast to famine: sediment supply control on Laramide basin fill: Geology, v. 34, p. 197-200, d.

Carroll, A.R., Doebbert, A.C., Booth, A.L., Chamberlain,C.P., Rhodes-Carson, M., Smith, E., Johnson, C.M., and Beard, B.L., 2008, Capture of high altitude precipitationby a low altitude Eocene lake, western U.S.: Geology, v. 36, p. 791–794.

Cederbom, C.E., Sinclair, H.D., Schlunegger, F., and Rahn, M.K., 2004, Climate-induced rebound and exhumation of the European Alps: Geology, v. 32, p. 709-712, .

Cerling, T.E., Harris, J.M., MacFadden, B.J., Leakey, M.G., Quade, J., Eisenmann, V., and Ehleringer, J.R., 1997, Global vegetation change through the Miocene/Pliocene boundary: Nature, v. 389, p. 153–158.

Cerling TE, Quade J (1993) Stable carbon and oxygen isotopes in soil carbonates. *In:* Continental Indicators of Climate. Swart P, McKenzie JA, Lohman KC (eds) Proceedings of Chapman Conference, Jackson Hole, Wyoming, American Geophysical Union Monograph 78:217-231

Cerling, T.E., 1984, The stable isotopic composition of modern soil carbonate and its relation to climate: Earth and Planetary Science Letters, v. 71, p. 229-240.

Chamley, H., 1989, Clay sedimentology: Berlin, Springer-Verlag, 623p.

Charreau, J., Chen, Y., Gilder, S., Dominguez, S., Avouac, J.P., Sen S., Sun, D.J., Li, Y.A., and Wang, M.W., 2005, Magnetostratigraphy and rock magnetism of the Neogene Kuitun He section (northwest China): Implications for late Cenozoic uplift of the Tian Shan mountains: Earth and Planetary Science Letters, v. 230, p. 177-192.

Chemenda A.I., Burg, J.P., and Mattauer, M., 2000, Evolutionary model of the Himalaya Tibet system: geopoem: based on new modelling, geological and geophysical data: Earth and Planetary Science Letters, v.174, p. 397-409.

Clevis, Q., de Jager, G., Nijman, W., and de Boer, P.L., 2004, Stratigraphic signatures of translation of thrust-sheet top basins over low-angle detachment faults: Basin Research, v. 16, p. 145-163.

Clift, P.D., 2006, Controls on the erosion of Cenozoic Asia and flux of clastic sediment in the ocean: Earth and Planetary Science letters, v. 241, p. 571-580, doi:10.1016/j.epsl.2005.11.028

Clift, P.D., Hodges, K.V., Heslop, D., Hanningan, R., Van Long, H., and Calves, G., 2008, Correlation of Himalayan exhumation rates and Asia monsoon intensity: Nature Geoscience, v. 1, p.875-880.

Copley, A., and J. Jackson (2006), Active tectonics of the Turkish-Iranian Plateau; Tectonics, 25, TC6006, p. 1-19.

Coutand, I., Carrapa, B., Deeken, A., Schmitt, A.K., Sobel, E.R., and Strecker, M.R., 2006, Orogenic plateau formation and lateral growth of compressional basins and ranges: insights from sandstone petrography and detrital apatite fission-track thermochronology in the Angastaco Basin, NW Argentina: Basin Research, v. 18, p. 1–26.

Dahlen, F.A., 1990, Critical taper model of fold-and-thrust belts and accretionary wedges: AnnualRev. Earth Planet. Sci., v. 88, p. 55-99,.

Daneshian, J., and Ramezani Dana, L., 2007, Early Miocene benthic foraminifera and biostratigraphy of the Qom Formation, Deh Namak, Central Iran: Journal of Asian Earth Science, v. 29, p. 844-858.

Dayem, K.E.P., Molnar, P., Clark, M.K., and Houseman G.A., 2009, Far-field lithospheric deformation in Tibet during continental collision: Tectonics, v. 28, TC6005, p. 1-8.

Davila, M.F., and Astini, R.A., 2007, Cenozoic provenance history of synorogenic conglomerates in western Argentina (Famatina belt): Implications for Central Andean development: Geological Society of America Bulletin, v. 119, p. 609-622.

Davis, D., Suppe, J., and Dahlen, F.A., 1983, Mechanics of fold-and-thrust belts and accretionary wedges: Journal of Geophysical Research, v. 88, p.1153–1172.

Davis, J.H., and von Blanckenburg, F., 1995, Slab breakoff: A model of lithosphere detachment and its test in the magmatism and deformation of collisional orogens: Earth and Planetary, Science letters, v. 129, p. 85-102.

Davoudian, A.R., Genser, J., Dachs, E., and Shabanian, N., 2008, Petrology of eclogites from north of Shahrekord, Sanandaj-Sirjan zone, Iran: Mineralogy and Petrology, v. 92, p. 393-413.

Davoudzadeh, M., Lammerer, B., and Weber-Diefenbach, K., 1997, Paleogeography, stratigraphy, and tectonics of the Tertiary of Iran: Neues Jahrbuch für Geologie und Paläontologie Abhandlungen, v. 205, p. 33-67.

DeCelles, P.G., Gehrels, G.E, Najiman, Y., Martin, A.J., Carter, A., and Garzanti, E., 2004, Detrital geochronology and geochemistry of Cretaceous–Early Miocene strata of Nepal: implications for timing and diachroneity of initial Himalayan orogenesis: Earth and Planetary Science letters, v. 227, p. 313-330.

DeCelles, P.G., and Giles, K.A., 1996, Foreland basins systems: Basin Research, v. 8, p. 105-123.

DeCelles, P.G., Gray, M.B., Ridgway, K.D., Cole, R.B., Srivastava, P., Pequera, N.and Pivnik, D.A., 1991, Kinematic history of a foreland uplift from Paleocene synorogenic conglomerate, Beartooth Range, Wyoming and Montana: Geological Society of America Bulletin, v. 103, p. 1458–1475.

De Franco, R., Govers, R., and Wortel, R., 2008, Dynamics of continental collision: influence of plate contact: Geophysical Journal International, v. 174, p. 1101-1120.

Dehghani, G. A., and Makris, J.,1984, The gravity field and crustal structure of Iran: Neues Jahrbuch für Geologie und Palaontologie Abhandlungen, v. 168, no. 2/3, p. 215–229.

Densmore A.L., Allen, P.A., and Simpson, G., 2007, Development and response of a coupled catchment fan system under changing tectonic and climatic forcing: Journal of Geophysical Research, v. 112, p. F01002, p. 1-16.

Dettman, D.L., Fang, X., Garzoine, C.N., and Li, J., 2003, Uplift-driven climate change at 12 Ma: a long δ18O record from the NE margin of the Tibetan Plateau: Earth and Planetary Science Letters, v. 214, p. 267–277.

Dewey, J.F., Hempton, M.R., Kidd, W.F.S., Saroglu, F., and Şengör, A.M.C., 1986, Shortening of continental lithosphere: The tectonics of eastern Anatolia, A young collision zone: Geological Society of America, Special Publication, v. 19, 3 – 36.

Dewey, J.F., Pitman III, W.C., Ryan, W.B.F., and Bonnin, J., 1973, Plate Tectonics and the Evolution of the Alpine System: Geological Society of America Bulletin, v. 84, p. 3137– 3180.

Dickinson, W.R., 1974, Plate tectonics and sedimentation, in: Dickinson W.R., eds, Tectonics and Sedimentation, Special Publication Society Economic Paleontologists & Mineralogists, 22, 1-27, Tulsa, Oklahoma.

Dutton, A., Wilkinson, B.H., Welker, J.M., Bowen, G.J., and Lohmann, K.C., 2005, Spatial distribution and seasonal variation in 18O/16O of modern precipitation and river water across the conterminous USA: Hydrological Processes, v. 19, p. 4121–4146.

Eberhart-Phillips, D., Reyners, M.E., 1997, Continental subduction and three-dimensional crustal structure the northern South Island, New Zealand: .Journal of Geophysical Research, v. 102(B6), p. 11843-11861.

Echavarría, L., Hernández, R., Allmendinger, R.W., and Reynolds, J., 2003, Subandean thrust and fold belt of northwestern Argentina: Geometry and timing of the Andean evolution: America Association of Petroleum Geology Bulletin, v. 87, p. 965-985.

Ehlers T.A., and Poulsen, C.J., 2009, Influence of Andean uplift on climate and paleoaltimetry estimates: Earth and Planetary Science Letters, v. 281, p. 238-248.

Ernst, W.G., 1999, Horneblende, the continent marker-Evolution of H_2O_2 during circum-Pacif subduction versus continental collision: Geology, v.27, p. 675-678.

Ershov, A.V., Brunet, M.F., Nikishin, A.M., Bolotov, S.N., Nazarevich, B.P., and Korotaev, M.V., 2003, Northern Caucasus basin: Thermal history and synthesis of subsidence models: Sedimentary Geology, 2006, v.156, p. 95–118.

Eshel, G., and Farrell, B.F., 2000, Mechanism of Eastern Mediterranean rainfall variability: Journal of the Atmospheric Sciences, v. 57, p. 3119- 3232.

Faccenda, M., Minelli, G., and Gerya, T.V., 2009, Coupled and decoupled regimes of continental collision: numerical modeling: Earth and Planetary Science Letters, v. 278, p. 337-349.

Fakhari, M.D., Axen, G.J., Horton, B.K., Hassanzadeh, J., and Amini, A., 2008, Revised age of proximal deposits in the Zagros foreland basin and implications for Cenozoic evolution of the High Zagros: Tectonophysics, v. 451, p. 170-185.

Fan, G., Wallace, T., and Zhao, D., 1998, Tomographic images of deep velocity structure beneath the Eastern and Southern Carpathians, Romania: implications for continental collision: Journal of Geophysical Research, v. 103, p. 2705–2723.

Farzipour-Saein, A, Yassaghi, A., Sherkati, S. and Koyi H., 2009, Basin evolution of the Lurestan region in the Zagros fold-and-thrust belt, Iran: Journal of Petroleum Geology, v. 32, p. 5-20.

Flemings, P.B., and Jordan, T.E., 1990, Stratigraphic modeling of foreland basins: interpreting thrust deformation and lithosphere rheology: Geology, v. 18, p. 430-434.

Garzanti, E., 2008, When and were did India and Asia collide?: Comment: Journal of Geophysical Research, v. 113, B04411, p. 1-4.

Garzanti, E., Doglioni, C., Vezzoli, G., and Andó, S, 2007, Orogenic belts and orogenic sediment provenance: The Journal of Geology, v. 115, p. 315-334.

Garzione, C.N., Dettman, D.L., and Horton, B.K., 2004. Carbonate oxygen isotope paleoaltimetry: evaluating the effect of diagenesis on paleoelevation estimates for the Tibetan plateau: Palaeogeography Palaeoclimatology Palaeoecology, v. 212, p. 119–140.

Garzione, C.N., Hoke, G.D., Libarkin, J.C., Withers, S., MacFadden, B., Eiler, J., and Mulch, A., 2008, The Rise of the Andes: Science, v. 320, p. 1304-1307.

Garzione, C.N., Molnar, P., Libarkin, J.C, MacFadden, B.J., 2006, Rapid late Miocene rise of the Bolivian Altiplano: Evidence for removal of mantle lithosphere: Earth and Planetary Science Letters, 241, p. 543-556,.

Gilder, S., Chen, Y., and Sen S., 2001, Oligo-Miocene magnetostratigraphy and rock magnetism of the Xishuigou section, Subei (Gansu Province, western China) and implications for shallow inclinations in central Asia: Journal of Geophysical Research, v. 106 (30), p505-30,521.

Guest, B., Axen, G.J., Lam, P.S., and Hassanzadeh, J., 2006a, Late Cenozoic shortening in the west central Alborz mountains, northern Iran, by combined conjugate strike-slip and thin-skinned deformation: Geosphere, v. 2, p. 35-52.

Guest, B., Guest, A. and Axen, G.J., 2007, Late Tertiary tectonic evolution of northern Iran: A case for simple crustal folding: Global Planetary Change, v.58, p.435–453.

Guest B., Horton, B.K., Axen, G.J.; Hassanzadeh, J., and McIntosh, W.C., 2007, Middle to late Cenozoic basin evolution in the western Alborz Mountains: Implications for the onset of collisional deformation in northern Iran: Tectonics, v. 26, p. TC6011, p. 1-26.

Guest, B., Stockli, D.F., Grove, M., Axen, G.J., Lam, P.S, and Hassanzadeh, J., 2006b, Thermal histories from the central Alborz mountains, northern Iran: Implications for the spatial and temporal distribution of deformation in northern Iran: Geological Society of America Bulletin, v. 118, p. 1507-152.

Guillot, S., Garzanti, E., Baratoux, D., Marquer, D., Mahéo, G., and de Sigoyer, J., 2003, Reconstructing the total shortening history of the NW Himalaya: Geochemistry Geophysics Geosystems, v. 7, 1064, p. 1-22.

Guo, Z., Wilson, M., and Liu, J, 2007, Post-collisional adakites in south Tibet: products of partial melting of subduction-modified lower crust: Lithos, v. 96, p. 205-224.

Gurnis, M., 1992, Rapid continental subsidence following the initiation and evolution of subduction: Science, v. 255, p. 1556–1558.

Hafkenscheid, E., Wortel, M.J.R., and Spakman, W, 2006, Subduction history of the Tethyan region derived from seismic tomography and tectonic reconstructions: Journal of Geophysical Research, v. 111, B08401, p. 1-26.

Haghipour, A., Taraz, H, and Vahdati Daneshmand, F., 1987, Geological map of Tehran quadrangle: Geological Survey of Iran, scale 1:250,000, 1 sheet.

Harzhauser, M., Piller,W.E., Steininger, F.F., 2002. Circum-Mediterranean Oligo-Miocene biogeographic evolution — the gastropods' point of view: Palaeogeography Palaeoclimatology Palaeoecology, v. 183, p. 103–133.

Heermance R.V., Chien, J., Burbank, D.W., and Wang, C., 2007, Chronology and tectonic controls of Late Tertiary deposition in the southwestern Tian Shan foreland, NW China: Basin Research, v. 19, p. 599-632.

Heller, P.L., Angevine, C.L., Winslow, N.S., and Paola, C., 1988, Two-phase stratigraphic model of foreland basin sequences: Geology, v. 16, p. 501-504.

Henderson A.K., and Shuman, B.N., 2009, Hydrogen and oxygen isotopic compositions of lake water in the western United States: Geological Society of American Bulletin, v. 121, p. 1179-1189.

Hessami, K., Koyi, H.A., Talbot, C.J., Tabasi, H., and Shabanian, E., 2001, Progressive unconformities within an evolving foreland fold-thrust belt, Zagros Mountains: Journal of the Geological Society, v. 158, p. 969–981.

Hill, R.J., 1991. Expanded use of the Rietveld method in studies of phase abundance in multiphase mixtures: Powder Diffraction, v. 6 (2), p. 74–77.

Hilley, G.E., Blisniuk, P., and Strecker M.R., 2005, Mechanics and erosion of basement-cored uplift provinces: Journal of Geophysical Research, Solid Earth, v. 110, p. B12409, p. 1-22

Hoffman, P.F., and Grotzinger, J.P., 1993, Orographic precipitation, erosional unloading, and tectonic style: Geology, v. 21, p. 195-198.

Hogg, S.E., 1982, Sheetfloods, Sheetwash, Sheetflow, or...?: Earth Science Reviews, v.18, p. 59-76.

Hollingsworth, J., Jackson, J., Walker, R., Geitanchi, M. and Bolourchi, M., 2006, Strike-slip faulting, rotation, and along-strike elongation in the Kopeh Dagh mountains, NE Iran: Geophysical Journal International, v. 166, p. 1161-1177.

Hollingsworth, J., Jackson, J., Walker, R., Nazari, H., 2009, Extrusion tectonics and subduction in the eastern South Caspian region since 10 Ma: Geology, v. 36, p. 763-766.

Homke, S., Verges, J., Garces, M., Emami, M., and Karpuz, R., 2004, Magnetostratigraphy of Miocene-Pliocene Zagros foreland deposits in the front of the Push-e-Kush Arc (Lurestan Province, Iran): Earth and Planetary Science Letters, v. 225, p. 397–410.

Homke, S., Verges, J., Serra-Kiel, J., Bernaola, G., Sharp, I., Garcés, M., Monetro-Verdú I., Karpuz, R., and Goodarzi, M.H., 2009, Late Cretaceous Paleocene formation of the proto-Zagros foreland basin, Lurestan Province, SW Iran: Geological Society of America Bulletin, v. 121, p. 963-978.

Horton, B.K., and DeCelles, P.G., 2001, Modern and ancient fluvial megafans in the foreland basin system of the central Andes, southern Bolivia: Implications for drainage network evolution in fold-thrust belts: Basin Research, v. 13, p. 43-63.

Horton, B.K., Hassanzadeh, J., Stockli, D.F., Axen, G.J, Gillis, R.J., Guest, B., Amini, A., Fakhari, M.D., Zamanzadeh, S.M., and Grove, M., 2008, Detritial zircon provenance of Neoproterozoic to Cenozoic deposits in Iran: implications for chronostratigraphy and collision tectonics: Tectonophysics, v. 451, p. 97-122.

Hoth, S., Adam, J., Kukowski, N., and Oncken, O., 2006, Influence of erosion on the kinematics of bivergent orgens. results from scaled sandbox simulations, in: S. Willett et al., eds, Tectonics, Climate and Landscape Evolution, Penrose Conference Series, Spec. Pap. Geol. Soc. Am., v. 398, p. 201–225.

Hoth, S., Hoffmann-Rothe, A., and Kukowski N., 2007, Frontal accretion: An internal clock for bivergent wedge deformation and surface uplift: Journal of Geophysical Research, v. 112, p. B06408, p. 1-17.

Huntington, K.W., Ehlers, T.A., Hodges, K.V, Whipp, D.M., Jr., 2007, Topography, exhumation pathway, age uncertainties, and the interpretation of thermochronometer data: Tectonics, v. 26, TC4012, p. 1-23.

Jackson, J. A., and D. P. McKenzie (1984), Active tectonics of the Alpine-Himalayan belt between western Turkey and Pakistan: Geophysical Journal of the Royal Astronomical Society, v. 77, p. 185-264,

Jackson, J., Haines, J., and Holt, W., 1995, The accommodation of Arabia-Eurasia plate convergence in Iran: Journal of Geophysical Research, v. 100, p. 15,205-15,219.

Jackson, J., Priestly, K., Allen, M.B., and Berberian, M., 2002, Active tectonics of the South Caspian Basin: Geophysical Journal, International, v. 148, p. 214 – 245.

Jackson, M.P.A., Cornelius, R.R., Craig, C.H., Gansser, A., Stöcklin, J., and Talbot, C.J., 1990, Salt diapirs of the Great Kavir, central Iran: Boulder, Geological Society of America Memoir, v. 177, Geological Society of America, 139 p.

Jahangiri, A., 2007, Post-collisional Miocene adakitic volcanism in NW Iran: Geochemical and geodynamic implications: Journal of Asian Earth Science, v. 30, p. 437-447.

Jia, G., Peng, P., Zhao, Q., Jian, Z., 2003, Changes in terrestrial ecosystem since 30 Ma in East Asia: stable isotope evidence from black carbon in the South China Sea: Geology, v. 31 p. 1093–1096.

Jolivet, L., and Faccenna C., 2000, Mediterranean extension and the Africa-Eurasia collision, Tectonics, v. 19, p. 1095-1106.

Jones, R.W., and Simmons M.D., 1997, A review of the stratigraphy of Eastern Paratethys (Oligocene-Holocene), with particular emphasis on the Black Sea, in: Robinson, A., eds., Regional and petroleum geology of the Black Sea and surrounding region, in, America Association of Petroleum Geologists Memoir, v. 68, p. 39–52.

Jordan, T.E., 1981, Thrust loads and foreland basin evolution, Cretaceous, western United States: America Association of Petroleum Geologists Bulletin, v. 65, p. 2506–2520.

Jordan, T. E., and Allmendinger, R. W., 1986, The Sierras Pampeanas of Argentina: a modern analogue of Laramide deformation: American Journal of Science, v. 286, p. 737–764.

Jordan, T.E., Flemings, P.B., and Beers, J.A., 1988, Dating thrust-fault activity by use of foreland-basin strata, in: Kleinspehn K. L., and C. Paola, C., eds., New perspectives in basin analysis, Springer-Verlag, NewYork, p. 307 – 330.

Jordan, T.E., Isacks, B.L., Allmendinger R.W., Brewer, J.A., Ramos, V.A., and Ando, C.J., 1983, Andean tectonics related to geometry of subducted Nazca plate: Geological Society of American Bulletin, v. 94, p. 341-361.

Jouzel, J., Alley, R. B., Cuffey, K. M., Dansgaard, W., Grootes, P. M., Hoffman, G., Johnson, S. J., Koster, R. D., Peel, D., Shuman, C. A., Stievenard, M., Stuiver, M., and White, J. C.,1997, Validity of the temperature reconstruction from water isotopes in ice cores: Journal of Geophysical Research, v. 102, p. 26,471–26,487.

Kent-Corson, M.L, Ritts, B.D., Zhuang, G., Bovet, P.M, Graham, S.A., and Chamberlin, C.P., 2009, Stable isotopic constraints on the tectonic, topographic, and climatic evolution of the northern margin of the Tibetan Plateau: Earth and Planetary Science Letters, v. 282, p. 158-166.

Keskin, M., 2003, Magma generation by slab steepening and breakoff beneath a subduction-accretion complex: an alternative model for collision-related volcanism in Eastern Anatolia, Turkey: Journal of Geophysical Research Letters, v. 30, 208046, p. 1-6.

Kim, S.T., and O’Neil, J.R., 1997, Equilibrium and non-equilibrium oxygen isotope effects in synthetic carbonates: Geochimica and Cosmochimica Acta, v. 61, p. 3461-3475.

Kingston, J.D., Marino, B.D., and Hill, A., 1994, Isotopic evidence for Neogene hominid paleoenvironments in the Kenya Rift Valley: Science, v. 264, p. 955–959.

Kirschbaum, M.A., McCabe, P.J., 1992, Controls on the accumulation of coal and on the development of anastomosed fluvial systems in the Cretaceous Dakota Formation of southern Utah: Sedimentology, v. 39, p. 581– 598.

Kirschvink, J.L., 1980, The Least-Squares line and plane and analysis of paleomagnetic data: Geophysical Journal of the Royal Astronomical Society, v. 62, p. 699-718.

Kleinert, K., and Strecker, M.R., 2001, Climate change in response to orographic barrier uplift: Paleosol and stable isotope evidence from the late Neogene Santa María basin, northwestern Argentina: Geological Society of America Bulletin, v. 113, p. 728–742.

Koons, P.O., Zeitler, P.K., Chamberlain, C.P., Craw, D., and Meltzer, A.S., 2002, Mechanical links between erosion and metamorphism in Nanga Parbat, Pakistan Himalaya: American Journal of Science, v. 302, p. 749-773.

Köster, J., Rospondek, M., Schouten, S., Kotorba, M., Zurbrzycki, A., and Sinninghe Damste, J.S., 1998, Biomarker geochemestry of a foreland basin: the Oligocene Menilite Formation of Flysch Carpathians of Southest Poland: Organic Geochemestry, v. 29, p. 649-669.

Kutzbach, J.E., Guetter, P.J., Ruddiman,W.F., Prell,W.L.,1989. Sensitivity of climate to late Cenozoic uplift in southeast Asia and the American West; numerical experiments: Journal of Geophysical Research, v. 94, p. 18,393–18,407.

Landgraf, A., Ballato, P., Strecker, M.R., Friedrich, A., Tabatabaei, S.H., and Shahpasandzadeh M., 2009, Fault-kinematic and geomorphic observations along the North Tehran Thrust and Mosha Fasham Fault, Alborz mountains, Iran: implications for fault-system evolution and interaction in a changing tectonic regime: Geophysical Journal International, v. 177, p. 676-690.

Liu X., and Yin, Z.Y, 2001, Spatial and temporal variation of summer precipitation over the Eastern Tibet Plateau and the North Atlantic Oscillation: Journal of Climate, v. 14, p. 2896-2909.

Liutkus, C.M., Wright, J.D., Ashley, G.M., and Sikes, N.E., 2005, Paleoenvironmental interpretation of lake-margin deposits using δ^{23}C and δ^{18}O results from early Pleistocene carbonate rhizoliths, Olduvai Gorge, Tanzania: Geology, v. 33, p. 377-380.

Lowenstein T.K., and Hardie, L.A, 1985, Criteria for the recognition of salt-pan evaporites: Sedimentology, v. 32, p. 627-644.

Lock, J., and Willet, S, 2008, Low-temperature thermochronometric ages in fold-and-thrust-belts: Earth and Planetary Science Letters, v.456, p. 147-162.

MacFadden, B.J., Wang, Y., Cerling, T.E., and Anaya, F., 1994, South American fossil mammals and carbon isotopes: a 25 millionyear sequence from the Bolivian Andes: Palaeogeography Palaeoclimatology, Palaeoecology, v. 107, p. 257– 268.

Maggi, A., Jackson, J.A., Priestley, K., and Baker C., 2000, A reassessment of focal depth distributions in southern Iran, the Tien Shan and northern India: do earthquakes really occur in the continental mantle: Geophysical Journal International, v. 143, p. 629-661.

Maggi, A., and Priestley, K., 2005, Surface waveform tomography of the Turkish-Iranian plateau**:** Surface waveform tomography of the Turkish–Iranian plateau**:** Geophysical Journal International, v. 160, p. 1068-1080.

Maher, B.A., and Thompson R., 1991, Mineral magnetic record of the Chinese loess and paleosols: Geology, v. 19, p. 3–6.

Manabe, S., and Broccoli, A.J., 1990, Mountains and arid climates of middle latitudes: Science, v. 247, p. 192–195.

Mangino, S., and Priestley, K., 1998, The crustal structure of the southern Caspian region: Geophysical Journal International, V: 133, P: 630-648.

Makaske, B., Smith, D.G., and Berendsen, H.J.A., 2002, Avulsions, channel evolution and floodplain sedimentation rates of the anastomosing upper Columbia River, British Columbia, Canada: Sedimentology, v. 49, p. 1049–1071.

Marchant, R.H., and Stampfli, G.M., 1998, Subduction of continental crust in Western Alps: Tectonophysics, v.269, p. 217-235.

Marr, J.G., Swenson, J.B., Paola, C., and Voller, V.R., 2000, A two diffusion model of fluvial stratigraphy in closed depositional basins: Basin Research, v. 12, p. 381–398.

Masek, J.G., and Duncan, C.C., 1998, Minumum-work mountain building: Journal of Geophysical Research, v. 103, p. 907-917.

Masson, F., Anvari, M., Djamour, Y., Walpersdorf, A., Tavakoli, F., Daignieres, M., Nankali, H., and van Gorp, S., 2007, Large-scale velocity field and strain tensor in Iran inferred from GPS measurements: new insight for the present-day deformation pattern within NE Iran: Geophysical Journal International, v. 170, p. 436-440.

Masson, F., Djamour, Y., Van Gorp, S., Chéry, J., Tavakoli, F., Nankali, H., and Vernant, P., 2006, Extension in NW Iran driven by the motion of the South Caspian Basin: Earth and Planetary Science letters, v. 252, p. 180-188.

McCarthy, P.J., Martini, I.P., and Leckie, D.A., 1997, Anatomy and evolution of a Lower Cretaceous alluvial plain: sedimentology and paleosols in the upper Blairmore Group, south-western Alberta, Canada: Sedimentology, v. 44, p. 197– 220.

McFadden, P.L., and. McElhinny, M.W., 1990 Classification of the reversal test in palaeomagnetism: Geophysical Journal International v. 130, p. 725-729.

McKenzie, D.P., 1978, Some remarks on the development of sedimentary basins. Earth Planet. Sci. Lett., 40, 25–32.

McQuarrie, N., Stock, J.M., Verdel, C., and Wernicke, B.P., 2003, Cenozoic evolution of Neotethys and implications for the causes of plate motions: Geophysical. Research. Letters, v. 30, 2036, p. 1-6.

Meigs, J.A., Burbank, D.W., Beck, R.A., 1995, Middle-Late Miocene (>10 Ma) formation of the Main Boundary thrust in the western Himalaya: Geology, v. 23, p. 423-426.

Métivier, F., Gaudemer, Y., Tapponnier, P., and Klein, M., 1999, Mass accumulation rates in Asia during the Cenozoic: Geophysical Journal International, v. 137, p. 280-318.

Miall, A.D., 1996, The Geology of Fluvial Deposits: Berlin, Springer-Verlag, 581 p.

Mitrovica, J. X., Beaumont, C., and Jarvis, G. T., 1989, Tilting of the continental interiors by the dynamical effects of subduction: Tectonics, v. 8, p. 1079–1094.

Mo, X., Hou, Z., Niu, Y., Dong, G., Qu, X., Zhao Z., and Yang, Z., 2007, Mantle contributions to crustal thckening during continental collision: Evidence from Cenozoic igneous rocks in southern Tibet: Lithos, v. 96, p. 225-242.

Molnar, P., 2004, Late Cenozoic increase in accumulation rates of terrestrial sediment: How might climate change have affected erosion rates?, Annual Reviews of Earth and Planetary Science, v. 32, p. 67-89.

Molnar, P., 2005, Mio-Pliocene growth of the Tibetan plateau and evolution of East Asian climate: Paleontologia Electronica, v. 8, p. 1-23

Molnar, P., and England, P., 1990, Late Cenozoic uplift of mountain ranges and global climatic change: chicken or egg?: Nature, v. 346, p. 29-34.

Molnar, P., and Stock, J.M., 2009, Slowing of India’s convergence with Eurasia since 20 Ma., and its implications for Tibetan mantle dynamics, v. 28, TC3001, p.1-11.

Molnar, P., and Tapponnier, P., 1975, Cenozoic tectonics of Asia: Effects of a continental collision: Science, v. 189, p. 419-426.

Montgomery, D.R., and Brandon, M.T., 2002, Topographic controls on erosion rates in tectonically active mountain ranges: Earth and Planetary Science Letters, v. 201, p. 481–489.

Mora, A., Parra, M., Strecker, M.R., Sobel, E.R., Hooghiemstra, H., Torres, V., and Jaramillo J.V., 2008, Climatic forcing of asymmetric orogenic evolution in the Eastern Cordillera of Colombia: Geological Society of America Bulletin., v. 120, p. 930-949.

Morales, J., Serrano, I., Jabaloy, A., Galindo-Zaldívar, J., Zhao, D., Torcal, F. Vidal F., and González Lodeiro, F., 1999, Active continental subduction beneath the Betic Cordillera and the Alborán Sea: Geology, v. 27, p. 735-738.

Moritz, R., Ghazban, F., and Singer, B.S., 2006, Eocene gold ore formation at Muteh, Sanandaj-Sirjan tectonic zone, western Iran: a result of late-stage extension and exhumation of metamorphic basement rocks within the Zagros orogen: Economic Geology, v. 101, p. 1497-1524.

Morley, C., Kongwung, B., Julapour, A.A., Abdolghafourian, M., Hajian, M., Waples, D., Warren, J., Otterdoom, H., Srisuriyon, K., and Kazemi, H., 2009, Structural development of the major Late Cenozoic basin and transpressional belt in Central Iran: the Central Basin in the Qom-Saveh area: Geosphere, v. 5, p.325-362

Morrill, C., and Koch, P.L., 2002, Elevation or alteration? Evaluation of isotopic constraints on paleoaltitudes surrounding the Eocene Green River Basin: Geology, v. 30, p. 151-154.

Mortimer, E., Carrapa, B., Coutand, I., Schoenbohm, L., Sobel, E.R., Sosa Gomez, J., and Strecker, M.R., 2007, Fragmentation of a foreland basin in response to out-of-sequence basement uplifts and structural reactivation: El Cajón-Campo del Arenal basin, NW Argentina: Geological Society of America Bulletin, v. 119, p. 637-653.

Mouthereau, F., Lacombe, O., and Meyer, B., 2006, The Zagros folded belt (Fars, Iran): constraints from topography and critical wedge modelling, Geophysical Journal International, v. 165, p. 336-356.

Mulch, A. and Chamberlin, C.P., 2006, The rise and growth of Tibet: Nature, v. 439, p. 670-671.

Mulch, A. and Chamberlain, C.P., 2007, Stable Isotope Paleoaltimetry in Orogenic Belts - The silicate record in surface and crustal geological archives: Reviews in Mineralogy and Geochemistry, v. 66, p. 89-118.

Mulch A., Graham, S.A., and Chamberlin, C.P., 2006, Hydrogen isotopes in Eocene River gravels and paleoelevation of the Sierra Nevada: Science, v. 113, p. 87-89.

Mulch, A., Sarna-Wojcicki, A.S., Perkins, M.E., and Chamberlain C.P., 2008, A Miocene to Pliocene climate and elevation record of the Sierra Nevada and Great Basin region: Proceedings of the National Academy of Sciences, v. 105, p. 6819-6824.

Mulch A., Uba, C., Strecker, M.R., Schönberg, R., and Chamberlain, C.P. (in review): Stable and radiogenic isotope records of late Miocene climate variability and surface elevation in the central Andes.

Nadirov, R.S., Bagirov, E., Tagiyev, M., and Lerche, I., 1997, Flexural plate subsidence, sedimentation rates, and structural development of the super-deep south Caspian basin: Marin and Petroleum, Geology, v. 14, p. 383 – 400.

Najman, Y, 2006, The detritial record of orogenesis: a review of approaches and techniques used in the Himalayan sedimentary basins: Earth and Science Reviews, v 74, p.1-72.

Najman, Y., and Garzanti, E., 2000, Reconstructing early Himalayan tectonic evolution and paleogeography from Tertiary foreland basin sedimentary rocks, northern India: Geological Society of America Bulletin, v. 112, p. 435-449.

Naylor, M., and Sinclair H.D., 2007, Reconciling punctuated thrust deformation in the context of orogenesis: Implications for the localisation of uplift and exhumation, Geology, v. 35, p. 559-562.

Negredo, A.M., Sabadini, R., and Giunchi, C., 1997, Interplay between subduction and continental convergence: A three-dimensional dynamic model for the Central Mediterranean: Geophysical Journal International, v. 131, p. F9– F13.

Omrani J., Agard, P., Whitechurch, H., Benoit, M., Protuteau, G., and Jolivet, L., 2008, Arc-magmatism and subduction history beneath the Zagros Mounatins, Iran: A new report of adakites and geodynamic consequences: Lithos, v. 106, p. 380-398.

Ori, G.G., and Friend P.F., 1986, Sedimentary basins formed and carried piggyback on active thrust sheets: Geology, v. 12, p. 475-478.

Paik I.S., and Kim H.J., 2006, Playa lake and sheetflood deposits of the Upper Cretaceous Jindong Formation, Korea: Occurrences and palaeoenvironments: Sedimentary Geology, v. 187, p.83-103.

Paola, C., Heller, P.L., and Angevine C.L., 1992, The large-scale dynamics of grain-size variation in alluvial basins, 1: Theory: Basin Research, v. 4, p. 73-90.

Parra, M., Mora, A., Jaramillo, C., Strecker, M.R., Sobel, E.R., Quiroz, L., Rueda, M., and Torres, V., 2009, Orogenic wedge advance in the northern Andes: Evidence from the Oligocene-Miocene sedimentary record of the Medina Basin, Eastern Cordillera, Colombia: Geological Society of America Bulletin, v. 121, p. 780-800.

Parra, M., Mora, A., Sobel, E.R., Strecker, M.R., Gonzales, R., 2009, Episodic orogenic front migration in the northern Andes: Constraints from low-temperature thermochronology in the Eastern Cordillera, Colombia: Tectonics, v.28, TC4004, p. 1-27

Paul, A., Kaviani A., Hatzfeld, D., Vergne, J., and Mohammad Mokhtari, 2006, Seismological evidence for crustal-scale thrusting in the Zagros mountain belt (Iran)**:** Geophysical Journal International, v. 166, p. 227-237.

Pavlis, G.L., and Das, S., The Pamir-Hindu Kush seismic zone as a strain marker for flow in the upper mantle: Tectonics, v. 19, p. 103–115.

Poage M.A., and Chamberlain, C.P., 2001, Empirical relationships between elevation and the stable isotope composition of precipitation and surface waters: considerations for studies of paleoelevation change: American Journal of Science, v. 301, p. 1–15

Quade, J., Cater, J..M.L., Ojha, T.P., Adam, J., and Harrison, T.M., 1995, Late Miocene environmental change in Nepal and the northern Indian subcontinent: Stable isotopic evidence from paleosols: Geological Society of America. Bulletin, v. 107, p. 1381–1397.

Quade, J., Garzione, C.N., and Eiler, J., 2007, Paleoelevation reconstruction using pedogenic carbonates: Reviews in Mineralogy and Geochemestry, v. 66, p. 53-87.

Quade, J, Rech, J.A., Latorre, C, Betancourt, J.L., Gleason, E, and Kalin, M.T.K., 2007b, Soils at the hyperarid margin: the isotopic composition of soil carbonate from the Atacama Desert: Geochimica Cosmochimica Acta, v. 71, p. 3772-3795.

Rahimpour-Bonab, H., and Kalantarzadeh Z., 2006, Origin of secondary potash deposits: a case from Miocene evaporites of NW Central Iran: Journal of Asian Earth Science, v. 25, p. 157 – 166.

Rahimpour Bonab H., Shariatinia, Z., and Siemann, M.G., 2007, Role of rifting in evaporite deposition in the Great Kavir Basin, central Iran, in Scrhreiber, B.C., et al., eds., Evaporites through Space and Time: London, The Geological Society, p. 69-85.

Ranalli, G., Pellegrini, R., and D`Affizi, S., 2000, Time dependent of negative buoyancy and subduction of continental lithosphere, Journal of Geodynamics, v. 30, p. 539-555.

Regard, V., Faccenna, C., Martinod, J., Bellier, O., and Thomas, J.C., 2003, From subduction to collision: control of deep processes on the evolution of convergent plate boundary: Journal of Geophysical Research, v. 108, B42208, p. 1-13.

Reiners, P.W., and M.T. Brandon, 2006, Using thermochronology to understand orogenic erosion: Annual Review of Earth and Planetary Sciences, v. 34, p. 419-466.

Reiners, P.W., Rhlers, T.A., Garver, J.I., Mitchell, S.G., Montgomery, D.R, Vance, J.A., and Nicolescu, S., 2002, Late Miocene exhumation and uplift of the Washington Cascade Range: Geology, v.30, p. 767-770., doi: 10.1130/0091-7613(2002)030<0767:LMEAUO>2.0.CO;2.

Reuter, M., Piller, W.E., Harzhauser, M., Mandic, O., Berning, B., Rögl, F., Kroh, A., Aubry, M.P., Wielandt-Schuster, U., and Hamedani, A., 2007, The Oligi-/Miocene Qom Formation (Iran): evidence for an early Burdigalian restriction of the Tethyan seaway and closure of ist Iranian gateways: International Journal of Earth Science, v. 98, p. 627-650, doi: 10.1007/s00531-007-0269-9.

Rezaeian, M., Hovius, N., Dadson, S.J., and, Allen, M.B, 2004, Erosion of the Alborz mountains constrained by river gauging, Eos Trans. AGU, Fall Meet., Suppl., Abstract T31B-1289.

Rezaeian, M., 2008, Coupled tectonics, erosion and climate in the Alborz Mountains (PhD. thesis): Cambridge, University of Cambridge, 237 p.

Riba, O., 1976, Syntectonic unconformities of the Alto Cardener, Spanish Pyrenees: A genetic interpretation: Sedimentary Geology, v. 15, p. 213-233.

Rieben, H. 1955, The geology of the Tehran plain: America Journal of Science, v. 253, p. 617-639.

Rietveld, H.M., 1969, A profile refinement method for nuclear and magnetic structures, Journal of Applied Crystallography, v. 2, p. 65-71

Ritz, J.-F., Nazari, H., Ghassemi, A., Salamati, R., Shafei, A., Solaymani, S., and Vernant, P., 2006, Active transtension inside central Alborz: A new insight into northern Iran – southern Caspian geodynamics, Geology, v. 34, p. 477-480.

Robertson, A.H.F., Ustaömer, T., Parlak, O., Ünlügenç, U.C., Taşli, K., and İnan, N., 2006, The Berit transect of the Tauride thrust belt, S Turkey: Late Cretaceous-Early Cenozoic accretionary/collisional processes related to closure of the Southern Neotethys: Journal of Asian Earth Sciences, v. 27, p. 108-145.

Rowley, D.B., Currie, B.S., 2006. Palaeo-altimetry of the late Eocene to Miocene Lunpola basin, central Tibet. Nature, v. 439, p. 677–681, doi:10.1038/nature04506.

Ruddiman, W.F., Kutzbach, J.E., 1989. Forcing of late Cenozoic northern hemisphere climate by plateau uplift n southern Asia and the American West: Journal of Geophysical Research, v. 94, p. 18409–18427.

Schuster, F., and Wielandt, U., 1999, Oligocene and Early Miocene coral faunas from Iran: palaeoecology and palaeobiogeography, International Journal of Earth Science, v. 88, p. 571–581, doi: 10.1007/s005310050285.

Simpson, G.D.H., 2006, Modelling interactions between fold-thrust belt deformation, foreland flexure and surface mass transport, Basin Research, v. 18, p. 125-143..

Sinclair, H.D., Coakley, B.J., Allen, P.A., and Watts, A.B., 1991, Simulation of foreland basin stratigraphy using a diffusion model of mountain belt uplift and erosion: an example from the central Alps, Switzerland, Tectonics, 10, 599 – 620.

Sinclair, H.D., Gibson, M., Naylor, M., and Morris, R.G., 2005, Asymmetric growth of the Pyrenees revealed through measurements and modeling of orogenic fluxes: American Journal of Science, v. 305, p. 369-406.

Smith, R.B., 1982, Synoptic observations and theory of orographically disturbed wind and pressure: Journal of Atmospheric Science, v. 39, p. 60-70.

Smith, D.G., 1986, Anastomosing river deposits, sedimentation rates and basin subsidence, Magdalena River, northwestern Columbia, South America: Sedimentary Geology v. 46, p. 177– 196.

Smith, D.G., Smith, N.D., 1980, Sedimentation in anastomosed river systems: examples from alluvial valleys near Banff, Alberta: Journal of Sedimentary Petrology, v. 50, p. 157– 164.

Smith G.A., Wang, Y., Cerling, T.E., and Geissman, J.W., 1993, Comparison of a paleosol-carbonate isotope record to other record of Pliocene-Early Pleistocene climate in the Western United States, v. 21, p. 691-694.

Smoot, J.P., 1983, Depositional subenvironments in an arid closed basin; the Wilkins Peak Member of the Green River Formation (Eocene), Wyoming, USA: Sedimentology, v. 30, p. 801–827.

Sobel, E. R., Chen, J., and Heermance R.V., 2006, Late Oligocene–early Miocene initiation of shortening in the southwestern Chinese Tian Shan: Implications for Neogene shortening rate variations, Earth Planet. Science Letters, v. 247, p. 70–81.

Sobel, E.R., Hilley, G.E., and Strecker, M.R., 2003, Formation of internally drained contractional basins by aridity-limited bedrock incision: Journal of Geophysical Research, v. 108, B7 2344, .p. 1-23.

Sobel ER, Strecker MR. 2003. Uplift, exhumation and precipitation: tectonic and climatic control of late Cenozoic landscape evolution in the northern Sierras Pampeanas, Argentina: *Basin Research*, v. 15, p. 431–451.

Sourieau, A., and Granet, M., 1995, A tomographic study of the lithosphere beneath the Pyrenees from local and teleseismic data: Journal of Geophysical Research, v. 100, p. 18,117–18,134.

Spötl, C., and Vennemann, T., 2003, Continuous-flow IRMS analysis of carbonate minerals: Rapid Communication in Mass Spectrometry, v. 17, p. 1004–1006.

Stanistreet I.G., and McCarthy, T.S., 1993, The Okavango Fan and the classification of subaerial fan systems: Sedimentary Geology, v. 85, p. 115-133.

Stille, P., Steinmann, M., and Riggs, S. R., 1996, Nd isotope evidence for the evolution of the paleocurrents in the Atlantic andTethys Oceans during the past 180 Ma: Earth and Planetary Science Letters, v. 144, p. 9-19.

Stockli, D.F., Hassanzadeh, J., Stockli, L.D., Axen, G.J., Walker, J.D., and Dewane, T.J., 2004, Structural and geochronological evidence for Oligo-Miocene intraarc low-angle detachment faulting in the Takab-Zanjan area, NW Iran: Geological Society of America Abstracts with Programs, v. 36, no. 5, p. 319.

Stöcklin, J., 1968, Structural history and tectonics of Iran: A review: America Association of Petroleum Geologists Bulletin, v. 52, p. 1229–1258.

Strecker M.R., Alonso, R., Bookhagen, B., Carrapa, B., Coutand, I., Hain, M.P., Hilley, G.E., Mortimer, E., Schenbohm, L., and Sobel., E.R., 2009, Does the topographic distribution of the central Andean Puna Plateau result from climatic or geodynamic processes?: Geology, v. 37, p.643-646.

Strecker, M.R., Alonso, R., Bookhagen, B., Carrapa, B., Hilley, G.E., Sobel, E.R., and Trauth, M.H., 2007, Tectonics and climate of the Southern Central Andes: Annual Review of Earth and Planetary Sciences, v. 35, p. 747–787.

Talbot, M.R., 1990, A review of the paleohydrological interpretation of carbon and oxygen isotopic ratios in primary lacustrine carbonates: Chemical Geology, v. 80, p. 261–279.

Talbot, M.R., and Kelts, K., 1990, Paleolimnological signatures from carbon and oxygen isotopic ratios in carbonates from organic carbon-rich lacustrine sediments, *in* Katz, B.J., ed., Lacustrine basin exploration: Case studies and modern analogs: Tulsa, Oklahoma, American Association of Petroleum Geologists Memoir 50, p. 99–112.

Talebian, M., and Jackson, J.A., 2002, Offset on the Main Recent Fault of NW Iran and implications for the late Cenozoic tectonics of the Arabia-Eurasia collision zone: Geophysical Journal International, v. 150, p. 422-439.

Thiede, R.C., Arrowsmith, J. R., Bookhagen, B., McWilliams, M.O., Sobel, E.R., and Strecker, M.R., 2005, From tectonically to erosionally controlled development of the Himalayan orogen: Geology, v. 33, p. 689-692.

Thiede R.C., Ehlers, T.A., Bookhagen, B, and Strecker M.R., 2009, Erosional variability along the northwest Himalaya, Journal of Geophisical Reasearch, v. 114, F01015, p. 1-19

Thompson, R., and Oldfield, F., 1986, Environmental Magnetism: London, Allen and Unwin, 227 p.

Toby, B.H. (2001): EXPGUI, a graphical user interface for GSAS: Journal of Applied Crystallography, v. 34, p. 210-213

Toussaint,G., Burov,E.; and Avouac,J.P., 2004, Tectonic evolution of a continental collision zone: A thermomechanical numerical mode: Tectonics, v. 23, TC6003, p. 1-24.

Tucker M. E., and Wright, V.P., 1990, Carbonate Sedimentology: Oxford, Blackwell Science, 482 p.

Uba, C.E., Heubeck, C., and Hulka, C., 2005, Facies analysis and basin architecture of the Neogene Subandean synorogenic wedge, southern Bolivia: Sedimentary Geology, v. 180, p. 91–123.

Uba, C.E., Strecker, M.R., and Schmitt, A.K., 2007, Increased sediment accumulation rates and climatic forcing in the central Andes during the late Miocene: Geology, v. 35, p. 979-982.

Vachon R.W., White, J.W.C., Gutmann, E., and Welker, J.M., 2007, Amount-weighted annual isotopic ($\delta^{18}O$) values are affected by the seasonality of precipitation: A sensitive study: Geophysical research letters, v. 34, L21707, p. 1-5

Vahdati Daneshmand, 1991, Geological map of Amol quadrangle, Geological Survey of Iran, scale 1:250,000, 1 sheet.

Vahdati Daneshmand, 1997, Geological map of East of Tehran quadrangle, Geological Survey of Iran, scale 1:100,000, 1 sheet.

Vahdati Daneshmand, F., and Saidi, A., 1991, Geological map of Sari quadrangle, Geological Survey of Iran, scale 1:250,000, 1 sheet.

Van Dam, J.A., Geographic and temporal patterns in the late Neogene (12-3Ma) aridification of Europe: The use of small mammals as paleoprecipitation proxies, Palaeogeography Palaeoclimatology Palaeoecology, v. 238, p. 190-218.

Van der Voo, R., Spakman, W., and Bijwaard, H., 1999, Tethyan subducted slabs under India: Earth Planetary Science Letters, v. 171, p. 7–20.

Verdel, C., Wernicke, B. P., Ramezani, J., Hassanzadeh, J., Renne, P.R., and Spell T.L., 2007, Tertiary Cordilleran-style metamorphic core complexes in the Saghand region of central Iran: Geological Society of America Bulletin, v. 119, p. 961-977.

Velde, B., 1995, Composition and mineralogy of clay minerals, *in* Velde, B., ed., Origin and mineralogy of clays: New York, Springer-Verlag, p. 8–42.

Verdel, C.S., 2008, I. Cenozoic geology of Iran: an integrated study of extensional tectonics and related volcanism (PhD. thesis): Pasadena, California Institute of Technology University of Cambridge, 182 p.

Vernant, P., et al., 2004a, Present-day crustal deformation and plate kinematics in the Middle East constrained by GPS measurements in Iran and northern Oman: Geophysical Journal International, v. 157, p. 381–398.

Vernant, P., Chery, J., Bayer, R., Djamour, Y., Masson, F., Nankali, H., Ritz, J.F., Sedighi, M., and Tavakoli, F., 2004b, Deciphering oblique shortening of central Alborz in Iran using geodetic data, Earth and Planetary Science Letters, v. 223, p. 177-185.

Vincent, S.J., Allen, M.B., Ismail-Zadeh, A.D., Flecker, R., Foland, K.A., and Simmons, M.D., 2005, Insights from the Talysh of Azerbaijan into the Paleogene evolution of the south Caspian region: Geological Society of America Bulletin, v. 117, p. 1513-1533.

Vincent, S.J., Morton, A.C., Carter, A., Gibbs, S., and Barabadze, T.G., 2007, Oligocene uplift of the Western Greater Caucasus: an effect of initial Arabia–Eurasia collision: Terranova, v. 19, p. 160-166.

Walpersdorf, A., Hatzfeld, D., Nankali, H., Tavakoli, F., Nilforoushan, F., Tatar, M., Vernant, P., Chéry, J., and Masson, F., 2006, Difference in the GPS deformation pattern of North and Central Zagros (Iran), Geophysical, Journal, International, v. 167, p. 1077 – 1088.

Westaway, R., 1994, Present-day kinematics of the Middle East and eastern Mediterranean: Journal of Geophysical Research, v. 99, p. 12,071-12,090.

Whipple, K., and Meade B.J., 2004, Controls on the strength of coupling among climate, erosion, and deformation in two-sided, frictional orogenic wedges at steady state: Journal of Geophysical Research, v. VOL. 109, F01011, p. 1-24.

Willett, S.D., 1999, Orogeny and orography; the effects of erosion on the structure of mountain belts: Journal of Geophysical Research, v. 104, p. 28,957 – 28,982.

Willett, S., Beaumont, C., and Fullsack, P., 1993, Mechanical model for the tectonics of doubly vergent compressional orogens: Geology, v. 21, p. 371-374.

Wilmsen, M., Fürsich, F.T., Seyed-Emami, K., Majidifard, M.R., and Taheri, J., 2009, The Cimmerian Orogeny, in northern Iran: tectono-stratigraphic evidence from the foreland: Terranova, v. 21, p. 211-218.

Wobus, C.W., Hodges, K.V., and Whipple, K.X., 2003, Has focused denudation sustained active thrusting at the Himalayan topographic front?: Geology, v. 31, p. 861-864.

Woodruff, F., and Savin, S.M., 1989, Miocene deepwater oceanography: Paleoceanography, v. 4, p. 87–140.

Yassaghi A., and Madanipour, S, 2008, Influence of a transverse basement fault on along-strike variations in the geometry of an inverted normal fault: case study of the Mosha Fault, Central Alborz Range, Iran: Journal of Structural Geology, v.30, p. 1507-1519.

Yilmaz, Y., 1993. New evidence and model on the evolution of the southeast Anatolian orogen: Bulletin of the Geological Society of America, v. 105, p. 251–271.

Zachos, J., Pagani, M., Sloan, L., Thomas, E., and Billups K., 2001, Trends, rhythms and aberrations in global climate 65 Ma to Present: Science, v. 292, p. 686-693.

Zaitchik, B.F., Evans, J.P., and Smith, R.B., 2007, Regional impact of an elevated heat source: the Zagros Plateau of Iran: Journal of Climate, v. 20, p. 4133-4146.

Zanchi, A., Berra, F., Mattei, M., Ghassemi, M., and Sabouri, J., 2006, Inversion tectonics in central Alborz, Iran: Journal of Structural Geology, v. 28, p. 2023-2037.

Zhang, P., Molnar, P., and Downs W.R., 2001, Increased sedimentation rates and grain sizes 2–4 Myr ago due to the influence of climate change on erosion rates: Nature, v. 410, p. 891-897.

APPENDIX 1

Paleomagnetic data

This dataset contains paleomagnetic data from the southern Alborz mountains, N Iran. Samples were collected in 2005. A 6500-m-thick stratigraphic section was sampled for a total of 369 samples. Sample analyses were completed from 2006 to 2007 at the Geoforschungszentrum Potsdam, Section 3.3. Details and analytical techniques are described in chapter 2.

TABLE A1.1: SAMPLES LIST INCLUDING STRATIGRAPHIC POSITION, CHARACTERISTIC REMANENT MAGNETIZATION (ChRM), VIRTUAL GEOMAGNETIC POLE (VGP), AND MAGNETIC POLARITY. ChRM AND VGP ARE EXPRESSED IN TILT-CORRECTED COORDINATES.

Sample ID	Stratigraphic position (m)	ChRM inclination (Dec°)	ChRM declination (Dec°)	VGP latitude (Dec°)	VGP longitude (Dec°)	Polarity
I-237b-2	6515	41.5	-46.6	48.3	-41.8	N
I-6560a2	6455	-30.0	158.2	-62.6	101.9	R
I5-235b-2	6450	-7.5	188.2	-57.5	35.8	R
I-6530c	6425	-41.5	161.0	-69.9	111.2	R
I-6500b	6395	-18.3	208.0	-53.5	-0.1	R
I-6485b	6380	40.5	21.0	68.0	169.4	N
I-6455a	6350	46.1	16.5	73.9	166.2	N
I-6450b2	6345	68.0	50.3	51.1	101.4	N
I-6440b2	6335	10.0	20.1	54.4	-164.8	N
I-6425a2	6320	47.6	19.8	72.0	157.5	N
I-6415a	6310	26.3	27.7	57.1	175.0	N
I-6380a	6275	23.6	38.5	48.3	165.0	N
I-6355a	6250	36.0	3.9	74.2	-142.3	N
I-6345a	6240	40.7	24.0	65.9	164.9	N
I-6325a	6220	52.2	-33.3	62.4	-34.6	N
I-6265a3	6160	55.7	-69.2	35.2	-16.2	N
I-6250a	6145	46.0	-10.9	77.7	-76.7	N
I-6215a	6110	12.5	41.7	41.9	168.4	N
I-6205a2	6100	4.7	-0.9	56.9	-127.2	N
I-6190a2	6085	28.8	28.5	57.6	172.0	N
I-6180a2	6075	30.8	1.7	71.1	-133.9	N
I-6165a2	6060	13.3	55.5	31.7	156.8	N
I5-226b-2	6055	34.2	-2.6	73.2	-120.5	N
I-6155a2	6050	20.3	49.5	38.7	157.6	N
I-6125a1	6020	-44.6	160.0	-70.6	118.6	R
I5-225b-4	6010	-20.9	214.1	-50.5	-8.8	R
I-6110a1	6005	-51.6	176.9	-85.9	90.5	R
I-6095a2	5990	-31.1	230.9	-41.2	-30.1	R
I-6050a	5945	52.1	13.8	78.3	150.5	N
I-6040a2	5935	-35.9	169.9	-72.1	83.6	R
I-6030a	5925	-29.2	216.8	-51.7	-17.4	R
I-6020a2	5915	-9.6	186.6	-58.8	38.4	R
I-6010b1	5905	-43.6	224.3	-50.8	-36.7	R
I-5995a2	5890	-35.7	220.3	-51.4	-25.9	R
I-5980a2	5875	-59.0	185.7	-83.7	-84.4	R
I-5970a2	5865	-47.0	210.5	-63.3	-31.9	R
I-5930a2	5825	-31.0	166.1	-67.6	88.2	R
I-5900a2	5805	-35.1	150.9	-59.8	116.8	R
I-5870a2	5765	-14.6	214.3	-47.9	-5.4	R
I-5855b	5750	-9.8	205.9	-51.3	7.1	R
I5-216b-2	5740	-14.7	215.5	-47.2	-6.8	R
I5840a	5735	-11.1	183.1	-60.1	44.9	R
I5-215-1	5730	16.2	-25.3	54.3	-82.4	N
I-5830b	5725	32.7	43.6	47.6	154.1	N

I-5555a2	5675	42.3	-50.6	45.3	-38.7	N
I-5495a2	5615	66.8	9.3	74.4	74.0	N
I-5460b1	5580	34.0	24.7	62.5	172.2	N
I-5430a2	5550	39.4	31.0	60.1	158.6	N
I5-209b-2	5545	44.9	27.4	64.9	154.3	N
I-5390a2	5510	32.5	-30.7	57.5	-64.0	N
I-5380a	5500	42.4	1.5	79.0	-136.2	N
I-5320b	5440	79.3	16.9	54.8	61.4	N
I-5255a	5375	-26.2	182.9	-68.3	43.5	R
I-5225b	5345	21.8	36.1	49.4	168.5	N
I-5215b	5335	62.3	-17.0	74.5	-1.5	N
I-5170a3	5290	39.0	25.7	63.9	165.0	N
I-5115	5235	-43.6	168.5	-76.0	99.0	R
I5-198b-4	5220	-27.9	202.5	-61.2	1.0	R
I-5095a1	5215	-18.8	208.8	-53.2	-1.4	R
I-5070b	5190	-29.0	195.5	-65.7	12.2	R
I5050b	5170	-24.5	167.1	-64.6	81.7	R
I-5040a2	5160	-38.0	201.5	-66.5	-7.8	R
I-5030b	5150	-20.1	189.1	-63.6	30.6	R
I5-195b-3	5145	-47.8	207.2	-66.2	-30.7	R
I-5020b2	5140	-26.1	228.8	-41.2	-25.2	R
I-5010a	5130	5.6	34.6	44.3	178.7	N
I-4965b	5085	26.1	-2.0	68.3	-123.5	N
I-4950b2	5070	54.8	62.8	39.7	121.8	N
I-4935a	5055	31.9	23.8	62.1	175.5	N
I-4920a	5040	4.6	58.0	27.1	159.1	N
I-4900a	5020	11.0	16.6	56.4	-159.9	N
I-4875a	4995	39.9	-13.2	72.9	-83.3	N
I-4865a	4985	21.1	46.7	41.2	159.4	N
I-4850a	4970	46.8	-16.3	74.3	-62.5	N
I-4830a1	4950	49.5	13.7	77.5	160.9	N
I-4800a	4920	40.8	3.6	77.6	-144.4	N
I-4705b	4825	-16.5	199.8	-57.5	12.5	R
I-4695a2	4815	-5.6	213.0	-45.3	0.5	R
I-4680a2	4800	38.6	9.1	74.2	-161.5	N
I-4670a2	4790	38.3	0.8	76.1	-131.8	N
I-4650a	4770	44.6	7.7	78.7	-166.8	N
I5-180b-2	4760	77.0	54.8	46.3	80.9	N
I-4580a	4700	-35.7	191.9	-71.2	14.3	R
I5-177b-2	4660	-52.2	159.9	-73.2	137.9	R
I-4475b	4595	64.1	-38.5	59.3	-7.1	N
I-4475a2-bis	4585	37.3	14.6	70.6	-174.0	N
I-4445a2	4565	33.5	24.1	62.7	173.5	N
I-4400b	4520	41.8	53.8	42.5	139.5	N
I-4370c	4490	73.0	22.0	62.7	76.3	N
I-4350a	4470	58.3	17.3	75.8	121.3	N
I-4325a	4445	49.3	37.1	58.5	140.0	N
I-4295a	4415	46.6	8.6	79.5	-175.1	N
I-4260b	4380	22.1	-11.0	64.1	-103.5	N
I-4250a1	4370	33.0	28.0	59.7	168.9	N
I-4235a3	4355	59.1	37.1	60.5	121.2	N
I-4210b2	4330	46.3	44.4	51.6	140.1	N
I-4160b	4280	43.5	-11.3	76.0	-81.6	N
I-4150b	4270	35.7	11.4	71.4	-164.5	N
I-4130c	4250	29.0	20.3	63.1	-176.4	N
I-4115c	4235	44.7	4.3	80.2	-151.9	N
I-4095a	4215	27.7	64.2	29.4	143.6	N
I-4060a	4180	19.9	25.8	55.6	-178.2	N
I-4045d	4165	70.5	-33.6	59.9	11.5	N
I-4010b	4130	75.0	-6.9	63.3	43.9	N
I-3930a	4050	77.0	55.4	46.0	80.9	N
I-3920a2	4040	41.8	39.4	54.3	148.7	N
I-3910c	4030	35.5	54.2	40.1	144.5	N
I-3835c	3955	54.2	-4.4	86.3	-48.3	N
I-3715a	3835	67.1	67.2	40.2	102.4	N
I-3700b	3820	62.6	-28.7	66.5	-9.0	N
I-3700b1_bi	3810	59.6	48.1	52.2	118.7	N

I-3670a2	3790	42.2	-6.6	77.6	-99.6	N
I-3650b	3770	39.5	30.6	60.4	158.8	N
I-3630b	3750	69.2	55.8	47.6	99.1	N
I-3610a1	3680	67.1	-58.0	46.2	-1.1	N
I-3545b1	3655	-26.4	142.5	-50.1	118.2	R
I-3500a2	3620	-2.6	218.6	-40.5	-4.0	R
I-3460a	3600	71.3	44.0	54.0	92.6	N
I-3450a	3570	70.9	16.2	67.2	75.4	N
I-3410b2	3530	57.2	-67.2	37.2	-14.9	N
I-3390b	3510	-55.7	213.6	-62.9	-50.7	R
I5-150b-2	3505	-39.4	151.9	-62.3	120.6	R
I-3355b	3475	70.4	42.3	55.2	94.3	N
I-3345a	3465	58.7	-51.9	49.1	-17.2	N
I-3345d	3465	38.6	-40.7	52.1	-48.8	N
I-3335b	3455	61.5	59.4	44.3	113.2	N
I-3315b1	3436	68.8	-6.5	72.6	37.7	N
I-3265c	3385	65.0	-15.5	66.5	138.3	N
I-3240c	3360	65.2	-5.4	77.5	34.2	N
I-3215c	3335	53.6	-64.4	38.0	-20.4	N
I-3185a2	3305	37.2	-0.7	75.4	-126.4	N
I5-145b-4	3300	27.8	12.2	66.7	-159.9	N
I-3150a	3270	-45.6	233.4	-44.1	-43.9	R
I-3130d	3250	45.6	-71.1	29.9	-25.3	N
I-3110a	3230	30.1	12.5	67.7	-162.2	N
I-3015d	3135	47.7	-16.8	74.3	-59.2	N
I-3005e	3125	-61.0	205.4	-69.2	-65.1	R
I-2985a	3105	-50.5	229.7	-48.7	-47.7	R
I-2970a1	3090	63.0	67.3	39.1	109.1	N
I5-139b-1	3080	73.8	31.7	58.2	81.3	N
I-2935b	3055	69.3	-9.8	71.1	32.5	N
I-2915a	3035	-0.7	160.1	-50.4	83.4	R
I-2895a2	3015	-38.2	214.8	-56.6	-23.6	R
I5-136b-2	2975	-14.7	210.7	-50.3	-1.4	R
I-2850b2	2970	48.3	75.7	27.3	123.1	N
I5-134b-1	2963	71.4	88.8	29.4	91.0	N
I-2832c	2957	-10.3	176.5	24.7	152.2	R
I5-133b-2	2952	11.4	63.7	-59.6	58.0	N
I5-131b-3	2925	-40.4	222.5	-51.3	-32.1	R
I-2785b	2905	-67.7	183.3	-74.6	-120.9	R
I-2765a	2885	-17.6	200.0	-57.9	11.7	R
I-2735a	2855	20.9	22.0	58.3	-173.3	N
I-2720a	2840	70.0	-46.2	53.2	6.0	N
I-2705c	2825	67.9	-14.6	71.2	21.5	N
I-2695b	2815	58.4	21.8	72.3	122.6	N
I-2670a	2790	-9.8	205.6	-51.5	7.4	R
I-2640a	2760	-23.0	213.6	-51.7	-9.6	R
I-2620d	2740	61.3	70.3	36.4	110.9	N
I-2585a	2705	57.4	-1.3	87.2	30.0	N
I-2570c	2690	60.2	-17.8	74.9	-11.2	N
I-2555a2	2675	55.2	9.4	82.3	136.3	N
I-2545b	2665	42.3	13.8	73.8	179.9	N
I-2495a1	2615	-3.5	204.3	-49.5	11.9	R
I-2480b	2600	53.7	46.9	51.9	128.9	N
I-2440b	2560	-32.4	246.5	-29.0	-40.5	R
I-2415b1	2535	27.4	-88.6	9.5	-27.7	N
I-2405a2	2525	-21.4	247.5	-24.6	-35.0	R
I-2380a	2500	-13.6	173.9	-60.9	63.7	R
I-2355a	2475	69.2	22.3	66.6	86.6	N
I-2318b	2438	59.9	66.3	38.8	114.0	N
I5-117b-2	2420	-2.7	189.9	-54.7	33.9	R
I-2290a2	2410	65.6	6.7	76.7	71.0	N
I-2255a	2375	66.3	36.0	60.5	103.1	N
I-2220b	2340	67.2	38.7	58.5	101.4	N
I-2195b	2315	76.1	-56.9	45.8	18.9	N
I-2168b	2288	55.6	-38.7	58.8	-26.1	N
I5-114b-4	2285	-50.0	227.4	-50.4	-46.1	R
I-2145a	2265	-6.3	223.1	-38.7	-9.9	R

I-2133a	2253	-19.1	226.1	-41.0	-19.0	R
I-2123b	2243	-43.6	201.6	-69.0	-16.6	R
I-2085c	2205	-19.6	215.2	-49.3	-9.2	R
I-2045b1	2165	-38.2	219.7	-52.7	-27.7	R
I-2030a2	2150	-11.3	235.4	-31.2	-22.1	R
I5-106b-1	2140	-44.5	161.8	-71.9	115.6	R
I-2015a	2135	-18.5	239.2	-30.5	-28.3	R
I-2005b	2125	-59.1	182.7	-85.1	-103.7	R
I-1980b	2100	-40.5	179.4	-77.7	53.7	R
I-1967a2	2087	46.2	-77.5	25.1	-21.8	N
I-1937a	2057	51.5	-82.0	23.8	-15.3	N
I-1900a3	2020	24.7	25.1	58.1	179.6	N
I-1885a2	2005	41.8	7.3	77.1	-159.9	N
I-1858c	1978	-46.4	199.2	-71.9	-19.1	R
I-1845a	1965	-18.4	192.1	-61.8	25.2	R
I-1745b	1865	-35.0	199.2	-66.6	-0.4	R
I-1735a	1855	-31.5	125.7	-38.7	134.9	R
I-1715c	1835	38.7	-14.2	71.6	-82.6	N
I-1690b	1810	70.7	34.1	59.5	90.5	N
I-1680a	1800	62.1	-27.6	67.4	-9.8	N
I5-91b-3	1793	68.4	-0.9	73.8	49.2	N
I-1667a2	1787	40.4	42.4	51.3	148.0	N
I-1650a1	1770	76.8	6.4	60.2	56.6	N
I-1625c	1745	60.7	-48.6	52.0	-14.3	N
I-1612b	1732	76.7	-52.5	47.4	21.1	N
I-1585a	1705	-31.8	158.4	-63.6	103.2	R
I-1585c2	1691	-35.5	216.8	-54.1	-22.7	R
I5-87-3	1685	68.1	-28.4	64.2	7.9	N
I-1555b	1675	75.0	14.6	70.1	1.1	N
I-1540a	1660	46.3	48.4	48.5	138.0	N
I5-78-2	1600	51.1	17.5	51.3	146.2	N
I5-76-3	1535	-21.8	177.2	-65.8	57.9	R
I-1520c1	1520	-34.9	214.4	-55.7	-19.9	R
I-1500d	1500	49.7	-27.9	66.1	-42.8	N
I-1487d	1487	35.1	41.0	50.6	154.1	N
I-1475a1	1475	-9.4	250.0	-19.0	-31.0	R
I-1440b	1440	-35.8	212.8	-57.2	-19.3	R
I-1425a	1425	36.5	24.2	63.9	170.1	N
I-1340b	1340	60.6	-5.9	82.3	16.1	N
I-1330b2	1331	-66.8	192.6	-73.3	-99.1	R
I-1320a	1320	-33.9	214.3	-55.4	-18.9	R
I-1310c	1310	-2.3	214.4	-43.1	0.4	R
I5-75b-4	1305	63.0	-62.7	42.3	-7.9	N
I-1300a	1300	29.8	21.7	62.6	-179.4	N
I5-73-3	1295	61.6	-38.8	59.3	-13.1	N
I-1290a	1290	43.1	37.9	55.9	148.2	N
I-1280b	1280	-33.8	145.3	-55.0	121.4	R
I-1030b	1030	69.1	-5.0	72.5	41.0	N
I-950b	950	48.7	15.5	75.7	160.7	N
I-915c	915	20.4	51.5	37.2	156.1	N
I-900b	900	-20.5	188.9	-63.9	30.8	R
I-875b	875	-37.7	237.4	-38.2	-39.1	R
I-855b	855	-28.3	210.0	-56.3	-9.5	R
I-845a	845	66.1	37.1	59.8	103.9	N
I-835b	835	38.8	31.6	59.4	158.7	N
I-815a	815	-24.5	201.8	-60.0	4.7	R
I-798a	798	-21.9	238.0	-32.5	-29.3	R
I-780b1	780	-25.5	180.4	-68.0	50.1	R
I-770a	770	-19.0	168.6	-62.3	76.0	R
I-760b	760	62.3	31.4	64.6	112.8	N
I-748a	748	34.5	10.3	71.2	-160.6	N
I-723a1	723	66.1	-60.3	44.6	-2.8	N
I-693b	693	19.1	44.6	42.1	162.3	N
I-678c	678	63.3	9.3	78.2	85.2	N
I-658c	658	-18.9	231.5	-36.7	-23.0	R
I-648a2	648	-11.4	223.7	-40.1	-12.9	R
I-638a	638	-20.3	195.5	-61.3	17.9	R

I-623a	623	-22.3	217.5	-48.6	-13.2	R
I--590b	590	-29.9	205.9	-59.8	-5.6	R
I-575a	575	-16.0	156.8	-55.5	94.6	R
I-560c	560	-11.8	163.9	-57.0	81.6	R
I-544b	544	-47.1	144.9	-59.5	137.5	R
I-522c	522	-16.2	186.4	-62.3	37.5	R
I-515b	515	-47.9	224.6	-52.0	-41.9	R
I-483b	483	-19.5	226.8	-40.6	-19.7	R
I-458c	458	-22.1	219.4	-47.1	-14.9	R
I-442a2	442	-15.5	213.4	-48.9	-4.9	R
I-425b	425	-39.9	173.8	-76.2	75.8	R
I-410a2	410	-9.1	250.0	-18.9	-30.8	R
I-395a	395	-68.1	181.1	-74.3	-126.4	R
I-377a2	377	-19.5	184.3	-64.3	41.3	R
I-362a	362	-34.2	222.9	-48.7	-26.6	R
I-352a	353	-17.5	205.0	-55.1	4.4	R
I-318a	318	-26.2	168.2	-65.9	80.2	R
I-310a	310	-52.0	205.6	-68.7	-38.8	R
I-297a	297	-53.3	184.4	-86.1	-16.1	R
I-285a	285	-42.9	168.2	-75.4	98.3	R
I-260e	260	-24.6	192.9	-64.7	20.5	R
I-247a	247	-44.6	140.9	-55.5	136.8	R
I5-53b-4	177	-44.5	234.7	-42.7	-43.4	R
I-165c	165	50.0	82.8	22.6	118.5	N
I5-44-3	150	46.5	77.1	25.5	124.0	N
I-135b	135	17.6	44.0	42.1	163.7	N
I-108a	108	4.8	15.0	54.2	-155.0	N
I5-37-3	100	47.8	28.8	64.9	148.0	N
I-75a	75	13.6	38.2	44.9	171.1	N
I35b	35	54.0	-48.8	50.4	-25.5	N

TABLE A1.2: SAMPLES LIST INCLUDING STRATIGRAPHIC POSITION, SATURATION ISOTHERMAL REMANENET MAGNETIZATION RECORDED WITH A MAGNEIC FIELD OF 2700 mT (SIRM), AND S-PARAMETER.

Sample ID	**Stratigraphic position (m)**	**SIRM (mA/m)**	**S=1/2*[1-(IRM$_{-0.2T}$/SIRM)]**
I5-237b-3	6515	1916	0.71
I-6560b	6465	8816	0.88
I-6540b1	6445	10001	0.89
I-6485a	6390	7773	0.87
I-6450a3	6355	7574	0.88
I-6405c	6310	4520	0.85
I-6380b	6285	5170	0.86
I-6355b	6260	11602	0.84
I5-229b-3	6225	20556	0.87
I5-227b-3	6105	6249	0.83
I-6180c	6085	6152	0.92
I-6155b	6060	5909	0.88
I5-225b-3	6010	10956	0.88
I-6085c-1	5990	6436	0.78
I-605b1	5955	2099	0.86
I-6040a1	5945	7957	0.93
I-6020b2	5925	4898	0.85
I-6010b2	5915	5662	0.88
I-5995b1	5900	3468	0.82
I-5930b3	5835	5022	0.88
I-5915a1	5820	8674	0.91
I5-215-2	5730	7930	0.92
I-5555c	5675	3223	0.84
I-5495a1	5615	4816	0.89
I-5900a1	5590	4755	0.85
I-5460a1	5580	7585	0.86
I-5665c1	5570	17924	0.92
I-5870b	5550	9192	0.89
I5-209b-1	5545	15758	0.89

I-5600b2	5505	17215	0.92
I-5380c	5500	4501	0.70
I-5255b	5375	5426	0.88
I-5215a	5335	3331	0.83
I-5170a1	5290	13160	0.80
I5-195b-2	5220	7470	0.88
I-5050d	5170	2386	0.75
I5-198b-2	5145	12819	0.84
I-5020a3	5140	9986	0.76
I-4965d	5085	6572	0.74
I5-188b-1	5060	9153	0.86
I-4935b	5055	3154	0.64
I-4865b	4985	7779	0.75
I-4850e	4970	12727	0.79
I-4830c	4950	3595	0.77
I-4705a	4825	2044	0.72
I-4695c1	4815	5672	0.80
I-4680b1	4800	4420	0.85
I-4670b2	4790	6726	0.90
I-4650c	4770	6310	0.84
I5-180b-3	4760	6513	0.86
I-4580b	4700	3799	0.71
I-4550c	4670	6147	0.83
I-4475e	4595	1994	0.72
I-4445b	4565	3931	0.68
I-4370b	4490	2905	0.77
I-4340d	4460	4159	0.79
I-4250c	4370	5649	0.83
I-4235b3	4355	4222	0.70
I.4160c	4280	10750	0.83
I-4130d	4250	2132	0.58
I-4095b	4215	1048	0.58
I-4045c	4165	11446	0.89
I-4010a	4130	8816	0.91
I-3930b	4070	22926	0.95
I-3930c	4050	4132	0.88
I-3910a1	4030	5380	0.81
I-3835e	3955	10338	0.93
I-3715b	3835	7622	0.87
I-3670b	3790	11969	0.84
I-3630a	3750	12256	0.84
I-3610b	3730	10336	0.87
I5-153b-1	3650	8968	0.78
I-3500c	3620	13247	0.87
I-3460b	3580	9781	0.88
I5-150b-3	3505	7973	0.75
I-3315a1	3435	10344	0.88
I-3240a	3360	15881	0.83
I5-145b-3	3300	5595	0.76
I-3175b	3295	4722	0.79
I-3160b1	3280	26426	0.89
I-3130a2	3250	10450	0.82
I5-143b-1	3170	20498	0.86
I-3040a2	3160	18380	0.82
I-3005a	3125	8805	0.84
I-2985c	3105	2673	0.45
I-2970b2	3090	20841	0.83
I5-139b-2	3080	15973	0.84
I5-136b-4	3030	11351	0.82
I-2895a1	3015	7675	0.75
I-2875b	2995	6878	0.61
I-2865b	2985	4927	0.64
I5-133b-3	2930	17368	0.87
I5-131b-4	2920	26636	0.83
I-2765a	2885	7054	0.70
I-2705e	2835	16737	0.90
I-2705a	2825	25744	0.87

I-2670b	2790	10319	0.84

TABLE A1.3: SAMPLES LIST INCLUDING STRATIGRAPHIC POSITION, NORMAL REMANENT MAGNETIZATION (NRM), BULK SUSCEPTIBILITY (K).

Sample ID	**Stratigraphic position (m)**	**NRM (mA/m)**	**K (10^{-6} SI)**
I5-237b-2	6515	13.64	240
I-6560a2	6455	8.40	1550
I5-235b-2	6450	5.36	1660
I-6550a1	6445	10.61	2115
I-6540a1	6435	21.32	3150
I-6530c	6425	8.91	2010
I-6500b	6395	6.51	1180
I-6485a	6380	14.89	2060
I-6455a	6350	30.41	2540
I-6450b2	6345	13.70	1440
I-6440b2	6335	9.53	1725
I-6425a1	6320	18.97	3205
I-6415a	6310	12.64	1170
I-6405a	6300	4.73	1040
I-6380a	6275	16.95	575
I-6355a	6250	45.64	2580
I-6345a	6240	11.97	1175
I5-229b-1	6225	14.71	430
I-6325a	6220	15.15	1665
I-6275a1	6170	18.81	1075
I-6265a3	6160	10.69	975
I-6250a	6145	11.69	505
I-6215a	6110	13.05	725
I5-227b-2	6105	4.15	1150
I-6205a2	6100	11.20	1650
I-6190a2	6085	11.16	1065
I-6180a2	6075	11.59	1170
I-6165a2	6060	19.39	1395
I5-226b-2	6055	16.39	740
I-6155a2	6050	8.45	1235
I-6125a1	6020	8.86	1395
I5-225b-4	6010	6.62	1330
I-6110a1	6005	10.97	2145
I-6095a2	5990	5.28	665
I-6085a2	5980	6.04	185
I-6075b	5970	15.14	1200
I-6050a	5945	5.50	535
I-6040a2	5935	10.14	1605
I-6030a	5925	7.99	525
I-6020a2	5915	10.16	595
I-6010b1	5905	4.09	1190
I-5995b1	5890	4.14	985
I-5980a2	5875	8.35	1365
I-5970a2	5865	16.80	1195
I-5930a2	5825	5.84	1545
I-5685a	5810	4.82	515
I-5900a2	5805	30.67	1105
I-5665b	5785	51.92	2415
I-5870a2	5765	22.58	1205
I-5640a	5760	24.61	1935
I-5855b	5750	18.92	1340
I-5635	5755	11.97	1795
I-5855b	5750	18.92	1340
I5-216b-2	5745	34.80	1585
I-5840a	5735	8.25	1415
I-5830b	5725	7.72	1435
I-5600a2	5720	26.42	2030
I-5555a2	5675	6.42	935

I-5525a	5645	29.40	2575
I-5495a2	5615	8.87	1210
I-5460b1	5580	31.81	1445
I-5450a2	5571	10.76	1380
I-5430a2	5550	4.18	295
I5-209b-2	5545	24.06	2230
I-5390a2	5510	16.30	540
I-5380a	5500	16.39	370
I-5320b	5440	36.13	1290
I-5300b1	5420	11.07	940
I-5255a	5375	11.47	15
I-5225b	5345	14.90	540
I-5215b	5335	15.48	595
I-5170a3	5290	11.41	945
I-5115	5235	6.37	1225
I5-198b-4	5220	14.87	855
I-5095a1	5215	8.74	825
I-5070b	5190	4.89	35
I-5050b	5170	2.34	165
I-5040a2	5160	8.04	965
I-5030a	5150	13.50	745
I5-195b-3	5145	10.66	750
I-5020b2	5140	16.18	895
I-5010a	5130	8.82	505
I-4965b	5085	8.54	395
I-4950b2	5070	21.96	875
I5-188b-2	5060	3.53	80
I-4935a	5055	4.84	430
I-4920a	5040	8.15	345
I-4900a	5020	14.41	665
I-4875a	4995	9.45	355
I-4865a	4985	10.83	795
I-4850a	4970	27.35	1085
I-4830a1	4950	9.19	390
I-4800a	4920	7.92	5
I-4705b	4825	3.29	310
I-4695a2	4815	9.65	490
I-4680a2	4800	13.18	1145
I-4670a1	4790	36.39	900
I-4650a	4770	27.00	880
I5-180b-2	4760	28.89	1040
I-4580a	4700	13.35	295
I-4550b	4670	19.14	710
I5-177b-2	4660	6.91	235
I-4475b	4595	6.32	275
I-4475a1-bis	4585	18.84	940
I-4445a2	4565	8.52	460
I-4400b	4520	5.50	430
I-4370c	4490	6.01	320
I-4350a	4470	22.76	890
I-4340b	4460	10.76	545
I-4325a	4445	6.78	225
I-4295a	4415	8.84	300
I-4260b	4380	9.73	360
I-4250a1	4370	17.06	605
I-4235a3	4355	14.76	605
I-4210b2	4330	22.18	1030
I-4160b	4280	29.47	1070
I-4150b	4270	4.64	220
I-4130c	4250	2.99	105
I-4115c	4235	14.33	635
I-4095a	4215	5.05	320
I-4060a	4180	7.39	50
I-4045d	4165	91.13	2290
I-4010b	4130	41.07	1520
I-3930a	4050	122.81	4695
I-3920a2	4040	26.44	855

I-3910c	4030	20.23	645
I-3835c	3955	60.42	2255
I-3745c	3865	46.73	2215
I-3715a	3835	62.36	1715
I-3700b	3820	18.85	775
I-3700b1-bis	3810	23.98	890
I-3670a2	3790	45.98	1795
I-3650b	3770	60.23	2305
I-3630b	3750	67.41	2980
I-3610a1	3730	52.78	1825
I-3595a2	3715	27.85	1510
I-3545b1	3665	12.67	740
I5-153b-3	3650	22.10	1075
I-3500a2	3620	90.88	4440
I-3485b	3605	17.82	1225
I-3460a	3580	44.15	1805
I-3450a	3570	72.13	2650
I-3410b2	3530	128.94	5335
I-3390b	3510	18.28	1065
I5-150b-2	3505	17.40	965
I-3355b	3475	25.69	1030
I-3345a	3465	61.09	2430
I-3335b	3455	48.99	2170
I-3315b1	3436	49.90	2080
I-3285a2	3405	18.15	785
I-3265b	3385	77.22	3880
I-3240b	3360	95.21	3770
I-3215c	3335	5.73	165
I-3200a	3320	14.52	650
I-3185a2	3305	91.68	3775
I5-145b-4	3300	27.25	905
I-3160b2	3281	114.20	6090
I-3150a	3270	13.58	595
I-3130d	3250	34.02	1555
I-3110a	3230	34.31	1535
I-3075b2	3195	120.20	6170
I5-143b-3	3170	24.97	1680
I-3040c	3160	91.14	5230
I-3015d	3135	34.07	1545
I-3005e	3125	57.63	1830
I-2985a	3105	15.86	655
I-2970a1	3090	89.94	4870
I5-139b-1	3080	51.96	2415
I-2935b	3055	43.19	2010
I-2915a	3035	11.88	5
I-2895a2	3015	16.59	1060
I-2875a1	2995	15.45	635
I-2865a1	2985	21.23	955
I5-136b-2	2975	22.50	965
I-2850b2	2970	37.00	1775
I5-134b-1	2960	22.51	765
I-2832c	2952	26.66	1640
I5-133b-2	2930	42.55	1665
I5-131b-3	2925	54.66	3410
I-2800b	2920	64.59	175
I-2785b	2905	18.83	890
I-2765a	2885	16.30	1045
I-2735a	2855	56.12	2790
I-2720a	2840	46.13	2220
I-2705c	2825	83.77	5955
I-2695b	2815	53.39	35
I-2670a	2790	34.30	1840
I-2640a	2760	25.23	1155
I-2620d	2740	68.43	3830
I-2605b	2725	48.46	2540
I-2585a	2705	96.82	3795
I-2570c	2690	47.55	3890

I-2555a2	2675	17.15	540
I-2545b	2665	38.70	1680
I-2515a1	2635	44.98	2690
I-2495a1	2615	20.18	895
I-2480b	2600	81.30	4290
I-2440b	2560	6.38	400
I-2415b1	2535	17.91	880
I-2405a2	2525	13.06	995
I-2380a	2500	17.26	735
I-2355a	2455	115.84	770
I-2318b	2438	51.17	2160
I5-117b-2	2420	7.63	355
I-2290a2	2410	50.57	1725
I-2255a	2375	67.47	3680
I-2220b	2340	31.66	1220
I-2195b	2315	177.86	8110
I-2168b	2288	21.53	1100
I5-114b-4	2285	24.44	1140
I-2145a	2265	13.74	560
I-2133a	2253	26.86	1255
I-2123b	2243	3.87	210
I-2100a	2220	95.23	4005
I-2085c	2205	16.70	745
I-2045b1	2165	28.29	1585
I-2030a1	2150	39.70	2365
I5-106b-1	2140	8.13	420
I-2015a	2135	6.29	5
I-2005b	2125	10.81	865
I-1992c	2112	37.62	1390
I-1980a	2100	7.85	450
I-1967a1	2087	3.23	150
I-1937a	2057	18.98	775
I-1927b	2047	59.86	2915
I-1915c	2035	42.71	2565
I-1900a3	2020	50.42	1720
I-1885a2	2005	60.27	3130
I-1858c	1978	10.29	550
I-1845a	1965	24.32	590
I-1825c	1945	20.29	85
I-1805c	1925	24.92	1240
I-1745b	1865	10.25	830
I-1735a	1855	2.67	210
I-1725b	1845	8.78	390
I-1715b	1835	13.48	470
I-1690b	1810	11.09	310
I-1680a	1800	10.93	50
I5-91b-3	1793	31.63	890
I-1667a2	1787	136.45	5020
I-1650a1	1770	45.96	1945
I-1625c	1745	54.40	2400
I-1612b	1732	56.39	2230
I-1600b	1720	223.50	12000
I-1585a	1705	4.26	290
I-1570c2	1691	23.83	1545
I5-87-3	1685	25.15	570
I-1555b	1675	12.44	370
I-1540a	1660	21.73	490
I5-76-3	1535	7.26	400
I-1520c1	1520	7.85	545
I-1510a2	1510	89.11	4745
I-1500d	1500	64.14	3765
I-1487d	1487	55.68	2435
I-1475a1	1475	18.66	980
I-1455a1	1455	30.68	950
I-1450a	1450	143.34	8525
I-1440b	1440	13.07	555
I-1425a	1425	22.02	835

I-1340b	1340	3.33	190
I-1330b2	1331	32.70	1630
I-1320a	1320	3.37	280
I-1310c	1310	3.22	200
I5-75b-4	1305	31.94	890
I-1300b	1300	4.51	270
I-5-73-3	1295	178.82	6340
I-1290a	1290	3.78	195
I-1280b	1280	13.28	405
I-1030b	1030	5.31	180
I-950b	950	7.09	265
I-915c	915	1.92	135
I-900b	900	1.99	75
I-875b	875	5.45	280
I-865b	865	13.55	595
I-855b	855	8.10	465
I-845a	845	25.98	125
I-835b	835	11.28	240
I-815a	816	8.70	45
I-798a	799	8.89	25
I-780b1	780	5.81	265
I-770a	770	1.62	40
I-760b	760	4.16	145
I-748a	749	5.27	75
I-723a1	724	6.18	5
I-693b	693	5.46	145
I-678c	678	46.87	1825
I-658c	658	4.01	175
I-648a2	648	29.52	1510
I-638a	639	6.66	85
I-623a	625	2.48	90
I-605a	605	10.28	85
I-590b	590	10.27	650
I-575a	575	18.09	60
I-560c	560	4.29	205
I-544b	544	2.24	185
I-534b1	534	1.48	140
I-522c	522	3.54	190
I-515b	515	2.30	200
I-495a1	495	4.04	40
I-483b	483	3.97	250
I-458c	458	4.04	210
I-442a2	442	2.06	150
I-425a	425	3.85	60
I-410a2	410	16.11	670
I-395a	396	6.34	5
I-377a2	377	13.53	705
I-362a	362	13.54	5
I-352a	353	54.90	2610
I-342c	342	11.08	25
I-318a	319	7.46	90
I-310a	311	5.43	5
I-297a	297	2.13	20
I-285a	285	4.41	5
I-260e	260	3.75	95
I-247a	247	3.41	15
I5-53b-4	177	7.01	100
I-165c	165	10.53	485
I5-44-3	150	1.54	30
I-135b	135	14.97	685
I-108a	109	50.04	350
I5-37-3	101	5.26	50
I-95a1	95	18.71	5
I-75a	76	5.74	5
I-65b1	65	5.01	190
I-35b	35	1.65	140

Appendix 2

Geochronology data

This dataset contains the methodology description and the data of the geochronology study conducted in the central southern Alborz mountains. Samples were collected during two field seasons between 2005 and 2006. Mineral separation was performed at the Institute of Geosciences of Potsdam University using standard techniques (crushing, sieving, magnetics, and heavy liquids). Seven samples were analyzed by means of the $^{40}Ar/^{39}Ar$ technique (Tables A2.1 to A2.8; Figs. A2.1 to A2.7). One sample was analyzed using the U-Th/He technique (Table A2.9).

$^{40}Ar/^{39}Ar$ geochronology

The $^{40}Ar/^{39}Ar$ isotopic dating technique is one of the most commonly applied dating method based on the production of ^{39}Ar from ^{39}K during the irradiation of fast neutrons in a nuclear reactor and the accumulation of ^{40}Ar derived from the radioactive decay of ^{40}K (McDougall, I. and T. M. Harrison 1999). At high temperatures diffusion processes lead to ^{40}Ar mobility and eventually loss, preventing gas accumulation. At lower temperature, resistance to diffusion processes increases and the system becomes progressively closed (closure temperature). The closure to diffusion processes is distinct among different minerals and it mainly depends on variations in chemical composition and cooling rates (e.g., Reiners and Brandon, 2006). This implies that the closure temperature represents a range rather than a unique value. For example, the closure temperature for hornblende ranges between 460° and 600°C, for biotite between 280° and 400°C, and for K feldspar it varies between 180° and 260°C (e.g., Reiners and Brandon, 2006). In case of volcanic rocks, if reheating up to the closure temperature did not occur (e.g., burrial, intrusion of magmatic bodies and/or circulation of high-temperature fluids), the Ar age represents the timing of eruption. Conversely, in case of intrusive bodies the Ar age reflects the cooling age below the closure temperature.

Here, we describe the well-established protocol followed by the $^{40}Ar/^{39}Ar$ geochronology laboratory in the Institute of Geosciences at the University of Potsdam, which has been working since 2005 (e.g., Bachmann et al., 2009; Carrapa et al., 2009). Standard thin sections were prepared from fresh samples, in order to evaluate the occurrence of potassium-bearing minerals and to eventually determine the degree of weathering. Fresh and euhedral, inclusion-free biotite, hornblende, and K feldspar crystals were hand picked. The grains were wrapped in commercial-grade Al foil and then packed in a 99.999% pure Al sample holder which was finally wrapped in a 0.5 mm thick Cd foil to cut off the unnecessary slow neutron flux. Irradiation was performed at the Geesthacht Neutron Facility (GeNF) of the GKSS research centre of Geesthacht, Germany for four days (96 hours). The samples were irradiated together with the Fish Canyon Tuff sanidine standard in order to obtain the J value parameter for monitoring neutron flux. The standard sanidine was prepared at the Geological Survey of Japan and the determined age is 27.5 Ma (Uto et al., 1997; Ishizuka et al., 2002). Furthermore, K_2SO_4 and CaF_2 crystals were also irradiated to correct for the interference of Ar isotopes produced by the reactions on K or Ca in the samples. After one month since the irradiation, the samples were brought back to Potsdam and measured in the laboratory.

The analytical procedure included: 1) extraction of gas by means of stepwise thermal heating with a 50W CO_2 New Wave Gantry Dual Wave laser ablation system (wavelength 10.6 micrometer) on grain samples generally from 0.1 mg to a few tens of mg; in each step, sample grains were heated by continuous a CO_2 laser beam with a similar diameter of the grain size for one to two minutes; 2) purification of the released gas with SAES Zr-Al alloy getters and a cold trap, where the metal finger-tube is cooled down to the freezing temperature of ethanol for 10 minutes; and 3) measurements of the purified Ar gas with a Micromass 5400 noble gas mass spectrometer with high sensitivity and ultra-low background. The mass spectrometer has a pulse-counting system with an electron multiplier for measuring precisely very small amounts of gas. The Ar isotopic ratios of each measurement were finally obtained after corrections of, mass discrimination of atmospheric argon, interference of Ar isotopes derived from Ca and K during irradiation, and the decay of the radiogenic Ar isotopes (^{37}Ar and ^{39}Ar) produced by the irradiation. The calculation of ages and errors followed the procedure described by Uto et al., (1997) (Table A2.1). From the J values obtained by the four irradiations, the error of the J value was estimated as 0.4 %. Additionally, as a routine in each irradiation, two biotite K-Ar age standards, Sori93 biotite (92.6±0.6 Ma; Sudo et al., 1998) and HD-B1 biotite (24.21±0.32 Ma; Hess and Lippolt, 1994), were also irradiated. The accuracy of the dating system at each irradiation and the J values were confirmed by the ^{40}Ar/^{39}Ar dating of those biotites.

In six samples, plateau ages were calculated as a weighted mean age of the steps of plateau, which was defined according to the following criteria: 1) the ages agree within 2 sigma errors, excluding the J value error (or including only Ar analytical error) between two contiguous steps; 2) the ages between the first and the last step agree within 2 sigma errors, excluding the J value error (or including only Ar analytical error); 3) the total ^{39}Ar amount in the plateau is greater than 50%; 4) in each step more than 3% of the total ^{39}Ar amount was released; and 5) the plateau is composed of at least three steps (Figs A2.1, A2.2, A2.3, A2.4, and A2.5; Tables A2.1, A2.2, A2.3, A2.4, A2.5, and A2.6).

In one sample these criteria were not satisfied and the weighted mean age for six steps presenting an almost flat spectrum, is our preferred interpretation (Figs. A2.6 and A2.7; Tables A2.7 and A2.8).

U-Th/He geochronology

U-Th/He dating is based on the radioactive decay of ^{238}U, ^{235}U, ^{232}Th, and to a lesser extent on ^{147}Sm to ^{4}He. As in the Ar system, He starts to be progressively retained in a crystal when the temperature drops beneath the closure temperature. The closure temperature depends of the cooling rate with fast rates reflecting higher closure temperatures. In the case of zircon it ranges between 140° and 210°C, while for apatite it varies between 80° and 40° (Reiners and Brandon, 2006). In this study we only use the technique on zircons.

Zircon U-Th/He dating was performed in the (U-Th)/He laboratory at the University of Kansas following the procedure described by Reiners et al. (2002, and 2004). Hand-picked zircons of 210 to 270 µm in length and 85 to 110 µm in width were wrapped in Pt foil, heated for 10 minutes at 1290°C, and reheated until >99% of He was extracted from the crystal. Subsequently, the zircons were dissolved using HF-HNO_3 and HCl pressure vessel digestion procedures. Finally, U and Th concentrations were obtained by isotope dilution ICP-MS analysis. The ages were corrected for α-ejection using the FT ejection correction method (Farley, 2002). Mean (U-Th)/He ages were calculated on the basis of three zircon replicate analyses. Analytical uncertainties are ca. 8% and correspond to ca. ±2 σ (Table A41. 9).

TABLE A2.1: ^{40}Ar/^{39}Ar SUMMURY TABLE

Sample ID	**Minerals**	**Latitude (°N)**	**Longitude (°E)**	**Age analysis**	**Plateau ^{39}Ar (%)**	**Age±1σ (Ma)**	**Rock type**
250706-01	Biotite	35.5079	52.1691	Plateau	95.8	36.02±0.15	Tuff
101006-10	Biotite	35.9601	51.0899	Plateau	95.1	39.26±0.18	Monzogranite
101006-10	K feld.	35.9601	51.0899	Plateau	50.6	36.76±0.10	Monzogranite
310505-02	Hornbl.	35.8375	51.7837	Plateau	57.2	38.47±0.10	Syenite
280505-03	K feld.	35.8526	51.8003	Plateau	91.9	38.92±0.08	Porphyric syenite
280505-02A	K feld.	35.8544	51.8024	Weighted mean	70.4	38.00±0.08	Alkali Granite
031006-13	Biotite	35.8127	51.7983	Plateau	70.4	38.80±0.18	Granite

TABLE A2.2: ^{40}Ar/^{39}Ar STEP-HEATING RESULTS OF SAMPLE 250706-01 (BIOTITE)

Laser output (%)	**^{40}Ar/^{39}Ar**	**^{37}Ar/^{39}Ar**	**^{37}Ar/^{39}Ar (x10^{-3})**	**K/Ca**	**^{40}Ar* (%)**	**^{39}Ar$_K$ (%)**	**^{40}Ar*/^{39}Ar$_K$**	**Age±1σ (Ma)**
1.4	266.7±4.20	27.5±12.1	843.82±21.3	0.02	7.8	0.5	21.6±5.4	64.3±15.8
1.6	130.0±4.10	8.0±20.0	420.0±17.0	0.07	5.6	0.4	7.0±4.0	22.0±3.0
1.8	48.90±0.40	11.0±5.0	126.0±7	0.05	26.8	1.2	13.0±2.0	40.0±7.0
2.0	20.57±0.07	6.2±1.5	27.6±1.5	0.09	64.2	2.1	13.3±0.5	39.9±1.5
2.2	14.93±0.14	2.2±1.1	11.0±0.9	0.27	80.2	3.8	12.0±0.3	36.1±1.0
2.4	13.75±0.07	2.4±0.6	5.6±0.6	0.24	90.2	5.4	12.4±0.2	37.4±0.6
2.6	13.34±0.09	1.9±0.9	4.3±0.7	0.31	92.4	7.0	12.3±0.3	37.2±0.8
2.8	13.62±0.04	0.6±1.7	5.5±0.6	1.05	88.5	7.3	12.1±0.3	36.3±0.9
3.0	13.50±0.04	2.0±1.1	5.1±0.4	0.30	90.7	6.7	12.3±0.2	36.9±0.6
3.2	12.82±0.06	1.4±0.6	3.2±0.6	0.41	94.0	9.4	12.1±0.2	36.3±0.6
3.4	12.51±0.06	0.1±1.4	1.0±0.3	7.75	97.7	10.0	12.2±0.2	36.8±0.7
3.6	12.32±0.04	1.1±0.8	1.7±0.2	0.55	97.0	12.5	12.0±0.1	36.0±0.4
4.0	12.01±0.02	0.4±0.2	0.9±0.1	1.48	98.2	33.6	11.8±0.1	35.5±0.2

Total gas age: 36.41±0.21 Ma
Plateau age: 36.02±0.15 Ma
Plateau steps: 9 (from laser output 2.2 to 4.0 %)
^{39}Ar amount in the plateau: 95.8 %
J: 0.00169
Lab. code: C08079
Laser intensity: 50 W=100 %

TABLE A2.3: ^{40}Ar/^{39}Ar STEP-HEATING RESULTS OF SAMPLE 101006-01 (BIOTITE)

Laser output (%)	**^{40}Ar/^{39}Ar**	**^{37}Ar/^{39}Ar**	**^{37}Ar/^{39}Ar (x10^{-3})**	**K/Ca**	**^{40}Ar* (%)**	**^{39}Ar$_K$ (%)**	**^{40}Ar*/^{39}Ar$_K$**	**Age±1σ (Ma)**
1.4	1856.02±42.03	36.23±4.48	6237.95±149.25	0.01	0.94	0.40	18.04±14.81	54.07±43.71
1.8	288.52±0.49	6.06±0.86	917.63±6.63	0.10	6.29	2.44	18.25±1.93	54.69±5.69
1.2	31.26±0.15	1.70±0.19	62.12±1.09	0.35	41.97	8.76	13.14±0.32	39.54±0.96
2.4	18.77±0.09	2.41±1.44	21.10±0.80	0.24	68.44	7.53	12.87±0.31	38.74±0.94
2.6	17.07±0.13	4.95±0.91	14.40±0.41	0.12	78.82	9.28	13.52±0.20	40.65±0.61
2.8	17.71±0.10	1.78±0.22	16.07±0.59	0.33	74.50	8.39	13.22±0.19	39.76±0.59
3.0	15.04±0.06	0.58±0.71	6.64±0.49	1.02	87.46	12.26	13.16±0.18	39.60±0.56
3.2	14.71±0.05	0.66±0.75	6.23±0.34	0.89	88.07	10.39	12.96±0.15	39.01±0.47
3.4	13.75±0.06	0.77±0.88	3.34±0.30	0.76	93.56	14.85	12.87±0.16	38.73±0.49
3.6	13.45±0.07	1.25±0.58	2.34±0.19	0.47	96.06	12.19	12.94±0.12	38.93±0.38
3.4	13.41±0.07	1.64±0.71	2.08±0.35	0.36	97.00	11.49	13.03±0.16	39.20±0.49
3.6	14.08±0.11	7.47±3.23	2.33±1.38	0.08	87.73	2.02	12.45±0.60	37.47±1.79

Total gas age: 39.71 ± 0.29 Ma
Plateau age: 39.26 ± 0.18 Ma
Plateau steps: 9 (from laser output 2.6 to 3.4 %)
^{39}Ar amount in the plateau: 95.1 %
J: 0.001686
Lab. code: C08078
Laser intensity: 50 W=100 %

TABLE A2.4: ^{40}Ar/^{39}Ar STEP-HEATING RESULTS OF SAMPLE 101006-10 (FOR K FELDSPAR)

Laser output (%)	**^{40}Ar/^{39}Ar**	**^{37}Ar/^{39}Ar**	**^{37}Ar/^{39}Ar ($\times 10^{-3}$)**	**K/Ca**	**^{40}Ar* (%)**	**^{39}Ar$_K$ (%)**	**^{40}Ar*/^{39}Ar$_K$**	**Age±1σ (Ma)**
1.4	732.32±9.81	18.78±10.07	2271.31±35.69	0.03	8.68	0.46	64.77±5.95	186.97±16.34
1.6	87.47±0.47	0.28±1.68	241.04±1.80	2.09	18.61	1.62	16.29±0.46	48.87±1.38
2.0	25.80±0.07	0.83±0.54	45.23±0.29	0.70	48.62	7.27	12.55±0.12	37.79±0.38
2.6	13.43±0.01	0.08±0.05	5.14±0.06	6.92	88.77	27.67	11.93±0.02	35.92±0.16
2.8	13.17±0.01	0.04±0.12	3.46±0.02	14.85	92.28	28.46	12.16±0.02	36.60±0.16
3.2	13.19±0.02	0.22±0.10	3.54±0.07	2.62	92.29	10.50	12.17±0.03	36.66±0.17
3.6	13.09±0.05	0.26±0.25	2.86±0.14	2.23	93.80	6.05	12.28±0.07	36.97±0.25
4.0	13.01±0.03	0.31±0.36	2.36±0.15	1.89	94.96	5.58	12.36±0.07	37.20±0.26
5.0	13.52±0.02	0.26±0.28	5.22±0.06	2.27	88.85	12.41	12.02±0.05	36.19±0.20

Total gas age: 37.43±0.10 Ma
Plateau age: 36.76±0.10 Ma
Plateau steps: 4 (from laser output 2.8 to 4.0 %)
^{39}Ar amount in the plateau: 50.6 %
J: 0.00169
Lab. code: C08081
Laser intensity: 50 W=100 %

TABLE A2.5: ^{40}Ar/^{39}Ar STEP-HEATING RESULTS OF SAMPLE 310505-02 (HORNBLENDE)

Laser output (%)	**^{40}Ar/^{39}Ar**	**^{37}Ar/^{39}Ar**	**^{37}Ar/^{39}Ar ($\times 10^{-3}$)**	**K/Ca**	**^{40}Ar* (%)**	**^{39}Ar$_K$ (%)**	**^{40}Ar*/^{39}Ar$_K$**	**Age±1σ (Ma)**
3.0	19.37±0.04	2.40±0.01	33.94±0.24	0.24	49.76	11.23	9.66±0.07	34.85±0.30
3.4	11.85±0.02	2.78±0.01	5.67±0.04	0.21	88.78	31.60	10.54±0.02	38.00±0.17
3.6	11.44±0.02	2.83±0.01	3.86±0.06	0.21	93.12	21.16	10.68±0.02	38.49±0.17
3.8	11.40±0.02	2.83±0.02	3.63±0.07	0.21	93.70	20.34	10.71±0.03	38.61±0.18
4.4	12.07±0.02	2.81±0.01	6.15±0.06	0.21	87.85	15.67	10.63±0.02	38.31±0.18

Total gas age: 37.92±0.05 Ma
Plateau age: 38.47±0.10 Ma
Plateau steps: 3 (from laser output 3.6 to 4.4 %)
^{39}Ar amount in the plateau: 57.2 %
J: 0.00202
Lab. code: C07228
Laser intensity: 50 W=100 %

TABLE A2.6: ^{40}Ar/^{39}Ar STEP-HEATING RESULTS OF SAMPLE 280505-03 (K FELDSPAR)

Laser output (%)	**^{40}Ar/^{39}Ar**	**^{37}Ar/^{39}Ar**	**^{37}Ar/^{39}Ar ($\times 10^{-3}$)**	**K/Ca**	**^{40}Ar* (%)**	**^{39}Ar$_K$ (%)**	**^{40}Ar*/^{39}Ar$_K$**	**Age±1σ (Ma)**
1.4	15.05±0.04	0.05±0.01	8.27±0.11	1.38	83.80	8.07	12.62±0.04	45.38±0.24
1.6	10.95±0.03	0.06±0.01	0.35±0.07	0.04	99.13	8.91	10.86±0.04	39.12±0.20
1.8	11.10±0.01	0.06±0.00	1.19±0.03	0.57	96.90	33.32	10.76±0.01	38.76±0.16
2.2	10.97±0.01	0.04±0.00	0.62±0.04	3.14	98.39	28.58	10.79±0.02	38.89±0.17
3.2	11.05±0.01	0.05±0.01	0.62±0.08	2.37	98.40	15.98	10.88±0.03	39.19±0.18
4.4	11.35±0.03	0.04±0.02	2.29±0.22	3.37	94.09	5.15	10.68±0.07	38.48±0.29

Total gas age: 39.42±0.03 Ma
Plateau age: 38.92±0.08 Ma
Plateau steps: 5 (from laser output 1.6 to 4.4 %)
^{39}Ar amount in the plateau: 91.9 %
J: 0.00202
Lab. code: C07229
Laser intensity: 50W=100%

TABLE A2.7: ^{40}Ar/^{39}Ar STEP-HEATING RESULTS OF SAMPLE 280505-02A (K-FELDSPAR)

Laser output (%)	**^{40}Ar/^{39}Ar**	**^{37}Ar/^{39}Ar**	**^{37}Ar/^{39}Ar (x10^{-3})**	**K/Ca**	**^{40}Ar* (%)**	**^{39}Ar$_K$ (%)**	**^{40}Ar*/^{39}Ar$_K$**	**Age±1σ (Ma)**
1.4	52.22±0.12	0.02±0.01	128.29±0.60	5.20	27.40	3.28	14.31±0.16	51.38±0.60
1.6	12.98±0.03	0.02±0.01	9.22±0.20	7.56	79.03	6.71	10.26±0.06	37.00±0.27
1.8	12.04±0.02	0.03±0.00	5.02±0.10	8.18	87.71	13.51	10.56±0.04	38.07±0.20
2.0	16.43±0.02	0.05±0.00	21.07±0.07	2.65	62.13	38.27	10.21±0.02	36.80±0.17
2.2	13.35±0.03	0.02±0.01	8.53±0.12	3.79	81.13	12.49	10.83±0.04	39.02±0.22
2.8	15.06±0.02	0.03±0.00	15.11±0.10	0.62	70.38	17.28	10.60±0.03	38.20±0.19
3.2-6.6	13.02±0.02	0.02±0.01	7.19±0.13	2.89	83.69	8.45	10.89±0.04	39.25±0.22

Total gas age: 38.19±0.05 Ma
Preferred age:
Weighted mean age: 38.0±0.08 Ma
Weighted mean age steps: 6 (from 1.6 to 6.6 %)
^{39}Ar* amount in the weighted mean age: 70.4%
Alternative age:
Weighted mean age: 38.76±0.12Ma
Weighted mean age steps: 3 (from 2.2 to 6.6 %)
^{39}Ar* amount in the weighted mean age: 38.2%
Inverse isochron age :39.3±0.22Ma
^{40}Ar/^{36}Ar intercept=265±2
MSWD: 6,12
J: 0.00202
Lab. code: C07227
Laser intensity: 50W=100%

TABLE A2.8: ^{40}Ar/^{39}Ar STEP-HEATING RESULTS OF SAMPLE 031006-13 (BIOTITE)

Laser output (%)	**^{40}Ar/^{39}Ar**	**^{37}Ar/^{39}Ar**	**^{37}Ar/^{39}Ar (x10^{-3})**	**K/Ca**	**^{40}Ar* (%)**	**^{39}Ar$_K$ (%)**	**^{40}Ar*/^{39}Ar$_K$**	**Age±1σ (Ma)**
1.4	9623.84±308.	4.21±4.46	32877.3±1063	0.14	0.00	3.43	0.02±44.79	0.06±136.2
1.6	913.38±8.02	9.03±7.20	3070.94±27.4	0.06	0.78	4.94	7.15±1.98	21.63±5.95
1.8	177.42±0.46	1.18±0.17	571.18±2.36	0.50	4.95	7.18	8.80±0.56	26.56±1.67
2.0	72.78±0.28	1.00±0.14	207.33±1.51	0.59	16.00	8.48	11.65±0.41	35.10±1.23
2.2	36.60±0.12	0.75±0.11	81.45±0.76	0.79	34.51	11.36	12.64±0.23	38.04±0.69
2.4	25.76±0.11	0.76±0.11	43.12±0.66	0.77	50.91	11.18	13.12±0.20	39.48±0.63
2.6	22.10±0.05	0.30±0.38	32.74±0.61	1.93	56.40	9.54	12.47±0.19	37.54±0.58
2.8	17.89±0.14	0.33±0.44	19.05±0.54	1.78	68.78	9.08	12.31±0.19	37.05±0.59
3.0	16.49±0.05	0.38±0.39	12.66±0.35	1.55	77.61	13.70	12.80±0.12	38.52±0.39
3.2	14.31±0.03	0.56±0.12	4.29±0.20	1.06	91.64	15.50	13.12±0.07	39.48±0.26
3.4	15.64±0.06	1.82±0.39	7.57±0.56	0.32	87.21	4.72	13.66±0.18	41.08±0.56
4.0	17.46±0.16	9.55±2.76	12.82±1.76	0.06	85.40	0.89	15.05±0.65	45.20±1.95

Total gas age: 35.39±4.64 Ma
Plateau age: 38.8±0.18 Ma
Plateau steps: 6
^{39}Ar* amount in the plateau : 70.4%
J: 0.00169
Lab. code: C08080
Laser intensity: 50W=100%

TABLE A2.9: ZIRCOM U-Th/He RESULTS OF SAMPLE TSK01-B. BOLD REPRESENTS THE MEAN AGE

Age (Ma)	**Error (Ma)**	**U (ppm)**	**Th (ppm)**	**Th/U**	**He [nmol/g]**	**Mass [µg]**	**Ft**	**sdev**	**Rock type**
47.4	3.8	415.5	253.3	0.6	99.75	13.9	0.82		andesite
49.5	4.0	429.4	318.4	0.7	104.93	7.2	0.78		
45.4	3.6	513.0	400.4	0.8	117.98	10.1	0.79		
47.4	**3.8**	**452.6**	**324.0**	**0.7**	**107.55**	**10.4**	**0.80**	**2.1**	

Sample location: lat. 35.558°N. long.52.094°E

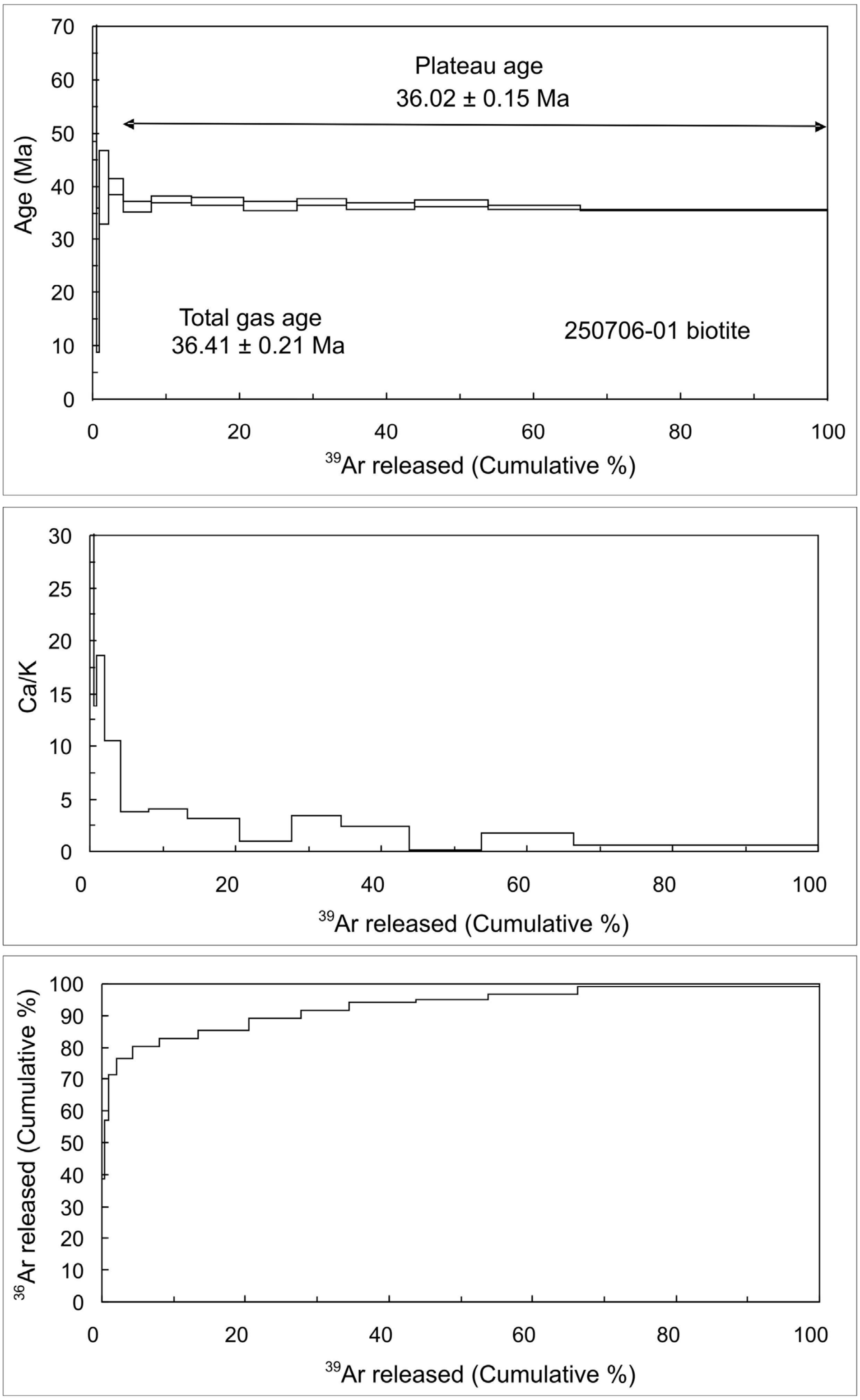

Figure A2.1: ^{40}Ar/^{39}Ar age spectrum of sample 250706-1. All errors are 2σ.

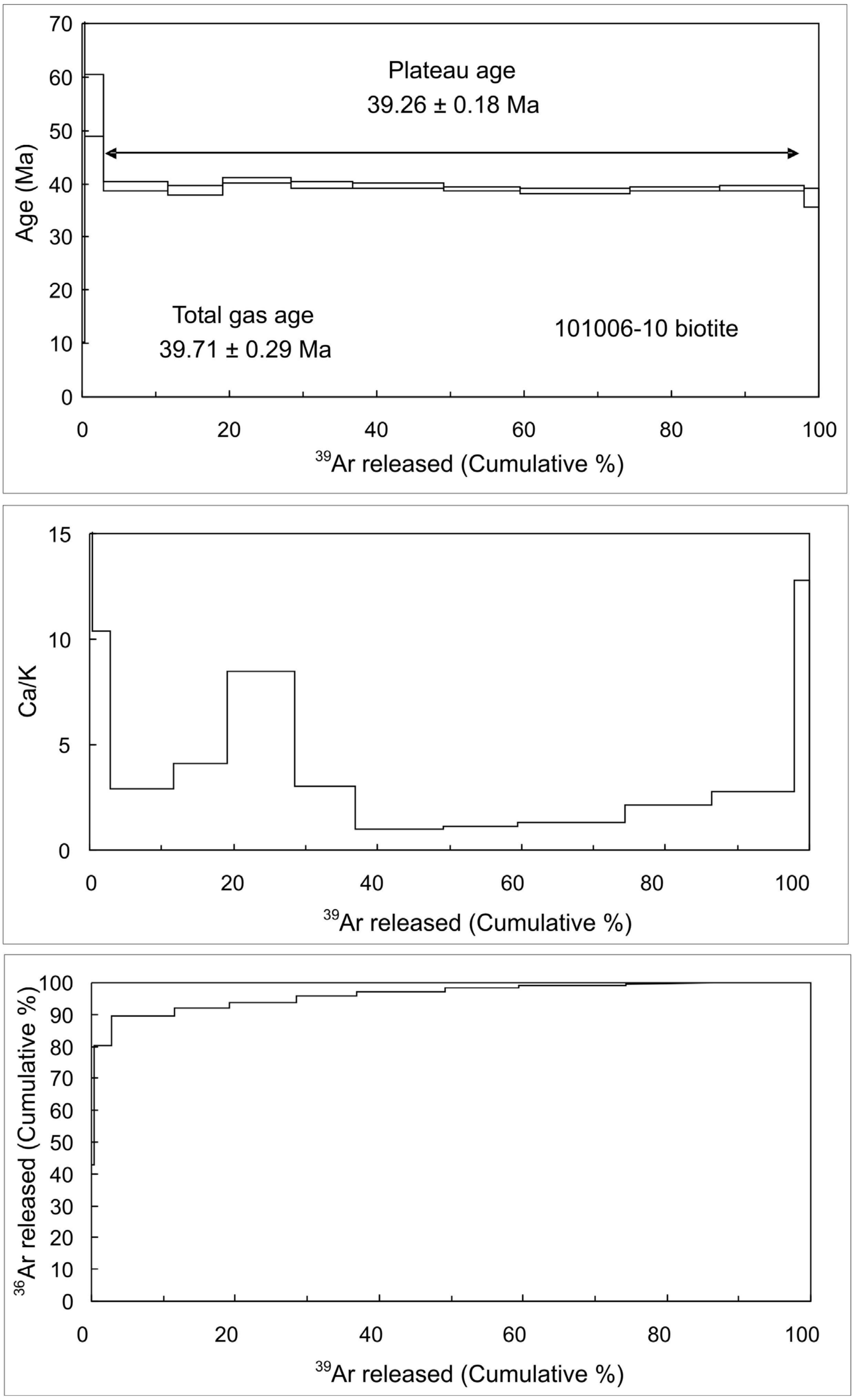

Figure A2.2: $^{40}Ar/^{39}Ar$ age spectrum of sample 101006-10. All errors are 2σ.

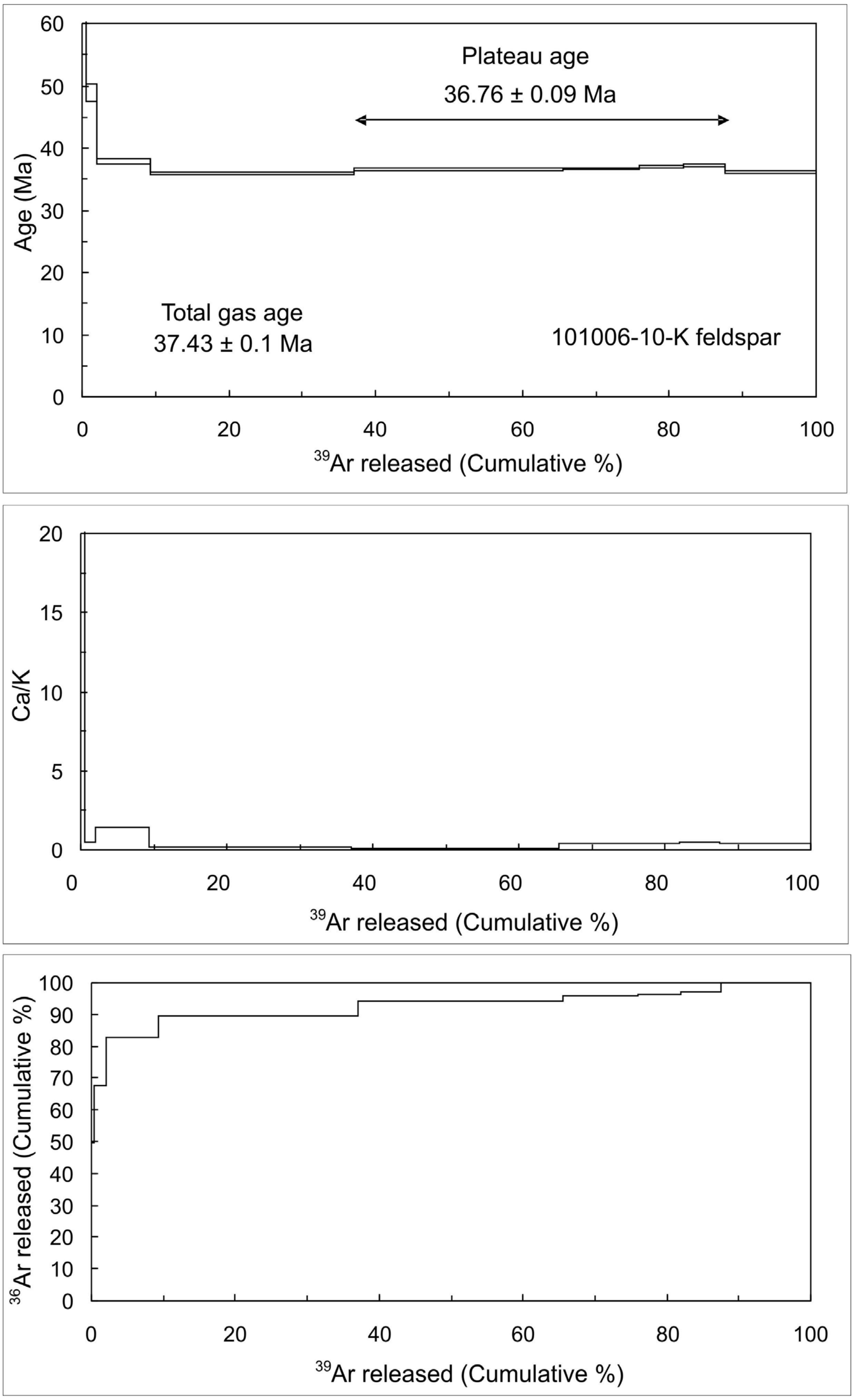

Figure A2.3: ^{40}Ar/^{39}Ar age spectrum of sample 101006-10. All errors are 2σ.

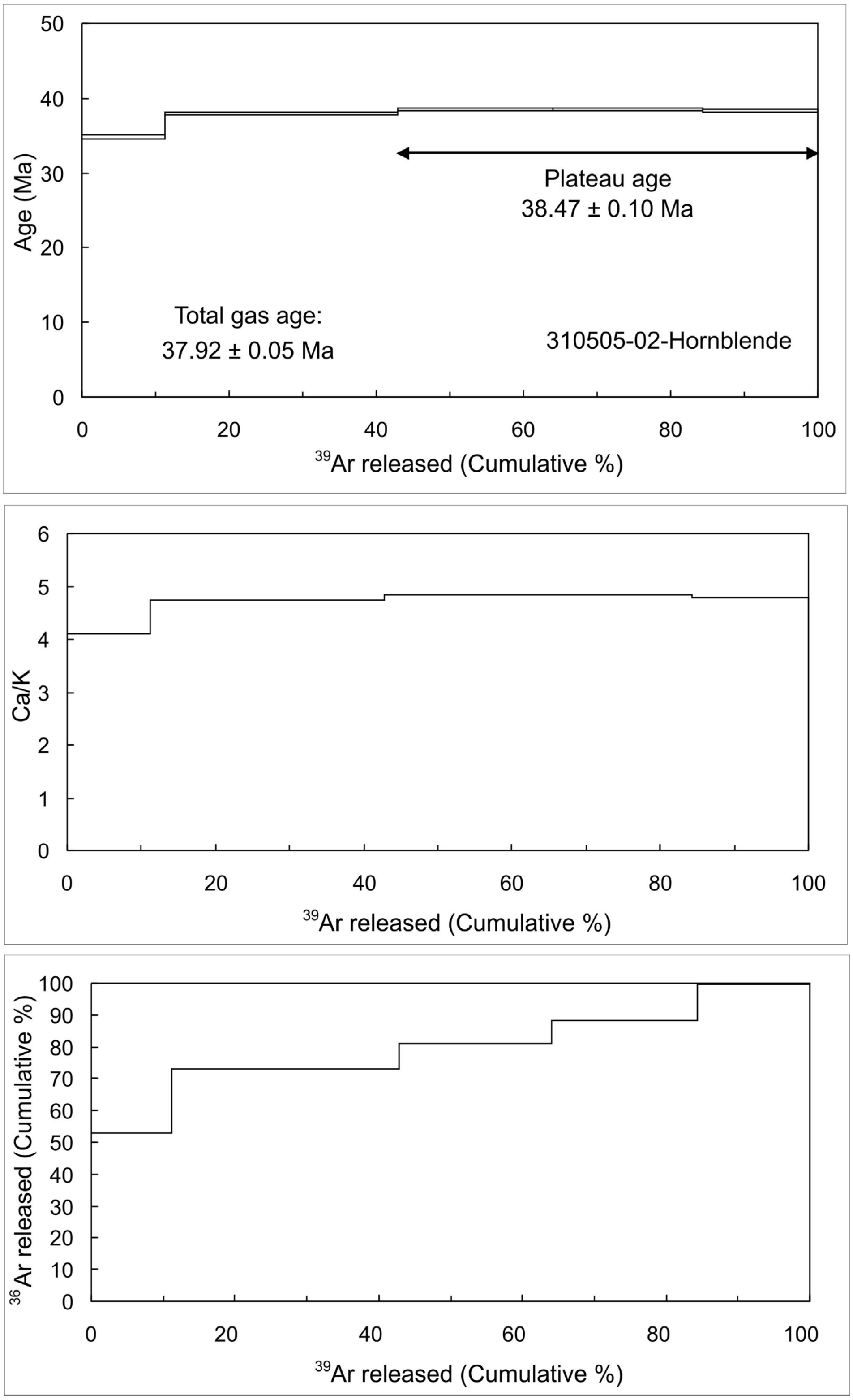

Figure A2.4**:** $^{40}Ar/^{39}Ar$ age spectrum. All errors are 2σ.

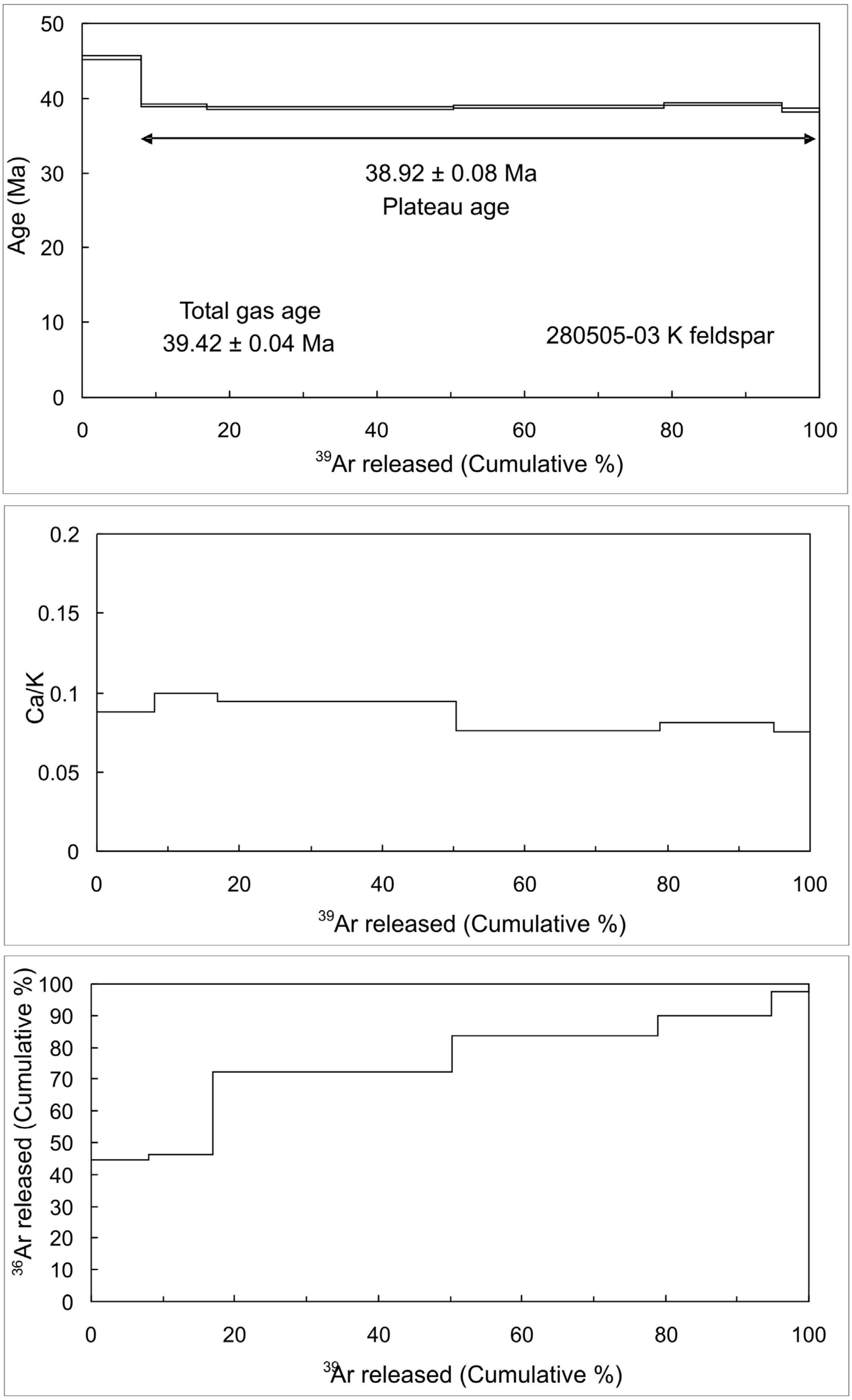

Figure A2.5**:** ^{40}Ar/^{39}Ar age spectrum of sample 280505-03. All errors are 2σ.

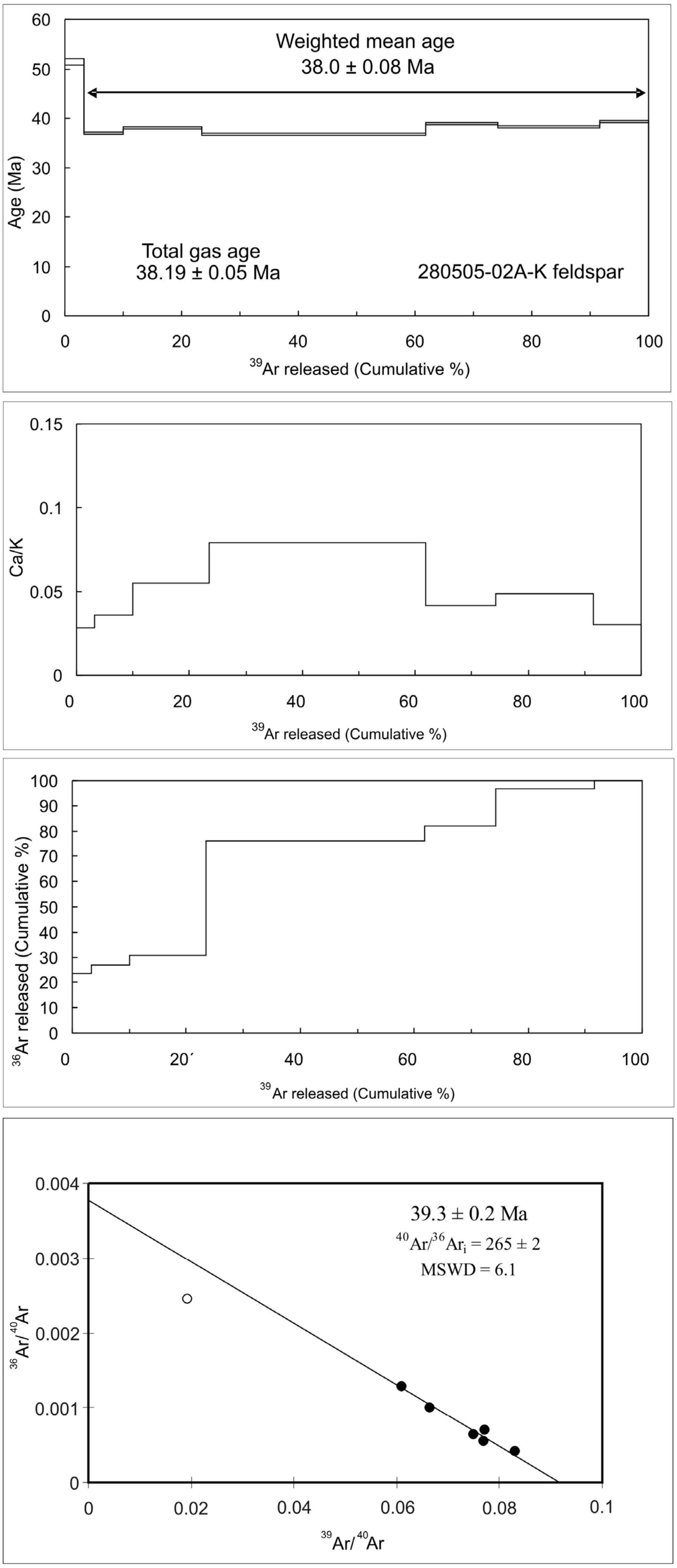

Figure A2.6**:** ^{40}Ar/^{39}Ar age spectrum and inverse isochron of sample 280505-02. Solid circles represent heating steps from 1.6 to 6.6 % of laser output. All errors are 2σ.

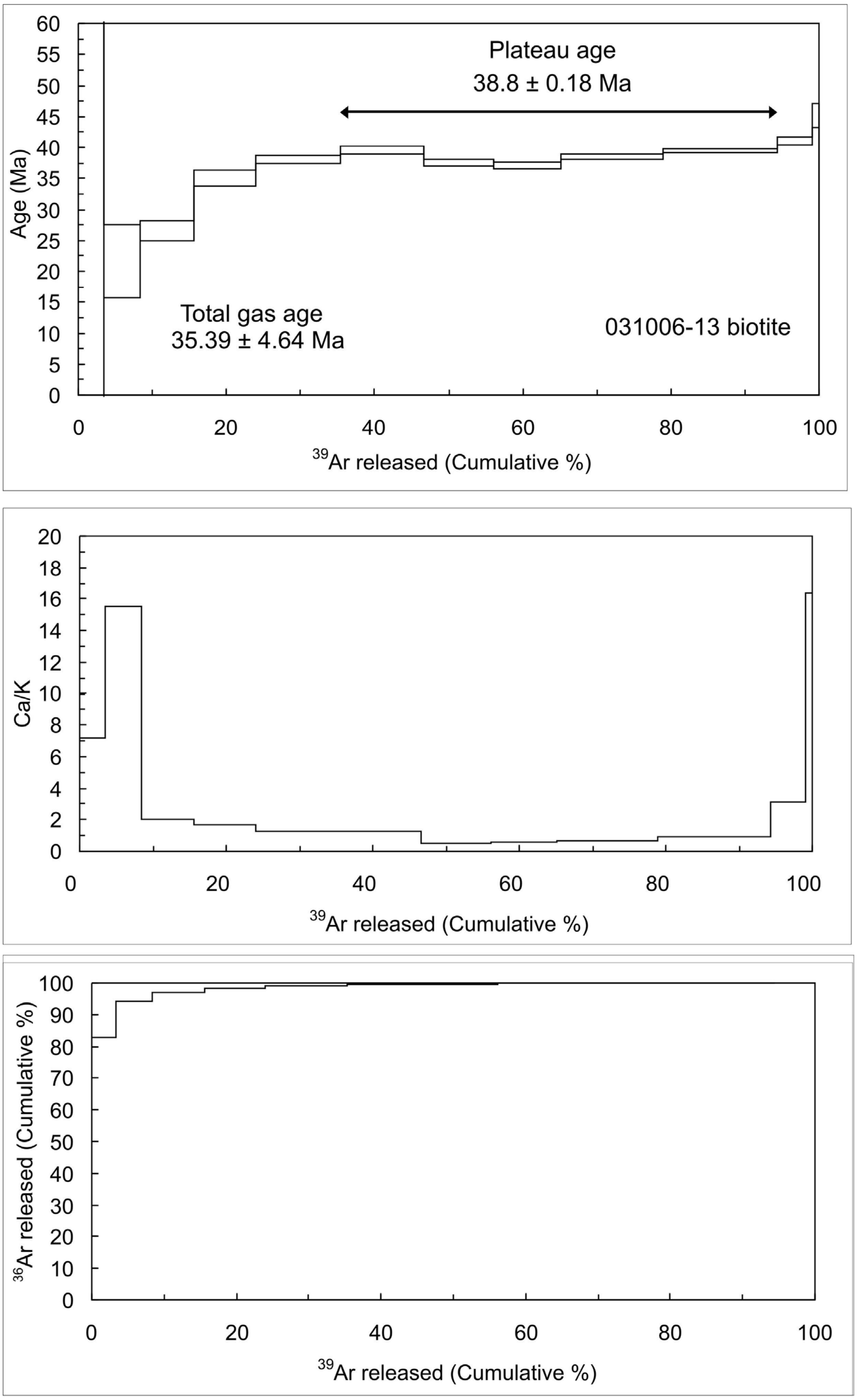

Figure A2.7**:** ^{40}Ar/^{39}Ar age spectrum of sample 031006-13. All errors are 2σ.

References

Bachmann, R., Oncken, O., Glodny, J., Seifert, W., Georgieva, V., and Sudo, M., 2009, Exposed plate interface in the European Alps reveals fabric styles and gradients related to an ancient seismogenic coupling zone: Journal of Geophysical Research v. 114, p. B05402, doi:10.1029/2008JB005927.

Carrapa, B., DeCelles, P.G., Reiners, P.W. Gehrels, G.E., and Sudo M., 2009, Apatite triple dating and white mica ^{40}Ar/^{39}Ar thermochronology of syntectonic detritus in the Central Andes: A multiphase tectonothermal history: Geology, v. 37, p. 407–410, doi:10.1130/G25698A.1.

Farley, K.A., 2002, (U–Th)/He dating: techniques, calibrations, and applications, *in* Porcelli D.P., et al., eds., Noble Gases in Geochemistry and Cosmochemistry, Reviews of Mineralogy, vol. 47, p. 819–844, doi: 10.2138/rmg.2002.47.18.

Hess, J.C. and Lippolt H.J., 1994, Compilation of K-Ar measurements on HD-B1 standard biotite, 1994 status report, *in* Odin G.S., eds., Phanerozoic time Scale, Bulletin of Liaison and Informations, Paris, IUGS Subcommision Geochronology, p. 19-23.

Ishizuka, O., Yuasa M., and Uto K., 2002, Evidence of porphyry copper-type hydrothermal activity from a submerged remnant back-arc volcano of the Izu-Bonin arc: Implication for the volcanotectonic history of back-arc seamounts: Earth and Planetary Science Letters, v. 198, p. 381-399, doi:10.1016/S0012-821X(02)00515-0.

McDougall, I., and Harrison, T.M., 1999, Geochronology and thermochronology by the ^{40}Ar/^{39}Ar method (Second Edition), Oxford, Oxford University Press, p. 269.

Reiners, P.W., and Brandon M.T., 2006, Using thermochronology to understand orogenic erosion: Annual Review of Earth Planetary Sciences, v. 34, p. 419–466, doi:10.1146/annurev.earth.34.031405.125202.

Reiners, P.W., Farley, K.A., and Hickes, H.J., 2002, He diffusion and (U–Th)/He thermochronometry of zircon: initial results from Fish Canyon Tuff and Gold Butte, Nevada: Tectonophysics, v. 349, p. 247–308, doi:10.1016/S0040-1951(02)00058-6.

Reiners, P.W., Spell, T.L., Nicolescu, S., and Zanetti, K.A., 2004, Zircon (U–Th)/He thermochronometry: He diffusion and comparisons with 40Ar/39Ar dating: Geochimica et Cosmochimica Acta, v. 68, p. 1857–1887, doi:10.1016/j.gca.2003.10.021.

Sudo, M., Uto, K., Anno, K., Ishizuka, O., and Schiumi, S., 1998, SORI93 biotite: A new mineral standard for K-Ar dating: Geochemical journal, v. 32, p. 49-58.

Uto, K., Ishizuka, O., Matsumoto, A., Kamioka H., and Togashi S., 1997, Laser-heating ^{40}Ar/^{39}Ar dating system of the Geological Survey of Japan: System outline and preliminary results: Bulletin of the Geological Survey of Japan, v. 48, p. 23-46,

Appendix 3

Sandstone petrography data

Fine to coarse grained sandstone samples were collected during four field seasons between 2005 and 2008. In the Kond Basin the sampling density for the Oligocene-early Miocene is in average one sample every ca. 70 m corresponding to one sample every ca. 1 m.y.. In the Eyvanekey basin the sampling density for the Oligocene-early Miocene interval is one sample every ca. 100 m (one sample every ca. 2.1 m.y.), while for the early to late Miocene is one sample every ca. 130 m (one sample every ca. 0.2 m.y.). In the Semnan basin the sampling density for the Miocene is one sample every ca. 380 m corresponding to ca. one sample every ca. 1 m.y.. This sampling density implies a good chance to have representative samples at the temporal resolution of 1 to 2 m.y. for the Oligocene, and less than 1 m.y for the Miocene.

Standard petrographic thin sections were prepared in the laboratory at the Institute of Geosciences, Potsdam University. At least 450 points per thin section were counted, according to the standard Gazzi-Dickinson counting method (e.g., Ingersoll et al., 1984). This is the most common technique used in provenance analysis, because it provides reliable modal compositions independent of grain size, depositional environment, and/or distance from the sediment-source area (e.g., Ingersoll et al., 1984). Petrographic counting parameters are shown in table DR2.1. Recalculated modal point-count data for the Kond, Eyvanekey and Semnan basins are recorded in tables DR2.2, 3, and 4.

TABLE A3.1: SANDSTONE POINTS COUNT PARAMETERS

Parameters (Q,F,Ls,C)	**Framework grains**
Q (quartz)	QZ monocrystalline (>62µm)
Q	Coarse polycrystalline QZ (>62µm)
Q	Fine polycrystalline QZ
Q	QZ(>62µm) in plutonic rock
Q	QZ(>62µm) in metamorphic rock
Q	QZ(>62µm) in volcanic rock
F (feldspar)	K monocrystalline (>62µm)
F	K(>62µm) in plutonic rock
F	K(>62µm) in volcanic rock
F	P monocrystalline (>62µm)
F	P(>62µm) in plutonic rock
F	P(>62µm) in metamorphic rock
F	P(>62µm) in volcanic rock
Lt (lithic)	Metamorphic lithic (with constituents <62µm)
Lt	Volcanic lithic (with constituents <62µm)
Lt	Clastic lithic (with constituents<62µm)
/	Single biotites/chlorites (>62µm)
/	Single muscovite (>62µm)
/	Single heavy minerals (>62µm)
/	Heavy mineral (>62µm) in crystalline rock
/	Heavy mineral (>62µm) in volcanic or clastic rock
/	Oxidized clast
/	Analcime
C (carbonate)	Sparry calcite (>62µm)
C	Mudstone-wackestone
C	Microsparitic limestone (with constituents <62µm)
C	Recrystallized limestone (with constituents >62µm)
C	Bioclast
	Cement, matrix, silt, porosity
	Glauconite
	Coarse silt
	Clay matrix/cement with fine-grained Fe oxides and/or hidroxides
	Pseudo-matrix (microsparite)
	Carbonate cement
	Calcitic overgrowth
	Other cements
	Intergranular porosity
	Oversized pore
Parameters (Lm,Lv,Ls,C)	**Fine lithics**
Lm (metamorphic)	Fine QZ
Lm	Quarzite
Lm	Phyllite
Lm	Fine micaschist
Lm	Schist QZ+Muscovite
Lv (volcanic)	Volcanic with effusive texture
Lv	Volcanic (mainly glass partially recrystallized)
Ls (sedimentary)	Argillite
Ls	Siltite
C (carbonate)	Sparry calcite (>62µm)
C	Mudstone-wackestone
C	Microsparitic limestone (with constituents <62µm)
C	Recrystallized limestone (with constituents >62µm)
C	Bioclast

TABLE A3.2: RECALCULATED MODAL POINT COUNT DATA FOR THE KOND BASIN

Formation	**Sample number**	**Stratigraphic position (m)**	**Q (%)**	**F (%)**	**L+C (%)**	**Lm (%)**	**Lv (%)**	**Ls+C (%)**
Stratigraphic section 1 (Emameh)								
LRF	AMP01	0	4.1	36.9	59.0	1.2	98.4	0.5
LRF	AMP01B	130	3.1	42.4	54.5	2.2	94.4	3.4
LRF	AMP02	157	2.9	45.4	51.7	0.6	92.6	6.9
LRF	AMP03	184	4.0	47.9	48.2	0.7	82.4	16.9
Stratigraphic section 2 (Kond)								
LRF	KD-01	11	2.0	32.2	65.8	0.5	93.4	6.1
LRF	KD-02	47	1.0	30.8	68.2	0.5	88.2	11.3
LRF	KD-03	84	5.8	44.9	49.2	3.6	91.5	4.8
LRF	KD-04	152	9.6	42.5	47.9	2.8	88.9	8.3
LRF	KD-05	227	2.9	27.5	69.6	2.7	94.2	3.1
Stratigraphic section 3 (Barg-e-Jahan)								
LRF	BEJ-04	46	5.2	26.9	68.0	2.8	84.9	12.4
LRF	BEJ-05	73	3.3	51.3	45.4	2.8	89.4	7.8
LRF	BEJ-07	145	21.3	8.4	70.3	8.1	60.7	31.2
LRF	BEJ-08	173	44.7	19.6	35.6	18.2	68.6	13.1
LRF	BEJ-01	518	4.7	43.5	51.8	1.6	93.6	4.8
URF	BEJ-02	571	2.0	32.3	65.6	0.5	89.0	10.5
URF	BEJ-03	621	4.3	29.9	65.8	0.0	82.1	17.9
Stratigraphic section 4 (Ira)								
LRF	LBO-01	29	5.3	30.7	54.0	3.0	90.9	6.1
URF	LBO-02	60	11.0	47.5	41.5	7.7	88.8	3.5

TABLE A3.3: RECALCULATED MODAL POINT COUNT DATA FOR THE SEMNAN BASIN

Formation	**Sample number**	**Stratigraphic position (m)**	**Q (%)**	**F (%)**	**L+C (%)**	**Lm (%)**	**Lv (%)**	**Ls+C (%)**
Stratigraphic section 8 (Semnan)								
URF	AE-05	413	19.3	25.1	55.6	10.6	77.7	11.7
URF	AE-09	813	21.7	21.7	56.5	23.9	52.1	23.9
URF	AE-10	846	23.6	14.9	61.5	24.2	68.3	7.5
URF	AE-13	1610	32.4	10.9	56.8	7.7	38.3	54.1
URF	AE-15	1770	30.5	9.1	60.4	6.6	37.1	56.3
URF	AE-17	2015	35.3	4.8	59.8	3.2	50.5	46.2
URF	AE-20	2495	24.7	4.1	71.2	7.7	42.6	49.8
URF	AE-22	2769	30.7	5.0	64.3	3.0	47.5	49.5
URF	AE-25	3141	27.2	10.1	62.7	8.3	45.8	45.8

TABLE A.3.4: RECALCULATED MODAL POINT COUNT DATA FOR THE EYVANEKEY BASIN

Formation	Sample number	Stratigraphic position (m)	Q (%)	F (%)	L+C (%)	Lm (%)	Lv (%)	Ls+C (%)
Stratigraphic section 6 (Tanghe east)								
LRF	TAN-01	42	7.9	50.3	41.8	0.0	93.2	6.8
LRF	TAN-02	120	3.8	45.3	50.9	0.0	89.4	10.6
LRF	TAN-03	206	6.5	42.2	51.3	0.0	87.6	12.4
Stratigraphic section 7 (Eyvanekey)								
LRF	I5-13	0	5.6	41.7	52.8	1.7	81.6	16.7
LRF	I5-19	13	7.5	34.8	57.7	1.8	90.9	7.3
URF	I5-31	303	7.7	34.4	57.9	1.2	84.4	14.4
URF	I5-35	315	5.9	34.4	59.7	5.3	87.7	7.0
URF	I5-36	323	4.1	25.8	70.1	1.0	96.9	2.1
URF	I5-40	339	6.4	28.3	65.2	0.7	90.8	8.5
URF	I5-46	419	6.5	23.1	70.4	1.7	97.2	1.1
URF	I5-48	523	9.3	28.7	62.0	2.6	82.8	14.6
URF	I5-55	763	22.5	18.9	58.6	29.0	61.1	9.9
URF	I5-59	995	21.3	28.7	50.0	36.3	47.6	16.1
URF	I5-60	1094	20.7	23.7	55.6	36.2	43.5	20.3
URF	I5-65	1194	19.5	35.1	45.5	27.8	43.2	29.0
URF	I5-67	1218	19.8	21.1	59.1	33.2	48.0	18.9
URF	I5-70	1318	13.8	41.1	45.1	28.9	55.9	15.1
URF	I5-72	1602	20.8	30.2	49.1	32.6	49.3	18.1
URF	I5-77	1702	18.0	36.1	45.9	19.3	67.7	13.0
URF	I5-79	1738	14.8	33.3	51.9	7.5	82.7	9.8
URF	I5-81	1764	6.5	21.8	71.7	2.6	94.7	2.6
URF	I5-82	1774	17.9	33.0	49.1	36.3	57.7	6.0
URF	I5-83	1790	17.3	27.5	55.2	26.3	65.1	8.6
URF	I5-86	1830	26.8	16.6	56.6	29.7	44.2	26.1
URF	I5-89	1870	12.6	30.3	57.1	13.2	82.6	4.1
URF	I5-92	1898	9.6	24.1	66.4	20.3	77.5	2.3
URF	I5-95B	2029	8.5	26.8	64.7	2.2	87.1	10.7
URF	I5-98	2097	21.9	30.6	47.5	36.6	51.0	12.4
URF	I5-103	2193	27.6	30.7	41.7	46.9	46.3	6.8
URF	I5-113	2483	21.4	24.0	54.6	28.7	61.9	9.4
URF	I5-120	2631	21.1	30.9	48.0	51.6	31.7	16.8
URF	I5-125	2825	28.7	24.4	46.9	47.2	39.6	13.2
URF	I5-128	2937	17.3	35.0	47.7	32.1	52.8	15.1
URF	I5-139	3212	21.9	30.2	47.9	30.9	51.4	17.7
URF	I5-142	3292	17.2	25.4	57.3	22.4	65.7	11.9
URF	I5-146	3440	20.1	29.9	50.0	20.4	55.5	24.1
URF	I5-151	3640	26.5	28.6	44.9	32.3	44.1	23.6
URF	I5-152	3728	22.8	31.4	45.8	38.0	52.5	9.5
URF	I5-156	3836	24.1	18.5	57.4	25.6	46.4	28.0
URF	I5-161	4011	28.8	28.8	42.5	44.8	50.0	5.2
URF	I5-164	4159	26.2	36.9	36.9	29.8	51.2	19.0
URF	I5-172	4503	22.9	17.9	59.2	4.9	20.4	74.7
URF	I5-180	4839	14.9	16.4	68.7	4.2	72.5	23.3
URF	I5-188	5008	33.8	11.0	55.2	10.2	30.7	59.1
URF	I5-190	5074	34.9	14.9	50.2	13.1	31.7	55.2
URF	I5-198	5288	20.3	13.2	66.6	6.4	62.8	30.7
URF	I5-200	5394	27.5	13.6	59.0	8.3	39.6	52.1

URF	I5-203	5470	16.8	23.9	59.3	5.9	81.2	12.9
URF	I5-207	5636	13.4	12.2	74.4	0.8	62.4	36.8
URF	I5-210B	5710	9.1	19.6	71.3	3.6	72.7	23.7
URF	I5-212	5734	14.1	17.8	68.1	2.4	75.0	22.6
URF	I5-218	5838	16.5	16.8	66.7	3.2	82.5	14.3
URF	I5-219	5918	17.2	21.6	61.1	6.4	71.1	22.5
URF	I5-221	6163	10.5	12.9	76.6	1.9	77.3	20.8
URF	I5-225	6265	32.8	10.3	56.9	2.1	54.8	43.2
URF	I5-232	6569	9.8	21.5	68.7	5.9	79.6	14.5
URF	I5-235	6653	8.7	12.0	79.2	1.5	77.2	21.3
URF	I5-239	6729	12.9	4.8	82.3	2.3	77.6	20.1
URF	I5-240	6777	15.6	16.7	67.7	4.0	68.7	27.4

References

Ingersoll, R.V., Bullard, T.F., Ford, R.L., Grimm, J.P., Pickle, J.D., and Sares, S.W., 1984, The effect of grain size on detrital modes: A test of the Gazzi-Dickinson point-counting method: Journal of Sedimentary Petrology, v.54, p. 103–116.

APPENDIX 4

X ray diffraction data

The mudstone samples were crushed by hand with an agate mortar, dispersed in deionised water, and disaggregated using ultrasonic treatment. The clay-sized fraction (<2 μm) was separated by differential settling. The aqueous suspension of each fraction was pipetted and dried at 50°C on zero-background sample holders. The oriented air-dried samples were glycolated and then heated up to 330°C and 530°C for 30 minutes. In order to perform a qualitative mineralogical analysis of the clay-sized fraction, x-ray diffraction patterns were acquired form oriented air-dried (Fig. A4.1), glycolated (Fig. A4.2), and thermally treated (330°C, Fig. A4.3; 530°C, Fig. A4.4) samples.

Illite-bearing samples exhibit peaks at ca. 10 Å, 5 Å, and 3.3 Å corresponding to the (001), (002) and (003) crystallographic planes, respectively. The position of these peaks does not change after glycolation and thermal treatment.

Cholrite-bearing samples present a peak at ca. 14.2 Å corresponding to the crystallographic plane (001). This peak is preserved after glycolation and with the thermal treatment the intensity tends to increase. Peaks at ca. 7.1 Å, 4.7 Å, and 3.5 Å represent the (002), (003) and (004) crystallographic planes, respectively. These peaks disappear after the thermal treatment at 530 °C.

Vermiculite-bearing samples show pronounced peaks at 14.1 (002) Å and 12.3 Å. With glycolation a new peak between 16.4 Å and 16.9 Å appears, while the 12.3 Å peak disappears. With thermal treatment the intensity of the 14.1 Å peak decreases dramatically, while a new peak at ca. 10 Å forms, overlapping the illite (001) peak.

Palygorskite-bearing samples present a peak at ca. 10.5 Å, which partially overlaps with the ca. 10 Å peak (001) of illite. This peak does not change position with the glycolation, but with thermal treatment tends to be less intense and to disappear at 530 °C.

In order to perform a quantitative mineralogical analysis of bulk-rock, x-ray diffraction patterns of randomly oriented whole-rock powders were acquired, and Rietveld refinement was performed (Fig. A4.5, A4.6, A4.7, A4.8).

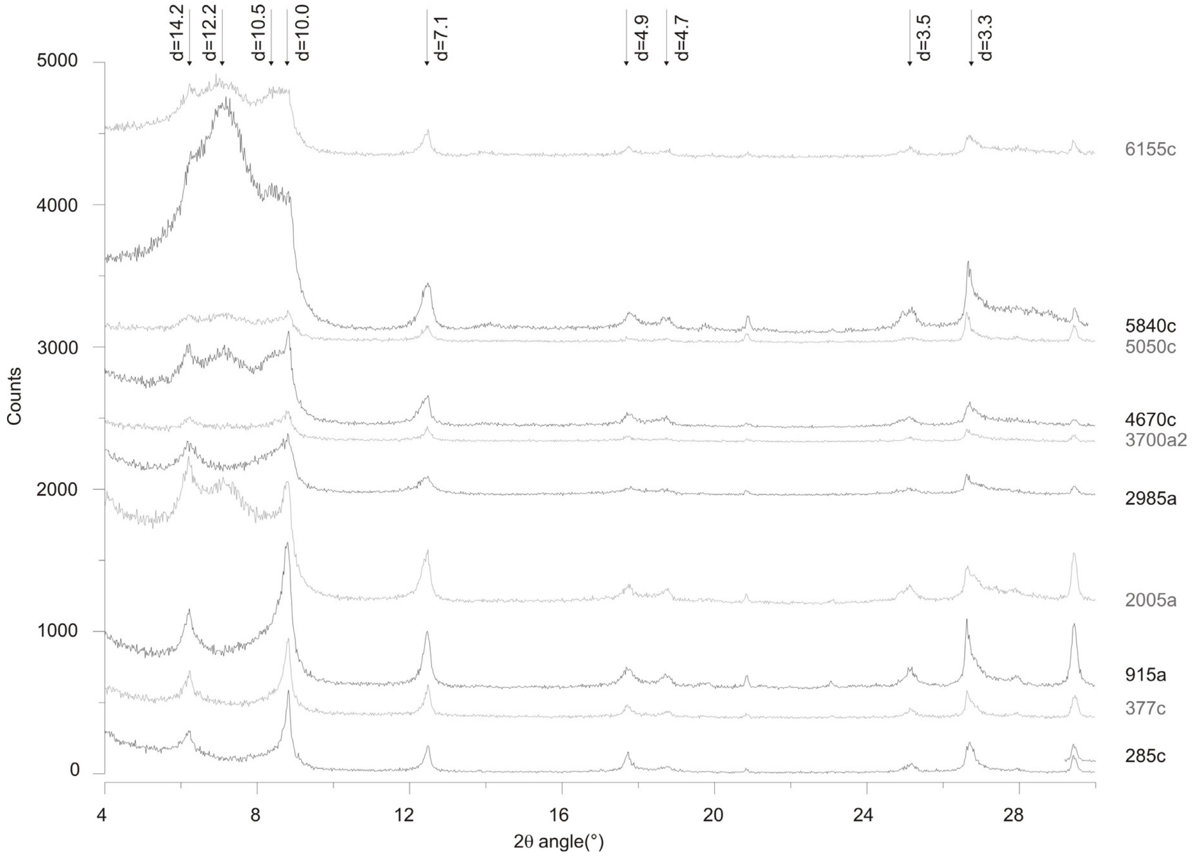

Figure A4.1: Diffraction patterns of oriented air-dried samples

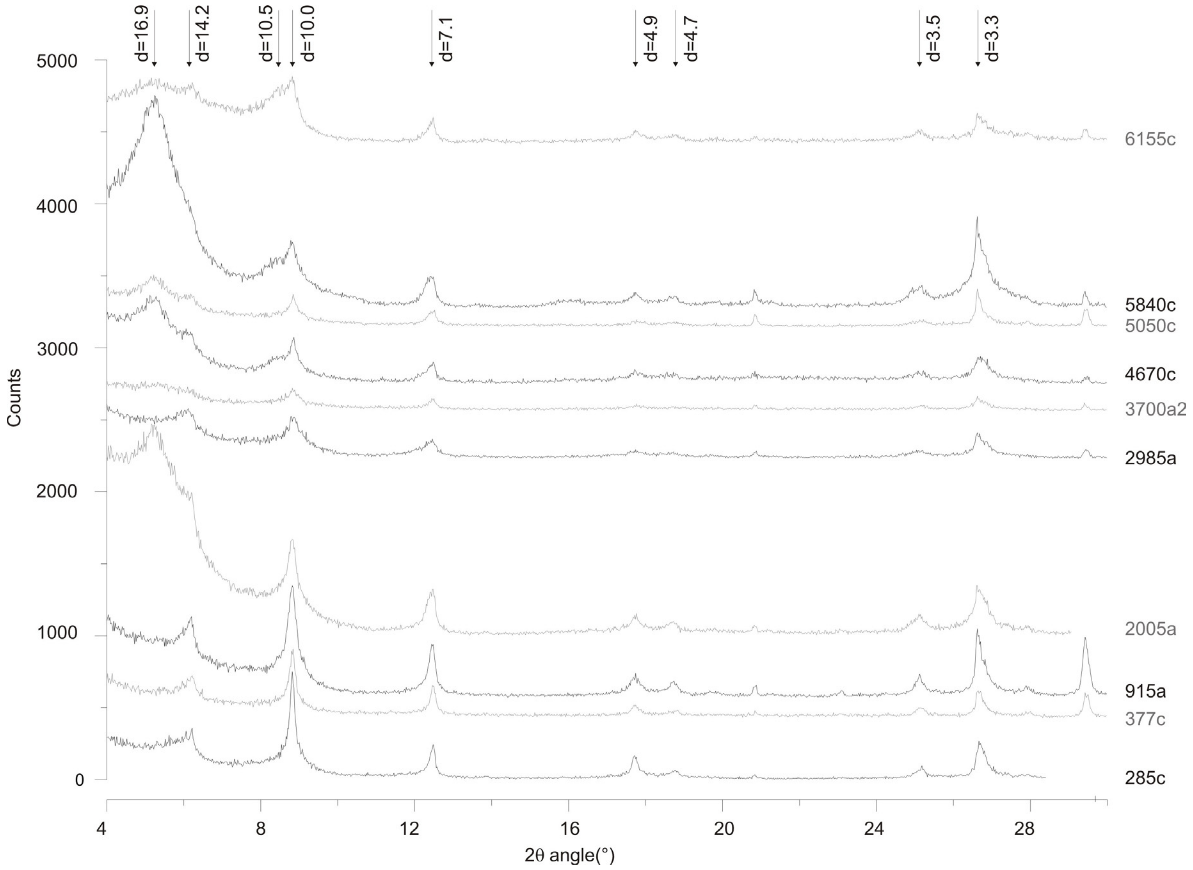

Figure A4.2: Diffraction patterns of glycolated samples

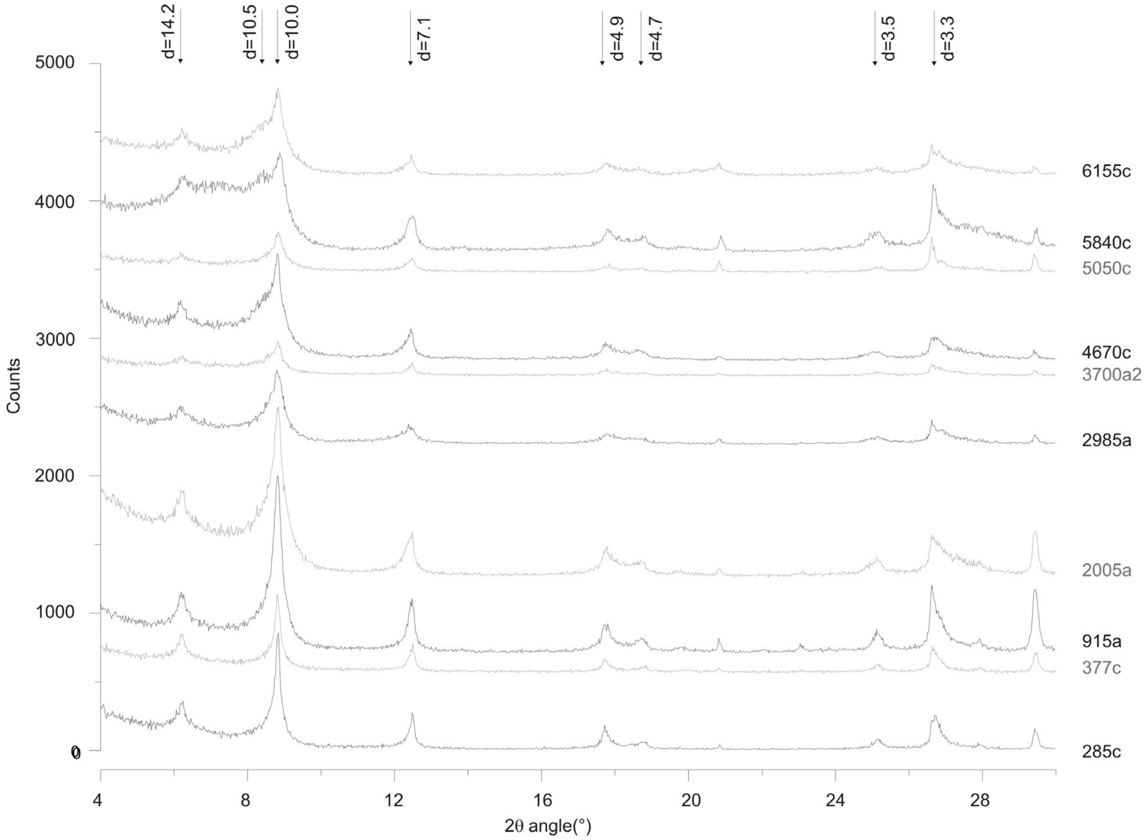

Figure A4.3: Diffraction patterns of thermally treated samples (330°C)

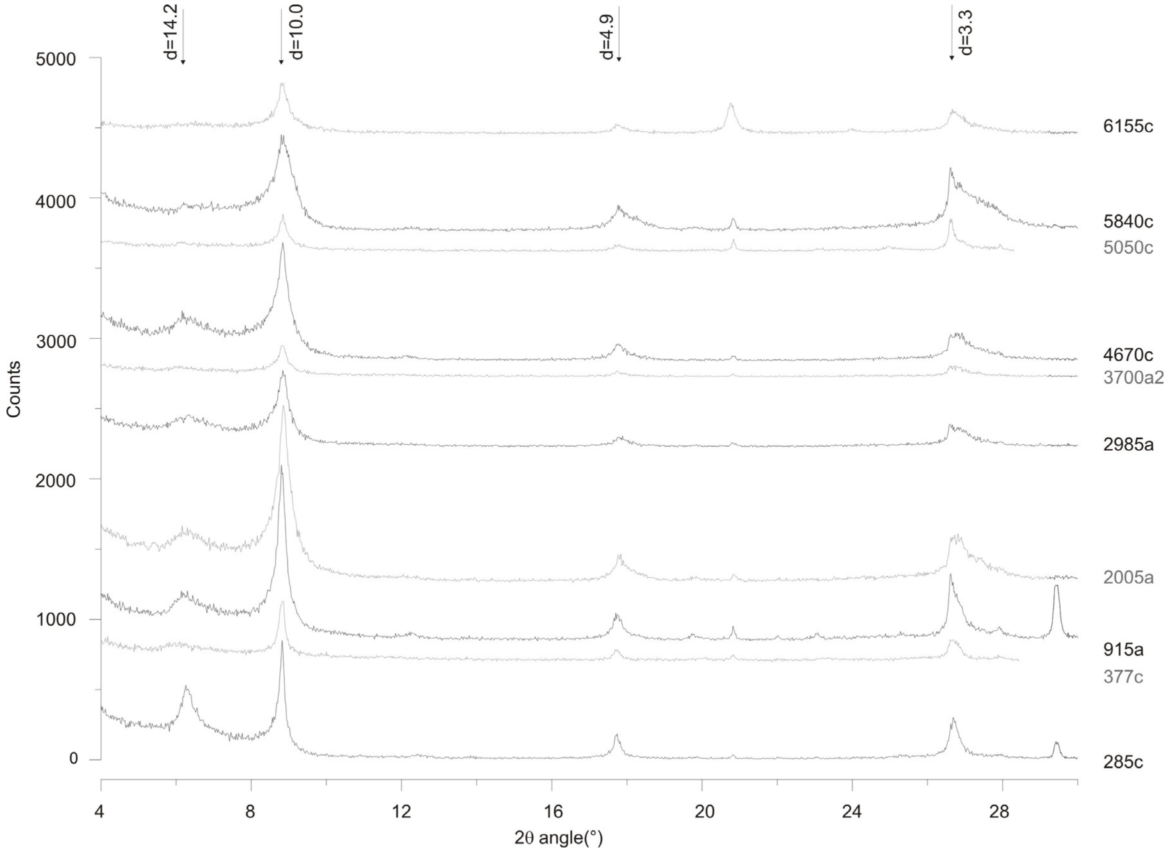

Figure A4.4: Diffraction patterns of thermally treated samples (530°C)

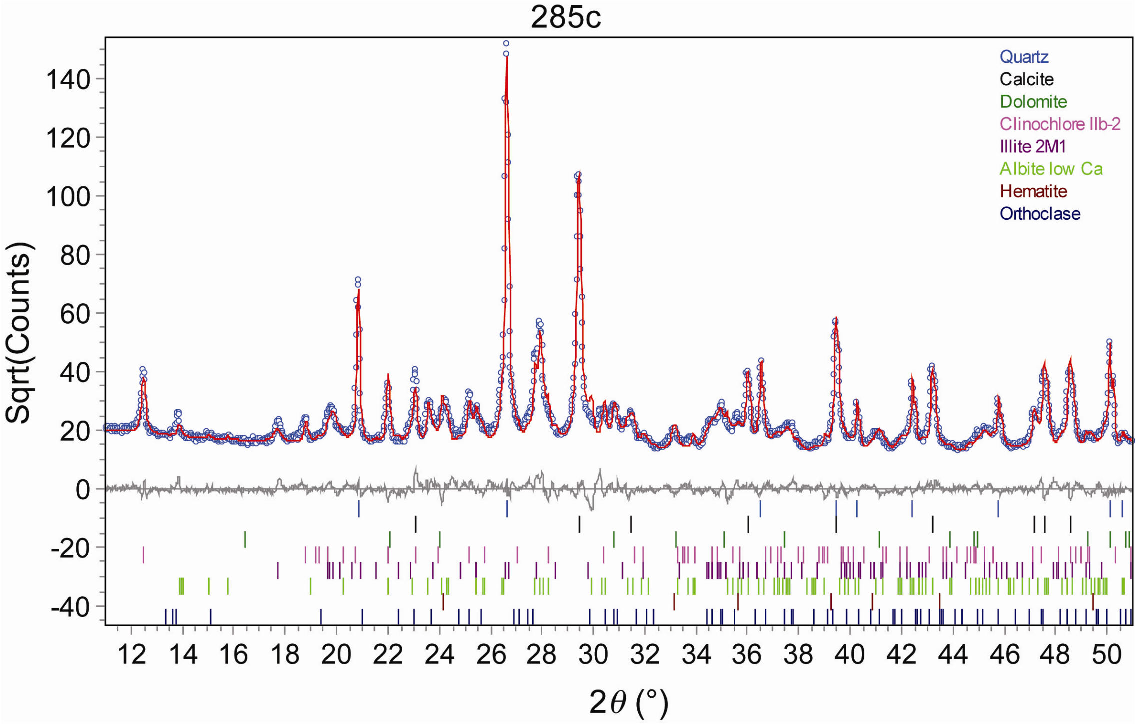

Figure A4.5: Observed profile (blue circles), calculated profile (red line), and profile difference (gray) for sample 285c. The tickmarks represent the calculate reflection positions of each mineralogical phase.

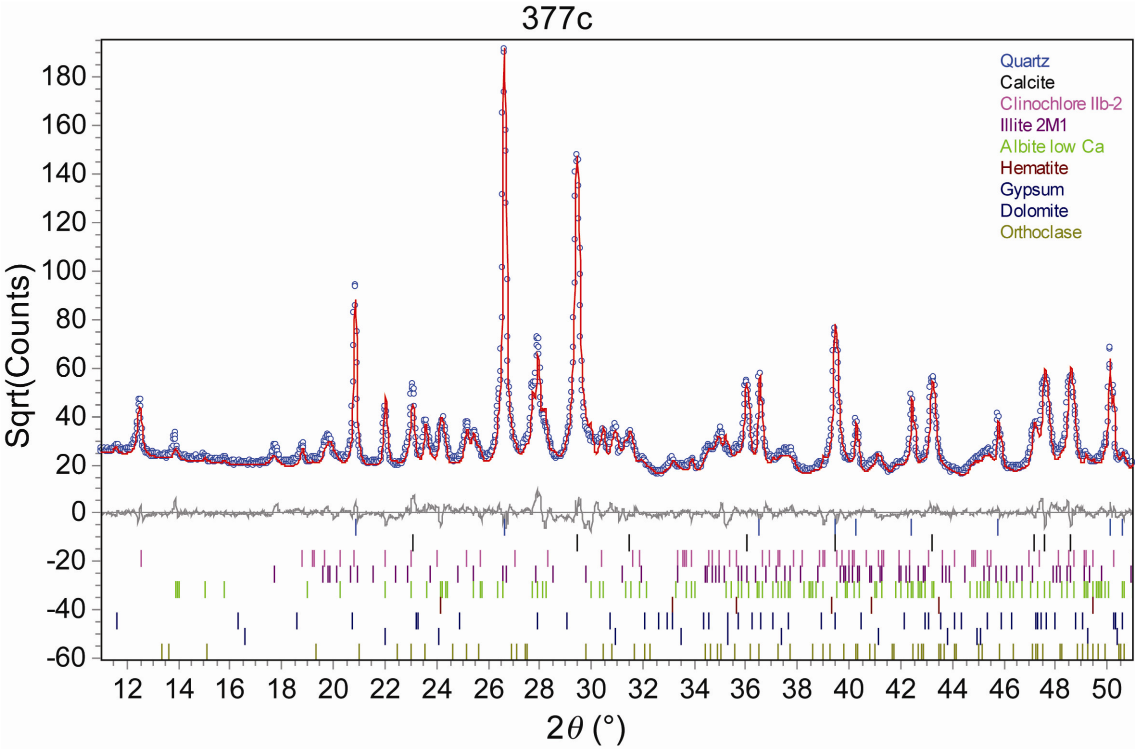

Figure A4.6: Observed profile (blue circles), calculated profile (red line), and profile difference (gray) for sample 377c. The tickmarks represent the calculate reflection positions of each mineralogical phase.

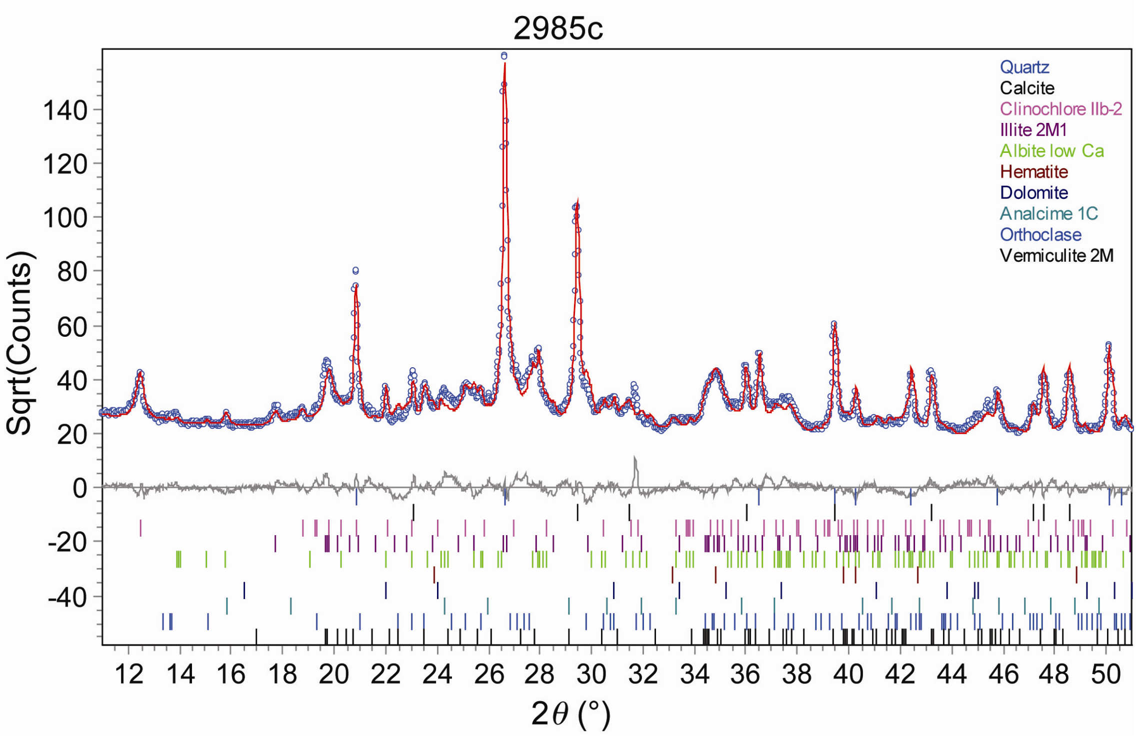

Figure A4.7: Observed profile (blue circles), calculated profile (red line), and profile difference (gray) for sample 2985c. The tickmarks represent the calculate reflection positions of each mineralogical phase.

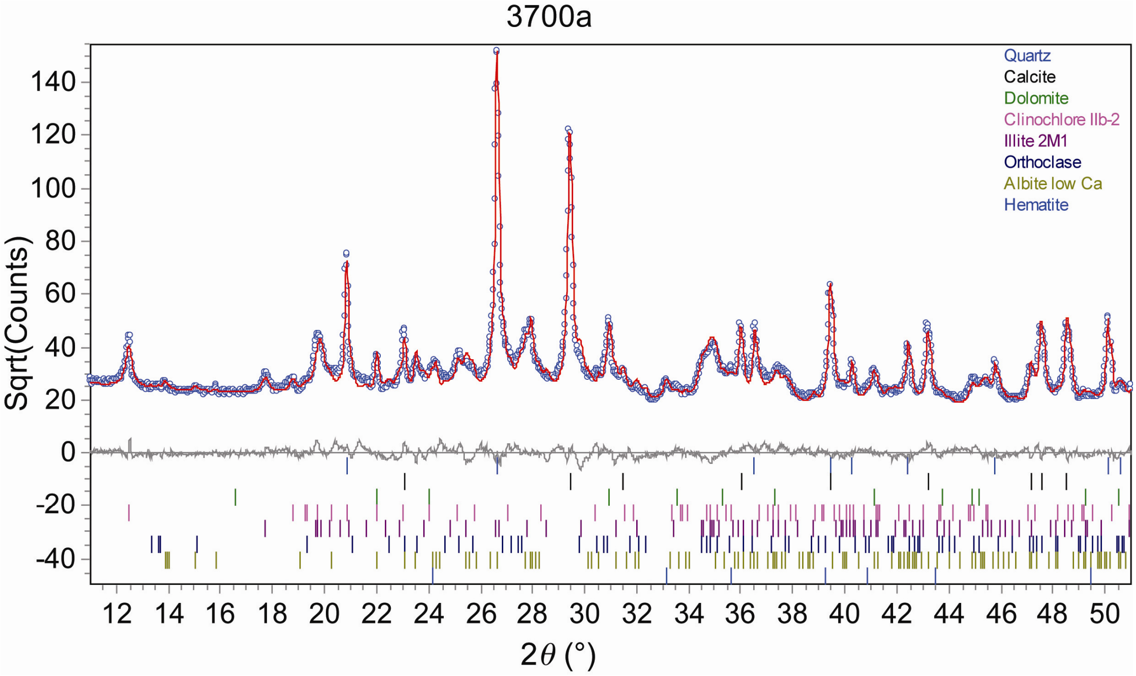

Figure A4.8: Observed profile (blue circles), calculated profile (red line), and profile difference (gray) for sample 3700a. The tickmarks represent the calculate reflection positions of each mineralogical phase.

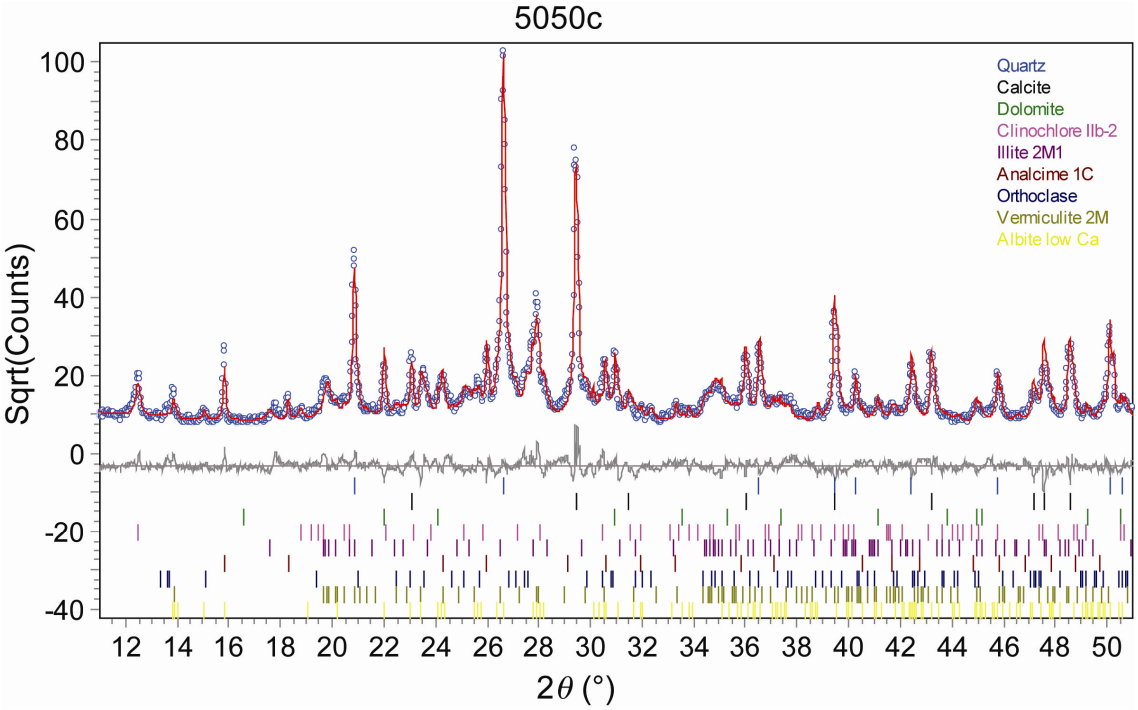

Figure A4.9: Observed profile (blue circles), calculated profile (red line), and profile difference (gray) for sample 5050c. The tickmarks represent the calculate reflection positions of each mineralogical phase.

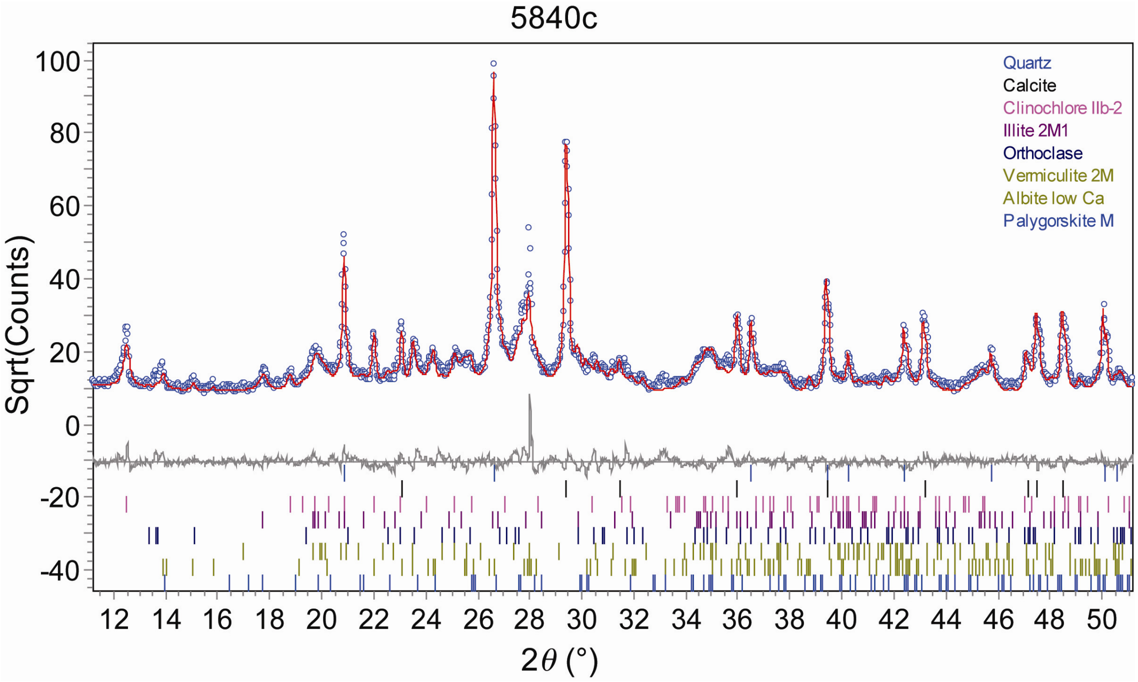

Figure A4.10: Observed profile (blue circles), calculated profile (red line), and profile difference (gray) for sample 5840c. The tickmarks represent the calculate reflection positions of each mineralogical phase.

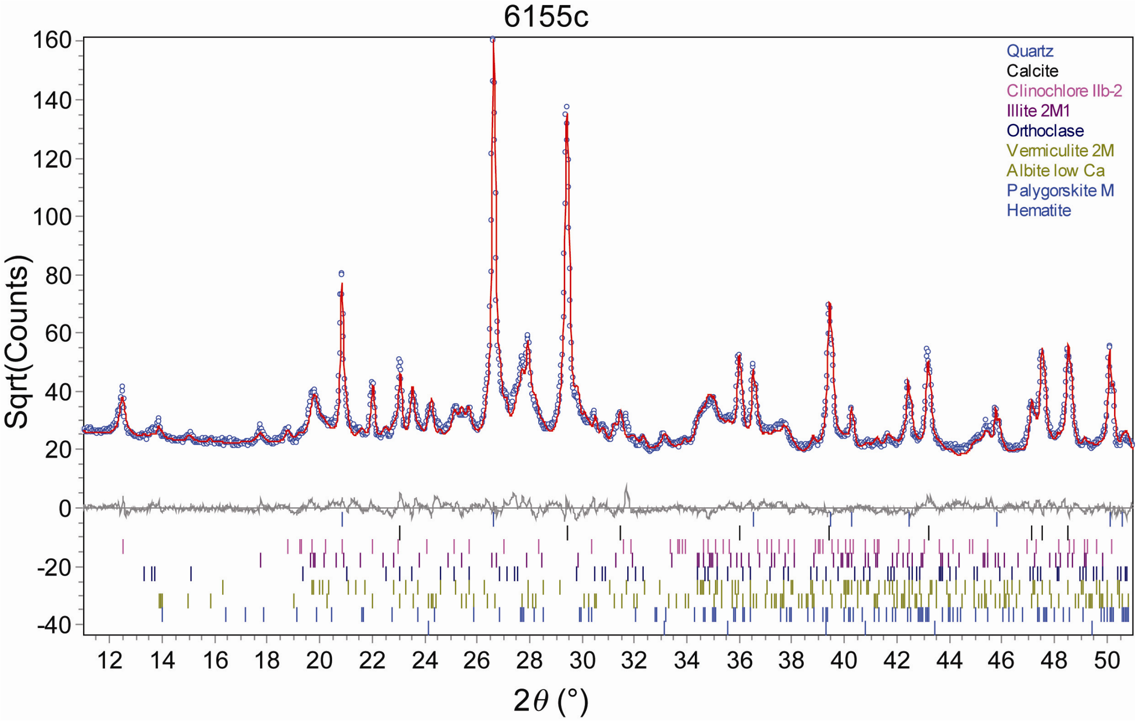

Figure A4.11: Observed profile (blue circles), calculated profile (red line), and profile difference (gray) for sample 6155c. The tickmarks represent the calculate reflection positions of each mineralogical phase.

APPENDIX 5

Stable isotope data

This dataset contains oxygen and carbon isotope data southern Alborz mountains, N Iran. Samples were collected in 2008. A ca. 6500-m-thick stratigraphic section (Eyvanekey stratigraphic section) was sampled for a total of 182 samples. Sample analyses were completed in 2009 at the Stable Isotope Laboratory at Leibniz Universität Hannover. Details and analytical techniques are described in chapter 4.

TABLE A5.1: RESULTS OF STABLE ISOTOPE ANALYSIS, INCLUDING SAMPLE TYPE (MUDSTONE AND CARBONATE; N=135; CALCRETE AND RHIZOLITH, N=47. ASTERISK MARKS AVERAGE OF TWO SAMPLES (SAME SAMPLE TYPE) FROM SAME HORIZONS. ITALIC INDICATES DIFFERENT SAMPLE FROM SAME HORIZONS

Sample ID	$\delta^{18}O$ (SMOW)	$\delta^{13}C$ (PDB)	Sample type	Stratigraphic level (m)	Latitude (°N)	Longitude (°E)
EV08-01 *	21.41	-5.31	Calcrete	25	35.48092	52.16447
EV08-02 *	21.52	-5.48	Calcrete	35	35.48092	52.16447
U1-01	22.13	-5.86	Calcrete	50	35.48052	52.16396
U1-02 *	22.45	-4.31	Mudstone	70	35.47030	52.19547
U1-03	22.03	-4.52	Mudstone	103	35.46980	52.19521
U1-03A	22.75	-2.63	Mudstone	130	35.46946	52.19513
U1-04 *	23.79	-3.49	Mudstone	233	35.46854	52.19396
U1-04A	24.96	-2.30	Mudstone	260	35.46833	52.19385
U1-05 *	23.51	-4.27	Mudstone	300	35.46764	52.19364
U1-05	24.55	-2.98	Mudstone	310	35.46746	52.19356
EV08-04	22.59	-4.54	Carbonate	311	35.46747	52.19352
EV08-05	22.47	-4.59	Carbonate	312	35.46747	52.19352
U1-05B *	24.33	-2.69	Mudstone	340	35.46687	52.19330
U1-06 *	24.38	-3.08	Mudstone	348	35.46680	52.19318
EV08-06	23.84	-3.33	Carbonate	357	35.46673	52.19318
EV08-07	23.12	-3.38	Mudstone	365	35.46665	52.19298
EV08-09 *	23.32	-4.31	Carbonate	435	35.46600	52.19215
U1-07A	23.90	-2.95	Mudstone	437	35.46597	52.19219
EV08-10	24.88	-3.40	Carbonate	474	35.46522	52.19215
U1-07B	24.99	-2.61	Mudstone	475	35.46548	52.19153
U1-08	23.78	-2.46	Mudstone	510	35.46508	52.19150
EV08-11	24.02	-4.19	Rhizolith	515	35.46497	52.19148
EV08-12	23.38	-3.34	Carbonate	518	35.46495	52.19138
U1-09	23.74	-2.54	Mudstone	567	35.46423	52.19090
EV08-13A	23.45	-4.19	Calcrete	570	35.46420	52.19082
EV08-13B	22.88	-5.24	Mudstone	571	35.46420	52.19082
EV08-14	23.66	-5.06	Carbonate	572	35.46420	52.19082
U1-09B	24.74	-3.23	Mudstone	578	35.46410	52.19081
U1-09C	24.64	-2.32	Mudstone	758	35.46327	52.18800
U1-10	24.47	-3.64	Mudstone	795	35.46161	52.18962
U1-09D	25.27	-4.14	Mudstone	818	35.46299	52.18581
U1-11	24.62	-2.87	Mudstone	828	35.46103	52.18830
EV08 15	23.29	-6.41	Mudstone	831	35.46257	52.18588
U1-09E	23.81	-3.14	Mudstone	835	35.46251	52.18581
EV08 17	22.63	-7.57	Calcrete	845	35.46273	52.18445
U1-13	24.49	-2.65	Mudstone	851	35.46229	52.18389
EV08 18	22.65	-6.30	Calcrete	852	35.46228	52.18378
U1-12	24.88	-2.45	Mudstone	855	35.45997	52.18653
U1-09F	24.40	-3.23	Mudstone	858	35.46235	52.18514
U1-14	24.43	-2.54	Mudstone	859	35.46233	52.18226
EV08 19	22.88	-5.21	Calcrete	860	35.46243	52.18180
EV08 20	22.77	-5.40	Rhizolith	868	35.46267	52.18078

U1-15	24.57	-2.87	Mudstone	885	35.46295	52.17831
U1-16	24.84	-2.50	Mudstone	1015	35.46152	52.17496
U1-17	25.21	-2.11	Mudstone	1320	35.45715	52.16834
EV08 58	24.90	-3.01	Mudstone	1324	35.45637	52.16712
U1-18	24.14	-3.50	Mudstone	1326	35.45604	52.16789
EV08 56	23.88	-5.03	Rhizolith	1334	35.45575	52.16843
EV08-59 *	23.46	-3.81	Carbonate	1350	35.45608	52.16708
EV08 57	24.03	-3.72	Mudstone	1362	35.45670	52.16735
U1-19	23.87	-4.15	Mudstone	1370	35.45561	52.16758
U1-20	24.96	-3.12	Mudstone	1415	35.45522	52.16712
EV08 55	23.72	-4.33	Carbonate	1420	35.45490	52.16763
EV08 21	23.06	-4.68	Carbonate	1424	35.45495	52.16734
U1-21	24.25	-3.03	Mudstone	1490	35.45384	52.16684
EV08 22	22.92	-5.64	Carbonate	1530	35.45353	52.16660
U1-22	24.63	-3.52	Mudstone	1540	35.45340	52.16677
U1-23	24.85	-3.98	Mudstone	1645	35.45138	52.16855
EV08 23	24.67	-4.20	Rhizolith	1728	35.44942	52.16685
EV08 24	23.66	-4.96	Rhizolith	1735	35.44918	52.16683
U1-25	23.64	-2.54	Mudstone	1748	35.44911	52.16688
U1-26	24.09	-4.10	Mudstone	1768	35.44859	52.16689
U1-27	24.32	-4.25	Mudstone	1790	35.44894	52.16522
EV08 25	23.80	-4.35	Mudstone	1805	35.44813	52.16673
U2-01	23.85	-2.89	Mudstone	1865	35.44612	52.16853
EV08 26	24.29	-3.42	Mudstone	1881	35.44875	52.16217
EV08 27	23.74	-3.92	Mudstone	1894	35.44820	52.16285
EV08 28	24.47	-2.94	Mudstone	1905	35.44828	52.16127
U2-03	23.41	-1.39	Mudstone	1910	35.44679	52.16293
EV08 29	24.58	-3.94	Carbonate	1912	35.44800	52.16135
U2-02 *	23.95	-3.26	Mudstone	1913	35.44621	52.16494
U2-04	24.17	-4.02	Mudstone	1916	35.44647	52.16315
U2-05	23.04	-4.22	Mudstone	1920	35.44616	52.16289
EV08 30	24.43	-5.78	Rhizolith	1925	35.44610	52.16188
U206	23.64	-4.32	Mudstone	1945	35.44446	52.16534
U207	24.29	-4.56	Mudstone	1990	35.44343	52.16586
EV08 33	23.30	-4.08	Rhizolith	2062	35.44330	52.15987
EV08 34	23.25	-5.62	Rhizolith	2110	35.44263	52.15902
U2-09	24.46	-4.61	Mudstone	2133	35.44098	52.16456
EV08 31 *	22.87	-5.57	Rhizolith	2138	35.44087	52.16453
EV08 32	23.49	-5.50	Rhizolith	2142	35.44078	52.16420
U2-10	25.38	-4.31	Mudstone	2182	35.44110	52.15904
U2-11	*24.86*	*-3.43*	*Mudstone*	*2212*	*35.44078*	*52.15775*
U2-11 T	*25.31*	*-4.18*	*Rhizolith*	*2212*	*35.44078*	*52.15775*
EV08 35	24.39	-4.43	Rhizolith	2218	35.44072	52.15765
EV08 36 *	24.51	-4.39	Rhizolith	2235	35.44052	52.15733
U2-12	24.14	-3.63	Mudstone	2238	35.44047	52.15739
EV08 37	23.39	-4.96	Rhizolith	2355	35.43862	52.15595
U2-13	*23.92*	*-4.77*	*Mudstone*	*2358*	*35.43859*	*52.15587*
U2-13 T	*23.70*	*-4.79*	*Rhizolith*	*2358*	*35.43859*	*52.15587*
EV08 38	24.08	-5.05	Rhizolith	2500	35.43658	52.15347
EV08 39A	*23.59*	*-4.83*	*Carbonate*	*2595*	*35.43417*	*52.15340*
EV08 39 B	*23.30*	*-6.57*	*Rhizolith*	*2595*	*35.43417*	*52.15340*
U2-15	25.20	-3.92	Mudstone	2610	35.43485	52.15120
EV08 40	23.60	-5.43	Carbonate	2704	35.43350	52.15073
U2-16	25.55	-4.22	Mudstone	2709	35.43342	52.15057
U2-17	*24.34*	*-3.77*	*Mudstone*	*2780*	*35.43212*	*52.15029*
U2-17-T	*23.03*	*-4.95*	*Rhizolith*	*2780*	*35.43212*	*52.15029*
U2-18	23.95	-5.02	Mudstone	2812	35.43045	52.15183
U2-19	24.27	-3.83	Mudstone	2885	35.42904	52.15118
EV08 41	23.17	-6.29	Carbonate	2949	35.42903	52.14718
U2-20	24.37	-3.44	Mudstone	2954	35.42889	52.14721
U2-21	25.49	-3.81	Mudstone	2975	35.42843	52.14668
EV08 42	24.33	-4.91	Calcrete	2981	35.42830	52.14678
U2-22	23.94	-4.23	Mudstone	2983	35.42823	52.14668
U2-23	23.97	-4.49	Mudstone	3020	35.42768	52.14655
U2-24	23.66	-3.75	Mudstone	3105	35.42648	52.14491
U2-25	*24.10*	*-5.02*	*Mudstone*	*3132*	*35.42606*	*52.14442*
U2-25 T	*22.34*	*-4.64*	*Rhizolith*	*3132*	*35.42606*	*52.14442*

EV08 43	23.09	-4.60	Rhizolith	3164	35.42533	52.14450
U2-26	24.79	-3.76	Mudstone	3171	35.42526	52.14436
U2-27	23.78	-4.01	Mudstone	3189	35.42465	52.14486
EV08 44	21.66	-4.46	Rhizolith	3199	35.42462	52.14448
U2-28	*22.94*	*-3.65*	*Mudstone*	*3210*	*35.42400*	*52.14526*
U2-28 T	*21.54*	*-2.74*	*Rhizolith*	*3210*	*35.42400*	*52.14526*
EV08 45 *	22.61	-3.97	Rhizolith	3285	35.42252	52.14477
U2-30	24.70	-3.55	Mudstone	3295	35.42218	52.14515
EV08 46	21.26	-5.11	Rhizolith	3320	35.42188	52.14505
U2-31	24.17	-3.72	Mudstone	3425	35.42013	52.14508
U2-32	24.36	-4.72	Mudstone	3485	35.41931	52.14527
U2-33	24.63	-2.88	Mudstone	3505	35.41780	52.14322
EV08 47	19.64	-7.07	Rhizolith	3618	35.41560	52.14372
U2-35	*24.00*	*-4.33*	*Mudstone*	*3628*	*35.41533*	*52.14377*
U2-35 T	*21.68*	*-4.44*	*Rhizolith*	*3628*	*35.41533*	*52.14377*
U2-34	24.42	-3.42	Mudstone	3635	35.41534	52.14338
EV08 48	21.91	-3.96	Rhizolith	3640	35.41530	52.14332
U2-36	*24.17*	*-3.03*	*Mudstone*	*3672*	*35.41428*	*52.14432*
U2-36 T	*21.56*	*-3.41*	*Rhizolith*	*3672*	*35.41428*	*52.14432*
EV08 49	20.52	-4.46	Rhizolith	3682	35.41042	52.15163
EV08 50	22.51	-4.43	Rhizolith	3718	35.40973	52.15155
U3-01 R	24.50	-3.49	Mudstone	3726	35.40962	52.15158
U3-02	24.23	-1.93	Mudstone	3779	35.40860	52.15152
U3-03	24.23	-3.24	Mudstone	3829	35.40706	52.15293
U3-04	23.68	-4.12	Mudstone	3925	35.40554	52.15186
U3-05	23.66	-3.84	Mudstone	4010	35.40425	52.15119
U3-06	23.08	-2.31	Mudstone	4090	35.40251	52.15157
U3-07	23.84	-4.08	Mudstone	4125	35.40234	52.15123
U3-08	24.34	-4.40	Mudstone	4195	35.40072	52.15106
U3-09	24.26	-4.03	Mudstone	4240	35.39966	52.15056
U3-10	24.39	-1.65	Mudstone	4355	35.39804	52.14976
U3-11	24.77	-2.34	Mudstone	4415	35.39708	52.14905
U3-12	23.74	-2.61	Mudstone	4448	35.39575	52.14850
U3-13	22.83	-4.09	Mudstone	4535	35.39507	52.14787
U3-14	25.28	-1.33	Mudstone	4750	35.39282	52.14662
U3-15	24.71	-2.30	Mudstone	4770	35.39108	52.14578
U3-16	22.89	-3.78	Mudstone	4835	35.39035	52.14453
U3-17	24.40	-2.82	Mudstone	5000	35.38797	52.14200
U3-18	23.33	-3.80	Mudstone	5065	35.38639	52.14229
U3-19	24.31	-2.62	Mudstone	5108	35.38644	52.14020
U3-20	23.57	-3.57	Mudstone	5135	35.38547	52.13937
EV08 51	21.98	-4.19	Rhizolith	5155	35.38527	52.13923
EV08 52	21.16	-3.76	Rhizolith	5158	35.38508	52.13900
U3-21	23.66	-4.50	Mudstone	5160	35.38501	52.13901
EV08 53	20.99	-4.29	Rhizolith	5175	35.38470	52.13870
EV08 54	21.90	-3.66	Rhizolith	5201	35.38425	52.13822
U3-22	24.17	-2.82	Mudstone	5215	35.38407	52.13820
U3-23	22.71	-3.98	Mudstone	5319	35.38233	52.13692
U3-24	24.02	-3.74	Mudstone	5360	35.38149	52.13658
U3-25	21.56	-5.20	Mudstone	5420	35.38111	52.13461
U3-26	23.87	-1.88	Mudstone	5500	35.38069	52.12976
U3-27	22.71	-3.69	Mudstone	5545	35.37980	52.12960
U3-29	21.67	-4.90	Mudstone	5590	35.37897	52.12876
U3-30 T	20.32	-5.01	Rhizolith	5633	35.37783	52.12854
U3-31	21.60	-4.35	Mudstone	5660	35.37684	52.12793
U3-32	23.40	-3.42	Mudstone	5875	35.36902	52.13440
U3-33	*23.62*	*-3.82*	*Mudstone*	*5900*	*35.36826*	*52.13506*
U3-33 T	*20.97*	*-5.80*	*Rhizolith*	*5900*	*35.36826*	*52.13506*
U3-34 T	19.91	-6.70	Rhizolith	5902	35.36820	52.13506
U3-35	21.45	-5.03	Mudstone	5925	35.36791	52.13484
U3-36	24.57	-2.57	Mudstone	5990	35.36691	52.13244
U3-37	23.85	-3.67	Mudstone	6005	35.36709	52.13010
U3-38	22.71	-3.45	Mudstone	6062	35.36585	52.13036
U3-39	*21.95*	*-4.70*	*Mudstone*	*6112*	*35.36574*	*52.12823*
U3-39 T	*20.63*	*-6.23*	*Rhizolith*	*6112*	*35.36574*	*52.12823*
U3-41	22.75	-4.31	Mudstone	6133	35.36378	52.12631
U3-40	22.77	-4.02	Mudstone	6145	35.36489	52.12815

U3-42	23.94	-3.00	Mudstone	6301	35.36274	52.12556
U3-43	23.22	-3.21	Mudstone	6350	35.36230	52.12466
U3-44	23.56	-3.17	Mudstone	6393	35.36267	52.12162
U3-45	22.15	-4.55	Mudstone	6425	35.36168	52.12073
U3-46	22.34	-3.35	Mudstone	6455	35.36151	52.11997